EUROPEAN ORGANIZATION FOR NUCLEAR RESEARCH

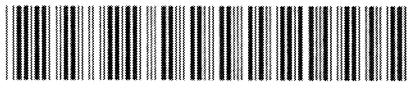

CERN/AC/95-05 (LHC)
20 October 1995

LHC

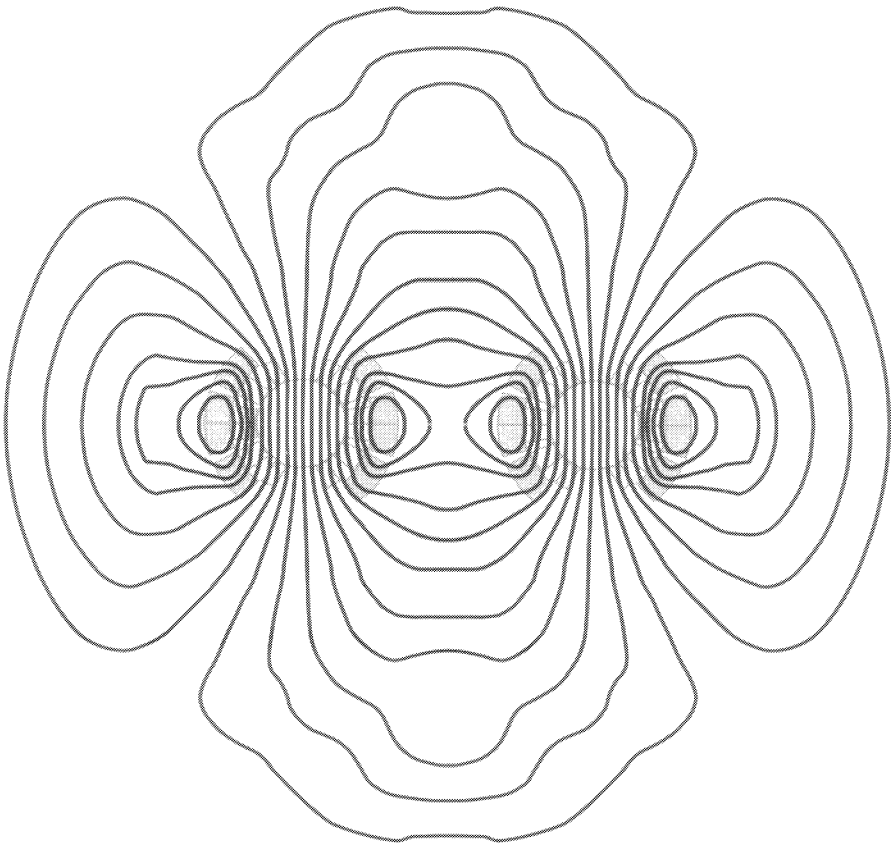

THE LARGE HADRON COLLIDER

Conceptual Design

The LHC Study Group

EUROPEAN ORGANIZATION FOR NUCLEAR RESEARCH

CERN/AC/95–05(LHC)
20 October 1995

THE LARGE HADRON COLLIDER

Conceptual Design

The LHC Study Group

Editors: P. Lefèvre
T. Pettersson

Sub-editors: D. Boussard
L. Evans
J. Gareyte
B. Jeanneret
J.P. Koutchouk
Ph. Lebrun
A. Mathewson
R. Perin
P. Proudlock
C. Rufer
K. Schindl
T. Taylor
E. Weisse

CERN Desktop Publishing Service
Cover by V. Frigo, CERN
Printed at CERN

Abstract

The Large Hadron Collider (LHC) project was approved by the CERN Council in December 1994. The machine will provide proton–proton collisions with a centre-of-mass energy of 14 TeV and a luminosity of 10^{34} cm^{-2} s^{-1}. It will also provide heavy (Pb) ion collisions with a centre-of-mass energy of more than 1000 TeV and a luminosity in excess of 10^{27} cm^{-2} s^{-1}.

The last version of the LHC design study, the so-called 'White Book', was published in November 1993. Since then, the design has considerably evolved and matured as a consequence of more detailed studies and cost comparisons, together with the results obtained from models and prototypes. The present document incorporates all changes with respect to the 'White Book' and will now serve as the basis for the detailed engineering design of the Large Hadron Collider.

Acknowledgements

The first joint CERN–ECFA study on the feasibility of constructing the LHC in the LEP tunnel took place more than ten years ago (Lausanne 1984). Since then, a considerable number of people have contributed to the LHC design study. In order to avoid errors or omission these people are not named individually, although their contributions are implicitly acknowledged in the references at the end of each section, and I thank them all.

I would like to thank the editors Pierre Lefèvre and Thomas Pettersson, and also the Desktop Publishing Service for their professionalism and patience in putting together this document.

Above all, I would like to thank Giorgio Brianti for his many years of dedicated work on this project, and for providing us with such a solid foundation on which to build.

L. Evans

Contents

Part I
Overview of the project

1 Introduction

Since the publication of the last design study of the LHC, the so-called 'White Book' [1] in November 1993, the machine design has been refined and a considerable number of modifications have been incorporated, although the main technical choices, namely a two-in-one magnet structure operating in superfluid helium, remain unchanged. In view of these modifications, it was therefore considered worthwhile to publish a new conceptual design of the LHC as an intermediate step towards a detailed engineering design report. The main changes are outlined below.

- The LHC will be installed on the tunnel floor after removing LEP instead of above the LEP ring as originally foreseen. This change simplifies the installation and removes the constraint that the LHC must exactly follow the geometry of LEP. The main advantage of this is that the dipoles in the dispersion suppressors can be identical to the arc dipoles. However, in order to preserve the e–p option, care will be taken to keep enough space free above the machine to allow the future installation of a lepton ring using existing LEP components.

- The number of crossing points where the beams pass from one ring to the other has been reduced from eight to four, in order to reduce costs and to better optimize the utility insertions containing RF, collimation and beam dump systems.

- The separation between the beams has been increased from 180 to 194 mm. This has many advantages including a lower collaring force needed during dipole fabrication. It also allows the design of the lattice quadrupole to be based on the same cable as the outer layer of the dipole, and makes the design of the enlarged quadrupoles in the beam dump insertion easier.

- The design of the collimation insertions now incorporates classical instead of superconducting magnets which are much more robust against beam loss on the collimators and considerably reduce the cryogenic infrastructure needed. A second collimation insertion has been added in order to improve efficiency.

- The beam dump insertion design has been modified in order to reduce considerably the number of fast pulsed magnets required to extract the beams.

- The insertion containing the radio-frequency system has been modified to allow the installation of separate cavities for the two beams instead of a common RF system. This reduces the beam loading by a factor of two and increases the flexibility of the system.

- The regular lattice period has been stretched by about 4.9 m, thus reducing the number of periods per octant from 24 to 23. This reduces the number of dipole units by 48 and the number of quadrupoles by 16. The dipole length has also been increased from 13.14 m to 14.2 m (magnetic) with a consequent reduction in the field needed for 7 TeV operation from 8.65 T to 8.36 T, giving an increased quench margin.

- The powering of the lattice quadrupoles has been separated from that of the dipoles in order to give more flexibility and to reduce costs by obviating the need for tuning quadrupoles. This also liberates valuable space to increase the integrated bending field.

- All heavy-current power supplies are concentrated at the even points where underground infrastructure for their installation already exists. Consequently the quadrupoles in the dispersion suppressors are powered in series with the lattice quadrupoles, and the tuning of the suppressors is carried out using separate low-current trim quadrupoles.

- Much of the cryogenic piping has been moved into a separate cryogenic distribution line (CDL) instead of being integrated into the magnet cryostat. This allows the diameter of the cold pumping line required for the production of primary superfluid helium to be increased such that it is possible to locate the cold compressor boxes and all eight cryogenic plants at the four even points. Together with the change of the power supply layout mentioned above, this results in a considerable reduction of civil engineering and infrastructure costs at the odd points. The extra cost of the CDL is offset by this saving, and results in a much more flexible and modular system.

- The allocation of straight sections for experiments and some utilities has been changed. The most important of these is the decision to interchange the beam dump originally foreseen to be at point 5, and the high luminosity p–p insertion at point 6, in order to allow civil engineering work on the experimental insertion to proceed with minimum perturbation to the LEP programme, and to maximize the use of the existing infrastructure.

- The transfer line between the SPS and the LHC for the clockwise rotating beam has been considerably modified. In the previous version the beam was extracted from point 5 of the SPS and injected into point 1 of the LHC, minimizing the tunnel length but requiring high field superconducting magnets on a steep slope. It has been found to be more economical to move the extraction to point 6 of the SPS, where an extraction system already exists, and to inject into point 2 of the LHC. This results in a considerably longer transfer tunnel but the increased cost is more than offset by the fact that the superconducting magnets foreseen for both beam lines can be replaced by classical magnets of a compact design.

- The naming convention has been adapted in order to bring it more into line with standard practice at the SPS and LEP. The new list of element names is given in Annex 2.

2 Machine performance

The main performance parameters for p–p operation remain unchanged when compared with the previous version [1], and are shown in Table 1. The design luminosity is

10^{34} cm^{-2} s^{-1} with simultaneous collisions at the two high-luminosity insertions. Increasing the number of simultaneously illuminated collision points would reduce the luminosity in these insertions.

In addition to p–p operation, the LHC will be able to collide heavy nuclei (Pb–Pb) produced in the existing CERN accelerator complex, giving an energy of 1150 TeV in the centre of mass (2.76 TeV/u and 7.0 TeV per charge). By modifying the existing antiproton ring (LEAR) into an ion accumulator in which strong electron cooling is applied, the peak luminosity can reach more than 10^{27} cm^{-2} s^{-1}. One important change compared to the previous design is the change of bunch spacing for ions from 135 ns to 125 ns, a multiple of the 25 ns bunch spacing for protons, in order to make the beam diagnostic electronics and experimental triggers compatible for both modes of operation.

The present study is limited to the proton–proton and ion options for the LHC. However, preliminary work on the e–p option reusing LEP components has shown that luminosities in excess of 10^{32} cm^{-2} s^{-1} could be achieved.

Table 1: LHC performance parameters

Energy	[TeV]	7.0
Dipole field	[T]	8.4
Coil aperture	[mm]	56
Distance between apertures	[mm]	194
Luminosity	[cm^{-2} s^{-1}]	10^{34}
Beam–beam parameter		0.0034
Injection energy	[GeV]	450
Circulating current/beam	[A]	0.54
Bunch spacing	[ns]	25
Particles per bunch		10^{11}
Stored beam energy	[MJ]	334
Normalized transverse emittance	[μm.rad]	3.75
r.m.s. bunch length	[m]	0.075
β-values at I.P. in collision	[m]	0.5
Full crossing angle	[μrad]	200
Beam lifetime	[h]	22
Luminosity lifetime	[h]	10
Energy loss per turn	[keV]	6.7
Critical photon energy	[eV]	44.1
Total radiated power per beam	[kW]	3.6

3 Layout

The basic layout of the machine (Fig. 1) mirrors that of LEP, with eight straight sections each approximately 528 m long, available for experimental insertions or utilities. The two high-luminosity insertions are located at diametrically opposite straight sections, point 1

(ATLAS) and point 5 (CMS). Two more experimental insertions are located at point 2 (ALICE Pb ions) and point 8 (B physics). These latter straight sections also contain the injection systems. The beams cross from one ring to the other only at these four locations.

The remaining four straight sections do not have beam crossings. Insertions 3 and 7 each contain two beam collimation systems using only classical magnets. These insertions are designed to be robust against the inevitable beam loss on the primary collimators, and to keep the amount of new infrastructure needed to an absolute minimum.

Insertion 4 contains the RF systems, which have now been separated for the two beams. The section can either be dedicated to RF or, at somewhat higher cost, space can be liberated to allow coexistence with a future experimental collision point.

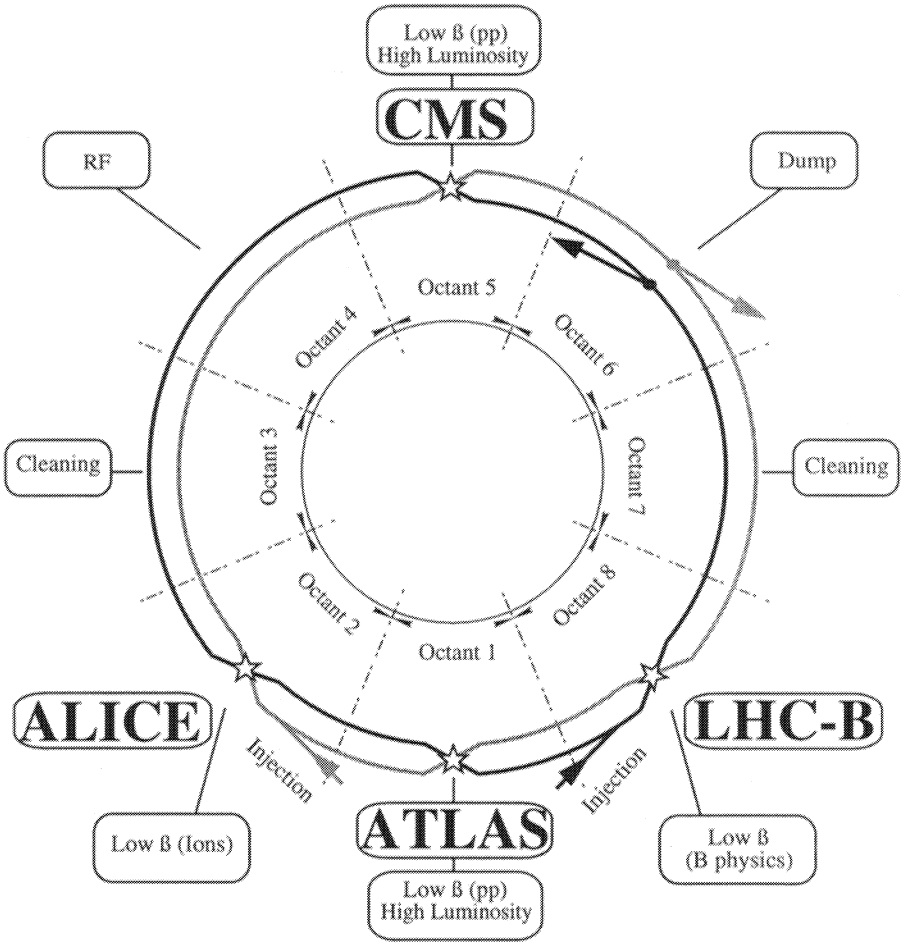

Figure 1: Schematic layout of the LHC

Finally, the straight section at point 6 contains the beam dump insertion. The beams are now extracted vertically from the machine using a combination of horizontally-deflecting fast-pulsed ('kicker') magnets and vertically-deflecting double-steel septum magnets.

4 Injectors and injection

The existing accelerator chain (Linac/Booster/PS/SPS) will be used for LHC injection. In order to achieve the emittance, intensity, and bunch spacing required, some modifications to the PS and Booster are necessary. In the Booster a new harmonic $h = 1$ system will be needed for acceleration with a superimposed $h = 2$ system for bunch shaping in order to minimize space-charge effects. In addition, the Booster's top energy will be upgraded from 1 GeV to 1.4 GeV in order to reduce space-charge effects at the PS injection.

In the PS the main hardware addition will be harmonic $h = 84$ (40 MHz) and $h = 168$ (80 MHz) RF systems for rebunching the beams with the 25 ns time structure for the LHC. In the SPS the main addition is a 400.8 MHz superconducting system (6 MV) in order to match the bunches to the LHC buckets, and possibly an 80 MHz (700 kV) RF system for capturing the injected beam.

A new extraction system at point 4 of the SPS is needed. Both injections into the LHC are made horizontally into the outside rings.

The filling sequence starts with three bunch trains injected into the SPS on three successive PS cycles at 3.6 s intervals, filling one third of the SPS circumference. The SPS then accelerates the beam to 450 GeV and transfers each batch (containing 2.4 10^{13} protons) to one or the other of the LHC rings. This is repeated 12 times per ring with a cycle time of 16.8 s. Once both rings are filled the beams are accelerated to nominal collision energy in about 20 min.

5 Magnets and cryogenics

Extensive model and prototype work has validated the main technical choices for the dipole design, namely the two-in-one concept where both magnetic channels are incorporated into a single iron yoke and cryostat, and cooled with superfluid helium in order to achieve the very high guide field required. Following positive experience with long prototypes, combined aluminium collars have been chosen instead of the alternative stainless steel ones in order to minimize the pre-stress required at room temperature, and to ensure the best possible parallelism between the dipole fields in the two channels.

Because of the modifications made to the lattice the dipole length has been increased to 14.2 m (magnetic), and the packing factor improved to give a reduction of about 0.3 T in nominal field with a consequent increase in margin. The quadrupole design concept remains unchanged except that decoupling the powering of the dipole and quadrupole allows more freedom for optimizing the coil design.

The principle of the cryogenic system is unchanged. The main layout modification with respect to the previous design is the concentration of the eight 18 kW cryogenic plants in pairs at the four even points where adequate infrastructure, including cooling towers and compressor buildings, already exist. The decision to move the cryogenic piping to a separate cryoline instead of integrating it in the magnet cryostat also allows the cold compressor boxes to be concentrated at the even points, thus considerably reducing civil engineering and infrastructure requirements at the odd points. The principle of the superfluid cooling scheme has now been validated on a simulation half-cell of the machine

(the string test facility). Experimental results from this facility may still modify some details of the design, for example the number and location of the quench relief valves.

6 Conclusions

The conceptual design of the LHC has now progressed to a point where the major technical decisions have been made. The following sections describe the machine layout and performance parameters, as well as the preliminary design of most of the major systems. This report will now serve as the basis for the detailed engineering design of the machine which will be described in the final design report to be published by the end of 1996.

References

[1] The Large Hadron Collider Accelerator Project, LHC CERN AC/93–03.

Part II

Technical description

1 Lattice and geometry

1.1 Introduction

The LHC layout is defined and constrained by the LEP tunnel geometry. The machine is constituted of eight bending arcs separated by eight insertions. In all of the insertion points (middle of the insertion) irrespective of their use, the reduction of the horizontal dispersion is achieved by 16 almost identical dispersion suppressors located at either end of the arcs. The two counter-rotating beams are separated horizontally by 194 mm in most of the machine, and are channelled through the same twin-bore magnets. The beams are exchanged from the inner to the outer ring and vice versa at points 1, 2, 5 and 8 (see Fig. 1 in Part I), where they collide. Their path lengths are therefore exactly identical. Before and after collision, the beams are brought together or separated by separation/recombination dipoles. At the crossing points, they intersect at an angle of 200 μrad.

LHC layout definitions

The description of the LHC is facilitated by introducing the following definitions:

- **Rings and beams**
  There are two rings, one ring per beam. Beam 1 refers to the beam circulating clockwise, beam 2 refers to the beam circulating anticlockwise.

- **Right and left**
  Describes the position in the tunnel (observer is inside looking out), same definition as in LEP.

- **Upstream/downstream**
  Always related to the direction of one of the two beams, if no beam (beam 1 or beam 2) is explicitly stated, beam 1 is taken as the default. This implies that stating a position as being 'upstream' without indicating any beam, is equivalent to stating that the position is to the left and vice versa.

- **Arc**
  The part of the ring occupied by regular half-cells with three dipoles and one quadrupole; does not contain the dispersion suppressor (DS).

- **Insertions (IR)**
  An insertion is the part of a ring between two arcs. It consists of one dispersion suppressor, one full straight section, and a second dispersion suppressor.

- **Straight sections**
  The term 'straight section' is reserved for the long quasi-straight sections between the upstream and downstream dispersion suppressors, including the separation/recombination magnets.

- **Insertion Point (IP)**
  Middle of the insertion, which is also an **Interaction Point** in those straight sections where the beams cross. The IPs are numbered IP1, IP2,..,IP8.

- **Sector**
  The part of a ring between two successive insertion points is called a sector. Sector 1–2 is situated between IP1 and IP2.

- **Octant**
  An octant starts in the centre of an arc and goes to the centre of the next downstream arc. An octant is constituted of an upstream and a downstream half-octant. A half-octant and a half-sector cover the same part of the collider even though they may not have the same number.

Table 1 below, and Fig. 1 in Part I show the current allocation of the intersection (or insertion) points for LEP 200 and the LHC.

Table 1: Allocation of the intersection points

Intersection point	Tunnel		LEP 200	LHC
	Depth (m)	Slope (%)		
I (Meyrin)	82.0	1.23	Injection in arcs	ATLAS
II (St Genis)	45.3	1.38	L3 and RF	ALICE and Injection
III (Crozet)	97.5	0.72		Cleaning
IV (Echenevex)	137.6	0.36	ALEPH and RF	RF
V (Cessy)	86.6	1.23		CMS
VI (Versonnex)	95.0	1.38	Opal and RF	Dump
VII (Ferney)	94.0	0.72		Cleaning
VIII (Mategnin)	98.8	0.36	Delphi and RF	LHC-B and Injection

The general numbering of the elements in the LHC is closely linked to the cell numbering scheme and the numbering of the quadrupoles within the cells. There are up to 33 quadrupoles per half-sector, numbered from 1 to 33 starting from an experimental IP to the mid-arc position as shown in Fig. 1.

For a non-crossing insertion, the quadrupoles are numbered from 2 or 3 to 33.

The separation or recombination dipoles are numbered D_1 to D_4 starting from the IP; D_1, D_2 are close to the IP and D_3, D_4 are close to the DS.

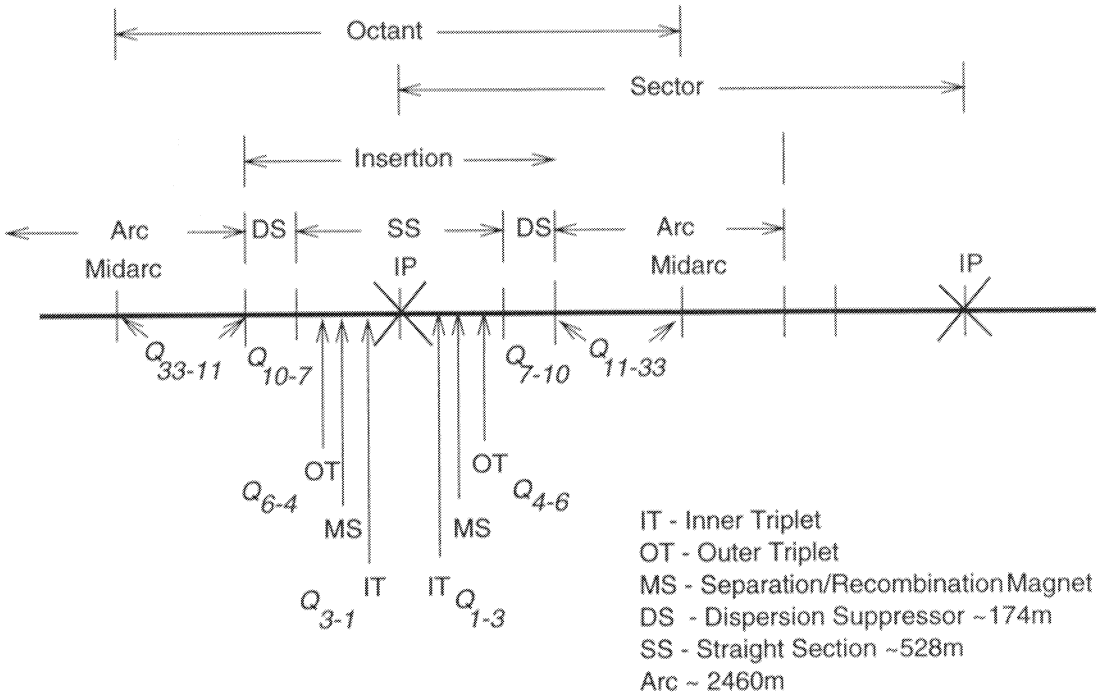

Figure 1: LHC definitions and conventions for quadrupole numbering

1.2 Lattice evolution

The present version of the LHC lattice is version 4.1 [1]. The preceding versions of the design are listed below with their essential features:

- **LHC version 1:** This version, studied in depth [2], features a dipole of 9.00 m length yielding 25 cells per arc with four dipoles per half-cell. It is the basis of the 'Pink Book' [3].
- **LHC version 2:** In version 2, the dipole length was increased to 13.145 m, yielding 24 cells per arc with three dipoles per half-cell. An enhancement of the β-beating associated with the coupling compensation caused difficulties in restoring the dynamic aperture. This version was the basis for the 'White Book'.
- **LHC version 3:** This was a test [4] of the longest possible dipole, i.e. 15.574 m, giving 21 cells/arc. The dynamic aperture was found to be marginal and the implementation of the long dipole difficult.
- **LHC version 4:** The dipole magnetic length is now 14.2 m, which yields 23 cells per arc. Using the experience accumulated in the study of the previous versions, these parameters appear to be a good compromise between an industrially achievable dipole length and dynamic aperture.

In addition to the change of the dipole length, this version of the lattice contains a significant modification of the machine layout: the beams collide at four points instead of eight. The other straight sections are used for machine utilities (RF acceleration, collimation, and dump). The beams are injected in the outer ring in Insertions 2 and 8 (see Fig. 1 in Part I). The cleaning insertions are now made of warm quadrupoles.

A first lattice was published as version 4.0 [5]. While version 4.0 was being developed, several ideas related to new constraints and standardization of the hardware emerged, and have now been implemented in version 4.1.

Differences in specifications relative to LHC lattice reference version 2

The following list summarizes the main differences between the former reference version 2 of the LHC and this, the present version 4.1.

1. **Crossings:** The two channels cross only where required, i.e. at points 1, 2, 5, and 8, thus reducing the super-periodicity from 4 to 1.

2. **Dipole length:** The magnetic length of the dipole was increased from 13.145 m to 14.2 m. The magnetic length is defined in operating conditions, i.e. at low temperature, for superconducting magnets. With three dipoles per half-cell, an arc is completely filled with 23 lattice cells.

3. **Cell quadrupoles:** In version 2, the arc cell quadrupoles were connected in series with the arc dipoles. The complementing cell tuning quadrupoles have been suppressed and the arc cell quadrupoles are now separately powered in series with an additional power supply for trimming between the focusing and defocusing circuits.

4. **Dispersion suppressor quadrupoles:** These elements are powered in series with the arc quadrupoles and complemented with individually powered trim quadrupoles.

5. **Connection space between cell quadrupole and dipole:** The available space between the short straight section assembly and the first dipole was increased from 299 mm to 520 mm to create the necessary installation conditions for the connections. As a consequence of these cell modifications, the arc length increases by 10.16 m, keeping the length of all other elements fixed.

6. **Centering of the cell quadrupoles:** Until the present lattice version the quadrupoles were not centred with respect to the bending centre of the dipoles within a cell. Because of the LHC antisymmetry, the cells of two consecutive arcs were mirror-symmetric and thus different. Centering the quadrupoles with respect to the bending centre of the dipoles yields identical cells in all arcs, thus reducing complexity. The price to pay is a tiny reduction of the length of the sextupole/dipole corrector magnet (4%), which, at this stage, seems acceptable.

7. **Suppression of the short dipoles:** The proposed idea of standardizing the dipole length in the arc and dispersion suppressors was implemented.

8. **Injection from outside:** The injection into Ring 1 was moved from IR1 in the inside ring (version 4.0) to IR2 in the outside ring which is a more advantageous configuration.

9. **Service insertions:** The cleaning, dump, and RF insertions are no longer variations of the general-purpose low-β insertion, but strictly tailored to their functionalities. The quadrupoles of the cleaning insertions are warm, providing an increased resistance to radiation. The minimization of the β-function at the interaction points was given high priority whilst the phase advance over the insertions was left free.

The optics functions of the experimental insertions retain the main features of the previous versions. They are all somewhat different with respect to quadrupole positions, gradients, and lengths. This is due to a large sensitivity of the optical matching to boundary conditions given the limited number of optical parameters and the tight space for insertions.

1.3 Geometry

Position of the LHC in the tunnel relative to LEP

The LHC arcs tend to be at the exterior of the theoretical position of the LEP machine by up to 4 cm (see Fig. 2). There is a larger excursion in the opposite direction in the dispersion suppressor by –10 cm due to the longer dipole magnets. This occurs 16 times over about 100 m and seems acceptable at this stage in the design work. It is not excluded that further optimization will decrease this excursion. The LHC circumference is kept equal to the present LEP circumference. This condition is optimum for SPS/LHC transfers, but may be slightly relaxed if necessary.

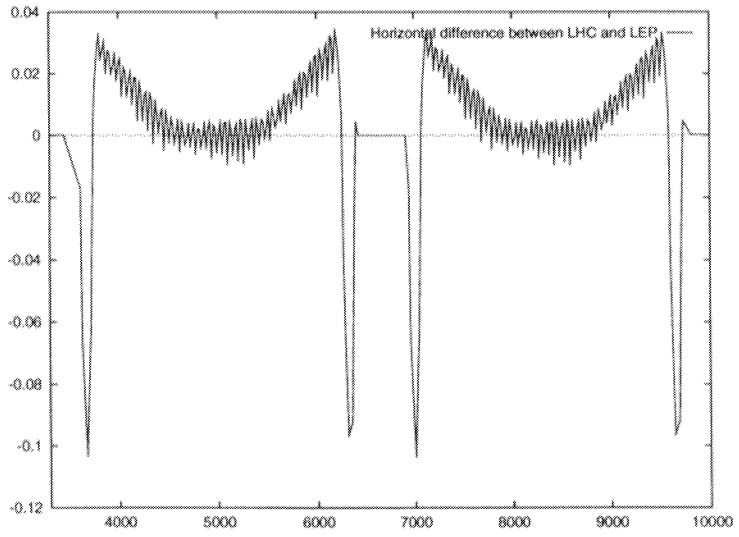

Figure 2: Horizontal position of the LHC compared with LEP in one quadrant in metres

Survey and alignment

To avoid any inconsistencies between the actual geometry of LEP, the existing tunnel, and the geometry of the LHC, the geodetic network based on LEP quadrupole sockets will be re-checked before being transferred to the floor of the tunnel. The initial positioning and alignment of the LHC components will be carried out using this new geodetic network. A final smoothing will then be made directly on the reference targets.

Two fiducial targets as well as a tilt reference will be installed on each cryostat. For the dipoles, their position will be measured with respect to the median geometrical axis of the two beam channels. The tilt reference will refer to the median magnetic plane. For the quadrupoles, the median magnetic axis of the two magnets will be the reference for defining the position of the fiducial references.

A particular effort is in progress in order to study the stability of the cold mass inside the cryostat with respect to the fiducial points used for alignment. The supporting system of the cryostats and the interconnections is designed to allow the positions of the cryostats to be adjusted in the tunnel when the magnets are cooled down and connected.

Special attention will be given to the alignment of the inner triplet quadrupoles, (low-β sections), which require a direct reference line through the experimental equipment. Optical systems operating in the vacuum pipe as well as stretched wire techniques can be used for this purpose.

References

[1] J.P. Koutchouk, R. Ostojic, T. Risselada, C. Rufer, W. Scandale, S. Weisz, The lattice layout and optics of LHC version 4.1, CERN SL/Note 95–38 (AP) and LHC Note 318.

[2] W. Scandale, The lattice of the LHC: version 1, CERN SL/91–03 (AP) and LHC Note 139 (1991).

[3] The 'Pink Book': Design study of the Large Hadron Collider, CERN 91–03 (1991).

[4] X. Luo, F. Méot, W. Scandale, The LHC lattice, version 3, SL/Note 94–28 (AP) (1994).

[5] A. Garren, X. Luo, F. Méot, W. Scandale, The LHC lattice, version 4.0, SL/Note 95–06 (AP) and LHC Note 314 (1995).

2 Optics and layout

The complete LHC lattice is composed of a succession of arcs and insertions, with the optics function of each insertion adapted to its particular use. The strong focusing of the low-β insertion requires the 'inner' quadrupole triplets to be positioned between the recombination and the collision point. They are therefore designed to have a single beam channel, focusing one beam when defocusing the other. In spite of this asymmetry, the two counter-rotating beams will see the same sequence of focusing and defocusing lenses by powering the 'inner' quadrupole triplets antisymmetrically around the interaction points. This antisymmetry is respected in the rest of the machine resulting in an exchange of the horizontal and vertical betatron planes from ring to ring, and octant to octant of the same ring.

This design concept requires equal horizontal and vertical emittances and provides round beams at the collision points. The main parameters of the layout and the optics functions are shown in Table 1.

Table 1: Layout and optics parameter list for the LHC

Parameter	Symbol	Unit	450 GeV/c	7000 GeV/c
Machine circumference	$2\pi R$	[m]	26658.883	
Number of arcs (pseudo-periodicity)			8	
Symmetry			Mirror/IP1–IP5	
Super-periodicity			1	
Lattice type			FODO, 2-in-1	
Ring separation		[mm]	194	
Number of lattice cells per arc			23	
Number of insertions			8	
Number of experimental insertions			4	
Free space for detectors (IP1/IP5)		[m]	$\pm$23	
Free space for detectors (IP2/IP8)		[m]	$\pm$21	
Total crossing angle at IP	Φ	[μrad]	200	
Guide field	$\mathcal{B}$	[T]	0.539	8.386
Bending radius	ρ	[m]	2784.32	
γ transition			53.7	
Momentum compaction	α		0.0003473	
Maximum β-value at injection		[m]	622	
Horizontal betatron tune	Q_x		63.28	
Vertical betatron tune	Q_y		63.31	
Length of the lattice cell	$2L$	[m]	106.92	
Nominal phase advance/cell	μ	[degree]	90	
Maximum β-value (cell)		[m]	182.7	
Maximum dispersion (cell)		[m]	2.15	
Transverse beam size (1 σ) in arc		[mm]	1.20	0.303
β at IP	β^*	[m]	6.0	0.50
Transverse beam size (1σ) at IP		[μm]		15.9
Transverse beam divergence at IP		[μrad]		31.7
Maximum β-value in exp. insertion		[m]	450	4423

Note that the relative position of the elements in the arc cells are identical but that in the insertions the element positions are mirrored around the IP. For the dispersion suppressor and straight section layout descriptions, the figures and the text refer to the part situated to the left of the IP. The length of the elements is the magnetic length at 1.9 K.

2.1 The arcs

The LHC circumference is made of eight arcs separated by insertions. Each of the eight arcs is composed of 23 arc cells, giving a total arc length of 2456.160 m. All arc cells are made of two identical half-cells (see Fig. 1) [1].

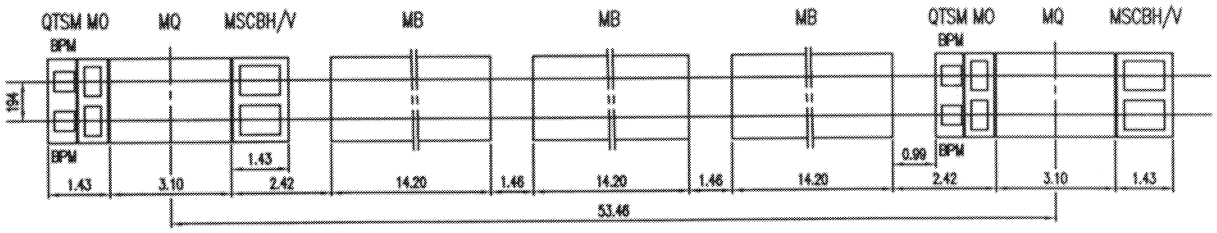

Figure 1: Layout of the arc half-cell

In the middle of each arc the sextupole corrector has been removed to leave space for a cryogenics cold feedbox. The impact on the beam dynamics of the removal of the sextupole has been evaluated and shown to be not significant [1]. However, the combined orbit corrector cannot be eliminated and at most a small reduction of its integrated strength would be acceptable.

The arc cell

The layout of an arc half-cell is shown in Fig. 1. It consists of a string of three 14.2 m twin-aperture dipoles and one 3.10 m quadrupole separated from the string by 2.42 m. The separation between the dipoles is 1.46 m, which includes 520 mm for connections between the cryostats. In the shadow of the dipole magnet ends, sextupole and decapole correctors are located on the right and left side, respectively. The bending centre of the three dipoles is therefore in the middle of the half-cell, eliminating the previous difference between the 'odd' and 'even' half-cells.

The arc quadrupole assembly has on its left side a beam position monitor (BPM) and an octupole, and on its right side a combined sextupole/dipole corrector. This layout is the same everywhere in the machine except in the mid-arc positions where, as already mentioned, the sextupole is removed to make room for a possible mid-arc cryogenic box.

The arc quadrupole cryostat vessel is symmetrical with respect to the quadrupole centre. Compared to version 1, the length of the sextupole/dipole corrector is reduced

[1] For symbol definitions, see Annex 2

by 4%, which is believed to be acceptable. Final values for the multipole strength will depend on the exact optics and should include requirements from the dynamic behaviour of the machine, yet to be estimated. The optical functions in the cell are shown in Fig. 2.

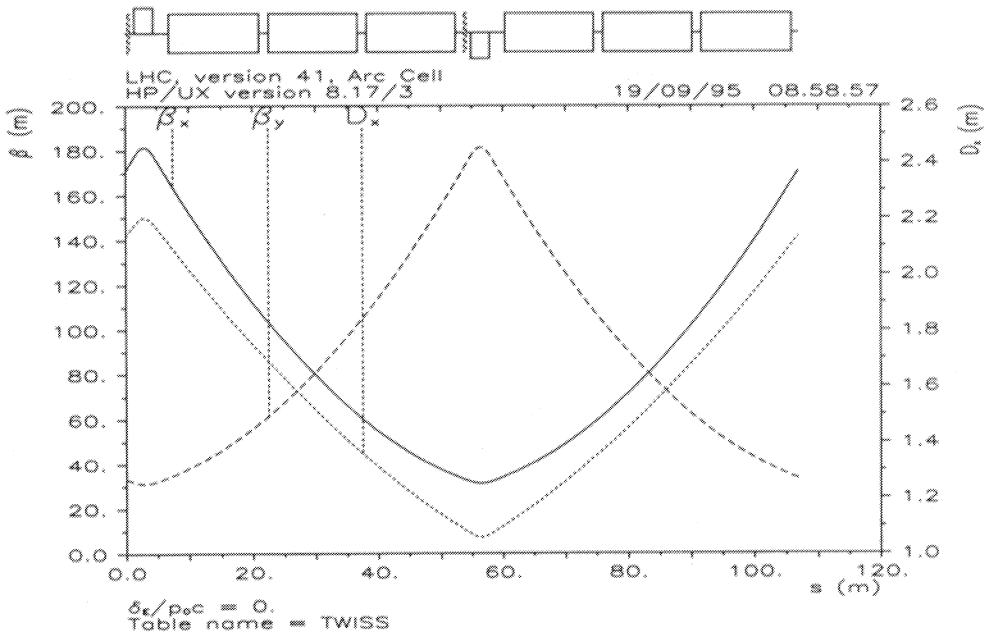

Figure 2: Optics of the standard arc cell

The nominal betatron phase advance is 90° per cell but it is in practice slightly adjustable in order to control the betatron tunes. With respect to versions 1 and 2, the maxima of the β and dispersion functions have increased with the cell length and the bending angle. This is expected to slightly decrease the dynamic aperture. The reserve in quadrupole strength is sufficient to separate the horizontal and vertical betatron phase advances by up to 16° per cell or 360° per arc to minimize coupling effects.

2.2 The dispersion suppressors

The two dispersion suppressor cells consist of four quadrupoles interleaved with four strings of two dipoles each. The dipoles have the same length as in the arc. The separation between the dipole strings is not regular in order to obtain almost exact superposition of the LHC and LEP interaction points, and to get adequate free space for the quadrupoles and associated correctors. It is the same in all 16 LHC dispersion suppressors. The layout of the 'odd' dispersion suppressor is shown in Fig. 3. Owing to the slightly irregular octagonal shape of the LEP tunnel, the length of the straight section adjacent to the arc, between Q10 and the first dipole, is 0.937 m shorter in the 'even' dispersion suppressors.

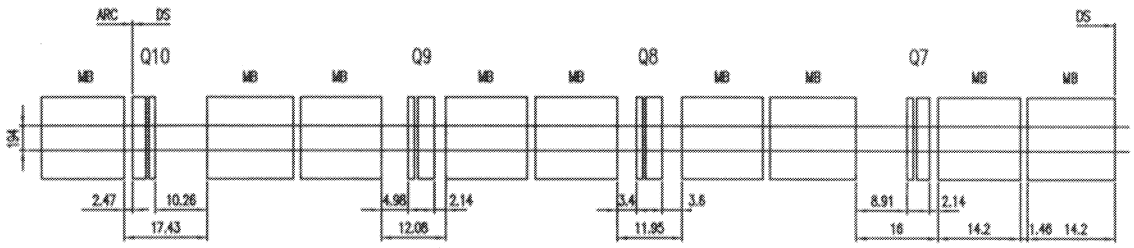

Figure 3: Layout of the 'odd' dispersion suppressor

The four quadrupoles of the dispersion suppressor are all powered in series with the arc cell quadrupoles. The Q7, Q8, and Q9 quadrupoles are 3.25 m long, and Q10 is a standard arc cell quadrupole of 3.1 m length. All quadrupole fields are adjusted with 1.5 m long trim quadrupoles having a maximum gradient of 120 T/m, and which are independently powered. To leave space for additional installations, the four quadrupoles are placed as close as possible to their associated dipole string.

The cryostat assemblies of the quadrupoles are shown in Fig. 4. The BPMs in the dispersion suppressor are placed on the right side of the quadrupoles, while the beam orbit dipole corrector for Q7, Q8 and Q9 and the combined sextupole/dipole corrector for Q10 are placed on the left side. In addition, two skew quadrupoles are provided next to Q8 and Q10.

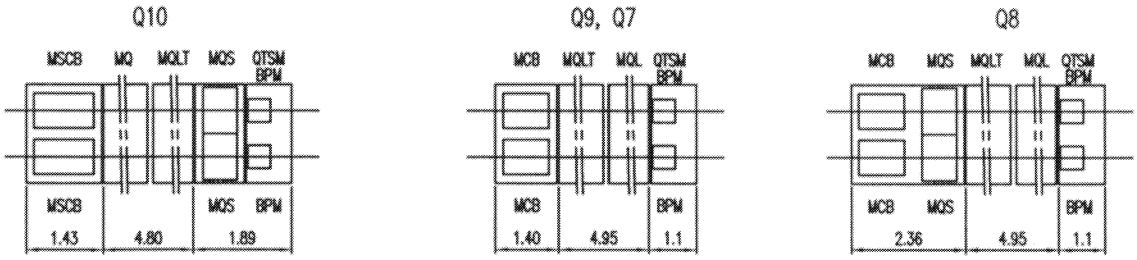

Figure 4: Cryostat assemblies of the quadrupoles in the dispersion suppressor

The quadrupoles of the dispersion suppressors contribute to the global matching of the insertions. As a consequence, the optics of the dispersion suppressor in the various types of insertion are different, even though their layouts are the same. However, in all cases the β-functions are sufficiently small to permit the use of quadrupoles with the same aperture as in the arc.

2.3 The high-luminosity insertions at IP1 and IP5

The high-luminosity insertions at points 1 and 5 are designed to achieve maximum luminosity for the two large LHC p–p experiments, while beam injection is accommodated in IR2 and IR8. The free space around the IPs has been increased to ± 23 m (see Fig. 5),

and Q1 now stands in the tunnel instead of being supported by a cantilever inside the experimental set-up as previously foreseen. This provides a better mechanical stability of the triplets, and is expected to result in a better operational performance. On the other hand, it causes some increase of the maximum β (see Fig. 6), partially compensated by an optimized design of the inner triplet [2]. The consequences of this modification on the dynamic aperture and the flexibility of the optics will be investigated.

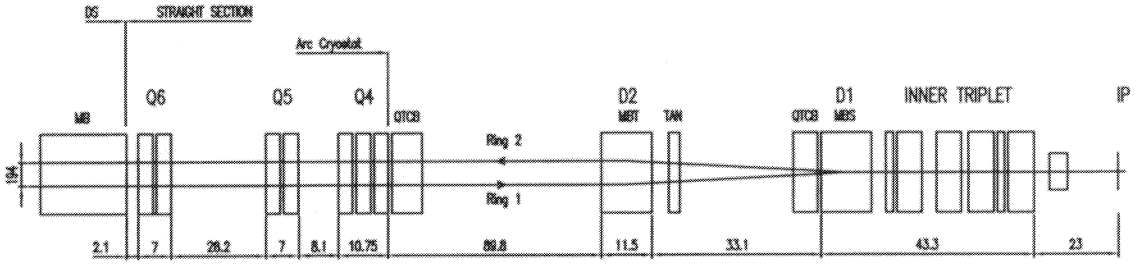

Figure 5: Layout of the left low-β Insertions 1 and 5

Apart from the dispersion suppressor (Section 2.2), each insertion comprises the following sections (Fig. 5), given in order from the interaction point:

- Free space of 23 m on each side of the IP; note however that a secondary particle absorber is placed 19 m from the IPs;
- Low-β (or 'inner') quadrupole triplet;
- Pair of separation dipoles;
- The matching (or 'outer') quadrupole triplet.

The position of the outer triplet has been adjusted to minimize the β-function at all stages of the β-squeeze; in this way regular aperture quadrupoles may be used everywhere except in the inner triplets. Linear and non-linear optics studies will be needed to assess the final layout and the maximum attainable β in the insertion quadrupoles. The optical functions of the insertion in collision and injection modes are shown in Fig. 6. The change of gradients during β-squeeze is kept smooth (see Fig. 7).

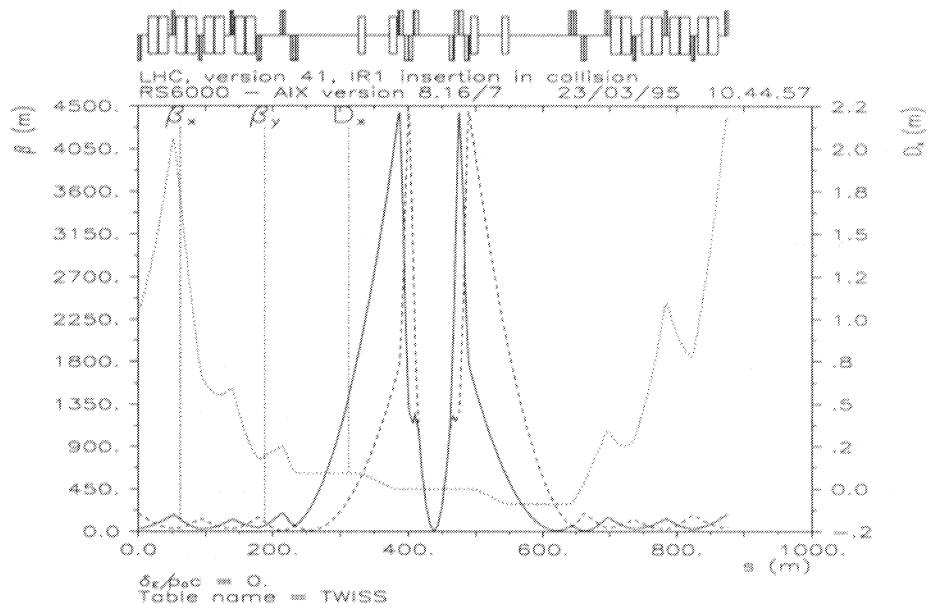

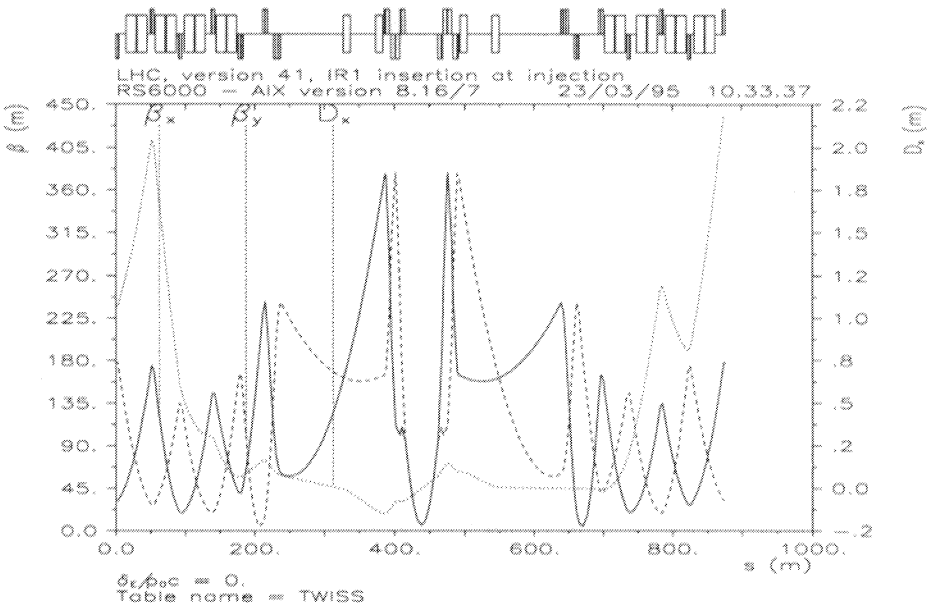

Figure 6: Collision (top) and injection (bottom) optics of the high-luminosity insertions at IP1 and IP5 for a β^* of 0.5 m and 6.0 m

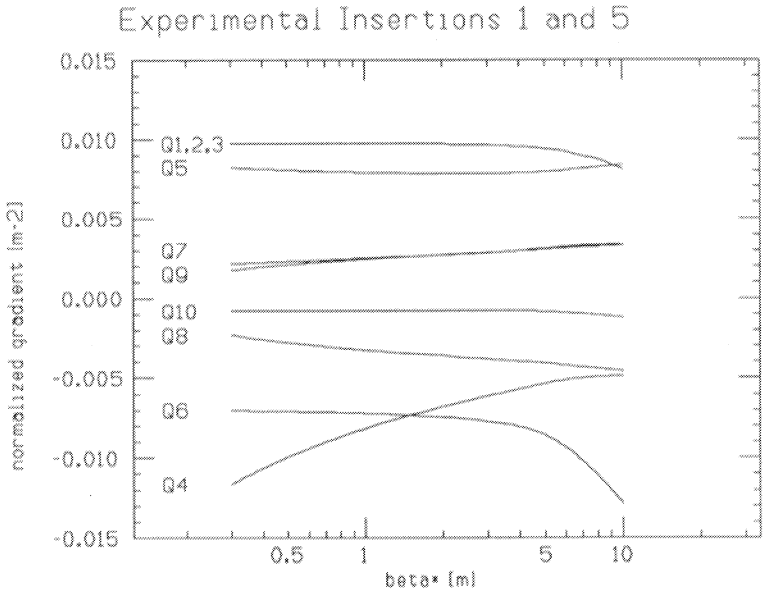

Figure 7: Variation of quadrupole gradients during β-squeeze at IP1 and IP5

The β^*-value chosen for injection is 6 m. It makes the best use of the normalized quadrupole aperture. Larger values of β^* may be possible.

The inner triplet

The layout of the low-β triplet is shown in Fig. 8. It comprises four identical 5.5 m long, 70 mm aperture quadrupoles which are powered in series, so that the two outer quadrupoles, Q1 and Q3 are focusing, while the inner two, Q2a and Q2b, forming the central optical element of the triplet, are defocusing. For reasons of alignment and protection from secondary particles, the front of the triplet casing in the high-luminosity insertions is 21.6 m from the interaction point (Fig. 9).

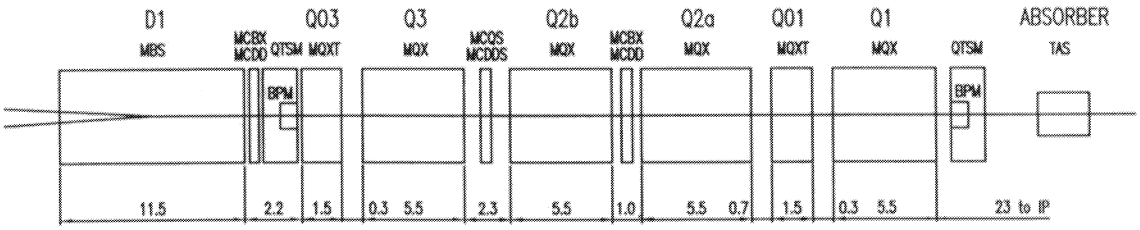

Figure 8: Layout of the left low-β triplet including D1

A 1.5 m long trim quadrupole (Q01) is located in between Q1 and Q2a. The gradient rating of this magnet is 120 T/m, while its aperture is increased ($\simeq$ 85 mm) to accommodate a secondary beam absorber. A similar quadrupole (Q03) with a trimming function only is placed to the left of Q3. The four trim quadrupoles of the two triplets residing on opposite sides of the interaction point are powered independently.

A number of correctors and beam observation monitors are installed in between the inner triplet quadrupoles. LEP indicates that such correctors are essential for the delicate tuning of the collision optics. The final position of the correctors and beam monitors inside the very compact inner triplet will only be settled after detailed design studies.

In front of Q1 and at a distance of 19 m from the interaction point, an approximately 1.8 m long absorber element is placed (see Fig. 9). This is required to protect the superconducting quadrupoles from the secondary particles. The absorber is made of copper and tungsten with an aperture of about 30 mm. The exact design of the aperture and of the front part of the absorber, which are needed to minimize the radiation into the machine and the backscattered radiation into the detector, is presently a subject of study.

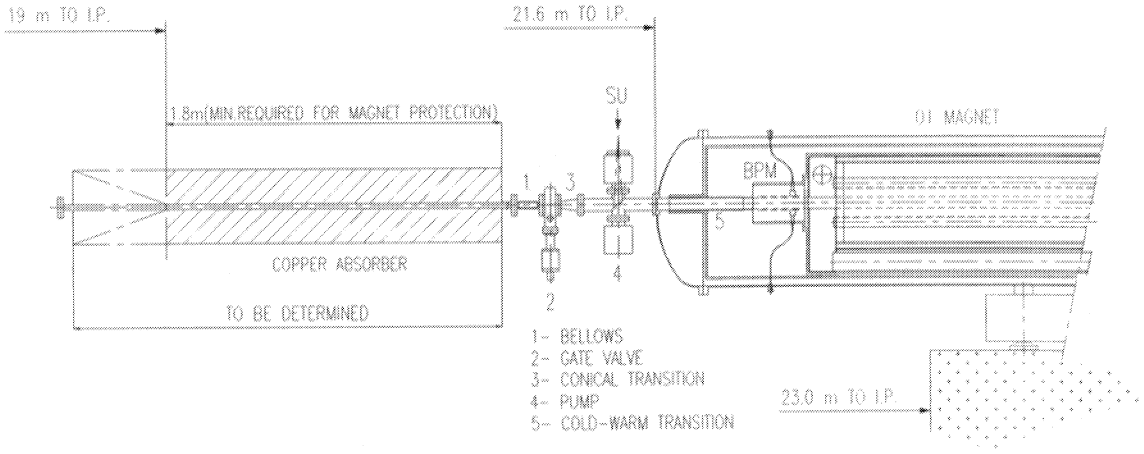

Figure 9: Interface between the low-β triplet and experiments in insertions 1 and 5

The space of about 2 m in between the absorber and the Q1 quadrupole is used to house a number of components: a beam-position monitor, cold-to-warm transition between the machine and detector vacuum chambers, a separation vacuum valve, and a pumping station combined with a surveyor's box needed for alignment, etc. These elements, as well as the vacuum chamber in the inner triplet, still need to be studied.

The power expected to be deposited by secondary particles in the low-β triplets of the high luminosity p–p insertions has been a matter of concern, and the layout and magnet specification have been studied in order to optimize this aspect of machine operation [3]. In general, the danger of quenching the low-β quadrupoles is linked more to the local energy deposition than to the overall power, both of which depend on the length, aperture and operating gradient of the magnets, and this is in particular the case for the Q1 magnet. Also, a large fraction of the power can be intercepted in secondary absorbers, located in

between the quadrupoles; an especially advantageous location is in between Q1 and Q2a. Nevertheless, a power density of a few mW/cm^{-3} is expected at the nominal luminosity of 10^{34} cm^{-2} s^{-1}. Such conditions are not expected during the initial period of operation and there will be ample time to adjust the protection before the risk of quenching due to secondaries becomes serious. However, the specification of the cryogenic system does take into account the important additional heat load due to the secondary particles at nominal luminosity.

The separation magnets

The separation of the two beams into their respective vacuum chambers must be made as close as possible to the interaction point in order to avoid the parasitic tune shift and non-linearities induced by beam–beam effects in parasitic crossings. For a bunch separation of 25 ns, such crossings occur every 3.75 m of the common vacuum chamber where the two beams travel together (between the Q3s of the left and right inner triplets). The separation is accomplished with a pair of bending magnets, D1 and D2. D1 is a single aperture dipole connected in opposition to D2, which is located 33.1 m further left; D2 is a twin aperture dipole of the same length as D1, but with an aperture separation of 194 mm.

As with the inner triplet, D1 is also submitted to intense irradiation by secondaries from the collisions. Its magnetic field deviates charged secondaries into its own coils, so that its aperture has to be at least 75 mm in order to avoid excessive energy deposit. The neutral secondaries are not deviated by D1 and will be stopped in a dedicated absorber placed a few metres to the right of the Y-shaped junction of the two beam chambers.

In the present design version of the machine, both D1 and D2 are 11.5 m long superconducting magnets operating at 4.4 T in collision mode. It has been suggested that both dipoles could be constructed on the basis of arc dipoles, by taking out the inner layer of the coil and redistributing the outer layer. In this case the aperture of the coil is 88 mm, which is beneficial both for the radiation heat load and the field quality of these magnets, which has to be considerably better than that of the arc dipoles.

The D1 cryostat is a prolongation of the inner triplet cryostat, while that of D2 is a stand alone unit. The heavy heat load along the inner triplet and D1 magnet imposes a cryogenic service module for each pair of magnets. These magnets are fed by a cold feedbox placed left of D1.

Other versions of beam separation at Insertions 1 and 5 are also possible and will be analysed in due course.

The outer triplet

The outer triplet quadrupoles, Q4, Q5, and Q6 are built of several units of dispersion suppressor-type quadrupoles. These magnets have the same cross-section as the arc quadrupoles, but are slightly longer, 3.25 m. The last quadrupole of the triplet, Q6, is adjacent to the dispersion suppressor, and is formed of two units of 3.25 m length. The other two quadrupoles, Q4 and Q5, are located respectively 52 m and 37 m away from the dispersion suppressor, and are formed of two and three units of 3.25 m length. As the experimental insertions 1 and 5 do not have any machine utilities, the free space between

Q4 and the separation dipole D2 has been slightly reduced with respect to previous versions (89.8 m) in order to improve the optics and operating conditions of the magnets. For purposes of insertion tuning, the outer triplet quadrupoles on the opposite sides of the insertion are powered independently (see Part III, Section 4).

All three quadrupoles sit in the continuous cryostat enclosure that extends from the middle of the arc to Q4. Whilst Q6 is equipped with the synchrotron radiation screen, continued from the dispersion suppressor, the other two quadrupoles, Q4 and Q5, do not have such a screen. The removal of the screen is required to reach a satisfactory mechanical aperture in these two magnets.

Similar to the arc quadrupole and the dispersion suppressor cryostats, the cryostat assemblies of Q4, Q5, and Q6, shown in Fig. 10, comprise horizontal and vertical beam orbit correctors and BPMs. In addition, two skew quadrupole families are installed next to Q6 and Q4. The Q4–Q6 quadrupole assemblies in other experimental insertions have identical cryostat assemblies.

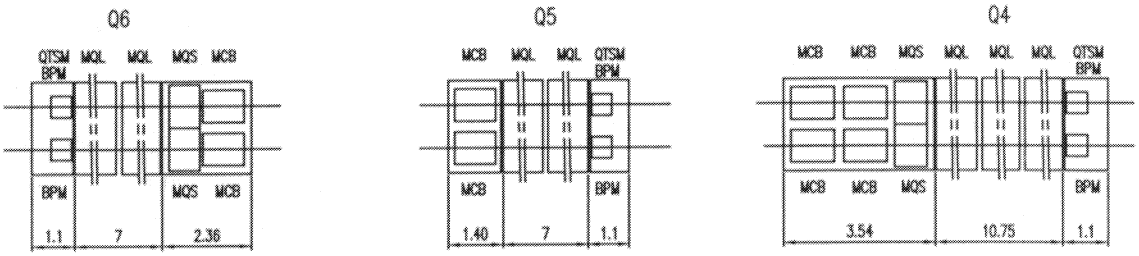

Figure 10: Cryostat assembly of the Q4, Q5, and Q6 outer triplet quadrupoles

2.4 The combined experimental and injection insertions at IP2 and IP8

In the present LHC layout, Insertions 2 and 8 are for beam injection into both rings, and additionally host respectively the heavy-ion experiment ALICE (IR2), and the B physics experiment (IR8).

Owing to the mirror symmetry of the LHC layout around the IP1–IP5 axis and because of the optical anti-symmetry of the insertions, Ring 1 in IR2 has the same hardware layout and optical performance as Ring 2 in IR8. The complementary rings in both insertions are, of course, also identical, but do not have the equipment associated with beam injection.

The left part of Ring 1 in Insertion 2 constitutes the following sections (see Fig. 11):

- Free space for the experiments (21 m on either side of the IP);
- Low-β (or 'inner') quadrupole triplet;
- Pair of separation dipoles;
- Injection section, with injection kicker and septum;
- The matching (or 'outer') quadrupole triplet.

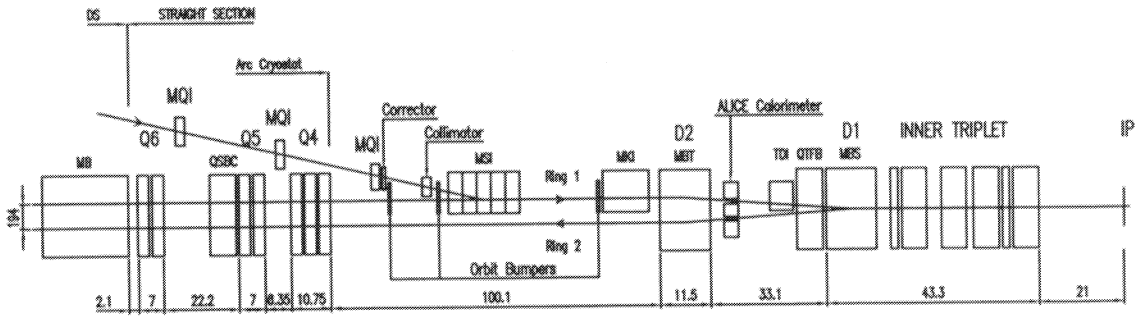

Figure 11: Layout of the left part of the low-β insertion at IP2

The right part is composed of identical elements with an inverted powering scheme, except that there are no injection elements. However, several beam stoppers are included for protecting the machine against incorrectly injected beams. They should restrict as much as possible the physical aperture to stop mis-injected beams and yet leave a sufficient aperture to let the accumulated beam circulate. In both insertions, injection is done into the outer ring. The required free space of 100 m between the outer triplet and the separator magnet D2, tightly constrains the insertion. This results in an increase of the β-function in the outer triplet at injection. The optics are shown in Fig. 12. The variation of the gradients during the β-squeeze is nevertheless quite smooth (see Fig. 13).

The inner triplet

The layout of the inner triplet in Insertions 2 and 8 is almost identical to that in high-luminosity Insertions 1 and 5, and is described in detail in Section 2.3. The only notable difference is that the experiments in these two insertions are not expected to produce high fluxes of secondary particles so that the primary absorber, which is essential for the protection of the low-β triplet in the high luminosity insertions, is considered unnecessary. As the free space for the experiment in all low-β insertions is the same, the inner triplet in IR2 and IR8 has therefore been moved by 2 m towards the IP, so that Q1 is magnetically 21 m from the interaction point.

The separation magnets

The separation of the two beams into their respective vacuum chambers is handled in IR2 and IR8 in the same way as in the high-luminosity insertions. For reasons of hardware standardization the same separation magnets are used, although the requirements for D1 as far as its resistance to secondary particle loss is concerned, are substantially less critical.

The relative position of the separation magnets with respect to the inner triplet is the same as in the two other low-β insertions. However, since the inner triplet is closer to the IP by 2 m, the space in between D2 and the outer triplet has increased correspondingly. This is an important gain since the free space in between these sections is used in the left part of IR2 and in the right part of IR8 for beam injection elements.

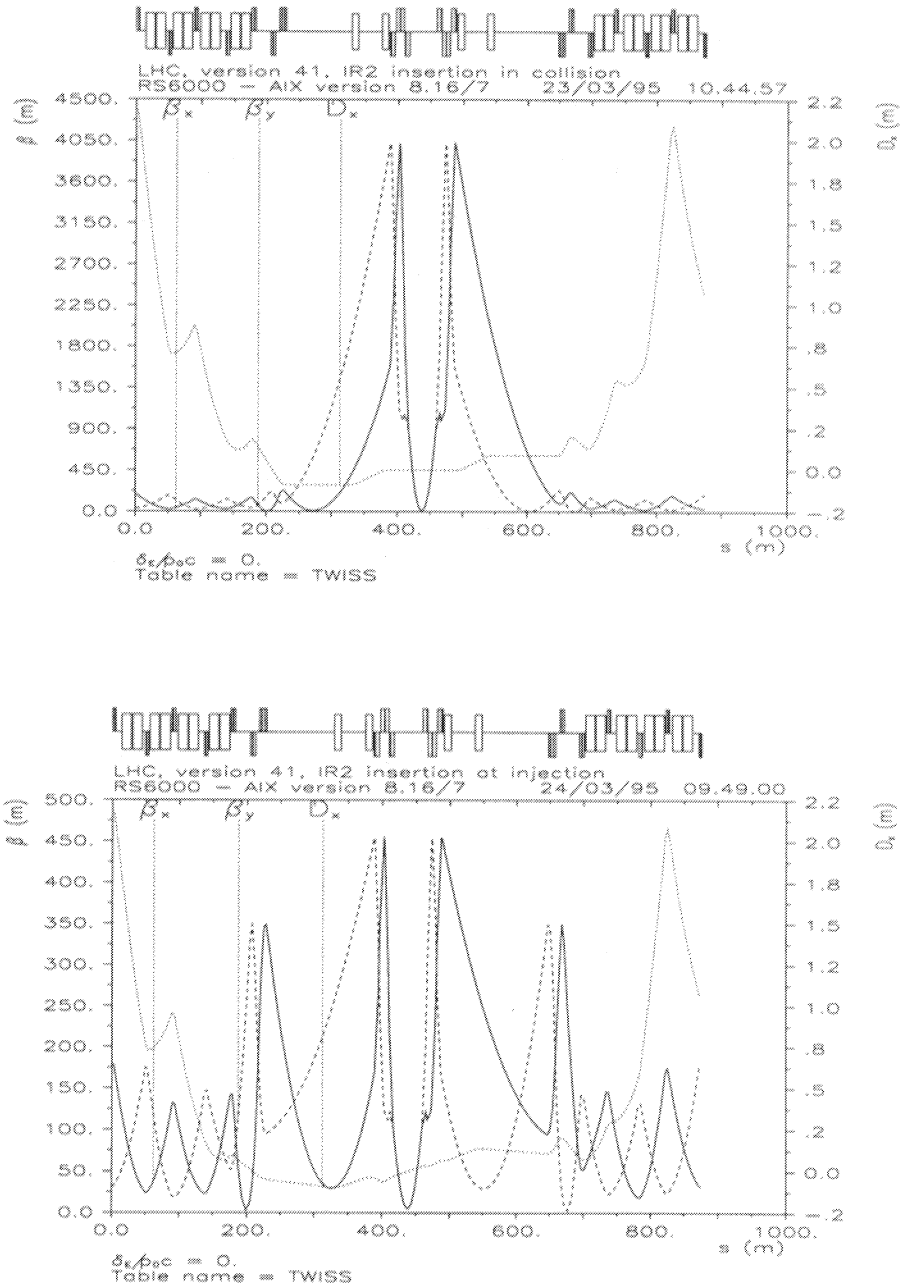

Figure 12: Collision (top) and injection (bottom) optics of the experimental/injection insertions at IP2 and IP8 for a β^* of 0.5 m and 4.5 m, respectively

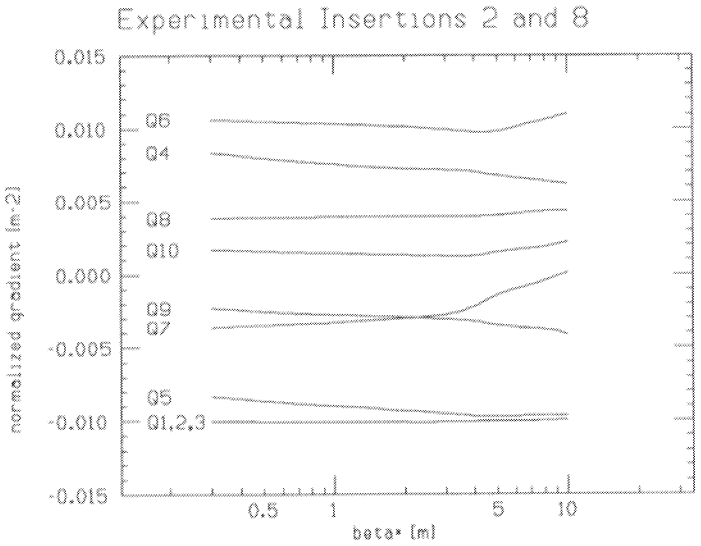

Figure 13: Variation of gradients during β-squeeze at IP2 and IP8

The outer triplet

As in Insertions 1 and 5, the outer triplet quadrupoles, Q4–Q6, are built of several units of dispersion suppressor-type quadrupoles. The Q6 quadrupole is adjacent to the dispersion suppressor, and is formed of two standard units. Because of the injection requirements the other two quadrupoles, Q4 and Q5, are closely packed and have been moved closer to the dispersion suppressor, leaving a drift space of 100 m to the separation dipole D2. As a result of these modifications, the β-functions in these quadrupoles are higher than in the outer triplet of the high-luminosity insertion. Their gradient rating is also somewhat increased, but can nevertheless be satisfied by assembling two (Q5) and three units (Q4) of 3.25 m dispersion suppressor quadrupoles.

As in the high-luminosity experimental insertions, the outer triplet quadrupoles sit in the continuous cryostat enclosure that extends from the middle of the arc to Q4, with the synchrotron radiation screen terminating at the level of Q6. In order to leave space for incoming injected beams, Q4 is equipped with a close-fitting cryostat.

Injection elements

The beam coming from the SPS approaches the two outer rings of the LHC (Ring 1 in Insertion 2 and Ring 2 in Insertion 8) from the exterior and is injected between Q4 and D2 by means of a horizontally-deflecting copper septum magnet and a kicker magnet. The orbit is adjusted by a set of three dipoles. In order to protect machine components from a badly injected beam, for example due to a kicker failure, a series of injection

beam stoppers, capable of withstanding the full SPS beam are placed at suitable phase distances. The required performance and main parameters of the injection elements are given in Table 2.

An alternative injection scheme combining a horizontally-deflecting steel septum magnet with a vertical kicker may have some advantages and is under study.

Table 2: Main parameters of the injection septum and kicker magnets (per beam)

	Units	Septum magnet	Kicker magnet (Travelling wave)
Bending strength	[Tm]	18	1.2
Nominal field	[T]	1.2	
Overall length	[m]	20	15
Physical aperture	[mm]		40×40
Rise time	[μs]		0.9
Flat top	[μs]		6.5
Decay time	[μs]		< 3
Flat top precision			1% p.t.p
Voltage	[kV]		60
Number of modules			4

2.5 The cleaning insertions at IP3 and IP7

The very important beam collimation functions are carried out in the betatron and momentum cleaning insertions. The deep underground location and the practical impossibility of any civil engineering work in Insertion 3 make it a well suited location for the betatron cleaning, which will inevitably produce large background radiation. This suggests the use of warm magnets, which is also in line with difficult cryogenic access at Point 3. The momentum cleaning, presently under study, is tentatively located in IR7, and has the same hardware layout as IR3. If this study demonstrates the feasibility of combining the two functions in IR3, then IR7 may be available for other purposes.

The layout and optical functions of the cleaning insertion at IP3 are shown in Figs. 14 and 15, respectively. The insertion consists of a 500 m warm straight section, with the two dispersion suppressors at each end. The cold section of the insertion, i.e. the main cryostat extending from the middle of the adjacent arcs, ends with the Q6 quadrupole. Just after the cold/warm transition, the two 'dogleg' dipoles, D3 and D4, increase the beam separation from 194 mm to 224 mm, which was found to be optimal for energy deposition on the right side of the insertion (see Section 4). The optical anti-symmetry and nominal beam separation of 194 mm are preserved by installing an identical arrangement at the exit of the straight section.

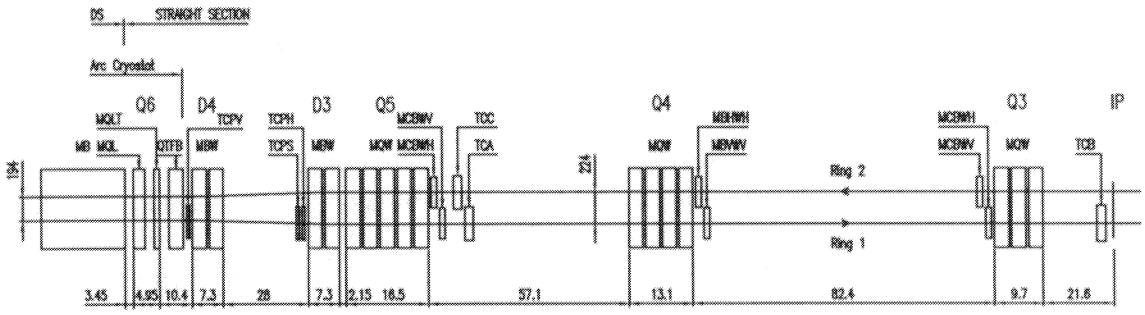

Figure 14: Layout of the cleaning insertion

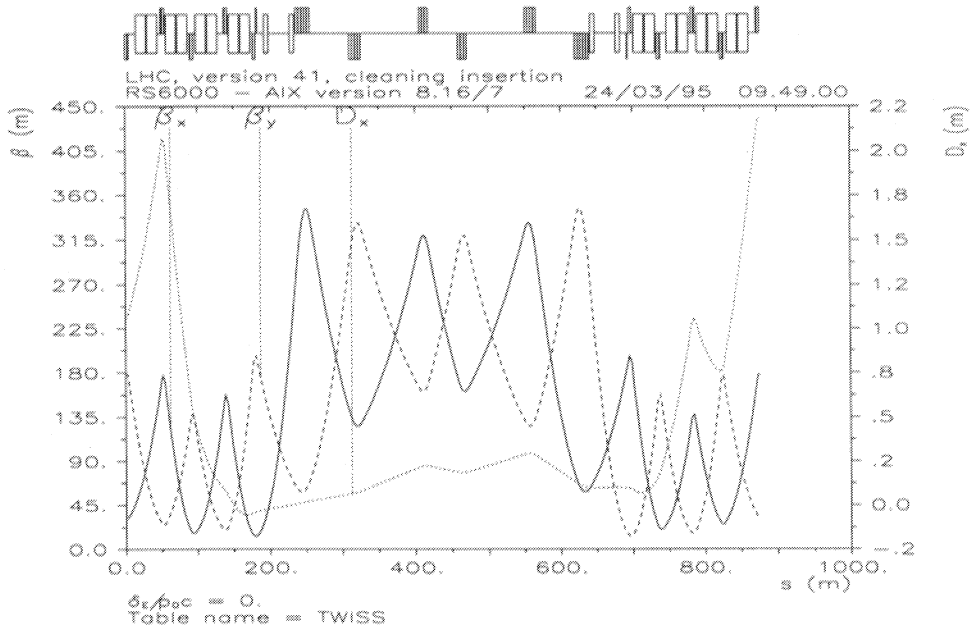

Figure 15: Optics of the cleaning insertions at IP3

The increased ring separation also makes it easier to design a 3-cell FODO structure made of warm two-in-one quadrupoles. The quadrupoles Q3, Q4, and Q5 are built of 3, 4, and 5 modules of 3.1 m, 37 T/m quadrupoles, respectively. The 3-cell FODO has maximum β values around 350 m and a total phase advance of 216°, which is suitable for collimation.

The three sets of primary collimators are located near Q6 (TCPV), and in front of D3 (TCPS and TCPH); the secondary collimators TCA and TCC are located on the right of Q5, while TCB is very near to the mid-point of the insertion. The performance of the collimation system is presented in detail in Section 4.

2.6 RF System at IP4

In the current version of the LHC lattice, the RF system is located in Insertion IR4. In order to install two separate RF systems, one for each beam, the separation between the two rings must be increased to more than 400 mm in a free space of about 40 m. In order to leave the possibility for a future experiment at IP4 open, the RF system is located sufficiently far away from the IP to enable beam recombination and installation of the detector. For this reason, four RF cavities are combined in a common cryostat to minimize their overall length; the second beam is inside the cryostat to minimize the required beam separation.

The layout of the insertion is shown in Fig. 16. The beam separation is increased from the nominal 194 mm to 420 mm by a pair of dipoles, D3 and D4, located immediately to the right of the Q6 quadrupole. It is at present foreseen that both dipoles will have two sections, each containing two RHIC main dipole coils with slightly different beam separations, 194 mm and 222 mm in D4, and 392 mm and 420 mm in D3, to accommodate better the diverging beams.

The matching section of the insertion consists of a tightly packed pair of Q4 and Q5 quadrupoles, each assembled from two 3.1 m long units. Each section consists of two separate cold masses assembled around the lattice quadrupole coil, with a beam separation of 420 mm. The integrated strength of these quadrupoles is sufficient for the tuning requirements of a low-β section for a potential future experiment.

The RF accelerating and damping cavities of Ring 1 are positioned to the right of Q4 in a free space with a beam separation of 420 mm. The total length of the RF system is slightly less than 40 m, so that the cavities are facing the klystron galleries that run parallel to the straight section of IR4, close to their middle. As indicated in Fig. 16, the remaining space between the RF system and the IP is around 130 m. This space is sufficient to locate a pair of recombination dipoles and a low-β triplet thus leaving a free space of 21 m for the experiment. However, for the time being the remainder of the straight section houses two 3.1 m long quadrupoles, Q2 and Q3, which are operated at 4.5 K. The insertion is completed on the right side of the IP by an identical magnet arrangement and the RF system of Ring 2.

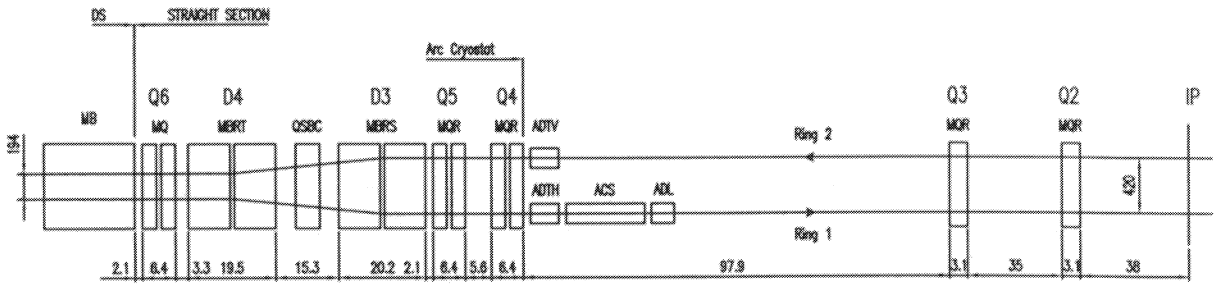

Figure 16: Layout of the IR4 fully dedicated to the RF system

The optics of the insertion are shown in Fig. 17. The betatron functions at the RF cavities are small (about 150 m) to reduce their contribution to the transverse impedance.

The transverse dampers sit close to the Q4 quadrupole where the β values are 200 m, chosen to give ample space for the beam in all of the matching quadrupoles. The dispersion in the RF region is made negligible to avoid the excitation of synchro-betatron resonances. The betatron phase advance is identical to that of the dump insertion to maintain the mirror symmetry of the machine.

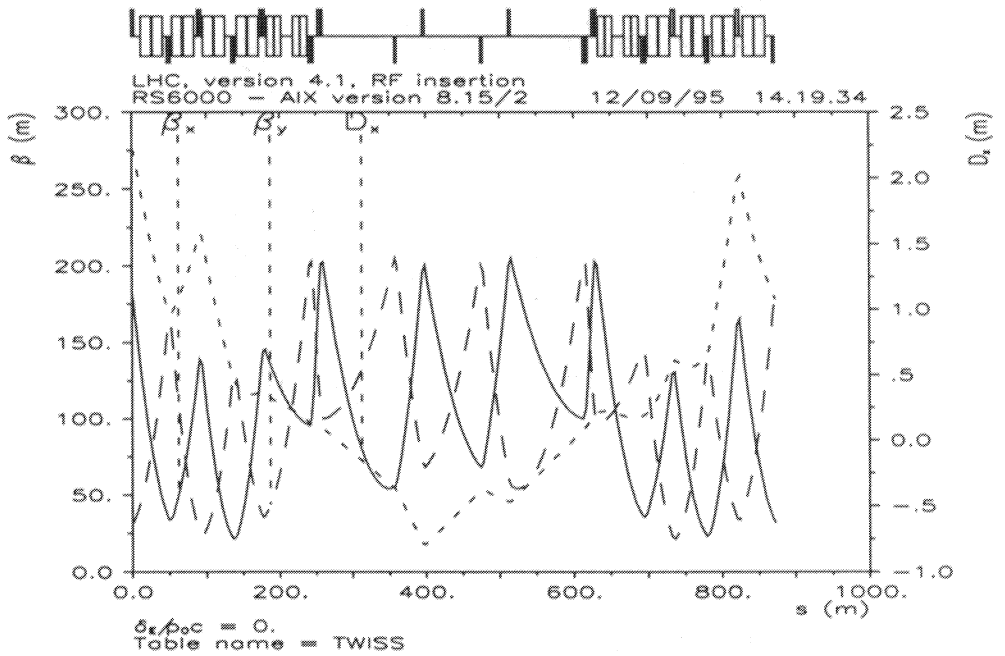

Figure 17: Optical functions of the RF insertion at IP4

2.7 The beam dump insertion at IP6

The purpose of the beam dumping system is to remove the beam safely from the collider at the end of a physics run, when the luminosity has degraded and a refill is necessary. It will also be used frequently during setting-up and machine studies, and must always be ready in case of equipment malfunction or abnormal beam behaviour which might lead to beam loss and quenching of superconducting magnets.

The principle of the beam dumping system is to horizontally kick the circulating beam into an iron septum magnet (see Fig. 18), which bends the beam vertically so that it can be transported to an external zone sufficiently far away ($\simeq$ 750 m) to permit beam dilution and shielding. Each ring of the LHC has its own beam dumping system but both systems are installed in IR6. In contrast to previous designs, the present version features parallel non-intersecting beams. With the septum placed at the centre of the insertion, the extraction of both beams can be optimized simultaneously. The layout of the insertion is shown in Fig. 19.

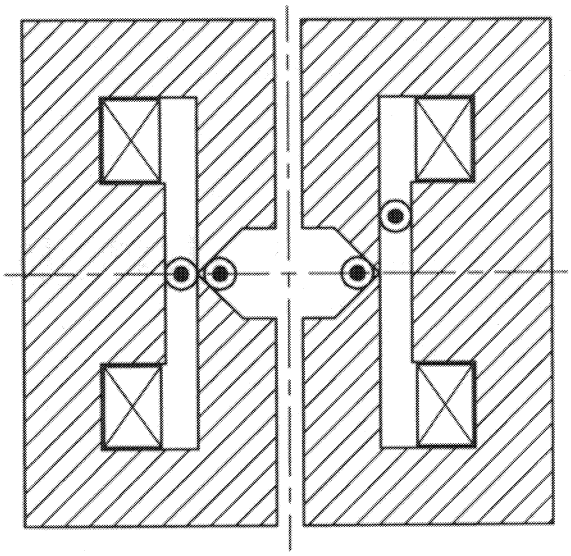

Figure 18: Cross-section of dual bore Lambertson septum

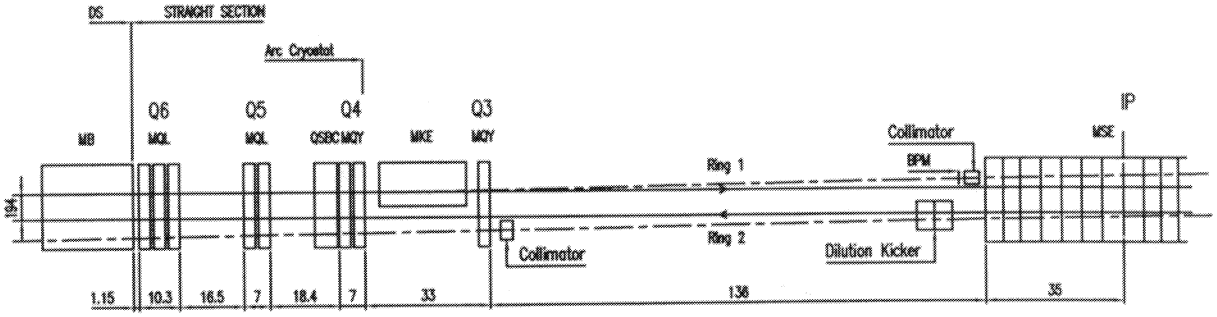

Figure 19: Layout of the beam dump insertion at IP6 (top view)

The insertion consists of a free section of about 400 m, with the two horizontally-deflecting kicker magnets located at each end. The vertically-deflecting iron septum magnet with a double aperture is installed in the centre. Immediately right of the septum magnet is a pair of orthogonally-deflecting kicker magnets which sweep the beam over the front face of the dump. A 3 μs gap is left in the circulating beam in order to avoid spreading a partially-deflected beam during the rise time of the kicker. To avoid damaging the iron septum, for example in case of bad synchronization of the kicker pulse with the beam gap, or due to its accidental firing, an absorber is installed at each entrance of the septum.

A suitable antisymmetric optics function for the insertion is made with a triplet of quadrupoles, Q3, Q4, and Q5, which are located on either side of the central straight section. The position of Q3 results from a compromise between the kicker efficiency and

the strength of the septum, taking into account realistic assumptions about the aperture of Q3 and the outer radius of its cryostat. Furthermore, it must be horizontally defocusing, so as to enhance the kick and produce a larger beam displacement in the septum. These constraints result in a very long drift ($\sim$ 340 m) between the left and right Q3, and a somewhat unfavourable optics function, with a β of 622 m in Q3 and Q4 (see Fig. 20), the largest around the LHC at injection. It is therefore envisaged that these two quadrupoles will be specially built units with a coil aperture of 70 mm. Their cryostats also need to have a smaller diameter to let pass the extracted beam. It might be possible to reduce the $\beta_{\max}$ to about 450 m by introducing a small warm quadrupole at each end of the septum. The remaining quadrupoles of the triplet Q5, and Q6 which ends the dispersion suppressor, are units of 3.25 m and 3.1 m length, respectively.

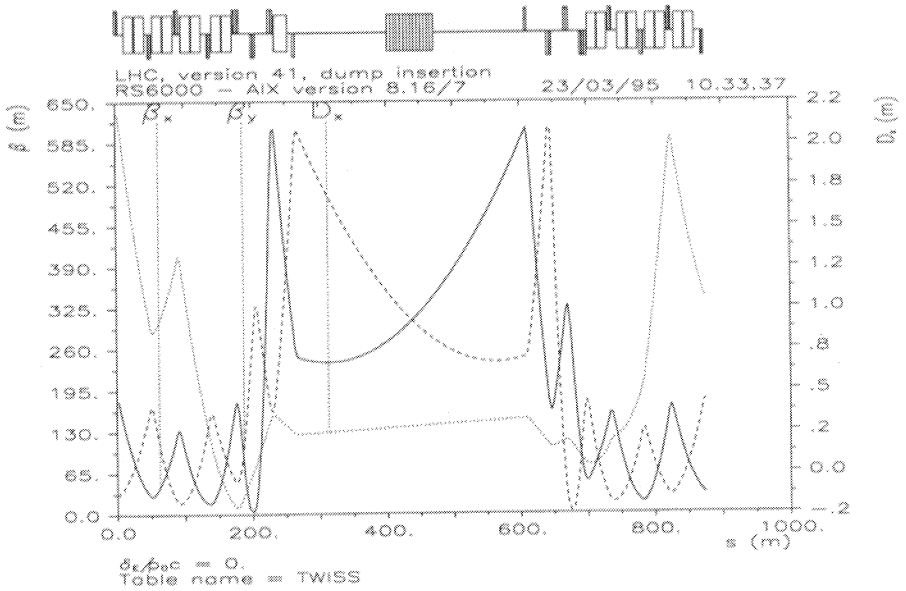

Figure 20: Optics of the dump insertion at IP6

The dump block (see Fig. 21), is installed in a cavern situated at the end of the straight transfer tunnel which emerges tangentially from the LEP tunnel. The central part of the dump is made of graphite which has a low atomic weight and density to dilute the particle cascades, and also has excellent mechanical properties up to temperatures as high as 2500°C. It is surrounded in turn by heavier materials, aluminium and iron, to obtain sufficient shielding against residual radiation within the compact overall dimensions. It is envisaged to make the iron part using the magnet yoke of CERN's decommissioned Synchrocyclotron.

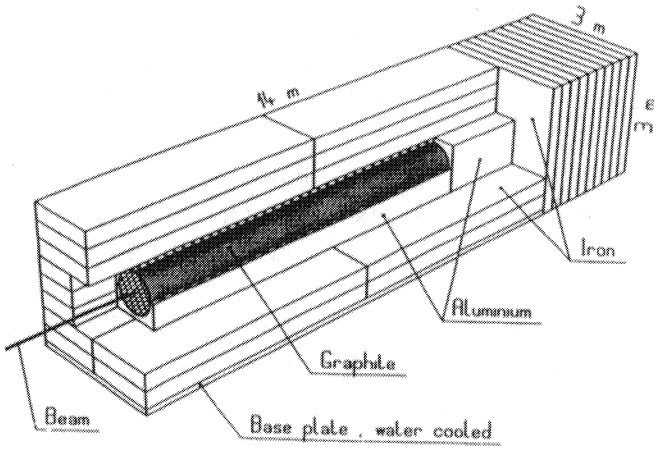

Figure 21: The dump block

The required performance and the main parameters of the extraction kicker, septum magnets, and of the diluter magnets are given in Table 3. A prototype kicker magnet module is under construction. It is made of cores wound from 0.05 mm thick tapes of silicon steel and a coil insulated with epoxy-impregnated mica tapes, assembled around a ceramic vacuum chamber. The generator, which must produce a 90 μs long current pulse of 30 kA with a rise time of 3 μs, is based on a capacitor discharge circuit with a diode stack parallel to the magnet to obtain the flat top length. Several types of high power switches, multistage ceramic thyratrons, pseudospark switches, and semiconductor switches are being tested.

Table 3: Main parameters of the extraction septum, kicker and diluter magnets (per beam)

	Units	Septum magnet	Kicker magnet	Diluter horiz.	Diluter vert.
Bending strength	[Tm]	60	7.1	7.0	7.0
Nominal field	[T]	1.0	0.51	1.2	1.2
Overall length	[m]	70	25	8	10
Gap/Beam aperture (horiz. $\times$ vert.)	[mm]	45	58×58	58×42	58×42
Rise time	[μs]	d.c.	3		
Frequency	[kHz]			14	14
Flat top	[μs]		90		
Voltage	[kV]		30	15	15
Number of modules		12	14	4	5

2.8 Periodicity and betatron tunes

The cleaning and dump insertions cannot be optimized with the same betatron phase advance as in the low-β insertions. Moreover, the experimental/injection insertion requires a minimization of the β-function which cannot be carried out if the phase advance is constrained. These insertions are thus somewhat different from the high-luminosity insertions (Table 4).

Table 4: Betatron phase advance (in turns) in the various insertions

Insertion	Phase advance
High-luminosity	2.43
Experimental/injection	2.57
Cleaning	1.80
Dump/RF	1.80

The super-periodicity is 1. In this case, all tunes are in principle equivalent. The phase advance in the arc cell is adjusted to make the operational tune:

$$Q_x = Q_y = 63.3 \ .$$

To reach this value, the lattice cell is tuned to 90.3°. Equal horizontal and vertical tunes are a feature of the antisymmetric design. The lattice cells are then adapted to separate slightly the tunes:

$$Q_x = 63.28 \qquad Q_y = 63.31 \ ,$$

resulting in a negligible mismatch. With a super-periodicity of one, the selection of the integer parts of the tunes requires that the strength of the resonances driven by the systematic field errors be calculated. This is a subject of further studies.

With respect to betatron coupling, the working point is equivalent to that of LHC version 1 [4]. The necessary changes to version 4.1 to make it robust against coupling will be the subject of later studies. In the meantime, a coupling correction scheme which allows full decoupling in static conditions, as discussed in Refs. [5, 6], is assumed.

2.9 Aperture

Two different types of aperture have to be considered: the mechanical aperture and the dynamic aperture. The LHC mechanical aperture is limited by collimators in order to localize the beam losses into a specific section, the beam cleaning section. The efficiency of beam cleaning is, however, strongly related to the aperture available around the ring. Large amplitude particles which escape from the cleaning system must be able to circulate without hitting the beam enclosure anywhere in the cold part of the machine, before being captured by the collimators on a later turn.

The dynamic aperture is usually smaller than the mechanical aperture and defines the maximum initial amplitude of particles which have to survive for millions of turns.

The mechanical aperture

The mechanical half-aperture A is the distance between the vacuum chamber centre line and the innermost obstacle. If it is different on the inner or outer side of the ring, or on the upper or lower side, the lowest value is retained for each plane. The mechanical half-aperture of dipoles or quadrupoles, for instance, is defined with an ideal beam screen installed.

The aperture $n\ \sigma$ available for the circulating beam is obtained using the following formula:

$$A\ =\ (n\ \sigma\ +\ \delta_p\ D_x) * k_\beta\ +\ (CO\ +\ \delta_{\rm sep})\ +\ (\delta_{\rm al}\ +\ \delta_{\rm tol})\ .$$

- The value of σ is deduced from the *nominal* emittance ϵ and the local value of β ($\sigma = \sqrt{\epsilon\beta}$).
- δ_p is the maximum relative momentum spread in the bunch taken as the half-bucket size, D_x is the local value of the dispersion.
- k_β is a coefficient measuring the effect of the modulation of the β and dispersion functions due to gradient errors. k_β is taken to be 1.1, corresponding to either a β-beating of 20% or a dispersion mismatch of 10%.
- CO is the expected maximum residual closed orbit deviation after correction. The value of 4 mm represents the peak value observed at injection over the last 10 runs of LEP in 1994.
- $\delta_{\rm sep}$ is the nominal half-beam separation with respect to the reference orbit. It is zero everywhere except in the single bore magnets, as required by the collision scheme.
- $\delta_{\rm tol}$ is the mechanical tolerance of the nominal aperture resulting from design, fabrication, and assembly for each magnet.
- $\delta_{\rm al}$ is the estimated alignment error of the magnets in the ring.

In contrast to the previous evaluation of the aperture, the betatron and momentum coordinates are now added linearly, since all phases in each degree of freedom are equally probable. The assumed closed orbit, dispersion, and β-beating are rather modest and imply a well controlled machine, especially during the ramp. The most restrictive apertures have been analysed for each section of the ring in *injection* conditions when the beam size is at a maximum. They are shown in Table 5 where the above formula has been applied.

The aperture required by the circulating beam is estimated to be 6 σ with respect to the closed orbit (3 σ for the beam distribution, 2 σ for transverse and longitudinal injection errors, and 1 σ for drifts in time of the orbit). The primary collimators in the cleaning insertions must therefore be positioned at 6 σ while the mechanical aperture all around the ring must exceed 10 σ to provide the 4 σ margin necessary for the collimator system to effectively protect the superconducting magnets [7, 8]. The available arc aperture (9 σ, see Table 5) does not quite meet this requirement. The possibilities of i) enlarging the mechanical aperture of the beam screen and ii) reducing the beam screen distance required for collimation are presently being studied.

Table 5: Aperture around the LHC ring

Element	H/V	Half-aperture [mm]	β [m]	D_x [m]	CO+δ_{sep} [mm]	δ_{al} [mm]	δ_{tol} [mm]	Value of σ[mm]	Number of σ's
Arcs									
QF	H	22.0	183	2.1	4.0	0.6	1.0	1.20	10.9
BPM	H	22.0	172	2.1	4.0	0.6	1.0	1.16	11.2
MB (QF side)	H	22.0	167	2.1	4.0	0.6	4.0	1.14	9.0
QD	V	22.0	183	0.6	4.0	0.6	1.0	1.20	12.0
BPM	V	22.0	172	0.6	4.0	0.6	1.0	1.16	12.4
MB (QD side)	V	22.0	167	0.6	4.0	0.6	4.0	1.14	10.2
Odd low-β insertions									
Q10	H/V	22.0	183	2.1	4.0	0.6	1.0	1.20	10.9
MB (Q10 side)	H/V	22.0	121	2.1	4.0	0.6	4.0	0.97	10.6
Q9	H/V	22.0	177	2.1	4.0	0.6	1.0	1.18	11.1
Q8	H/V	22.0	137	2.1	4.0	0.6	1.0	1.03	12.6
Q7	H/V	22.0	154	2.1	4.0	0.6	1.0	1.10	11.9
MB (Q6 side)	H/V	22.0	141	0.2	4.0	0.6	4.0	1.05	11.4
Q6	H/V	22.0	160	0.2	4.0	0.6	1.0	1.12	13.2
Q5	H/V	24.5	240	0.2	4.0	0.6	1.0	1.37	12.4
Q4	H/V	24.5	240	0.2	4.0	0.6	1.0	1.37	12.4
Q3, Q3T	H/V	31.5	377	0.2	5.0	0.6	1.0	1.72	13.1
Q2	H/V	31.5	377	0.2	5.0	0.6	1.0	1.72	13.1
Q1, Q1T	H/V	31.5	377	0.2	4.0	0.6	1.0	1.72	13.6
Even low-β insertions									
Q10	H/V	22.0	183	2.1	4.0	0.6	1.0	1.20	10.9
MB (Q10 side)	H/V	22.0	121	2.1	4.0	0.6	4.0	0.97	10.6
Q9	H/V	22.0	177	2.1	4.0	0.6	1.0	1.18	11.1
Q8	H/V	22.0	137	2.1	4.0	0.6	1.0	1.03	12.6
Q7	H/V	22.0	157	2.1	4.0	0.6	1.0	1.11	11.8
MB (Q6 side)	H/V	22.0	135	0.2	4.0	0.6	4.0	1.03	11.7
Q6	H/V	22.0	145	0.2	4.0	0.6	1.0	1.06	13.9
Q5	H/V	24.5	350	0.2	4.0	0.6	1.0	1.65	10.3
Q4	H/V	24.5	350	0.2	4.0	0.6	1.0	1.65	10.3
Q3, Q3T	H/V	31.5	455	0.2	5.0	0.6	1.0	1.89	11.9
Q2	H/V	31.5	455	0.2	5.0	0.6	1.0	1.89	11.9
Q1, Q1T	H/V	31.5	455	0.2	4.0	0.6	1.0	1.89	12.4
Beam cleaning insertion									
Q6, Q6T	H/V	22.0	212	0.2	4.0	0.6	0.7	1.29	11.7
Q5 (warm)	H/V	22.0	350	0.2	4.0	0.6	0.7	1.65	9.1
Q4 (warm)	H/V	22.0	350	0.2	4.0	0.6	0.7	1.65	9.1
Q3 (warm)	H/V	22.0	350	0.2	4.0	0.6	0.7	1.65	9.1
Beam dump insertion									
Q6	H/V	22.0	191	0.4	4.0	0.6	1.0	1.22	11.9
Q5	H/V	24.5	310	0.4	4.0	0.6	1.0	1.56	10.8
Q4	H/V	31.5	633	0.4	4.0	0.6	1.0	2.22	10.4
Q3	H/V	31.5	617	0.6	4.0	0.6	1.0	2.20	10.5

In the rest of the machine, the elements are designed for at least the arc-equivalent aperture. In the specific case of warm elements (extraction kickers, cleaning insertion), a small reduction of the aperture may be tolerated if particle losses at these locations can be shown not to induce quenches in the neighbouring superconducting equipment.

In *collision* conditions the beam sizes are much smaller, except in the inner triplet. In this case the inner triplet quadrupoles have a mechanical aperture corresponding to about 15 σ.

The dynamic aperture

In superconducting colliders the stable area in phase space is limited by the non-linear fields introduced by magnet imperfections or by the beam–beam effect. Above a certain oscillation amplitude the particle motion becomes unstable. The dynamic aperture which is also measured in units of the r.m.s. beam size is only a limitation at injection where the non-linearities are large due to persistent currents and where the beam has a large emittance.

The non-linearities are measured in terms of the high-order coefficients a_n and b_n of the complex field expansion

$$B_y + iB_x = B_1 \sum_n (b_n + ia_n)\,(z/R_r)^{n-1} \quad ,$$

where B_1 is the nominal vertical magnetic field[2], B_y and B_x are the actual components of the field in the vertical and horizontal planes, $R_r = 1$ cm is the reference radius, and $z = x + iy$. The values of the coefficients depend on the design and the size of the magnet coils; the values in Table 6 were used up to lattice version 4 and are the basis of the calculations presented in this section. More recent values are given in Part III, Section 1, and Tables 5 and 8 therein show a reduction of some low-order multipoles. It is possible to reduce the high-order coefficients by increasing the coil diameter. In the dipole case, keeping the field on the inner coil surface constant and enlarging the coil diameter reduces the coefficients a_n and b_n by the enlargement factor to the power $n-1$. The field quality of a quadrupole can also be improved by enlarging the aperture.

At the design stage of a machine the value of the dynamic aperture is evaluated by computer simulations. Errors from different sources are introduced in a tracking program in which particles launched with different initial amplitude and phase are followed over a large number of turns. Usually about 10^4 turns are sufficient to detect whether the particle motion is regular or chaotic. Chaotic particles will eventually be lost on the wall. This may take a long time close to the dynamic-aperture limit where particles are weakly chaotic. For some selected sets of parameters the tracking is pursued up to 10^5 or 10^6 turns. From this one obtains 'survival plots' showing the variation of the survival time as a function of the initial amplitude of the particles in the chaotic region. These plots are extrapolated to evaluate the maximum amplitude of particles which are likely to survive for 10^7 or 10^8 turns. In the majority of cases this amplitude is only slightly above the chaotic boundary, which can therefore be taken as a safe value for the long-term dynamic aperture.

[2]In the case of the quadrupole, the field B_1 is the value of the field 1 cm from the axis.

An extensive campaign of computer tracking was made to evaluate the LHC long-term dynamic aperture at injection energy using version 2 of the lattice and the table of magnetic errors available in 1993. It showed that when all known imperfections including residual closed-orbit deviations were taken into account, the available dynamic aperture was 6.5 $\sqrt{2}\,\sigma$. The factor $\sqrt{2}$, which did not appear in previous reports, is a safety margin introduced by tracking particles with equal horizontal and vertical starting amplitudes.

A later version 3 of the LHC featuring longer cells (21 per arc instead of 24 in version 2) was designed and its dynamic aperture evaluated. Owing to the larger β and dispersion, a reduction of dynamic aperture was expected and was confirmed by tracking to be 10%.

The present version 4 of the LHC lattice features 23 cells per arc and is an intermediate one between version 2 and version 3. Its dynamic aperture is being evaluated, and preliminary results indicate that it is about 6 $\sqrt{2}\,\sigma$. Considering that a computer model cannot incorporate all the possible imperfections of a real collider and that much work is still needed to take into account possible variations of the magnetic errors, this provides a safety margin which is judged adequate to ensure reliable operation of the machine.

Table 6: Field perturbations in the LHC magnet (at injection) assumed for tracking

Perturbation type	Straight Term	Straight Strength[1]	Skew Term	Skew Strength	Straight Term	Straight Strength[1]	Skew Term	Skew Strength
Field errors in dipole magnets								
	Mean field errors				**Random field errors**			
Dipole	b_1	0.0	a_1	0.0	b_1	0.0	a_1	0.0
Quadrupole	b_2	1.15	a_2	0.770	b_2	0.37	a_2	1.227
Sextupole	b_3	−3.8	a_3	0.086	b_3	0.882	a_3	0.186
Octupole	b_4	−0.11	a_4	0.023	b_4	0.055	a_4	0.186
Decapole	b_5	0.34	a_5	0.020	b_5	0.083	a_5	0.041
Dodecapole	b_6	−0.002	a_6	0.0	b_6	0.014	a_6	0.022
	b_7	0.035	a_7	0.00	b_7	0.012	a_7	0.011
	b_8	0.002	a_8	0.0	b_8	0.005	a_8	0.005
	b_9	0.007	a_9	0.0	b_9	0.003	a_9	0.004
	b_{10}	0.00	a_{10}	0.0	b_{10}	0.002	a_{10}	0.002
	b_{11}	0.004	a_{11}	0.0	b_{11}	0.001	a_{11}	0.001
Field errors in quadrupole magnets								
	Mean field errors				**Random field errors**			
Quadrupole	b_2	0.0	a_2	0.0	b_2	0.0	a_2	0.0
Sextupole	b_3	0.02	a_3	0.280	b_3	0.454	a_3	0.478
Octupole	b_4	0.190	a_4	0.01	b_4	0.133	a_4	0.188
Decapole	b_5	0.05	a_5	0.01	b_5	0.065	a_5	0.093
Dodecapole	b_6	−0.60	a_6	0.0	b_6	0.053	a_6	0.069
	b_7	0.0	a_7	0.0	b_7	0.012	a_7	0.013
	b_8	0.0	a_8	0.0	b_8	0.006	a_8	0.007
	b_9	0.0	a_9	0.0	b_9	0.007	a_9	0.004
	b_{10}	0.02	a_{10}	0.0	b_{10}	0.005	a_{10}	0.003
	b_{11}	0.0	a_{11}	0.0	b_{11}	0.002	a_{11}	0.002

[1] In units of 10^{-4} $\Delta B/B_1$ at 1 cm, where B_1 is the dipole field for dipoles, and the field at 1 cm from the axis for quadrupoles.

References

[1] J. Miles, The dynamic aperture of LHC version 2 with relocated and missing chromaticity sextupoles, SL/Note 95–36 (AP).

[2] R. Ostojic, T.M. Taylor, Proposal for an improved optical and systems design of the LHC low-β triplets, CERN AT/94–38 (MA) and LHC Note 293 (1994).

[3] A. Morsch, R. Ostojic, and T.M. Taylor, Progress in the System Design of the Inner Triplet of 70 mm Aperture Quadrupoles for the LHC Low-β Insertions, Proc. EPAC 94, London, June 1994, eds. V. Suller and C. Petit-Jean-Genaz (World Scientific, London, 1994) p. 40.

[4] S. Weisz, Coupling compensation in LHC, SL-Note 94–34 (AP) (1994).

[5] J.P. Koutchouk, Correction of the systematic and random betatron coupling in LHC with an application to LHC version 2, LHC Note 306 (1994).

[6] V. Ziemann, The effect of different skew quadrupole correction schemes on the dynamic aperture of LHC, LHC Note 305 (1994).

[7] T. Risselada, LHC dynamic aperture with a square beam screen cross section, SL-AP Note 91–21.

[8] J.B. Jeanneret and T. Trenkler, The principles of two stage betatron and momentum collimation in circular accelerators, SL/95–03 (AP).

3 Parameters and performance

3.1 Beam crossing angle

In order to reach very high luminosities the LHC uses two counter-rotating beams made up of a large number of closely spaced bunches (2835 bunches spaced 7.5 m apart). The two beams are made to cross at a small angle in order to avoid the thirty unwanted collisions which would otherwise occur in the 110 m long region at each crossing where they travel close to each other in the same pipe [1].

This angle Φ is limited by excursions of the beam trajectories in the quadrupole triplet near to the interaction point, yet must be larger than the divergence of the beam envelope in the interaction region which is proportional to the square root of the emittance, and inversely proportional to the square root of the value β^* of the beta function at the collision point.

In this way the constraints on Φ impose a lower limit on the value of β^* which can be used for a given emittance. With the parameters we have chosen, namely $\Phi = 200$ μrad and $\beta^* = 0.5$ m, the crossing angle provides a transverse separation of the beam trajectories of the order of 6–7 σ, which is sufficient to prevent particle collisions but not to suppress the long-range electromagnetic interactions between bunches. The result of these multiple interactions is a global tune shift and a tune spread.

3.2 Luminosity

The luminosity is given by

$$L = \frac{N^2 k_b f \gamma}{4\pi\varepsilon_n \beta^*} F \ ,$$

where N is the number of protons per bunch, k_b the number of bunches, f the revolution frequency, γ the relativistic factor, ε_n the normalized transverse emittance, β^* the value of the betatron function at the interaction point, and F the reduction factor caused by the crossing angle, which is about 0.9 in the LHC.

The most important luminosity limitation comes from the beam–beam interaction. This effect has two components in the case of the LHC. There is the unavoidable head-on interaction of the colliding beams at the interaction points and there is also the long-range interaction which occurs on either side of the interaction regions in the common stretch of the beam pipe in which both beams run side by side. The importance of the head-on interaction is determined by the beam–beam tune shift parameter ξ

$$\xi = N r_p / 4\pi\varepsilon_n \ ,$$

where r_p is the classical proton radius, whereas the long-range interaction depends on the total beam current and the crossing geometry. The head-on interaction excites high-order betatron resonances and creates a tune spread across the beam distribution, whereas the long-range interaction essentially adds a contribution to the tune spread. Experience at the SPS proton–antiproton collider has shown that both the beam–beam parameter ξ and the total tune spread have to stay below certain limits.

The total tolerable tune spread is limited by the maximum area of the tune diagram free of resonances of order less than 12. Such areas exist close to the diagonal in the vicinity of low-order resonances. In the case of the SPS the best working point was close to the 1/3 resonance where a tune spread of up to 0.02 could be accommodated. In a machine like the LHC, the strong excitation of the 1/3 resonance due to magnet errors is likely to reduce this value even further. We have therefore based the LHC nominal performance on a total tune spread of 0.015 of which 0.01 comes from the beam–beam effect, and the remaining 0.005 from the machine non-linearities. This is evaluated for particles with an amplitude of 4 σ. With two experiments operating simultaneously, the corresponding luminosity is

$$\mathcal{L} = 1\ 10^{34}\ \mathrm{cm}^{-2}\ \mathrm{s}^{-1}\ .$$

Table 1: LHC performance parameters

Energy	E	[TeV]	7.0
Dipole field	B	[T]	8.4
Luminosity	L	$[\mathrm{cm}^{-2}\ \mathrm{s}^{-1}]$	10^{34}
Beam–beam parameter	ξ		0.0034
Total beam–beam tune spread			0.01
Injection energy	E_i	[GeV]	450
Circulating current/beam	I_beam	[A]	0.53
Number of bunches	k_b		2835
Harmonic number	h_RF		35640
Bunch spacing	τ_b	[ns]	24.95
Particles per bunch	n_b		$1.05\ 10^{11}$
Stored beam energy	E_s	[MJ]	334
Normalized transverse emittance $(\beta\gamma)\sigma^2/\beta$	ε_n	[μm.rad]	3.75
Collisions			
β-value at I.P.	β^*	[m]	0.5
r.m.s. beam radius at I.P.	σ^*	[μm]	16
r.m.s. divergence at I.P.	σ'^*	[μrad]	32
Luminosity per bunch collision	L_b	$[\mathrm{cm}^{-2}]$	$3.14\ 10^{26}$
Crossing angle	ϕ	[μrad]	200
Number of events per crossing	n_c		19
Beam lifetime	τ_beam	[h]	22
Luminosity lifetime	τ_L	[h]	10

3.3 RF and bunch parameters

The bunch length must be small enough to keep the unavoidable degradation of luminosity caused by the beam crossing angle tolerable. On the other hand, the longitudinal emittance must be sufficiently large to reduce the Intra Beam Scattering (IBS) induced growth rate of the transverse emittances, both at injection and in collision. These conflicting requirements are satisfied with an RF operating at 400 MHz and a bunch longitudinal

emittance of 1 eV.s at injection and 2.5 eV.s at 7 TeV. The RF voltage needed to achieve this is modest (8 MV at injection and 16 MV in collision) and is provided by eight superconducting cavities for each beam. These have the advantage of a very low coupling impedance (very large beam pipe diameter) and allow the very severe beam loading conditions to be controlled. The r.m.s. bunch length is 13 cm at injection and 7.5 cm in collision (see Table 2 for RF related parameters).

Table 2: LHC parameters related to RF

			Injection	Collision
Intrabeam scattering growth time:				
Horizontal	τ_h	[h]	45	100
Longitudinal	τ_p	[h]	33	60
Radio frequency:				
RF voltage	V_{RF}	[MV]	8	16
Synchrotron tune	Q_s		$5.5\ 10^{-3}$	$1.9\ 10^{-3}$
Bunch area (2σ)	A_b	[eV.s]	1	2.5
Bucket area	A_{rf}	[eV.s]	1.46	8.7
Bucket half-height	$\Delta p/p$		$1\ 10^{-3}$	$3.6\ 10^{-4}$
r.m.s. bunch length	σ_s	[m]	0.13	0.075
r.m.s. energy spread	σ_e		$4.5\ 10^{-4}$	$1.0\ 10^{-4}$

3.4 Beam structure along the orbit

The wavelength corresponding to a 400 MHz RF frequency is 0.75 m or 2.5 ns and the harmonic number in the LHC is $h = 35640$. We have chosen to fill only every tenth RF bucket to obtain bunches separated by 25 ns. This value of the bunch separation is well suited for the experiments and at the same time gives the optimum overall performance of the machine for two high-luminosity experiments taking data at the same time.

In fact the beam only comprises 2835 bunches of 10^{11} protons each. Its detailed structure is governed by the injection scheme and the properties of the dump system. The bunches are formed in the 26 GeV PS with the correct 25 ns spacing by adiabatic capture of a previously debunched beam with a 40 MHz RF system. Three trains of 81 bunches each are transferred to the SPS on three consecutive PS cycles and stacked in the SPS one after the other to fill approximately 1/3 of the machine circumference with a total charge of $2.43\ 10^{13}$ protons. This is not far from the maximum beam handling capabilities of the SPS.

This beam is subsequently accelerated to 450 GeV and transferred to the LHC. This operation is repeated 12 times for each of the counter-rotating beams of the LHC.

At each transfer, enough space has to be reserved in between bunch trains to accommodate the rise time of the injection kickers. These holes have a length of 220 ns between each PS batch of 81 bunches (SPS injection kicker rise time) and 0.94 μs between the groups of 3 PS batches (LHC kicker rise time) as illustrated in Fig. 1.

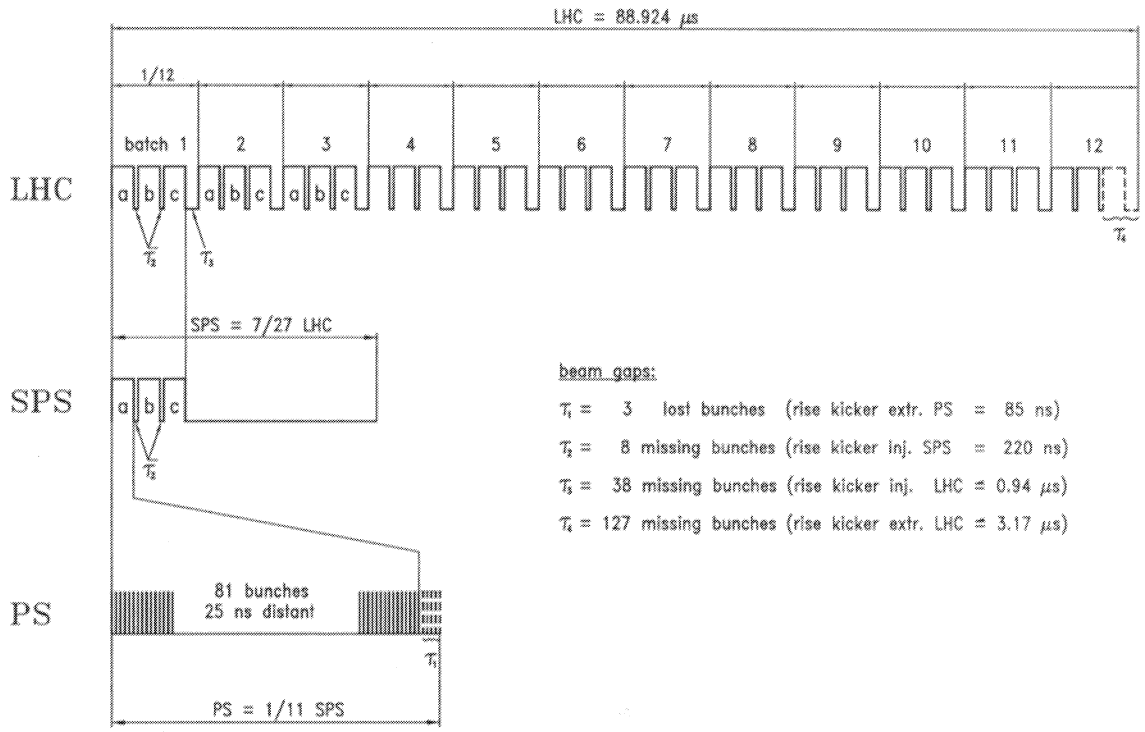

Figure 1: Bunch disposition in the LHC, SPS and PS

Finally, a longer gap of 3.17 μs has to be reserved to accommodate the rise time of the dump kicker, by eliminating one PS batch in the last transfer.

The disposition of the bunches in one LHC ring is represented by the formula:

$$3564 = 12 \times 297 = [(81b + 8e) \times 3 + 30e] \times 11 + [(81b + 8e) \times 2 + 119e] \ ,$$

in which b denotes an occupied bunch place and e an empty one.

The bunch structure obtained has implications in certain aspects of beam physics, in particular for the long range beam–beam effect.

3.5 Evolution of performance during the first years of operation

The LHC is the first superconducting collider foreseen to operate with a large value of the beam current. Superconducting magnets tolerate only extremely small beam losses. In order to prevent excessive quenching of the magnets the particles in the beam halo which slowly diffuse out towards the beam-pipe walls have to be intercepted very efficiently by collimators in a warm section of the machine. Although we do not yet know with precision the tolerance level of the LHC magnets to beam losses, after careful studies we are confident that a collimation system can be built to give adequate performance, and two straight sections have been reserved for this purpose.

However, learning how to operate the LHC in such conditions will take some time, and the initial commissioning of the machine will be done with beams of much smaller

intensity than the nominal one. In order to avoid a dramatic reduction of luminosity, proportional to the square of the beam current, in this case we have to operate with a reduced transverse emittance ε_n. This is possible as long as the transverse beam density N/ε_n stays below its nominal value, which is limited by beam–beam effects in the LHC and space-charge problems in the injectors. Provided the transfer and inflection systems are suitably upgraded to preserve the required small emittance all along the injection chain, luminosity can be produced in proportion to the beam current. This of course does not hold for very small currents because there is a lower limit to the emittance achievable after a long chain of transfers.

After about one year of commissioning it is reasonable to expect that the LHC could be operated with one tenth to one fifth of the nominal beam current. Assuming that an emittance as low as 1 μm could be achieved, a luminosity of 10^{33} cm^{-2} s^{-1} would be provided with a beam current of 16% of the nominal value (see Table 3).

Table 3: LHC parameters: commissioning and nominal

Parameter	Symbol	Unit	Commissioning	Nominal
Luminosity	L	[cm^{-2} s^{-1}]	10^{33}	10^{34}
Circulating current/beam	I_{beam}	[A]	0.087	0.53
Particles per bunch	n_{b}		$0.17\ 10^{11}$	$1.05\ 10^{11}$
Number of bunches	k_{b}		2835	2835
Normalized transverse emittance	ε_{n}	[μm.rad]	1	3.75
Beam–beam parameter	ξ		0.0021	0.0034

3.6 Proton losses and their contribution to cryogenic load

The impact of a high-energy hadron on the beam screen induces a shower well beyond the beam screen, so that more than 90% of the energy of the protons lost in a cold area is finally dissipated in the helium bath, contributing to the cryogenic load.

Some proton losses are due to machine imperfections. Many diffusion processes, either in the longitudinal or in the transverse phase-space contribute to these kinds of losses. Most of the initial phase of operation of the LHC, until the nominal performance is reached, will be devoted to improving the beam stability, with the aim of obtaining a single beam lifetime of approximately $\tau_b = 50$ h.

The rest of the losses result from nuclear interactions [2]. In proton–proton interactions, the collisions are elastic (cross-section $\sigma_{\mathrm{el}} = 40$ mbarn), single diffractive ($\sigma_{\mathrm{sd}} = 12$ mbarn) or inelastic ($\sigma_{\mathrm{in}} = 60$ mbarn). In beam–gas collisions, which occur all around the ring, single-diffractive events can be neglected. The residual gas is dominated by oxygen atoms in terms of cross-sections. The sharing between elastic and inelastic collisions is therefore 0.31/0.69. The beam–gas lifetime is very dependent on the history of the machine. After an initial period of primary desorption by the synchrotron radiation, a layer of molecules builds up at the surface of the beam screen (they are frozen at low temperature). These molecules are later kicked off the surface, again by the syn-

chrotron radiation (secondary desorption). They either stick again on the surface or are pumped through the holes of the beam screen. An equilibrium pressure proportional to the beam current is established, depending on the surface density of the frozen molecules. The pressure goes down asymptotically over the years at constant beam current. In the early days of operation, the desorption rate is high, but the beam current will be small (87 mA at the end of the first year). After three years of operation, at the nominal current I = 536 mA, the beam–gas lifetime is of the order of $\tau_{\rm beg} = 85$ h. These two parameters can be used to compute an upper limit of the expected beam–gas losses.

A list of the loss-inducing processes is given in Table 4 with the proton rates and the dissipated powers. The power dissipation is an upper limit estimation for the beam–gas losses, for which a factor of 3 smaller can be expected. The value given corresponds to a local loss of 58 mW/m for the two beams. The power escaping the collimation sections might all be lost in one sector of the ring.

Table 4: Beam losses and power deposition in He for the nominal LHC parameters (for the two beams and two low-β IR)

Source		Rate [p/s]	Total power [W]	Dissipated in He [W]	
Beam–gas	Inelastic	$2 \times 6.9\ 10^8$	2×770	2×770	All around the ring
	Elastic	$2 \times 2.9\ 10^8$	2×330		β-cleaning
Collisions	Inelastic	$4 \times 6\ 10^8$	4×670	4×185	Q-Triplet+D1+collimator in low-β IR
	Single diffractive	$4 \times 2.4\ 10^7$	4×30	4×27	DS in low-β IR
		$4 \times 9.6\ 10^7$	4×110		p-cleaning
	Elastic	$4 \times 4\ 10^8$	4×450		β-cleaning
Machine imperfections		$2 \times 1.65\ 10^9$	2×1850		β+p-cleaning
Cleaning total		$5.9\ 10^9$	6600		
Cleaning inefficiency		$5\ 10^7$		55	Erratic
Total losses		$9.75\ 10^9$	11000	2443	

Elastic interactions and machine imperfections

The protons which leave the stable phase-space volume, either because of machine imperfections or through nuclear elastic scattering do many machine turns until their amplitude reaches the aperture of the beam screen. They can therefore be absorbed by the collimators installed in a warm section [betatronic ($\beta-$)cleaning and momentum (p-)cleaning]. A marginal fraction of their energy will escape this area, estimated to be smaller than 1% (see Section 4.4).

Beam–gas inelastic interactions

The secondary particles emitted by a nuclear inelastic interaction with a nucleus of the residual gas in the vacuum chamber are swept out of the beam axis by the magnetic field of the bending magnets (charged particles) or go straight (neutral particles) and touch the vacuum chamber downstream of the primary interaction up to approximately 15 m. Almost all of the energy of the proton lost is therefore dissipated locally.

Inelastic and single-diffractive losses in proton–proton collisions

The secondary charged particles produced in proton–proton inelastic collisions are almost all absorbed in the triplet of quadrupoles and their protecting collimator, and in the D1 magnets installed on each side of the experimental areas. Figure 2 shows how the corresponding power, emerging from the interaction point and proportional to luminosity, is distributed amongst the elements of the insertion.

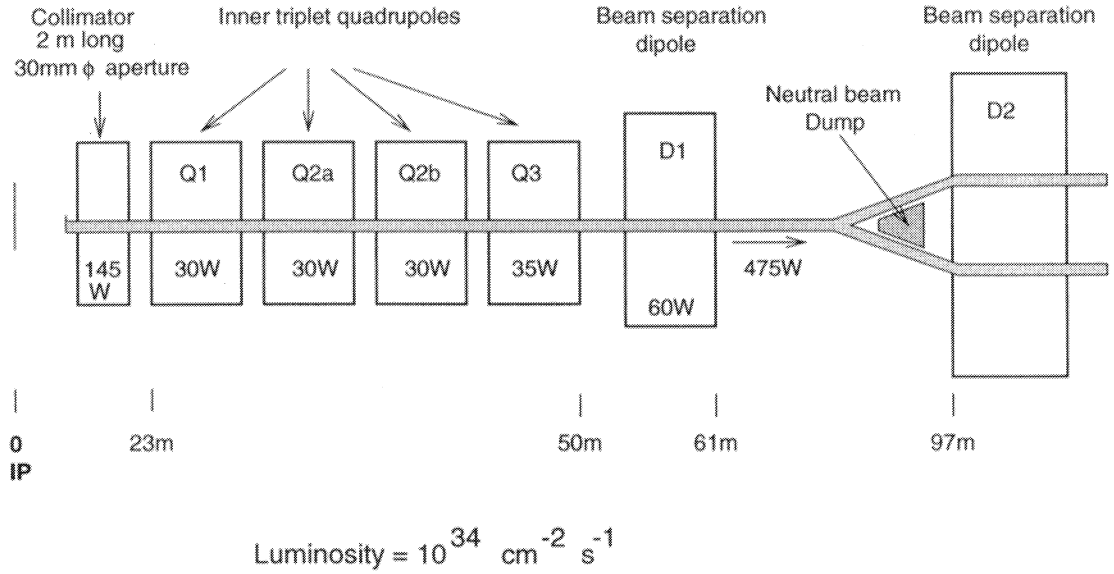

Figure 2: Power deposited in the machine near a high luminosity IP

The major fraction of the energy left by inelastic events (330 W) after D1 is transported by neutrals and will be absorbed by the neutral beam dump in front of D2. The next larger fraction corresponding to the protons emitted by single diffractive events has a momentum close to that of the beam. A substantial fraction (30 W) that has a large momentum offset is lost directly in the dispersion suppressor of the low-β IR, while the remaining fraction (110 W) is captured in the momentum cleaning section (p-cleaning) [3, 4, 5].

3.7 Duration of data-taking runs

At the design luminosity of 10^{34} cm^{-2} s^{-1} the initial characteristic decay time of the beam current due to the collisions themselves is 40 h. Neglecting all other sources of particle loss, this gives a luminosity half-life of 16 h. Taking into account all sources of loss as detailed in Table 4, the beam lifetime is reduced to 22 h and the luminosity lifetime to 10 h, as indicated in Table 1.

The optimum duration of an uninterrupted data-taking period depends both on the luminosity lifetime and on the time it takes to refill the machine. Although the beams can be injected into the two LHC rings in less than seven minutes, the overall interruption of data-taking is much longer. After the old beams have been dumped, one must lower the current in the magnetic systems to the injection values, tune the transfer and capture processes with pilot beams of small intensity, and, after the final transfers have been made, accelerate the beams to high energy and adjust collisions. When the operation of the LHC is well mastered this may take about 2 h. In this case the ratio of average to initial luminosity reaches a maximum of 0.6 if the physics data-taking lasts about 7 h, and refilling of the LHC is required two to three times per 24 h. In the first years of operation one may expect longer filling times, in which case it is advantageous to keep the beams in collision for longer periods.

3.8 Single-beam collective effects in the LHC

The effects considered in this section are only important for high-intensity beams. They include incoherent phenomena, concerning the behaviour of a single particle in the electromagnetic field produced by all the others, and coherent interactions of the beam with its surroundings, usually described in terms of coupling impedances. The second group can be further subdivided into single-bunch effects, associated with the broad band impedance of low-Q structures, and multi-bunch effects, dominated by the narrow band impedance of high-Q resonators. Landau damping of coherent beam oscillation modes that takes place providing their tune shifts remain within the incoherent tune spread can be considered as a bridge between incoherent and coherent phenomena.

The space charge of the beam gives rise to a detuning of the incoherent particle oscillations and affects the collective behaviour of the beam oscillation modes. The direct space charge tune shift at injection energy, corresponding to the nominal LHC bunch population of 1.05 10^{11} protons, is $\Delta Q = -1.2\ 10^{-3}$. Since particles in the core of the bunch are affected more than particles with large amplitudes, about 3/4 of this effect represents a tune spread which helps in the damping of coherent beam instabilities (with the exception of rigid dipole oscillations).

Owing to image currents induced on the beam pipe and on the ferromagnetic magnet poles, *all particles* suffer another incoherent detuning which has opposite signs in the two betatron planes. The vertical Laslett tune shift at injection, estimated assuming plane magnet poles with a distance of about 5 cm, is $\Delta Q_{\mathrm{v}} \simeq -1.8\ 10^{-2}$. This effect can be easily compensated by adjusting the tuning quadrupoles.

The LHC impedance budget at injection energy and at 7 TeV is summarized in Tables 5 and 6, respectively [6]. The dominant contribution to the transverse broad

band impedance at injection is given by the capacitive space-charge effect, which cancels almost exactly the estimated inductive impedance of the shielded bellows and monitor tanks. The result is a rather high threshold for the transverse mode-coupling instability, corresponding to more than five times the nominal bunch population.

The coherent tune shifts induced by the longitudinal broad band impedance for high-order modes should remain smaller than the synchrotron tune spread by a safety factor (of the order of 4). This requirement is rather stringent at top energy, when the r.m.s. bunch length is 7.5 cm, and the threshold bunch population corresponding to the suppression of Landau damping turns out to be 2.4 10^{11} particles.

The transverse resistive wall instability has a rise time longer than 100 machine revolutions and can thus be cured by feedback. This result corresponds to a beam screen with square geometry and rounded corners, working at 20 K, with a 50 μm copper layer of residual resistance ratio RRR = 100. About 10% of the machine circumference is assumed to be at room temperature, with a 2 mm thick beam pipe made of copper.

Table 5: LHC effective impedance (in Ω) at 450 GeV

Injection	$\mathrm{Im}\,(Z_\mathrm{L}/n)_\mathrm{eff}$	$\beta_\mathrm{av}\mathrm{Im}\,(Z_\mathrm{T})_\mathrm{eff} \times 10^{-6}$
Space charge	–0.0058	–442.3
Shielded bellows	0.0814	146.3
Monitor tanks	0.0400	214.6
Pumping slots	0.0156	38.9
Total broad band	0.1312	–42.5
Strip-line monitors	0.127	446.6
Abort kickers	0.007	182.4
SC cavities	0.010	0.4
Total low frequency	0.144	629.4

Table 6: LHC effective impedance (in Ω) at 7 TeV

Top energy	$\mathrm{Im}\,(Z_\mathrm{L}/n)_\mathrm{eff}$	$\beta_\mathrm{av}\mathrm{Im}\,(Z_\mathrm{T})_\mathrm{eff} \times 10^{-6}$
Space charge	$-3.3\ 10^{-5}$	–28.6
Shielded bellows	0.0815	148.8
Monitor tanks	0.0400	214.6
Pumping slots	0.0156	38.9
Total broad band	0.1371	373.7
Strip-line monitors	0.073	257.9
Abort kickers	0.004	109.1
SC cavities	0.010	0.4
Total low frequency	0.087	367.4

The parasitic losses for the LHC at top energy are summarized in Table 7. We have included an upper bound for the power loss due to the leakage of electromagnetic energy through a gap $\Delta = 0.01$ mm between the sliding contacts of the bellows. The latter is certainly a rather pessimistic assumption in view of the new bellows design having spring fingers at the entrance of the gap. The parasitic losses in the shielded bellows have been estimated using a broad band resonator model that does not properly describe the real part of the longitudinal impedance; the corresponding losses therefore only represent an upper bound. Resistive losses associated with possible welds in the beam screen have been estimated assuming two welds (for example, at the top and bottom of the screen), each with a width of 1 mm.

Table 7: Summary of parasitic losses for the LHC at 7 TeV

Power loss [kW]	For a single beam	Power loss per unit length [mW/m]
3.60	Incoherent synchrotron radiation	206
1.99	Resistive wall (20 K)	75
0.28	Welds	10
0.27	Pumping slots	10
< 0.82	Shielded bellows	< 31
$\ll 1.05$	Leaks in bellows gaps	$\ll 39$
8.01	Total	371

References

[1] W. Herr, LHC Note 301 (1994).

[2] L. Burnod, J.B. Jeanneret, Beam Losses and Collimation in the LHC: A Quantitative Approach, CERN SL/91–39 (EA), LHC Note 167 (1991).

[3] J.B. Jeanneret, Momentum Losses and Momentum Collimation in LHC, A First Approach, CERN SL/92–44 (EA), LHC Note 211 (1992).

[4] K. Eggert, A. Morsch, Particle Losses in the LHC Interaction Regions, CERN–AT/93–17 and LHC Note 229 (1993).

[5] A. Morsch, Local Power Distribution from Particle Losses in the LHC Inner Triplet Magnet Q1, CERN AT/94–06 (DI) and LHC Note 265 (1994).

[6] F. Ruggiero, CERN SL/95–09 (AP) and LHC Note 313 (1995).

4 Beam cleaning system

The necessity of beam cleaning with collimators in the LHC was demonstrated from the start of the project in Ref. [1]. A brief update of the expected losses related to quench level is presented, followed by the principles of collimation, the proposed location of the collimators in their dedicated Insertions IR3 and IR7 (see Part II, Section 2.5). The calculation of an efficiency, compared with the required performance is also shown.

4.1 Need for beam cleaning

Transient losses at injection

Even in good operational conditions, a finite fraction (estimated to $f \approx 5\%$) of the injected protons will lie outside their RF bucket at the beginning of the ramp of acceleration. The uncaptured protons are not accelerated and drift towards the vacuum chamber in a short time ($\delta t \leq 1$ s) when the magnetic field rises. The level of a transient loss of protons per metre capable of quenching a magnet has been recently reviewed [2] and is estimated to be of the order of $n_{\mathrm{q\ inj}} \approx 10^{10}$ pm^{-1}. Expected losses exceed the tolerable level by the inverse of the ratio (with $N_{\mathrm{stored}} = 3\ 10^{14}$ protons)

$$r_{\overline{\mathrm{RF}}} = \left(\frac{f \cdot N_{\mathrm{stored}}}{n_{\mathrm{q\ inj}}} \right)^{-1} \approx (1500\ \mathrm{m})^{-1}\ . \tag{1}$$

Steady losses at top energy

In collision mode, at nominal luminosity the rate of protons per beam leaving the stable central area is estimated to be $\dot{N}_{\mathrm{p\ top}} \approx 2.4\ 10^{9}$ ps^{-1}. The proton losses occur mostly in the betatronic plane in this case. A quench occurs in a superconducting magnet if, in a rather small azimuthal range, the rate of impacting protons per metre of vacuum chamber is larger than $\dot{n}_{\mathrm{q\ top}} \approx 7\ 10^{6}$ ps^{-1} m^{-1} see Ref. [2] and Part III, Section 1.2.2. The ratio of the two numbers is

$$r_{\mathrm{top\ coast}} = \left(\frac{\dot{N}_{\mathrm{p\ top}}}{\dot{n}_{\mathrm{q\ top}}} \right)^{-1} \approx (340\ \mathrm{m})^{-1}\ . \tag{2}$$

Definition

The cleaning system will absorb protons but some will be scattered. The latter are diluted in amplitude and phase by the scattering process, and a fraction of them will impinge the vacuum chamber in a section of limited aperture in the ring. A measure of the efficiency is defined by the product of the fraction of the protons which escape the system with a factor of longitudinal dilution and therefore has units $metre^{-1}$. This quantity, called *relative residual power*, must be smaller than the r factors computed above.

4.2 Betatron and momentum collimation

Both betatron and momentum collimation are needed in the LHC. The primary collimation must preserve the full nominal transverse emittance in the momentum range of the

RF bucket. At the same time the momentum distribution of the halo must be limited to the stable momentum range found to be $|\Delta p/p| \leq 3\ 10^{-3}$ [3].

Ideally the transverse amplitude limit set by the primary collimators should be the same for all momentum values. This implies zero dispersion values (H and V) at the primary collimators. For example, it is impossible to protect the low-β quadrupoles (located at zero dispersion) using a primary collimator at $D_x = 2$ m without cutting into the transverse emittance at the edges of the bucket.

On the other hand, a zero-dispersion collimator does not protect the non-zero dispersion regions of the machine against particles with large momentum errors. An efficient protection against these particles requires a large $D_x/\sqrt{\beta_x}$ value at the primary momentum collimator. With the geometry of the dispersion suppressor relative to the LEP tunnel, this is not easy to achieve and requires larger quadrupole strengths than needed for betatron collimation.

The betatron and momentum collimation systems will therefore be installed in two different insertions:

- IR3 optimized for betatron cleaning, with a zero dispersion function in the central straight section;
- IR7 optimized for momentum cleaning, with a dispersion oscillation as large as possible while keeping the $\beta_{\max}$ values at a reasonable level.

Several considerations apply in the same way to both betatron and momentum collimation. A formal and detailed approach is developed in Ref. [4]. It is shown that in the particular case of a straight section, the treatment of a momentum collimation system (or more exactly a combined betatron and momentum system, because the β function cannot vanish) is exactly reduced to the betatronic one if the dispersion satisfies the condition $D'/D = -\alpha_x/\beta_x$ at the horizontal primary collimator. In this case, the maximum amplitudes of the secondary halo are the same for all momentum deviations. Therefore most of the parameters and performances discussed below apply to both the momentum and the betatron collimation.

4.3 Two-stage collimation

Protection of the LHC requires a collimation transversely between the long-term dynamic aperture A_{long} (up to which trajectories have a stable amplitude) and the short-term one A_{short} (beyond which the motion becomes strongly chaotic). In terms of diffusion, in the region of amplitudes $A_{\text{long}} < A < A_{\text{short}}$, the drift speed of the halo remains in the range $dA/dt \approx 1\ \sigma$/s (σ is the r.m.s beam radius) and the impact parameter b of the protons on the primary jaw will be of the order $b \approx 1\ \mu$m [1, 5]. The fraction of the protons scattered elastically from the collimator jaw before absorption might thus be of the order of 50% [1]. Therefore, a two-stage collimation system (primary and secondary collimator) is required.

At injection, the aperture of the ring will be $A_{\text{ring}} = 10\ \sigma$. The maximum transverse amplitude of the secondary protons must therefore satisfy the condition $A_{x+y\ \text{sec}} < 10\ \sigma$. The primary collimators must therefore be positioned at a transverse distance $n_1 = 6\ \sigma$

from the beam axis (see below), and the secondary ones at $n_2\sigma = (n_1 + 1)\ \sigma$ to avoid a secondary collimator becoming a primary one because of operational errors.

4.4 The location of the collimators in IR3

How many collimators must be installed and where to locate them is discussed in detail in Ref. [4]. Basically, to reach the goal of $A_{\rm sec} < 10\ \sigma$, the primary halo must be cut at the distance $n_1 = 6$ radially, i.e. defining a circular cut in the normalized phase-space. This is done with three primary collimators, one horizontal (TCPH in Fig. 1), one vertical (TCPV) and one skewed at 45° in normalized x–y coordinates (TCPS). The three primary jaws must be located inside the upstream section of the dogleg dipoles (see layout of IR3). With the present optics, the TCPV is located near Q6 (large $\beta_{\rm y}$), and TCPH and TCPS are in front of the second dipole of the dogleg structure (large $\beta_{\rm x}$).

This layout can be slightly altered if radiation questions, presently being addressed, imply that the dipoles should be protected by inserting shielding material downstream of the primary collimators.

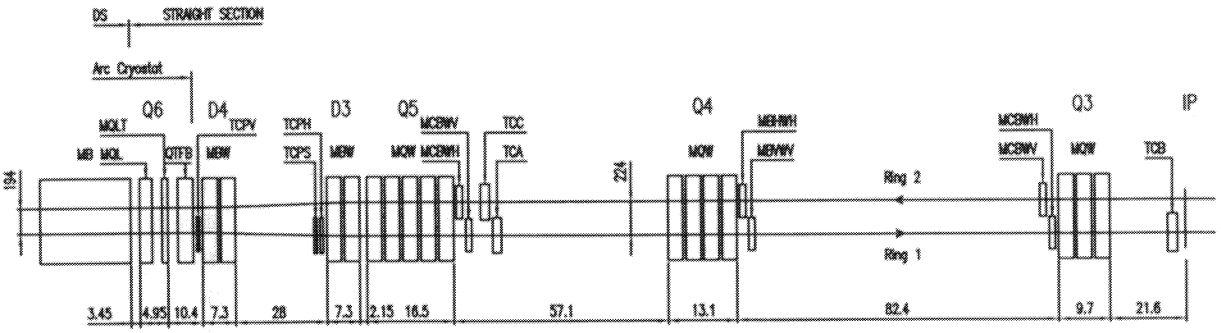

Figure 1: Layout of the cleaning insertion

To contain the secondary halo, circular collimators, in practice made of eight jaws forming an octogon, will be installed at three different longitudinal locations chosen with the simulation program COLOC [6]. The strategy used is to consider the primary collimators as pure scatterers and the secondary ones as black absorbers. A good solution is obtained when the largest secondary amplitudes are minimized and smaller than the acceptable $A_{\rm sec}$. With the present optics of IR3 the maximum excursions of the secondary halo are

$$A_{\rm x} = 7.6\ \sigma \quad A_{\rm z} = 7.3\ \sigma \quad A = 9.6\ \sigma\ . \tag{3}$$

If instead of a circular collimator, straight horizontal and vertical jaws were to be used, the secondary beam halo would extend up to $A = 11.2\ \sigma$, a value clearly too high. The location of the secondary collimators TCA, TCB and TCC is indicated in Fig. 1.

Currently, in the optimization program, the eight jaws of a given secondary collimator are all located at the same place. The above best figure for the secondary amplitudes can be improved by adjusting separately the longitudinal location of some of the jaws of the secondary collimators. This requires further study.

4.5 Dogleg

The secondary particles produced in the collimators have to be swept out of the beam axis by a so-called dogleg structure. The geometry of the dogleg structure is described in Section 2.5. The required value of d_{warm}, the separation of the beam axes through the collimation insertion, is determined by tracking the secondary particles (all charges and momenta) re-emitted by every collimator up to the downstream end of the dispersion suppressor (Q10) [7] with the computer program SOFT [8]. The spatial and angular distributions of the incoming protons on the different jaws are taken from data files generated by the program K2 [6] (see Section 4.6). Inelastic events are generated with the program PYTHIA [9]. A map of energy deposition is generated all along IR3 and its downstream dispersion suppressor.

With $d_{\text{warm}} = 194$ mm, the same as in the rest of the ring, the energy deposition has a maximum near Q7, where the dispersion grows fast. Above $d_{\text{warm}} = 224$ mm, this maximum goes down and crosses the level of deposition near Q9, where nearly on-momentum particles are lost which cannot be discarded by the dogleg. This separation can be reached with two dipole magnets of bending strength 11 Tm, separated by 40 m. A design study of the magnets has been presented [10]. The residual energy deposition per proton is given in Table 1.

Table 1: Residual power losses at injection and top energy. The primary collimators are located at $n_1 = 6\ \sigma$, and the aperture limitation in the ring is set to $A_{\text{ring}} = 10\ \sigma$.

	Injection	Top energy
	$\varepsilon_{\text{inj}}[\text{m}^{-1}]$	$\varepsilon_{\text{top}}[\text{m}^{-1}]$
Distant elastic losses	$2\ 10^{-5}$	$5\ 10^{-6}$
Losses in IR3-DS	$2\ 10^{-5}$	$3\ 10^{-5}$
Requested $r[\text{m}^{-1}]$	$7\ 10^{-4}$	$3\ 10^{-3}$
Estimated margin factor	33	100

Another interest of the dogleg structure is to avoid having several collimators exposed to the high flux of secondary particles emitted at another upstream jaw. This is important for the integrity of the cleaning system.

4.6 Performance

Definition and goal

The performance of the collimation system is evaluated by a detailed tracking of the particles which escape the cleaning section in spite of the tight secondary jaws (for example tertiary protons or neutrals not submitted to the optics).

The inefficiency of a collimation system can be defined by the ratio of the maximum residual power deposited per metre along the ring over the power related to the flux of protons falling on the collimators. This relative residual will be called ε and has unit 1/m.

The quantity ε can be compared to the r values given in Section 4.1. To compute ε, two kinds of particle which escape the cleaning section must be distinguished:

- Elastic escaping protons;
- Secondary particles from inelastic interactions.

In both cases, detailed simulations must be used and the locations of large residual losses $\varepsilon(s)$ be identified. The optics of the ring and of the cleaning section must be defined, the collimators must be located, and the material used for their jaws specified.

Elastic losses

The computer program K2 [6] is used to track protons through collimator jaws across the cleaning insertion and around the ring. The protons are made to drift slowly until they touch a collimator. The tracking is continued over as many turns as necessary until the proton has an inelastic interaction or goes beyond a variable aperture limitation in the ring. In the jaws, scattering with every significant kind of nuclear or electromagnetic elastic and diffractive process is implemented, depending on the atomic mass and atomic number of the jaw material. Statistics at stop points are recorded for further analysis. Amplitude and phases at the aperture limitation are recorded. This allows the computation of the longitudinal distribution of the residual losses in the ring and therefore the determination of the relative residual inefficiency parameter ε.

Collimator material

The choice of the material and of the size of the collimator jaws is a compromise between scattering and thermal properties. The jaw must not be deformed by a transient heat load. Therefore, materials with high thermal conductivity must be used. They must also have a large radiation length to avoid intense electromagnetic showers developing in the jaw. These considerations exclude insulators, heavy metals and too-long jaws.

The impact parameter of protons on secondary collimators will spread over millimetres, and thus edge scattering will not have significant effects. The jaw must then simply be a good absorber and copper is an adequate material.

Simulations indicate a preference for primary jaws made of light atoms. The outscattered protons get angular kicks much smaller than the beam divergence and therefore can do many turns before they are absorbed. This choice also fulfils the requirement of minimal showering in the jaw.

The efficiencies discussed below are computed with 200 mm long beryllium primary collimator jaws and 500 mm long copper secondary collimator jaws. Aluminium will also be considered for the primary jaws in further studies.

4.7 Efficiencies

The results presented here have been computed with the optics of IR3 and the collimator locations shown in Fig. 1, dedicated to betatron collimation.

The design of the momentum collimation in IR7 is not sufficiently advanced at present for a detailed simulation to be done. Strictly speaking, the results shown here are valid only for betatronic collimation. But as already mentioned, a correctly designed momentum cleaning must have similar performance at equal collimator opening, and therefore similar efficiencies.

Distant elastic losses

To escape the cleaning section and to touch the vacuum chamber, a proton must get a substantial angular kick in a secondary collimator. Elastic cross-sections fall rapidly with the angle, and therefore the rate of tertiary losses decreases with the actual value of an aperture limit of the ring. The level of the losses at an aperture limitation will therefore depend on the value of this aperture and not only on the properties of the cleaning system. In the design of IR3, the residual power in the case of distant losses increases only by a factor of 3 if the aperture limitation in the ring $A_{\text{ring}} = 10\ \sigma$ decreases by 1 σ, and, conversely, decreases by a factor of 3 if the aperture increases by 1 σ. The value $A_{\text{ring}} = 10\ \sigma$ is therefore not a sharp critical limit.

The longitudinal dilution of the losses near an aperture limitation is computed using the relation $d\psi = ds/\beta$. The conservative simplification $\beta = \beta_{\text{min,arc}}$ is currently being made in the calculations.

Numerical results

The results of the simulations are given in Table 1 for both the injection and the top energy, for distant elastic losses and inelastic losses in the dispersion suppressor of IR3 (the latter ones were discussed in Section 4.5).

The required efficiencies can be met with a two-stage system. The collimator jaws must define a circular cut in the transverse space, and three secondary collimators are needed to cut the secondary halo generated at the primary ones.

- At top energy, the limitation of efficiency appears in the dispersion suppressor of the cleaning insertion. The factor of margin $m = 100$ is good. It will allow a stored beam to be maintained even in somewhat unstable conditions.

- At injection energy, the residual power deposit is similar in both the dispersion suppressor and in the case of distant losses. The present collimator scheme offers a margin factor of $m = 33$, in the case of a transient loss of 5% of the beam. This means that a quench might even be avoided if all of the injected beam is not captured by the RF system. Of course, safety requires initiation of a dump action before the full beam is absorbed by the collimators. The same conclusions apply when an instability builds up after injection, also requiring the initiation of a dump action before a quench occurs.

- The rules to define a momentum collimation system exist. They remain to be applied to a case study, but most of the results obtained for betatronic collimation also apply to the momentum collimation, in particular the computation of efficiencies at similar effective collimator openings.

References

[1] L. Burnod and J.B. Jeanneret, Beam Losses and Collimation in the LHC: A Quantitative Approach, CERN SL/91–39 (EA), LHC Note 167 (1991).

[2] J.B. Jeanneret, D. Leroy, L. Oberli and T. Trenkler, Quench Levels and Transient Beam Losses in LHC Magnets, CERN SL/95–xx, in preparation.

[3] T. Risselada, Transverse and Momentum Shaping of the Circulating LHC Beam by the Primary Collimators, CERN SL/Note 95–32 (AP) (1995).

[4] T. Trenkler and J.B. Jeanneret, The Principles of the Two-stage Betatron and Momentum Collimation in Circular Accelerators, CERN SL/95–03 (AP), LHC Note 312 (1995).

[5] T. Risselada, The Effect of the Betatron Tune on the Impact Parameter at LHC Primary Collimators, CERN/SL/Note 92–16 (AP) (1992).

[6] T. Trenkler and J.B. Jeanneret, K2: A Software Package Evaluating Collimation Systems in Circular Colliders (Manual), CERN SL/Note 94–105 (AP) (1994).

[7] J.B. Jeanneret and T. Trenkler, LHC Cleaning Insertion: Some Parameters for the Dogleg and the Warm Quadrupoles, SL/Note 94–94 (AP), LHC Note 304 (1994).

[8] J.B. Jeanneret and T. Trenkler, The Secondary Off-Momentum Particle Tracking Program (SOFT), CERN SL/Note (AP), to be issued.

[9] T. Sjöstrand, The PYTHIA Program, Comput. Phys. Commun. **82** (1994) 74.

[10] M. Giesch, Design and Parameters of the Warm Magnets for the LHC Cleaning Insertions, CERN AT/95–04, LHC Note 311 (1995).

5 Radio frequency and feedback systems

5.1 Basic parameters

The machine parameters directly relevant to the design of the RF system are summarized in Table 1. The RF frequency, 400.8 MHz, is the highest multiple of the SPS RF frequency (200.4 MHz) compatible with the length of the SPS bunches at transfer. Higher multiples would be interesting to produce more economically the short bunches needed during collision; they would also lead to smaller-diameter cavities. Unfortunately, they cannot be used because of the above constraint at injection.

Table 1: Basic parameters relevant to the LHC RF system (protons)

	Unit	Injection 450 GeV	Collision 7 TeV
Frequency	[MHz]	400.789	400.790
Harmonic number		35640	35640
RF voltage	[MV]	8	16
Energy gain/turn (20 min ramping)	[keV]		485
Synchrotron frequency	[Hz]	62	21
Bucket area	[eV.s]	1.46	8.7
Bunch area (2σ)	[eV.s]	1	2.5
r.m.s bunch length (1/4 full bunch length)	[m]	0.13	0.075
r.m.s energy spread (1/4 full Δp/p)		$4.5\ 10^{-4}$	$1\ 10^{-4}$
Synchrotron radiation energy loss/turn	[keV]		7
Longitudinal damping time	[h]		12.5
Intensity per bunch		$1.05\ 10^{11}$	$1.05\ 10^{11}$
Intensity per beam	[A]	0.53	0.53
RF component of beam current (per beam)	[A]	0.93	1.15
Intrabeam scattering growth time:			
Horizontal	[h]	45	100
Longitudinal	[h]	33	60

The longitudinal emittance of the proton bunches is blown up from 1 eV.s at injection to 2.5 eV.s during storage to make the intrabeam scattering effects negligible. This, combined with the required bunch length of $\sigma_s = 7.5$ cm, determines the maximum circumferential RF voltage of 16 MV. With Pb ions, keeping the same RF voltage and bunch length entails a reduction of the intrabeam scattering lifetime. However, this is still considered acceptable: the overall luminosity lifetime becomes 6 to 10 h depending on the beam intensity.

Transient beam loading is the dominant factor in the design of the LHC RF system; this is due to the high RF beam current, combined with the presence of long gaps, in particular the beam dump gap, 3 μs long [1]. To minimize the effects of transient beam

loading, cavities with a high stored energy are preferred, as in high-intensity e^+e^- storage rings. Superconducting cavities with a wide beam tube aperture (30 cm) have been chosen for the LHC. Compared to conventional copper cavities they provide a gain of one order of magnitude against transient beam loading effects. A beneficial consequence of this choice is the very low contribution of the RF cavities to the overall machine impedance. Even with modest damping factors, the cavity higher-order modes should not drive any coupled bunch instabilities in the LHC.

Although the real power delivered to the beams is relatively modest (257 kW/beam during acceleration), the necessary installed power needed to handle them is much larger. The challenge in the design of the LHC RF system is precisely to minimize the beam handling power in order to arrive at acceptable parameters for the cavity RF couplers.

The cavity diameter is incompatible with the beam separation of 194 mm. In the original 'Pink Book' design, the cavities had to be located at a place where the two beams were almost collinear, i.e. close to an interaction region. In this case the beam current is doubled and it turned out that the power to be transmitted by the cavity couplers was unrealistic. Instead the beams will be separated by 420 mm to accommodate separate cavities for the two beams, staggered longitudinally to minimize the necessary separation. This solution has a number of advantages, the decisive one being that the transient beam loading effects and therefore also the coupler power are halved at injection. The RF cavities are located in IR4, where the two beams will be separated further, using pairs of superconducting dipoles. IR4 is already equipped with klystron power supplies and the electrical power distribution needed for the RF equipment.

5.2 The cavities

Eight single-cell superconducting cavities per beam are needed. The maximum operating voltage per cavity (2 MV) corresponds to the very conservative average accelerating field of 5 MV/m, easily achieved already in a prototype cavity [2]. The large tube diameter (30 cm) which makes the R/Q of the cavity low (high stored energy), connects all eight cavities of a row. This has the beneficial effect of reducing the R/Qs of most of the higher modes of the cavities [3]. These modes, except the first two deflecting ones around 500 MHz, propagate in the wide beam tube. Therefore they can be damped with devices located not very close to the cavity (broad band antennas mounted on the beam tube). The first two transverse modes can be damped with tuned antennas located close to the cavity. The required damping to achieve stability with natural Landau damping is fairly modest ($Q_{\mathrm{ext}} \cong 10^4$) [4].

The large tuning range of the cavity is needed to compensate the average reactive component of the beam. The LEP solution (magnetostrictive nickel bars) is difficult to apply in the LHC case because of the tuning range and the mechanical stiffness of the single-cell, wide-aperture cavity. New solutions are under study (e.g. giant magnetostriction materials), which will determine the (4.5 K operating temperature) cryostat design.

Figure 1 shows the preferred solution with warm actuators (mechanical and magnetostrictive) located outside the cryostat and connected to the cavity flanges with low

thermal conductivity, high tensile strength materials (carbon fiber and stainless steel). The second beam tube passes outside the helium tank, in the cryostat insulation vacuum.

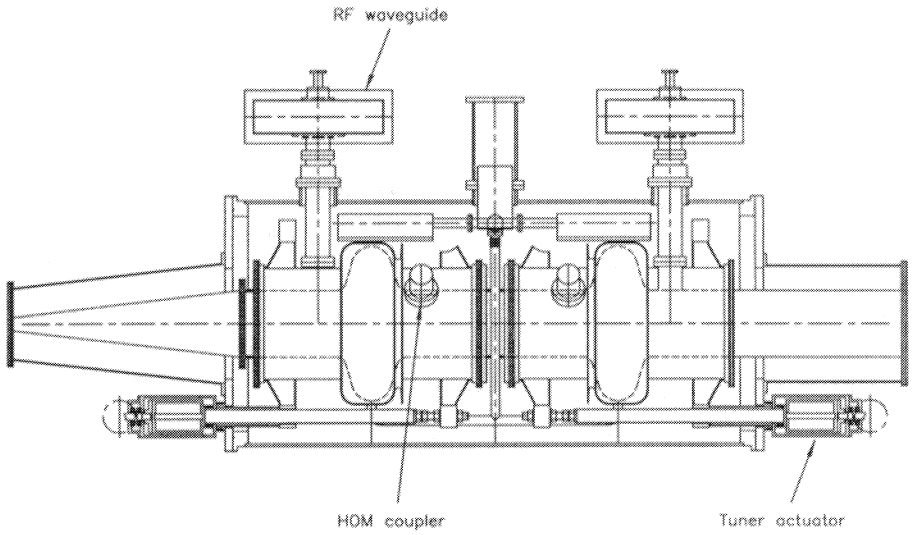

Figure 1: Superconducting RF cavity

The RF coupler is the most critical cavity component. It will be an upgraded version of the LEP coupler [5] scaled to 400 MHz. The coupling is variable (with a $\lambda/4$ long choke located outside the RF window) to minimize the coupler field both at injection and during storage, and to permit, if necessary, a higher cavity voltage for Pb ions with the same RF power. A d.c. bias of the inner conductor will be applied to suppress multipactoring in the coaxial part of the coupler.

5.3 Power requirements

The power delivered to the beam by each cavity during ramping is only 32 kW, but suppression of the beam-induced phase modulation at injection requires more than 100 kW. It is necessary to suppress the large phase modulation (up to 130° RF phase at injection) to minimize as much as possible capture losses, which may generate magnet quenches. This requires the power generator to inject a current in the cavity opposite the beam current. The corresponding power is optimized by adjusting the coupling factor of the RF coupler and the detuning angle of the cavity [6] (Table 2). During storage, phase modulation is no longer compensated (it would require even more power); however, the resulting displacement of the crossing points (± 2.6 mm at the odd points, zero at the even points) is negligible. Therefore the maximum steady power quoted in Table 2 is only needed during the injection flat bottom. The peak power corresponds to the compensation of an injected beam with a phase error of $\pm 15°$, and lasts a few synchrotron periods ($\cong$ 50 ms).

It would be desirable for the design of the critical low-level electronics (RF feedback in particular) to drive one cavity per klystron. However, the more economical solution

of having one klystron driving two cavities is being examined. The distance between klystron and cavities must be limited to at most 15–20 m. This is compatible with the installation of the klystrons in the klystron gallery, and the use of existing LEP high-voltage converters.

Table 2: Main Cavity Parameters

Number of cavities/beam		8
Maximum voltage/cavity	[MV]	2
Cavity R/Q	[Ω]	44.5
Cavity diameter at equator	[mm]	689
Tuning range	[kHz]	10
Frequency of the lowest HOMs (transverse)	[MHz]	503, 542
Coupler power (forward):		
Steady-state (injection)	[kW]	116
Peak	[kW]	176

5.4 Longitudinal feedback system

The design of the both the longitudinal and transverse dampers is dominated by the injection requirements, i.e. the capture losses must be kept as small as possible in the presence of phase injection errors, and the transverse emittance blow-up, resulting from decoherence induced by magnetic and space-charge non-linearities, must be minimized. Instability control, except for resistive wall at low frequency, is less demanding because superconducting cavities present small impedances. In most cases, Landau damping should prevent longitudinal and transverse coupled-bunch instabilities [7].

Longitudinal dampers are 200 MHz copper cavities, with little stored energy (high R/Q, large outside diameter). The low frequency is chosen to provide an almost uniform kick along the bunch length, at injection, and the high R/Q minimizes the power needed to act on each bunch independently. There are two (possibly three) feedback cavities per beam, also located in the region of enlarged beam separation.

Each cavity should provide a peak voltage of 110 kV (15° phase injection error, damping time of three synchrotron periods). It is driven by a tetrode amplifier located on the cavity itself in order to keep an approximately constant transformation ratio between anode voltage and cavity gap over the ±20 MHz operating range of the damper [8]. The power rating of the tetrode amplifier (50 kW) is determined by the necessary rate of change of the feedback voltage during the gap between two injected batches. The high-power bandwidth of the amplifier is much smaller than ±20 MHz as high power is only needed against injection transients.

The impedance of the feedback cavities will be kept low with RF feedback for the fundamental mode, and with tuned couplers for the few significant higher-order modes.

5.5 Transverse dampers

The transverse dampers are mainly aimed at reducing injection oscillations but should also reduce any emittance blow-up due to ground motion and to magnetic noise or ripple. At injection the gain should be large enough to keep emittance blow-up small (2.5%) in the presence of space-charge decoherence ($\Delta Q = 10^{-3}$). The necessary deflections can be achieved by four kickers, each consisting of a pair of electrostatic plates 1.5 m long with a gap of 45 mm and a maximum voltage of 8 kV. These deflectors, which are warm devices, could be installed in the region of the diverging beams. The electrostatic deflectors are excited by a pair of push-pull tetrodes driven by a broad band (20 MHz) amplifier. The same deflectors are used, up to the highest frequency of the damper (20 MHz), at a reduced voltage capability, limited by the anode-deflector capacitance and the peak current of the tube. This is adequate for correcting the effect of the injection kicker ripple (2 mm oscillation on the newly injected batch at a frequency of about 1 MHz), the resistive wall instability, and the transverse instabilities induced by narrow-band parasitic impedances. A dedicated transverse beam monitor, working at room temperature, will provide the damper signals (horizontal for one beam, vertical for the other). An additional signal, coming from one of the regular closed-orbit pick-ups, may be used to adjust for changes of the machine operating points.

References

[1] D. Boussard and V. Rödel, The LHC RF System, Proc. XV Internat. Conf. on High Energy Accelerators, Hamburg, July 1992, ed. J. Rossbach (World Scientific, Singapore, 1993).

[2] D. Boussard and V. Rödel, Status of the Superconducting 400 MHz Cavity for the LHC, CERN–SL/RF Note 95–2.

[3] A. Angelov and V. Rödel, Higher-order Modes and Loss Factors of the LHC 400 MHz Accelerating Structure, CERN–SL/RFS/Note 92–19 (1992).

[4] D. Boussard and E. Onillon, Damping Requirements of the Higher-order Modes of the LHC Cavities, CERN–SL/RFS Note 93–116.

[5] J. Tückmantel et al., Improvements to Power Couplers for the LEP2 Superconducting Cavities, Proc. 1995 Particle Accel. Conf., Dallas, and CERN–SL/95–40 (RF).

[6] D. Boussard, RF Power Requirements for a High-intensity Proton Collider, CERN SL/91–16 (RFS).

[7] D. Boussard and E. Onillon, Damping of Phase Errors at Injection in the LHC, Proc. 1993 Particle Accel. Conf., Washington DC, 1993, eds. C.W. Leeman and J.J. Bisognano (IEEE, Piscataway, N.J., 1994).

[8] W. Höfle, RF Power Requirements for the LHC Bunch-to-Bunch Longitudinal Feedback System, CERN SL/RF Note 94–60.

6 Transfer lines from the SPS

It has finally been decided to build these transfer lines with room-temperature magnets. Superconducting magnets were also considered, but detailed cost estimates have shown that the use of specially designed, small-aperture, room-temperature magnets is overall the most economic solution, both for construction as well as for running.

As a consequence, for injection into the clockwise circulating LHC ring, a different transfer line had to be chosen (Fig. 1). This new line, TI2, starts in the SPS at straight section LSS6 to end at the LHC near Point 2. It makes use of the existing SPS extraction system, follows for about 350 m the existing transfer line TT60, and branches off at the end of the underground switchyard TCC6. The part to be newly built is about 2.8 km long and consists of a central bending section of 48° deflection and two long straight sections at either end. Because of the inclination of the LEP tunnel, TI2 is almost horizontal.

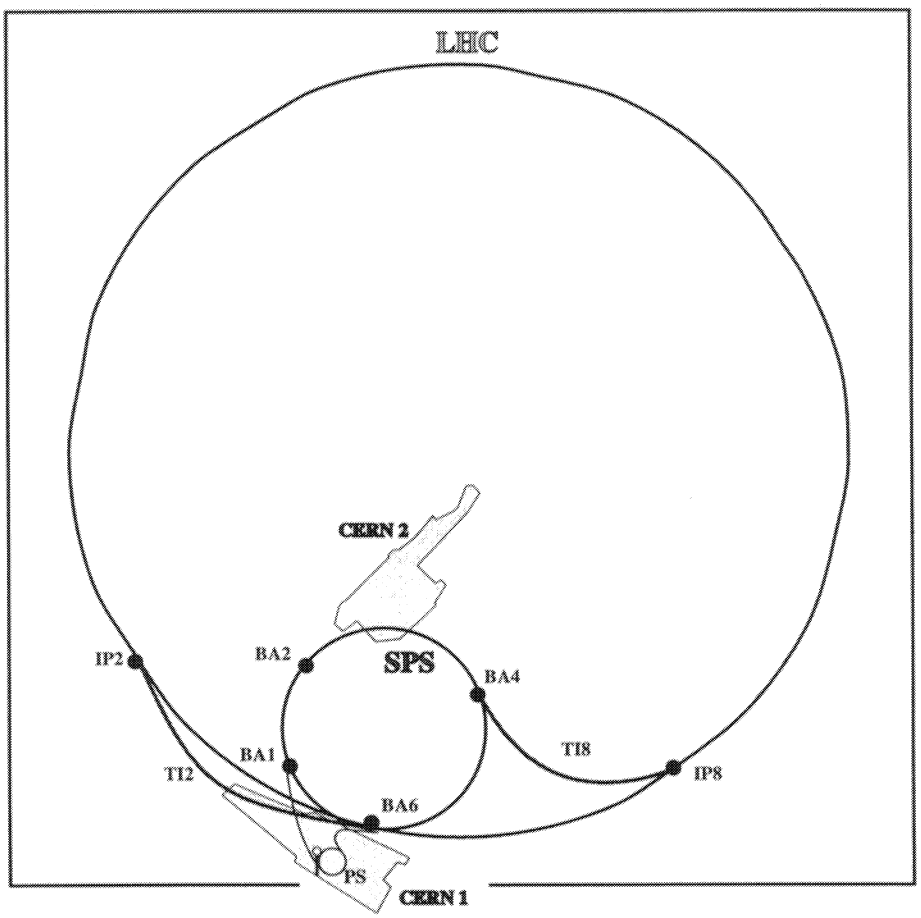

Figure 1: SPS–LHC transfer lines

The path of the transfer line TI8, for injection into the anticlockwise LHC ring, had to be adapted for the use of room-temperature magnets (Fig. 1). Starting at the SPS in LSS4, it follows a straight line for about 600 m and ends after a long bending section of

103° deflection near LHC Point 8. It has an overall length of about 2.6 km and is installed on a slope of 3.5% to overcome the difference in depth of the SPS and LEP tunnels of 72 m.

For the bending sections, a FODO lattice very similar to that of the SPS, with 4 dipoles per half-cell, has been chosen. The preliminary design of the dipoles assumes a length of 6.3 m, an aperture of 25 mm, and a nominal field of 1.8 T. Current and resistance of the coils are matched to the use of the available LEP power converters. The quadrupoles are assumed to have a length of 1.25 m, an aperture of 30 mm between pole tips, and a nominal gradient of 60 T/m. With these assumptions, and with the extra space needed for beam monitors and correction dipoles, the length of the half-cell has been fixed at 30.3 m.

The straight sections of TI2 and TI8, for most of the length, will use the same 1.25 m long quadrupoles as the bending sections. Towards the ends, for optical matching and for additional horizontal and vertical deflections, magnets with larger apertures are required. It is assumed that most of these magnets will come from present installations, which will no longer be in use.

The number of 6.3 m long dipoles and 1.25 m long quadrupoles required for the bending sections and the straight sections is as follows:

TI2: 112 dipoles and 82 quadrupoles
TI8: 240 dipoles and 76 quadrupoles.

It is possible to power the two beam lines from the existing SPS and LEP powering structures with only small additional expenditure and to make use of the existing infrastructure. The power consumption is low since these beam lines operate normally only during short periods when refilling the LHC.

7 Injectors

One of the big assets of the LHC project is the existence on the CERN site of a reliable chain of high-performance accelerators which are well suited to providing the LHC with its supply of protons. All CERN's proton machines play their role in the injection scheme for the LHC: the 50 MeV proton linac (Linac 2), the 1 GeV PS Booster (PSB), the 26 GeV PS, and finally the SPS which will inject protons at 450 GeV — its top energy — into the LHC. Two new beam lines at this energy are required to allow protons to be fed to the LHC in both the clockwise and anticlockwise direction, see Section 6, Fig. 1.

7.1 Injection scheme

The injector chain has to deliver a beam quality at least compatible with the nominal LHC performance. The beam has to fit into the tiny LHC dynamic aperture at injection while providing enough intensity to ensure high luminosity at collision. The longitudinal emittance of the bunches is determined by the need to keep the growth rate due to intrabeam scattering in the LHC within tolerable limits.

Experience shows that an injector machine should be capable of 'saturating' the client accelerator. That is why a higher performance level is aimed at, which ultimately should enable filling the LHC up to the beam–beam limit and bring the additional advantage of a welcome operational margin for the nominal beam. The beam parameters required at LHC injection are shown in Table 1:

Table 1: LHC injection beam parameters

Number of protons per bunch – nominal		10^{11}
– beam–beam limit		$1.7\ 10^{11}$
Bunch spacing	[ns]	24.95
Transverse emittance (r.m.s., normalized)	[μm]	3.5
Longitudinal emittance	[eV.s]	1

This beam cannot be produced by the injector chain as it stands now; most of the modifications, discussed below, are dictated by beam dynamics constraints in the accelerators involved. An overview of the major parameters of the injector chain [1] is compiled in Annex 1 and the bunch disposition in the PS, SPS, and the LHC is shown in Fig. 1, Part II, Section 3.4. Note that 24 SPS (72 PS, 144 PSB) cycles will fill both of the LHC rings in about seven minutes. A detailed analysis of the filling scheme (see Section 3.4), taking into account the rise/fall times of the various kicker magnets (including the LHC beam dumping kickers) yields 2835 bunches per LHC ring (3564 possible bunch places).

7.2 SPS

The SPS is limited by the total amount of particles it can accelerate, so only 3/11 of its circumference will be filled (by three PS cycles), requiring in turn 12 SPS pulses to fill one

LHC ring. A new superconducting RF system, 6 MV at 400.8 MHz, will be installed in order to compress the bunches longitudinally prior to ejection towards the LHC. Acceleration in the SPS will be done with the existing travelling-wave 200 MHz system whose amplifiers and couplers will be upgraded. During the ramp the longitudinal emittance will increase to 1 eV.s from the injection level. The choice of injection scheme will be determined by the microwave instability threshold and transient beam loading. Two solutions, the first to have short bunches with as high as possible momentum spread and the second, to use an additional low-frequency (80 MHz) RF system to capture longer bunches, are under study.

7.3 PS Complex

The proton intensity in the PS Complex required for the LHC is lower than the one currently achieved in operation. However, the normalized r.m.s. emittance (3 μm) will be much smaller than for other high-intensity beams, thus the ratio intensity/emittance (brilliance) is larger than usual and would lead to excessive space-charge effects. The proposal is to i) increase the output energy of the 1 GeV PSB to 1.4 GeV to lower the space-charge tune shift in the PS, and ii) fill the PS with two PSB batches, to ease the effect at PSB injection (50 MeV).

PS

The bunch spacing of 25 ns is impressed on the beam just before ejection, at 26 GeV/c, by two new fixed-frequency RF systems: a 40 MHz system to adiabatically capture the beam and generate the bunch distance, and an 80 MHz one to compress the 84 bunches to make them fit into the SPS 200 MHz buckets. Another novel feature is the two-batch filling on a 1.4 GeV magnet cycle front porch. The first PSB batch has to dwell for 1.2 s on the PS injection front porch until the second batch arrives and is particularly prone to space-charge effects, which become acceptable at the increased injection energy. The PS will accelerate on new harmonic numbers ($h = 8$ and $h = 16$ after bunch splitting) which implies an upgrade of the low-level electronics.

PS Booster

The incoherent Laslett tune shift, normally below 0.5 in space-charge limited machines, would be almost 1 at PSB injection (50 MeV) with the LHC beam. This figure is halved by filling the PS in two batches. (At present the PS is filled by sequentially transferring the four PSB rings, 1/4 of PS circumference each, within one batch.) A new RF system, tuned to the revolution frequency (RF harmonic $h = 1$) generates one bunch per PSB ring, enabling four of them to be lodged in half the PS circumference by appropriate synchronization and kicker timing adjustment. New bunch-flattening harmonic $h = 2$ systems have to be built as well, and the low-level electronics for the acceleration system must be adapted to the new RF harmonic number. The energy upgrade to 1.4 GeV is compatible with the PSB main magnet characteristics but calls for modifications of its main power converter. The line in which the four rings are recombined and transferred to the PS will have to be adapted to the new energy as well (magnets, power converters).

Linac 2
This very high intensity proton machine is now equipped with an RFQ (750 keV) as the injector and delivers beams of unprecedented brightness. A better understanding of the heavily space-charge dominated optics in Linac 2 and transfer lines, as well as some upgrading of the source and the RF systems, will enable this accelerator to approach an intensity of 180 mA (pulse length some 20 μs) at PSB entry.

Beam test
A partial beam test with the aim of assessing the ingredients of the proposed LHC proton filling scheme in the PS complex was carried out in 1993 [2]. To keep preparation simple, only PSB Ring 3 was involved in the test. The PSB proved capable of accelerating beam to 1.4 GeV, on $h = 1$, and the PS was successful in operating with a two-batch filling scheme as well as in accelerating using new RF harmonics. Beam emittances for both 'nominal' and 'beam–beam limit' intensity levels at 26 GeV/c were found to be comfortably within LHC specifications.

For the first physics runs, the LHC will require an 'initial' beam with 1.7 10^{10} p/bunch, in a normalized emittance of 1 μm. It will enable the LHC to operate at a luminosity of 10^{33} cm^{-2} s^{-1} with low proton currents. Although the brilliance of this beam is somewhat smaller than the nominal one, it is an open question whether the tiny emittance can be generated and preserved along the injector chain.

References

[1] E. Brouzet and K. Schindl, The LHC Proton Injector Chain, CERN/PS 93–39 (DI), CERN/SL 93–37 (AP), LHC Note 256, Oct. 1993.

[2] R. Cappi, R. Garoby, M. Martini, J.-P. Riunaud and K. Schindl, The PS as LHC Proton Source: Results of a Two-week Beam Test in December 1993, CERN/PS 94–11 (DI), LHC Note 266, June 1994.

8 The LHC as a lead-ion collider

The collision of ions in the LHC was already discussed in the 'Pink Book'. A number of modifications to the scheme and the progress made in the design justify a new description.

The acceleration of ions is a well-developed activity at CERN where the first ions were accelerated in the PS in 1976 and in the SPS in 1987. More recently a Lead-Ion Acceleration Facility (LIAF) has been constructed and was put into operation in autumn 1994; fixed-target experiments with 177 GeV/u Pb ions extracted from the SPS have been carried out.

The plans are now to extend this facility in order to support (after a moderate upgrading) lead-ion collisions with a centre-of-mass energy of 1148 TeV in the LHC. A list of parameters is given in Table 1.

Table 1: The LHC list of parameters: lead-ion collider (125 ns bunch spacing at SPS injection, one low-β experiment)

Lead-ion collider				
Energy per charge[a]	E/Q	[TeV/charge]	7	
Energy per nucleon[b]	E/A	[TeV/u]	2.76	
Centre-of-mass energy	$E_{\rm cm}$	[TeV]	1148	
Dipole field	$B_{\rm max}$	[T]	8.386	
Transverse normalized emittance	ϵ^*	[μm]	1.5	
β at IP (coll.)	β^*	[m]	0.5	
r.m.s beam radius at IP	σ^*	[μm]	15	
Crossing angle (per beam)		[μrad]	≤ 100	
Longitudinal emittance (inj.)	$\epsilon_{\rm l}$	[eV.s/charge]	1	
Longitudinal emittance (coll.)	$\epsilon_{\rm l}$	[eV.s/charge]	2.5	
r.m.s bunch length (coll.)	σ_s	[cm]	7.5	
r.m.s energy spread (coll.)	$\sigma_{E/E}$	10^{-3}	0.114	
Bunch spacing	$l_{\rm b}$	[ns]	124.75	
Bunch harmonic number	$h_{\rm b}$	Not integer	(712.8)	
Number of bunches per ring	$n_{\rm b}$		608	
Filling time per LHC ring		[min]	9.8	
Number of ions per bunch	$N_{\rm b}$	10^7	6.3	9.4
Number of ions per beam	N	10^{10}	3.5	5.2
Ion intensity per beam		[mA]	5.2	7.8
Initial luminosity per bunch	$\mathcal{L}_0^{\rm b}$	[10^{24} cm^{-2} s^{-1}]	1.4	3.2
Initial total luminosity	$\mathcal{L}_0$	[10^{27} cm^{-2} s^{-1}]	0.85	1.95
IBS emittance growth (inj.)		[h]	7.6	5.1
IBS emittance growth (coll.)		[h]	14.6	9.8
Luminosity lifetime		[h]	10	6.7

[a] $^{208}Pb^{82+}$ Mass number A = 208, Atomic number Z = 82, fully stripped i.e. charge state Q = 82.

[b] 1 atomic mass unit (amu) = 931.502 MeV/c^2 the rest mass of the fully stripped lead ion as expressed in amu is M_i = 207.93 $\approx$ A. By analogy with other publications the energy will be quoted as E/A instead of E/M_i.

Ions lighter than lead could also be accelerated in the CERN complex but, since at this stage no formal physics proposal has been discussed in the CERN committees, this section concentrates on lead ions.

8.1 Lead ions in the LHC

The performance of the LHC as a lead-ion collider with one interaction point is described below; it should be noted that the luminosities quoted will be lower if several IPs are illuminated concurrently:

- The energy of 1148 TeV in the centre of mass corresponding to the nominal LHC field of 8.386 T gives an energy of 574 TeV/ion for lead (2.76 TeV/u and 7.0 TeV per charge);
- The transverse normalized emittances (r.m.s. definitions) of the ion bunches, have been fixed at $\epsilon^* = 1.5$ μm, corresponding to the same size as the proton beam at the same field values in the SPS and the LHC. This represents a safe operational value;
- The luminosity lifetime is governed by the combination of two different processes [1]:
  - The intrabeam scattering (IBS) which blows up the bunches and thus reduces the luminosity; it strongly depends on the type of ion used and on the beam densities. A controlled longitudinal blow-up during acceleration (from 1.0 eV.s/charge to 2.5 eV.s/charge) will reduce its effect during the physics runs.
  - The nuclear effects at the collision points (electromagnetic dissociation and electron capture after a pair production), which reduce the luminosity through particle losses; these effects are machine independent and dominate for lead ions at the beginning of the collision run. However, computations of the luminosity lifetime have to include both the nuclear effects and the IBS effect [2].
- The initial number of particles per bunch and the initial luminosity per bunch are completely determined once the luminosity lifetime has been fixed. A luminosity lifetime of 10 h (chosen by analogy with the proton scheme), yields an initial total luminosity of $\mathcal{L}_0 = 8.5\ 10^{26}$ cm^{-2} s^{-1} with 608 bunches. In order to increase the initial luminosity to $\mathcal{L}_0 = 1.95\ 10^{27}$ cm^{-2} s^{-1}, one has to accept a luminosity lifetime lowered to 6.7 h (Fig. 1). The corresponding performance is detailed in Table 1.

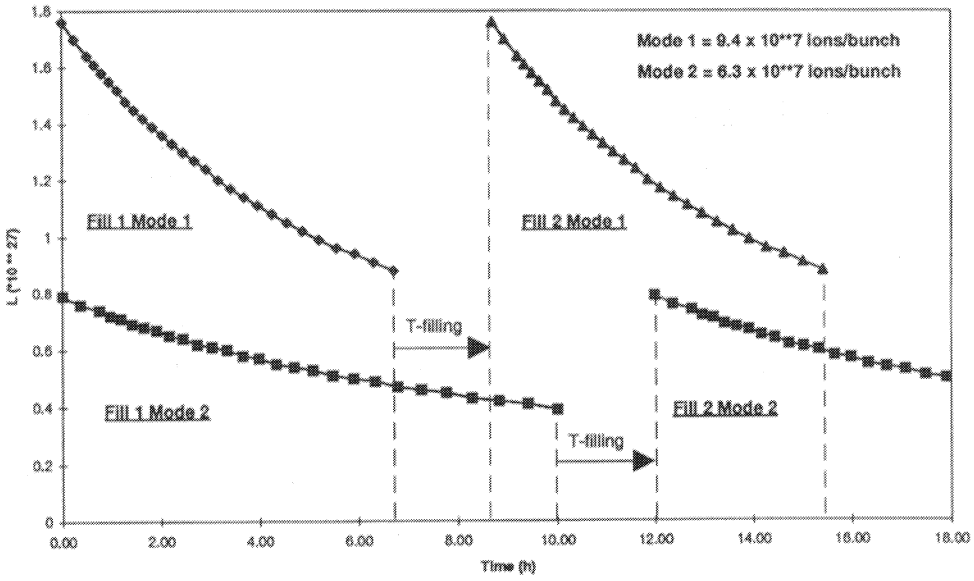

Figure 1: Luminosity plotted against time for the two cases of half-life 6.7 h and 10 h where T-filling represents the time between two physics runs

8.2 Ions in the injector complex

As shown above, the LHC has very precise requirements for the performance of the injector chain which has to provide the maximum number of bunches compatible with the filling scheme. In addition, the filling scheme of LHC must be compatible with a reasonable filling time. The injected bunches must have both the correct emittances and the correct number of lead ions. The present facility (LIAF) has to be upgraded in order to reach the required level of performance.

The Lead-Ion Acceleration Facility (LIAF)

The present facility [3] consists of a number of items with successive functions:

- An electron cyclotron resonance (ECR) source produces 80 μA of $^{208}Pb^{28+}$ at a kinetic energy of 2.7 keV/u;
- A 100 MHz RFQ accelerates the extracted ions to 250 keV/u;
- A new, specially built, interdigital-H (IH) linac with three tanks working at 100 and 200 MHz provides the ions with an output kinetic energy of 4.2 MeV/u;
- A stripper target followed by a magnetic filter delivers 22 μA of Pb^{53+} with a pulse length of 400 μs and a pulse rate of 1.2 s;

- The PS Booster (PSB) accelerates these stripped ions in its four rings to a kinetic energy of 94 MeV/u;
- The PS accelerates them further to 4.25 GeV/u;
- A stripper foil in the transfer line produces the final charge-state of Pb^{82+}, fully stripped ions;
- The ion beam is transferred to the SPS where it is debunched and recaptured at 200 MHz;
- The injection procedure is repeated three times before the SPS accelerates the bunches to the final energy of 177 GeV/u.

The LIAF was successfully put into operation in autumn 1994 and fixed-target experiments started data taking. Linac 3 has reached and even exceeded its design current of 22 μA of Pb^{+53} at 4.2 MeV/u. The peak intensity accelerated in the SPS was 3.0 10^8 Pb^{82+} ions per SPS cycle of 14.4 s, not far from the nominal 4.0 10^8 ions estimated from expected efficiencies in the injector chain.

The LHC injection scheme

A detailed analysis of the bunch cog-wheeling in the injector chain led to the conclusion that the optimum bunch spacing compatible with all machines would be 134.7 ns at the LHC collision energy, corresponding to 135 ns at the PS to SPS transfer. The bunch harmonic number (i.e. the number of bunch places for the LHC ring) would then be $h = 660$. Nevertheless the beam users have asked for a bunch spacing of the ions that is a multiple of the proton bunch spacing. This would permit proton experiments to use their basic electronic module timing (24.95 ns) to trigger on ion collisions and vice versa, ALICE would be able to trigger on proton collisions [4, 5]. The most convenient bunch spacing is 124.75 ns (5 times the proton bunch spacing), but the bunch harmonic number will no longer be an integer number (712.8). To ensure the crossings at IP1, IP2 and IP5, with a symmetry of eight, the bunches in each LHC ring have to be distributed in four bunch trains regularly spaced along the machine circumference.

The LIAF chain working with direct bunch-to-bucket transfer can only provide a bunch population of 3.4 10^6 ions per bunch, a factor of 20 to 30 lower than the number of ions specified above for optimum LHC luminosity, leading to a luminosity reduced by a factor of 400 to 900.

Several schemes were considered to fulfil the stringent LHC requirements. The basic idea of the one selected [6] is to use LEAR as an accumulation ring to accumulate 20 Linac 3 batches during one PS cycle, making extensive use of the powerful LEAR electron-cooling system. The injector chain is then modified (Fig. 2) as follows [7, 8]:

- The lead linac delivers a 60 μs, 22 μA pulse of Pb^{54+} at 4.2 MeV/u within a normalized emittance of 0.25 μm and a momentum spread of $\Delta p/p = 10^{-3}$. The pulse rate is 10 Hz. To diminish the rate of recombination in LEAR with the electrons of the electron cooling device, a charge state Pb^{54+} is chosen after the stripper target [9];

- The pulse is injected into LEAR via existing channels using multiturn injection (efficiency 50%). This accumulated beam is then cooled in LEAR in 0.1 s using electron cooling until a new linac pulse can be accepted. After the accumulation of 20 such batches the beam is captured on harmonic number $h = 4$. The beam contains 1.2 10^9 ions captured in four buckets with normalized transverse emittances $\epsilon_x = 1.0$ μm and $\epsilon_y = 0.5$ μm. The four bunches are then accelerated to 14.8 MeV/u and transferred directly into the PS without passing through the PSB;

- The PS, tuned to harmonic number $h = 32$, receives the LEAR bunches by direct bunch-to-bucket transfer and accelerates the bunches to a front porch at 258 MeV/u. This rapid acceleration is required in order to limit the losses due to the residual gas to the already large figure of 30–40%;

- The correct bunch spacing is achieved by a stepwise change of the harmonic number on the PS front porch, successively $h = 28$, 24, 20 and finally 17. The four consecutive bunches occupy approximately a quarter of the PS circumference. After a controlled blow-up of their longitudinal emittance to avoid excessive intrabeam scattering, the four bunches are accelerated in the PS to a momentum of 6.15 GeV/c/u. The final bunch spacing is then 125 ns;

- A bunch compression reduces the length to 4 ns, compatible with the SPS 200 MHz RF bucket, and the bunches are transferred to the SPS;

- The SPS receives four bunches in one batch, and 13 such batches are successively transferred into the SPS from the PS and stored in succession. The rise time of the SPS injection kicker will be reduced to 115 ns in order to adapt it to the gap between two consecutive bunches. These bunches are then accelerated using a fixed-frequency RF system;

- Twelve SPS batches are transferred to each LHC ring to form four bunch trains. Every bunch train is composed of three SPS batches separated by seven empty bunch places for the LHC injection kicker rise time; each bunch train is separated by eight empty bunch places plus an interval of 24.95 ns; the last SPS batch contains only nine PS batches in order to leave 24 empty bunch places for the rise time needed by the LHC beam dump extraction kicker.

  If b denotes an occupied bunch place and e an empty one, the structure of the 608 bunches for one LHC ring will be represented by:

  $$3 \times [3 \times (13 \times 4b + 7e) + e + 0.2e] + [2 \times (13 \times 4b + 7e) + (9 \times 4b + 24e + 0.2e)] = 712.8$$

  where $0.2e$ represents a gap of 24.95 ns.

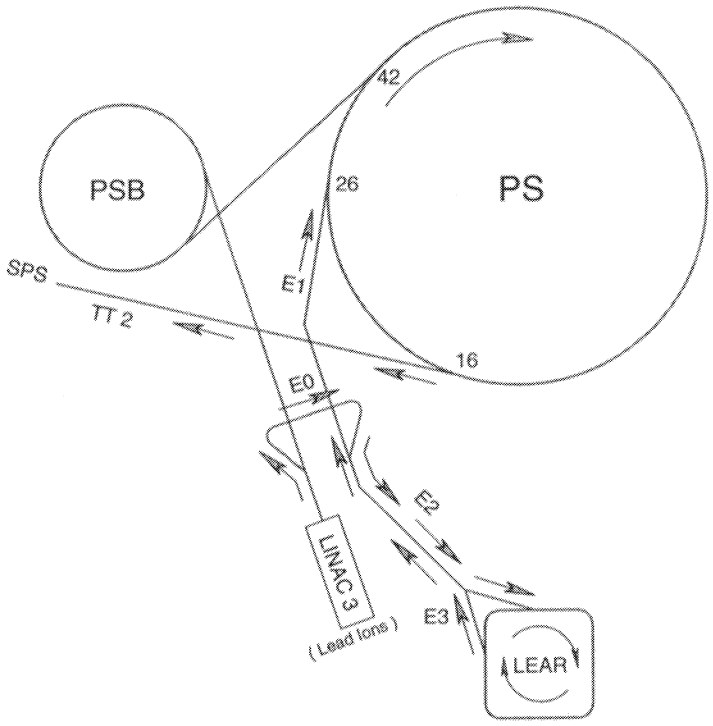

Figure 2: Lead ions: injector layout

The injector cycle uses 152 PS cycles, 12 SPS cycles for a total filling time of 9.8 min per LHC ring.

Hardware in the injectors

- The ECR source and Linac 3 must be upgraded to 10 Hz.
- The requirement to reduce the beam emittances by electron cooling in LEAR in less than 100 ms imposes a major upgrade. At present the cooling time of antiprotons is several seconds, and it scales roughly like Q^2/A [9]. An R&D programme including a high-perveance gun and some adaptation of the LEAR lattice is required. Part of it is already under way. Machine experiments with lead ions in LEAR have started with their first runs in December 1994 and July 1995 [10]. Critical issues which can be studied experimentally include cooling speeds, stacking schemes, losses due to charge exchanges with the residual gases, and recombination of lead ions with cooling electrons.

- The transfer scheme between machines is indicated in Fig. 2. The same line will be used to transfer ions from Linac 3 into LEAR and from LEAR to the PS. This implies polarity reversal of the line every cycle of 3.6 s. Some magnets will have to be changed to laminated ones. The injection/extraction equipment will have to be upgraded and rearranged.

- Power converters must be adapted to obtain the necessary fast acceleration in LEAR and polarity reversal in the transfer line.

- Several improvements to beam diagnostics, dampers, and controls are required.

- A dedicated PS beam control system must be developed for the intricate longitudinal beam manipulations.

- No major improvements are required in the PS and SPS which have already been adapted to the LIAF specifications, except the SPS injection kicker. The injection kicker rise time needs to be reduced from 220 ns to 115 ns.

8.3 The case of light ions

The use of the LHC for collisions of lighter ions, only recently being investigated, presents significantly different characteristics from all points of view: the interplay between nuclear effects and IBS is drastically different [2] so that a higher number of particles per bunch in the LHC would be possible. For this new mode of operation a different and more elaborate scheme is proposed for the injectors [5]. The energy of the ions stored in LEAR will be increased in order to allow for full stripping at the LEAR exit and a subsequent stacking in the PS. The PS will then be capable of transferring batches of 16 bunches into the SPS. Such a scheme could permit access to the higher luminosities possible in the the LHC. Measurements to determine the source performance with Kr and Ar in a charge state compatible with the transfer line to LEAR are foreseen in 1996. After such measurements it will be possible to provide more quantitative figures.

References

[1] D. Brandt, E. Brouzet and J. Gareyte, Heavy Ions in the SPS–LHC Complex, CERN–SL/AP/Note 92–47, LHC Note 208.

[2] D. Brandt, K. Eggert and A. Morsch, Luminosity Considerations for Different Ion Species, CERN–AT/DI/Note 94–05 ,CERN–SL/AP/Note 94–04, LHC Note 264.

[3] D. Warner (ed.) et al., CERN Heavy-ion Facility Design Report, CERN 93–01 (1993).

[4] LHC Experiment Machine Interface Committee, CERN–LL 94–3, LEMIC2.

[5] P. Lefèvre, Modifications to the Ion Scheme for the LHC, CERN–PS/DI/Note 95–09, LHC Note 324.

[6] P. Lefèvre and D. Möhl, Lead Ion Accumulation Scheme for LHC, CERN–PS/Note 93–45, LHC Note 257.

[7] P. Lefèvre and D. Möhl, A Low Energy Accumulation Ring of Ions for LHC, CERN–PS/DI/Note 93–62, LHC Note 259.

[8] E. Brouzet and K.H. Schindl (ed.), Heavy Ions in the LHC, CERN–SL/AP/Note 93–60, PS/DI/Note 93–18 (Tech.), LHC Note 225.

[9] J. Bober, I. Meshkov and G. Tranquille, Magnetized Electron Beam Cooling Time for Heavy Ions, CERN–PS/AR/Note 94–11.

[10] S. Baird et al., First Electron Cooling Tests with Pb^{53+} Ions, CERN–PS/AR/Note 95–06 (MD).
S. Baird et al., Beam Lifetime Tests for Pb^{52+}, Pb^{53+}, Pb^{54+} Ions Subject to Electron Cooling in LEAR (Performed in June 1995), CERN–PS/AR/Note 95–12.
Also to be published in Physics Letters B.

Part III
Superconducting technology

1 Magnets

1.1 Superconducting technology for accelerator magnets

There are two large operational accelerators based on superconducting magnets: the Tevatron (Fermilab) and HERA (Desy). Both make use of classical NbTi superconductors cooled with normal liquid helium at a temperature slightly above 4.2 K, and their operational fields are relatively low ($\sim$ 4 T for the Tevatron and 4.7 T for HERA). The HERA magnets were industrially manufactured. For the LHC to be installed in the existing LEP tunnel, it is attractive to push the field significantly higher, still retaining the well-proven fabrication methods of cables and coils made of NbTi superconductors. The only way of obtaining fields of 8 T or above with sufficient margin is to cool the magnets at a much lower temperature ($\geq$ 2 K). This technique has been applied successfully to the French Tokamak TORESUPRA in operation at Cadarache. Below 2.17 K, helium takes the so-called superfluid state, with much lower viscosity and much greater heat transmission capacity than normal helium. These properties can be used for the design of the cooling scheme, and in particular permit a drastic reduction of the helium flow through magnets.

On the other hand, the enthalpy of all metallic parts and in particular of the superconducting cables is reduced by almost an order of magnitude between 4.2 K and 1.8 K, with a consequent faster temperature rise for a given deposit of energy. This feature calls for particular care in limiting conductor motion. It should be noted that the electromagnetic forces on the conductor increase with B^2 and so does the stored electromagnetic energy, calling for stronger force-retaining structures and more elaborate quench protection systems than in previous projects.

Proton–proton colliders require two separate beam channels with fields equal in strength but opposite in directions. For the LHC, the compact 'two-in-one' design is adopted, whereby the two beam channels and their corresponding sets of coils are inserted in a unique structure and in a single cryostat [1, 2].

The novel features of the LHC magnets — namely high forces and stored energy, lower temperatures and 'two-in-one' structure — justified the undertaking of a substantial R&D programme in close co-operation with industry for both the magnets themselves and the cryogenic system. This programme, which included construction, test and measurement of several 1.3 m long models and 10 m long prototypes as well as the installation and operation of a string of magnets simulating the basic machine half-cell, has confirmed the soundness of the technical choices and the feasibility of the project [3]–[6].

The R&D has already answered the fundamental questions on the basic technical solutions for the LHC magnets:

- The superfluid helium, 1.9 K cooling of magnets in long horizontal cryostats has been proved feasible and reliable.

- It has been demonstrated for both short and long magnets that twin-aperture ('two-in-one') magnets behave as well as single-aperture magnets with respect to quench and training performance.

- It has been verified by measurements on model and prototype magnets that the required field quality can be achieved.
- It has been proved that an adequate margin with respect to the 8.4 T design field can be obtained.
- The industrialization of magnet manufacture is well advanced, since most of the short models and all of the 10 m long prototype magnets have been made by industry.

1.2 Dipole magnets for the arcs (Main dipoles)

1.2.1 Main features and parameters

The main parameters of the dipoles are listed in Table 1; Fig. 1 shows their transverse cross-section, and Fig. 2 their longitudinal cross-section. The design [7] is based on:

- design field: 8.40 T;
- twin-apertures in a common force-retaining structure/flux return yoke and cryostat;
- coil inner diameter: 56 mm;
- distance between the axes of the apertures: 194 mm;
- NbTi superconductor operating in superfluid helium at 1.9 K;
- two-shell coils with graded current density supported by collars and iron yoke surrounded and compressed by a shrinking cylinder.

The coils are formed of two winding layers made with keystoned cables of the same width but of different thicknesses, resulting from the desired grading of current density for optimum use of the superconducting material. The copper to superconductor ratios in the strands, different in the two layers, result from stability and protection considerations. Wedge-shaped copper spacers are inserted between blocks of conductors to produce the desired field quality and to approximate a quasi-circular coil geometry, compensating for the insufficient keystoning of the cables. These spacers are continued at the coil ends by saddle-shaped pieces which allow the winding and the mechanical confinement of the cables. The cables are insulated by two half overlapped wraps of polyimide tape and a third wrap of polyimide tape coated with a polyimide or epoxy adhesive and spaced by 2 mm. After winding, the adhesive is cured by heating each coil layer in a curing mould, which at the same time gives the final shape and size to the coil. A perforated glass-epoxy spacer is placed between the inner and the outer coil shells to provide channels for circulation of the cooling helium. The insulation to ground is composed of superposed polyimide film layers and includes the quench protection heaters.

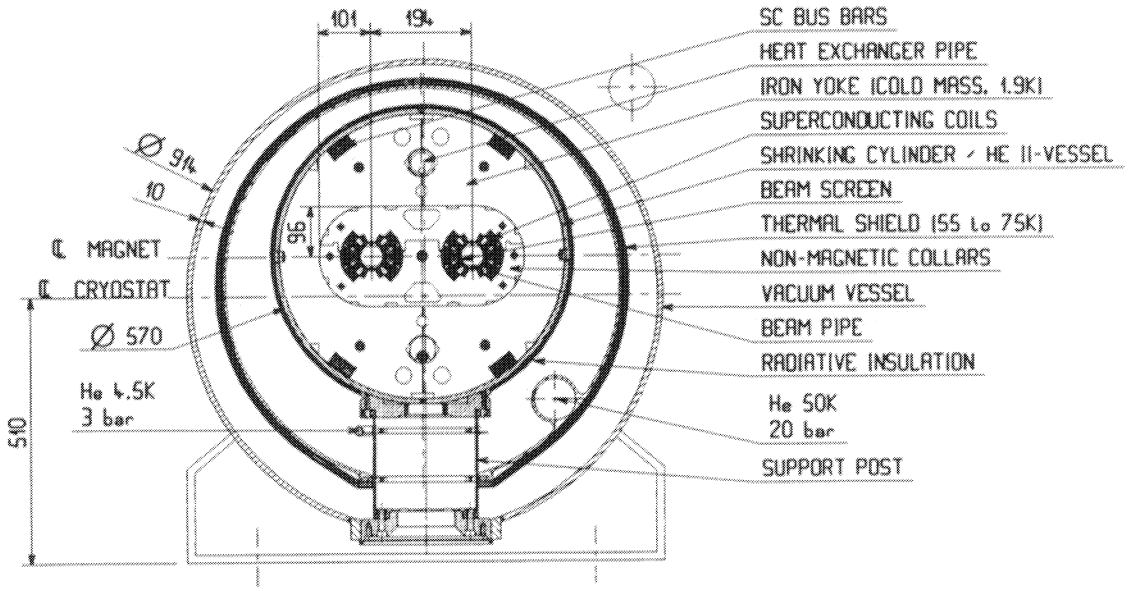

Figure 1: Dipole magnet cross-section

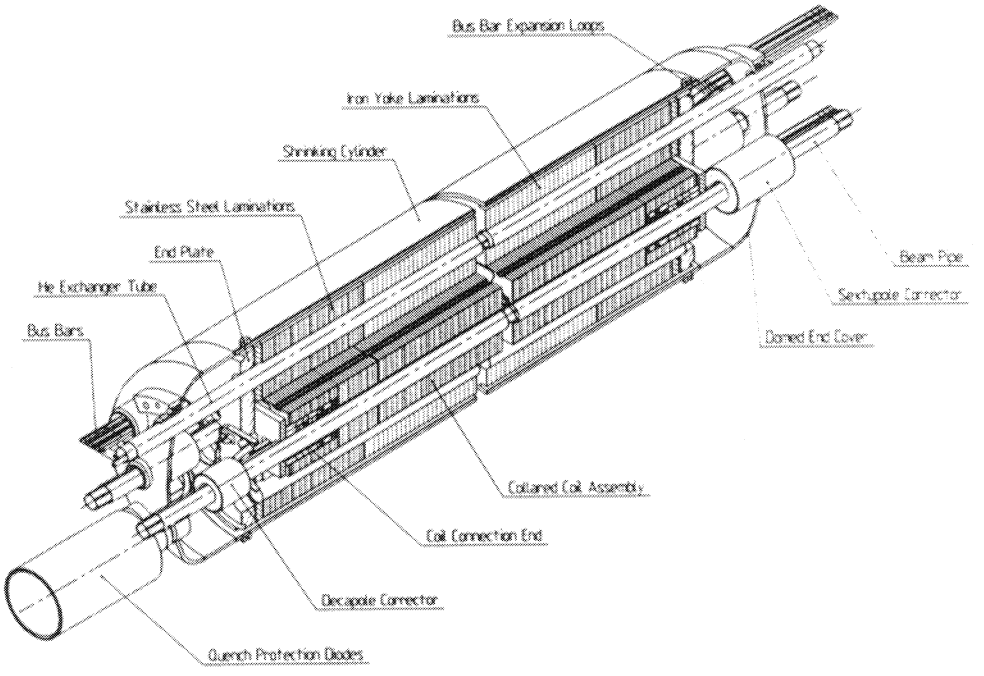

Figure 2: Dipole cold mass assembly

Table 1: Dipole Parameters

Operational field	[T]	8.40
Coil aperture	[mm]	56
Magnetic length	[m]	14.20
Operating current	[A]	11500
Operating temperature	[K]	1.9
Coils (two-shells construction)		
Coil inner diameter	[mm]	56
Coil outer diameter (incl. insulation to ground)	[mm]	120.5
Coil length (incl. end pieces)	[mm]	14467
Inner shell		
turns per beam channel		30
cable width	[mm]	15
thickness	[mm]	1.72/2.06
No. of strands		28
strand diameter	[mm]	1.065
filament diameter	[μm]	7
copper to superconductor ratio		1.6
Outer shell		
turns per beam channel		52
cable width	[mm]	15
thickness	[mm]	1.34/1.60
No. of strands		36
strand diameter	[mm]	0.825
filament diameter	[μm]	6
copper to superconductor ratio		1.9
Conductor insulation		
thickness of 1st tape (50% overlapped)	[mm]	2×0.025
thickness of 2nd tape (50% overlapped)	[mm]	2×0.025
thickness of the polyimide spacer layer	[mm]	0.070
compressed ins. azimuth. thickness: inner shell	[mm]	0.12
outer shell	[mm]	0.13
Thickness of perforated glass-epoxy	[mm]	0.5
Thickness of insulation to ground	[mm]	0.75
Structure		
Distance between aperture axes	[mm]	194
Collar height	[mm]	192
Collar width	[mm]	396
Yoke outer diameter	[mm]	550
Shrinking cylinder outer diameter	[mm]	570
Length of active part (incl. end plates)	[mm]	14603
Overall length of cold mass	[mm]	$\sim$ 15000
Mass of cold mass	[t]	23.8
Outer diameter of cryostat	[mm]	914
Overall mass of cryomagnet	[t]	$\sim$27.5
Other characteristics		
Stored energy for both channels (500 kJ/m)	[MJ]	7.1
Self-inductance for both channels (7.6 mH/m)	[mH]	108
Resultant of e.m. forces in the first coil quadrant: ΣFx	[MN/m]	1.7
ΣFy (inner layer)	[MN/m]	$-$ 0.14
ΣFy (outer layer)	[MN/m]	$-$ 0.60
Axial e.m. force on magnet ends (for both channels)	[MN]	0.50

The force containment structure consists of coil clamping elements, the collars, the iron yoke and the shrinking cylinder, which all contribute to producing the necessary azimuthal pre-compression in the coils and to prevent tensile stresses from arising in the coils under the action of the electromagnetic forces. The shrinking cylinder is at the same time the outer shell of the helium tank, whilst the inner wall forms the beam vacuum chamber. The assembly between these two cylindrical walls (the cold mass) is kept at 1.9 K. In order to reduce the heat load on the low-temperature cryogenic system, the heat generated by the proton beams from their synchrotron radiation and the effect of beam induced currents in the resistive wall is intercepted by a shield. This is inserted within the vacuum chamber and is cooled by helium circulating at 5–20 K.

The cold mass is closed at the ends by covers, welded to the shrinking cylinder, which leave passages for the beam vacuum chambers, a heat exchanger tube, and two pipes containing the main and the auxiliary electrical connections. The cover on the magnet electrical connections side also leaves a passage for a pipe leading to a pressure relief valve located in the junction space between the magnet units. All these pipes are welded to the end covers. Small sextupole and decapole magnets for the correction of systematic errors in the dipoles are placed around the beam pipes inside the end caps at the connection and at the return ends, respectively.

Main and auxiliary bus-bars to feed the magnets of the arcs and the dispersion suppressors are located in grooves in the iron yokes (Fig. 1).

The cold mass is installed inside a cryostat, see Section 1.2.6, whose main components are a radiation shield at 5 K, a thermal screen at 70 K, and the outer cylindrical wall of the vacuum vessel. The cold mass is supported by three feet made of composite material and having their cold end bolted to it. The central foot is fixed to the vacuum vessel whilst the other two can move on rollers to follow the thermal contraction/expansion of the cold mass. All parts between the beam vacuum chamber walls and shrinking cylinder are immersed in superfluid helium at atmospheric pressure and cooled by means of a corrugated heat-exchanger tube, in which two-phase low-pressure helium is circulated and acts as a heat sink. The cold mass will be bent to a 2700 m radius of curvature, with a horizontal sagitta of 9.7 mm in the centre, to match the beam paths. This will be done in one of the last phases of the magnet assembly, before welding together the two halves of the shrinking cylinder, which will be suitably pre-bent.

1.2.2 The cables

The transverse cross-section of the coils for the LHC 56 mm aperture dipole magnet shows two layers of different cables distributed in five blocks (Fig. 3). The cable used in the inner layer has 28 strands, each of 1.065 mm diameter, and the cable of the outer layer 36 strands, each of 0.825 mm diameter. The basic parameters of the two cables are given in Table 2.

The proposed filament size (7 μm for the inner strand and 6 μm for the outer layer) allows the fabrication of superconducting wires by a single stacking process. The persistent current sextupole component (expressed in relative error at 10 mm) is $-3.6\ 10^{-4}$ and the decapole component is $0.18\ 10^{-4}$ for these filament diameters. These error components,

discussed in Section 1.2.3, are corrected by small sextupole and decapole magnets located at each dipole end.

Table 2: Strand and cable characteristics

	Inner Layer	Outer Layer
Strand		
Diameter [mm]	1.065	0.825
Copper to superconductor ratio	1.6	1.9
Filament size [μm]	7	6
Number of filaments	8900	6500
RRR	≥ 70	≥ 70
Twist pitch (after cabling) [mm]	25	25
Critical current [A] 10 T, 1.9 K	≥ 515	
9 T, 1.9 K		≥ 380
Cable		
Number of strands	28	36
Cable dimension		
thin edge [mm]	1.72	1.34
thick edge [mm]	2.06	1.60
width [mm]	15.0	15.0
Transposition pitch [mm]	110	100
Keystone angle (degree)	1.30	1.0
Cabling angle (degree)	15.95	15.95
Aspect ratio	7.93	10.20
MIITS [300 K] [10^6 A^2 s]	45 [8 T]	30 [6 T]
Critical current I_c [A] 10 T, 1.9 K	≥ 13750	
9 T, 1.9 K		≥ 12950
dI_c/dB	> 4800	> 3650

Critical current densities in the superconductor

Considerable experience was gained during the manufacture of cables for the 10 m long dipole prototype for the R&D phase of the LHC programme. Twenty-four kilometres (6.75 t) of cable made of 26 strands of 1.29 mm diameter and 42 km (7.35 t) of cable using 40 strands of 0.84 mm diameter have been qualified. The process of fabrication of the wires and cables with NbTi filaments of 5 μm has been optimized for high fields. The current densities in the non-copper part of the strand cross-section used in the present definition of the cables correspond to the critical current densities measured on strands extracted from the finished cables at the 3 σ limit in the distribution curve of production. They are 980 A/mm^2 at 8 T, 4.2 K, for the inner layer and 2000 A/mm^2 at 6 T, 4.2 K, for the outer layer. Any further gain in the current densities during mass production will improve the temperature margin of the magnet.

The results of R&D magnets show that the short-sample quenching field of the dipole (B_{ss}) is within $\sim 2\%$ of the cable short-sample limit determined from strands extracted from the cables.

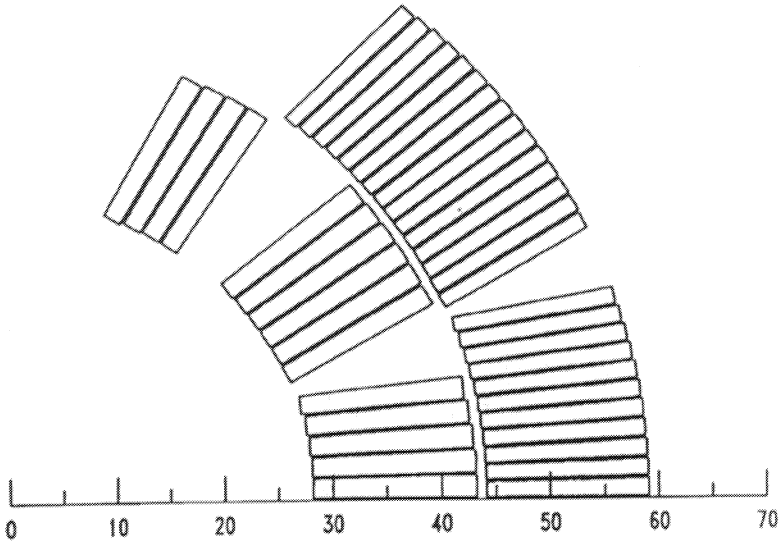

Figure 3: Conductor distribution in the dipole coil cross-section

Expected quench characteristics and temperature margin

Table 3 shows the peak field (B_p), the field margin and the temperature margin when the magnet operates at 8.40 T for the two layers of cable described in Section 1.3.2. The field margin is defined as the ratio of the operating field to the expected quenching field at the short-sample limit (B_{ss}). The reference temperature of the bath is 1.9 K (He between coil inner radius and cold bore). The current density in the copper at $B_0 = 8.40$ T in case of a quench is also given, as well as the expected hot-spot temperature in the outer layer and the maximum voltage across the outer layer calculated with the Quench Simulator QUABER [8]. The maximum voltage of 500 V corresponds to 20 V between turns (the interturn insulation is tested at room temperature with a voltage of 75 V). These two values have been calculated with a 80 ms delay for the quench detection and the active initiation of the quench over the volume of the outer layer triggered by the quench heaters. This time delay of 80 ms already produces 10.6 'MIITS' (MA^2s), corresponding to a hot-spot temperature of 60 K for a quench in the inner layer, or 80 K if the quench starts in the outer layer. For the particular case of a quench in the outer layer at $B_0 = 8.4$ T (with RRR-Cu = 70) the hot-spot temperature can be related to the current density in the copper by the approximate formula

$$\int_{\Delta t_{delay}}^{\infty} J_{cu}^2 dt + J_{cu,0}^2 \Delta t_{delay} \cong 1.30\ 10^5 \left(\frac{T}{375}\right)^{0.4} \left(1 + \frac{1}{\alpha}\right) ,$$

where α is the copper to superconductor ratio, T is the temperature of the hot spot, Δt_{delay} is the time delay for quench detection and heater initiated quench in the outer layer, and J_{cu} is the current density in the copper expressed in A/mm^2.

Table 3: Expected quench performance and temperature margin (B_0 = 8.40 T, I_0 = 11500 A, T_{bath} = 1.9 K)

Layer	B_p [T]	B_{margin} [%]	ΔT [K] margin	J_{cu} [A/mm^2]	T_{max} quench [K]	V_{max} [V]
Inner layer	8.81	87.3	1.40	749		
Outer layer	7.37	83.5	1.70	912	375	500

a.c. losses

During ramping and discharge of the current in the dipole magnet, losses occur due to hysteresis in the filaments, interfilament coupling through the Cu matrix, and interstrand coupling. The losses due to interstrand coupling depend strongly on the final resistivity of the copper, the coating of the strands, and the compression of the coils at low temperature. The power losses are mainly proportional to $(dB/dt)^2$ and inversely proportional to the interstrand contact resistance R_c.

Losses for a twin-aperture dipole have been estimated at 325 mW/m for a charging time of 1200 s, corresponding to an energy of 400 J/m transmitted to the helium bath and to specific power dissipation in the cables of 0.14 mW/cm^3.

In the case of discharge of the machine, the upper limit of the time constant is given by the characteristics of the diode heat sink of the quench protection system and the quench propagation to other magnets via bus-bars. In the tested 10 m long magnets, a linear discharge from 8.4 T with dB/dt of 0.12 T/s does not initiate a quench. An exponential discharge with a time constant of 100 s leads to a load of 2800 J/m. These estimated values correspond to an interstrand contact resistance of 1 $\mu\Omega$, the lowest expected limit from the point of view of losses.

Temperature margin

A superconductor stays in the superconducting state when the temperature, the magnetic field, and the current density are below their critical value. The temperature margin calculated in Table 3 is the difference between the bath temperature and the critical temperature at the design field and current.

During the ramping tests on model magnets, we have seen that the temperature of the superconductor can stay at 4 K in steady-state conditions above the λ point, without perturbations of the helium II bath. Experiments made by CEA-Saclay show that, with the existing insulation, the temperature difference between the conductor and the superfluid helium bath is 1 K for a power of 4 mW/cm^3 [9]. Encouraging results have been obtained in the laboratory with porous insulations, which show a very small ΔT because the heat is carried away by the superfluid helium.

Table 4 illustrates the distribution of the ΔT margin of 1.4 K for the inner layer. The main part of the temperature margin will be used for beam losses (5 mW/cm^3 corresponds to a loss of 8 10^6 protons/s in the inner layer of the dipole).

Table 4: Use of temperature margin

Phenomenon	Limits	ΔT
J_c measurement precision	$\pm 2.5\%$	± 0.05 K
Dissipation at $\rho = 10^{-14}$ Ωm*	< 0.5 mW/cm^3	0.27 K
Beam losses (7 10^6 p/s)	4.5 mW/cm^3	1.12 K
Ramping losses	0.14 mW/cm^3	0.035 K
TOTAL		~ 1.4 K

* The short sample critical current density is defined as the value at which the sample resistivity is $\rho = 10^{-14}$ Ωm.

1.2.3 The electromagnetic design

The coil is shaped to make the best use of a superconducting cable, whose current is limited by the peak field in the coil, and to produce a dipole field of the best possible homogeneity over the whole range of its operational excitation. The contribution of the iron yoke enhances the strength of the magnet and contains the magnetic flux in such a way that the field quality is maintained.

For defining the field quality we use the usual notation of harmonic multipole analysis, namely:

$$B_y + iB_x = B_1 \Sigma_n (b_n + ia_n)(Z/R_r)^{n-1} \ ,$$

where

B_1 = magnitude of dipole field in the y (vertical) direction;
b_n = normal multipole coefficient;
a_n = skew multipole coefficient;
Z = x + iy;
R_r = reference radius.

The index n = 1 describes the dipole field, n = 2 the quadrupole one, n = 3 the sextupole, and so on.

The conductor distribution in one coil quadrant is shown in Fig. 3. The increase of conductor peak field with respect to the field in the aperture centre B_0 is 4.5%, and the equivalent of 0.8% of the Ampère-turns are lost by saturation in the iron yoke for $B_0 = 8.40$ T.

Expected multipole fields at injection and at top field operation

The multipolar components, describing the perturbations with respect to the ideal dipole field, can be classified as those inherent in the design geometry, those generated by persistent currents in the superconductor filaments, and those due to fabrication tolerances

of the different components and of the tooling used to assemble them. While the first are multipoles which respect at least the symmetry given by the horizontal mid-plane, the second and third may present components which do not respect any symmetry and are responsible for any skew components appearing in the apertures. These may, moreover, be systematic, although in a series fabrication every effort will be made to keep them as small as possible. For this purpose thorough analysis of the measured magnetic field errors and their relation to the fabrication methods and tooling will be carried out in the production phase of the magnet pre-series. In addition, a certain spread must be expected for all systematic multipoles.

The lower-order multipoles tend to change with varying excitation. At low excitation these variations concern the multipoles created by persistent currents in the filaments — mainly sextupole, b_3, and decapole, b_5, components. When raising the current these perturbations die away. In the upper half of the excitation, multipoles caused by iron yoke saturation will appear. These again consist of sextupole and decapole components, but also of quadrupole, octupole, and higher-order components induced by the two-in-one geometry.

The yoke magnetic design was aimed at keeping these multipoles, and especially their variation over the whole range of excitation, to a minimum, while at the same time reaching the highest possible dipole field to maintain an adequate load line margin. Figure 4 shows the flux plot as computed for the coil collar yoke assembly and Table 5 gives the multipoles, expressed in relative field errors in 10^{-4} at 10 mm, at magnet excitation corresponding to beam injection and that of nominal operation. Table 5 also shows the spreads expected for each component expressed in one σ. These latter values were obtained by scaling the random errors of the measured multipoles of the HERA, RHIC and prototype LHC magnets to the dimensions of the LHC dipoles.

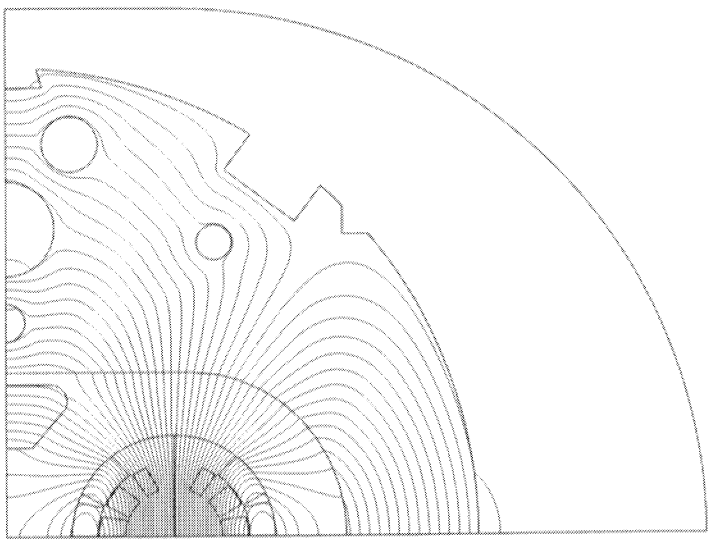

Figure 4: Dipole magnet flux plot

Table 5: Expected multipole performance, at injection and at 8.40 T (in units of 10^{-4} relative field error at 10 mm)

	At injection, 0.58 T				At nominal operation, 8.40T			
	Mean		Random		Mean		Random	
n	norm. b_n	skew a_n	norm. $\sigma[b_n]$	skew $\sigma[a_n]$	norm. b_n	skew a_n	norm. $\sigma[b_n]$	skew $[a_n]$
2	± 0.5	± 0.3	0.4	1.0	1.0 ± 0.5	± 0.3	0.4	1.0
3	-3.6 ± 0.3*	± 0.3	0.5	0.15	0.5 ± 0.3*	± 0.3	0.6	0.15
4	± 0.2	± 0.2	0.1	0.1	± 0.2	± 0.2	0.1	0.1
5	0.18 ± 0.05*	± 0.05	0.08	0.04	0.06 ± 0.05*	± 0.05	0.05	0.04
6	–0.004	0.0	0.02	0.01	–0.005	0.0	0.006	0.01
7	–0.026	0.0	0.01	0.01	0.006	0.0	0.009	0.003
8	0.0	0.0	0.005	0.005	0.0	0.0	0.001	0.002
9	0.006	0.0	0.003	0.004	–0.001	0.0	0.001	0.001
10	0.0	0.0	0.002	0.002	0.0	0.0	0.0	0.0
11	0.008	0.0	0.001	0.001	0.008	0.0	0.0	0.0

* Mean b_3 and b_5 will be compensated by correctors at each dipole end. The b_3 values in this table indicate the magnitude of the persistent current effect at injection and of the yoke saturation at operational conditions, the coil geometry being designed for $b_3 = 0$.

Table 6: Estimation of the additional magnetic errors during the ramp of the field for an interstrand contact resistance of 10 $\mu\Omega$ and a ramp rate of 8 T/20 min. Errors are proportional to 1/Rc × dB/dt

	Field at x = 1 cm [mT]		Relative field error at injection	
n	normal	skew	b_n	a_n
1	4.8		9.0	0
2	0.03	0.54	0.056	1.0
3	0.24	0.060	0.45	0.11
4	0.018	0.060	0.034	0.11
5	0.091	0.018	0.17	0.034

Based on the magnetic measurements in the superconducting dipole models, an estimation of the additional field errors due to interstrand eddy currents during the ramp of the field in the dipole is presented in Table 6. This estimation is made using a ramp rate of dB/dt = 8 T/20 min, and a crossing strand contact resistance of Rc = 10 $\mu\Omega$, which is the aim of the cable development. At a constant ramp rate the eddy currents produce a constant field, so that the relative field errors are highest at injection. The errors are proportional to 1/Rc × dB/dt and can therefore be diminished by slower ramping at the

beginning of the ramp. It is probable that b_1, b_3 and b_5 would be systematic, whereas b_2 and b_4 would be random [9].

1.2.4 Coils and insulation to ground

During operation, the primary source of heat to the coils is from lost particles, the synchrotron radiation, and the beam image current intercepted by the beam screen. An additional dynamic heat load results from losses during magnet ramping. This heat increases the superconductor temperature, which reduces the magnet operating margin. Particular care has therefore to be taken to provide a cable insulation which not only withstands the voltage between turns but is also sufficiently porous to let the superfluid helium carry away the heat. To avoid short-circuits, the insulation must also be robust, in order not to break during winding and curing. The basic cable insulation, which must safely withstand a turn-to-turn test voltage of 75 V, is composed of two polyimide layers wrapped around the cable, with 50% overlapping, and another polyimide tape wrapped onto the cable and spaced by 2 mm (Fig. 5). The resulting gap makes the coil porous by setting up channels for superfluid helium, without affecting the mechanical support between turns. Different options are being tested, while other materials and designs, which may give both better coil porosity and higher thermal conductivity, are being examined.

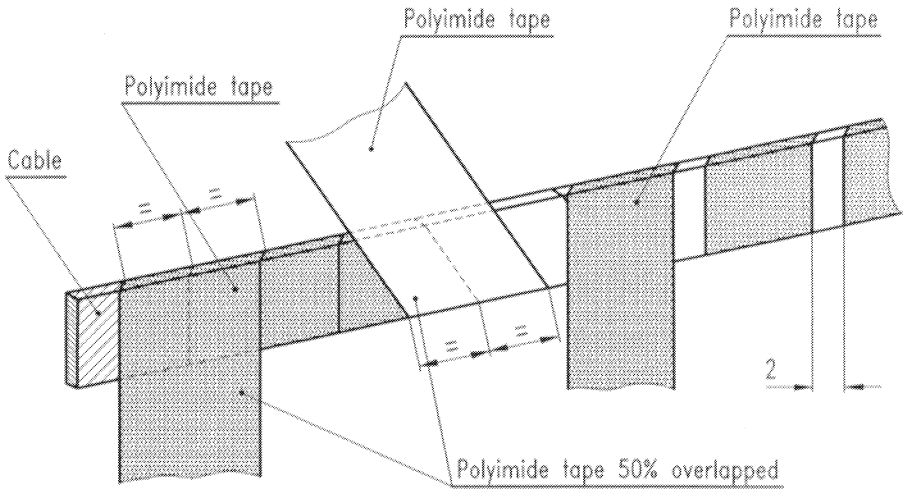

Figure 5: Conductor insulation

Integrated field harmonics are kept low by careful location and spacing of the conductors in the magnet's straight part and in the ends. Compared to earlier superconducting magnets, the ratio between conductor width and coil aperture is high. Special insulating fillers (end spacers) were therefore designed to confine the conductor to a consistent shape, close to a constant perimeter profile for each individual turn. Satisfactory shapes were determined using the approach of the minimum strain energy, in combination with

empirical methods. Several manufacturing options are being pursued, such as die-casting, moulding and machining, for producing the end spacers at the lowest possible cost.

Coils composed of two constant thickness layers with graded current density have been chosen. The two layers are joined together in the part of the inner cable that crosses over from the inner to the outer layer (ramp-splice) and are soldered to the outer layer cable. A strip of high conductivity copper is soldered to this cable in order to thermally stabilize and mechanically stiffen the ramp and its curved portion. Different ways of making the ramp-splice are under investigation and are being tested in models. At this time, a revision of the solution already used in 10 m long model dipoles is favoured because it appears to be the best compromise for magnetic length, current margin, manufacturing simplicity, reliability, and clamping of the soldered joint.

To stabilize and reinforce the coil leads, copper strips are soldered to the superconducting cable. The amount of copper complies with the permitted maximum temperature and the discharge time of the system.

Multipole components are generated by manufacturing errors related to tooling (winding mandrels, centre posts, sizing bars, curing moulds, liners, etc.) and the process. Very precise tooling (with tolerances of 20 μm on critical dimensions) is required and the process (curing temperatures and times, placement of the conductors) will be carefully checked and trimmed.

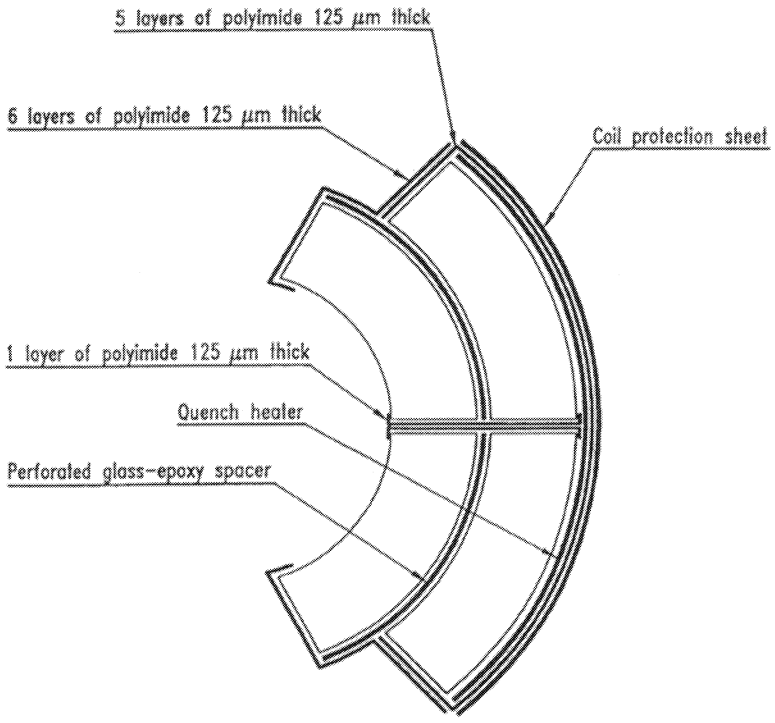

Figure 6: Ground insulation

The coil layers are separated radially by an insulating material. A slotted fibre-glass epoxy net is the adopted solution. The coils require additional insulation between poles and for the collars sitting at ground potential (Fig. 6). The ground insulation is composed of several polyimide film layers, cut azimuthally and longitudinally for reasons of assembly. Besides its electrical scope of preventing shorts from coil to coil (test at 3 kV in dry air) and from coil to ground (test at 5 kV in dry air), it also has the mechanical role of providing good slip surfaces during collaring, and a smooth surface over which both azimuthal and radial preloads are adequately distributed to avoid the deterioration of the insulation. Quench heaters are placed between the outer coil layers and the insulation to ground. They consist of stainless-steel strips, with about half of the length intermittently copper-clad (0.25 m with copper cladding alternating with 0.25 m without copper cladding). In case of quench, they rapidly heat up the conductors through the thermal barrier of the insulation. Collaring shims, which are located at the layer poles, and coil protection sheets located between the outer layer ground insulation and the inner collar surface, prevent damage due to contact with the serrated edges of collars. Moreover, the coil protection sheets help to avoid wrap breakdown and provide a continuous support to the conductors. A good slip surface between the collars and protection sheets is provided by coating the sheet with dry lubricant.

1.2.5 Mechanical structure

Description of the structure

The mechanical structure of the dipoles is designed to withstand the high forces generated in the magnet and limit as much as possible the coil deformation over the range of operation. The materials used for the most highly stressed components have, therefore, a high load-bearing capacity, high elastic moduli, good fatigue endurance and a good behaviour at cryogenic temperatures down to 1.9 K. Figure 7 shows the cross-section of the magnet cold mass. The coil support structure is formed by:

- Aluminium alloy collars common to both apertures. Inserts punched out of the same low-carbon-steel sheets as the yoke laminations maintain the required field distribution at all field levels, and at the same time firmly lock pairs of collars together. The collars are made of 3 mm thick high-strength aluminium alloy. The coils are assembled inside the collars and precompressed at room temperature.

- An iron yoke split into two at the vertical symmetry plane of the twin-aperture magnet. The gap is needed to compensate for the difference in thermal contraction of the iron yoke and the coil/collar assembly during cooling from room temperature to 1.9 K. The yoke is made of 6 mm thick low-carbon-steel laminations.

- A stainless steel outer cylinder. This part is welded with interference around the iron yoke in such a way that the required pre-stress is applied to the half-yokes at room temperature and in cold conditions after the closure of the yoke gap.

When current is flowing in the cables, the coils must be under compressive stress in order to avoid the appearance of sudden cracks or movements. Displacements and

deformations of the coils must be limited as much as possible. The necessary stiffness of the structure is reached when the following conditions are met:

a) the gap between the two iron yoke halves is closed before and during excitation,

b) a good contact is ensured between the iron yoke and the collars.

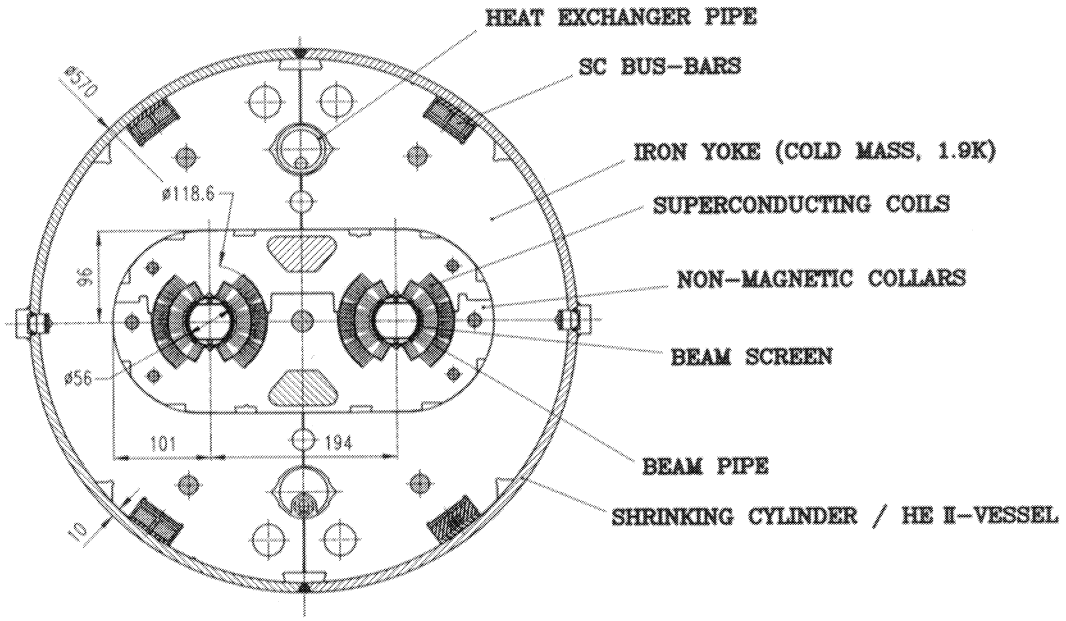

Figure 7: Dipole cold mass cross-section

To satisfy these conditions the relative dimensions of the components of the structure, the choice of materials, the pre-stress in the outer shrinking cylinder, and the dimension of the gap between the two half-yokes have been carefully determined. Furthermore, except for a short time during the collaring operation, the peak compressive stress in the coils at room temperature is limited to about 100 N/mm^2 to avoid creep of the insulation and of the copper.

The structural behaviour of a dipole, through the sequence of the assembly and excitation of the magnet, is described below.

Collaring

The collars are pressed around the coils to obtain an average compression of about 55 N/mm^2 for the inner layer and 45 N/mm^2 for the outer layer at the end of the process. The relative dimensions and elastic moduli of coils and collars to obtain the desired pre-stress are known from previous experience. During the collaring process, the compression of the coils can be 30–45% higher than the final required value depending on the method used to apply the load of the press. In fact, once the press force is released, the compressed coils expand the collars and part of the pre-stress is therefore lost. Around the locking

rods, the stress concentration reaches relatively high tensile values and the deformation of the locking sites contributes considerably to the global deformation of the collars and consequently to the loss of pre-stress at the end of the process. Thus a high-strength aluminium alloy has been selected for the collars in order to avoid plastic deformation.

Welding of the shrinking cylinder

The shrinking cylinder is welded with interference around the iron yoke. The interference generates a tensile stress of about 150 N/mm^2 in the cylinder. The greatest part of the force exerted by the shrinking cylinder is applied to the collar/coil assembly. It slightly deforms the collars and coils, increasing the compression at the top of the inner coil. To avoid a dangerous overcompression of the cables and insulation, a slot in the collar post is foreseen so that it behaves as a spring, releasing the pressure at room temperature, tracking the coil deformation, and shrinking during cooling and energizing. After complete assembly of the magnet the average pre-compression of the coils is about 75 N/mm^2 for the inner shell and 60 N/mm^2 for the outer shell.

Cooling from 293 K to 1.9 K

During cooling, the iron yoke closes completely. At 1.9 K the mating force between the two iron halves is around 2×1700 N per mm length. There is no loss of pre-stress in the coil during cool-down, thanks to the matched thermal contraction of the aluminium alloy collars.

Excitation at nominal field

At excitation, the iron gap stays closed and there is practically no change in the outer cylinder stress. The outward electromagnetic force (1700 N per mm length, per quadrant for a field $B_0 = 8.40$ T) is shared between the collars and the outer structure. The radial deformation in the median plane of the collared coils at this field excitation is about 0.04 mm. At the conductor short sample limit ($B_0 = 9.63$ T) the coils reach minimum compression at their top ($\sim$ 25 N/mm^2) and the maximum at the mid-plane ($\sim$ 100 N/mm^2).

Ends

In the coil ends, the bending of the blocks of cables and the different directions of the electromagnetic forces make the situation different from that in the straight part.

The ends are mounted inside the collars with much lower pre-stress (around 20–30 N/mm^2 in the azimuthal direction). In this region, part of the iron yoke is replaced by non-magnetic material in order to decrease the field. The choice of this material was largely dictated by its thermal contraction, which is as close as possible to that of iron. In this way, the external cylinder perfectly matches the inside structure in all conditions. The longitudinal resultant electromagnetic force is partly transmitted from the coils to the collars, yoke, and cylinder by friction. The remaining part directly loads the thick end plate. Measurements performed on model magnets indicate that the end plate takes 15–20% of the axial load.

1.2.6 Dipole cold mass and cryostat

The cross-section of the dipole cryomagnet is shown in Fig. 1. Figure 2 shows the longitudinal section of the cold mass.

The cryostat dimensions are largely dictated by the size of the dipole, and the very limited space in the tunnel. This constraint leads to the placing of only two cryogenic pipes within the cryostat.

The dipole cryostat [10] runs at three temperature levels, 1.9 K for the cold mass, and at 5–20 K and 50–70 K for the two intermediate heat intercept levels.

The dipole magnet, its connections, main and auxiliary bus-bars, both copper-stabilized, as well as bus-bar thermal expansion loops, are enclosed in a stainless steel skin, the shrinking cylinder, closed at its ends and forming the dipole cold mass to become a containment vessel filled with static pressurized superfluid helium at 1.9 K. Furthermore, the cold mass contains correction sextupoles and decapoles mounted on either end of the dipole. The two by-pass protection diodes are mounted in an appendix of the cryostat (see Fig. 2). A heat-exchanger tube, made out of corrugated copper, and the cold bores pass through the cold mass and are welded to close it at its extremities. The superfluid-helium cooling scheme is described in Section 2.

A dipole cryomagnet consists of a dipole cold mass assembled inside its cryostat, comprising a support system, cryogenic piping, radiative insulation and thermal shield, all contained within a vacuum vessel. The cryostat provides a stable mechanical support for its cold mass whilst limiting heat inleak to a level matching the strict heat-load budget of the LHC. The steady-state operational heat loads are estimated to be: 6.55 W/m at 50–70 K, 1.76 W/m at 5 K, and 0.35 W/m at 1.9 K. A detailed summary is given in Table 1, Part III, Section 2. The beam screen, a thermal interceptor for beam-induced heat losses cooled to 5–20 K, is mounted inside the cold bores of the cold mass. Each unit, together with its electrical, cryogenic and vacuum connections, is interchangeable with units upstream and downstream.

The dipole cold mass, weighing roughly 23.8 t, is linked to the cryostat by three support posts [11] each consisting of a low thermal conductivity composite tubular column mechanically interfaced via metallic top and bottom flanges and equipped with two intermediate thermal intercept plates supporting the thermal shields. These intercept plates are connected to the 5 K cryogenic tubes, and to the thermal shield which comprises the 50 K tube. The central support post is blocked to the vacuum vessel, the two others slide longitudinally.

Two thermal shields are installed to minimize heat inleaks to the cold mass at 1.9 K. The inner radiation screen uses multilayer superinsulation operating at 5–10 K, enclosing the cold mass. The outer thermal shield, which intercepts the largest fraction of incoming heat at 50–70 K, consists of a self-supporting aluminium screen covered with multilayer superinsulation. A helium-gas-cooled aluminium pipe forms part of the screen, which is divided into several segments to decrease movements during cool-down and warm-up. The vacuum vessel contains insulation vacuum at a pressure below 10^{-6} mbar, is made of construction steel to reduce costs and shield stray magnetic flux, and has stainless steel flanges. It is equipped with a safety lid which opens at less than 0.5 bar overpressure — all seals are radiation-resistant Viton^{TM} 'O-rings'. The mechanically rigid vacuum vessel will

itself be supported at two points, non-coincident with the support posts. Two alignment targets, at the first and third support posts, and one spirit level are mounted on the vacuum vessel. These outside references to the cold mass are established mechanically and verified on the magnet measurement bench with respect to the magnetic centres. The stability of the relationship between the targets and the magnetic centres will be checked with internal sensors. A series of tests on prototype magnets will confirm or invalidate the necessity of such a system [12].

The diagnostics feedthroughs are grouped close to the end flange at the electrical connections side. The diagnostic and control cables, also emerging from the cold mass end-flange, are brought to the vacuum vessel via instrumentation capillaries.

A retractable sliding sleeve with flexible bellow elements encloses the interconnect region between two cryomagnets, ensuring the continuity of the insulation vacuum; the radiative insulation and thermal shield are also continued across the interconnection region. All hydraulic connections and beam vacuum connections in the interconnect are welded.

1.3 The arc quadrupoles (Main quadrupoles)

1.3.1 Main parameters

The lattice quadrupoles are independently powered in two families (F and D) for each ring. The main parameters of the lattice quadrupole magnets are listed in Table 7.

The quadrupoles will differ from the quadrupole prototypes already built in collaboration with CEA-Saclay [13] in the conductor coil design, beam separation, yoke dimensions, and magnetic length.

Cable

The arc quadrupole has two layer coils with the same superconducting cable. The same type of cable as in the dipole outer shell will be used for the quadrupole. Its basic parameters are listed in Table 2.

Electromagnetic design

The design is governed by considerations similar to those for the dipoles. However, the saturation effects are much less pronounced. The two-in-one arrangement will mainly induce a dipole component at saturation. However, this is very small in relation to a displacement of the magnet centre of not more than 0.002 mm at nominal excitation. Table 8 shows the expected multipoles and their spreads at injection and nominal operation. At low excitation due to the persistent currents in the filaments a dodecapole and a small twenty-pole will appear and behave similarly to the sextupole and the decapole in the dipole magnets.

Table 7: Parameter list for LHC lattice quadrupole magnets

Operating quadrupole gradient value	[T/m]	223
Peak field in conductor	[T]	6.87
Margin in the load line		19.5%
Operating current	[A]	11780
Magnetic length	[m]	3.10
Distance between centres of apertures	[mm]	194
Inner coil aperture	[mm]	56
Outer coil diameter	[mm]	118.6
Outer collar diameter	[mm]	170
Inner yoke aperture diameter	[mm]	176
Outer yoke diameter	[mm]	456
Collar material		Stainless steel
Yoke material		Low carbon steel
Insulation thickness (azimuthally)	[mm]	0.130
No. of turns per coil inner layer		2+8
outer layer		7+7
No. of turns per aperture both layers		96
Stored energy (both apertures)	[kJ]	784
Self-inductance (both apertures)	[mH]	11.4
Resultant of the e.m. forces in the first octant		
ΣFx	[MN/m]	0.57
ΣFy	[MN/m]	–0.75

Table 8: Expected multipole performance, at injection and at nominal operation (in units of 10^{-4} relative field error at 10 mm)

	At injection, 14.5 T/m				At nominal operation, 223 T/m			
	Mean		Random		Mean		Random	
n	norm. b_n	skew a_n	norm. $\sigma[b_n]$	skew $\sigma[a_n]$	norm. b_n	skew a_n	norm. $\sigma[b_n]$	skew $[a_n]$
3	± 0.3	± 0.3	0.5	0.5	± 0.3	± 0.3	0.5	0.5
4	± 0.2	± 0.2	0.15	0.15	± 0.2	± 0.2	0.1	0.1
5	± 0.05	± 0.05	0.1	0.1	± 0.05	± 0.05	0.047	0.038
6	-0.6 ± 0.03	± 0.03	0.05	0.05	± 0.3	± 0.3	0.05	0.05
7	0.00	0.00	0.01	0.01	0.00	0.00	0.01	0.01
8	0.00	0.00	0.01	0.01	0.00	0.00	0.01	0.01
9	0.00	0.00	0.01	0.01	0.00	0.00	0.01	0.01
10	± 0.01	0.00	0.005	0.005	$\pm 0.0.01$	0.00	0.005	0.005
11			0.002	0.002			0.002	0.002

Coil design

Figure 8 shows the flux plot in the coil collar yoke assembly of the two-in-one quadrupole.

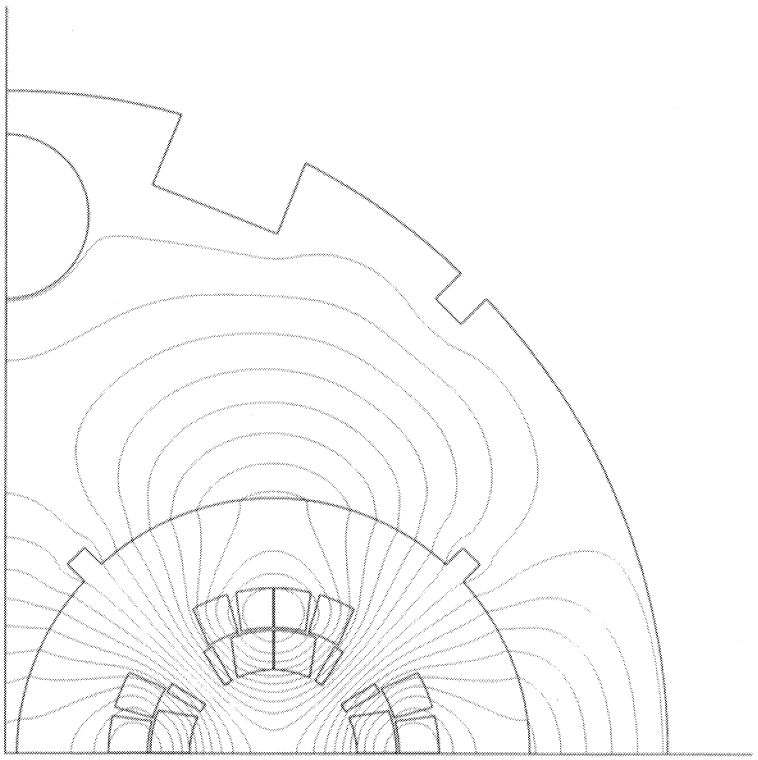

Figure 8: Flux plot in the cross-section of the main quadrupole

The cross-section of the coil is shown in Fig. 9. In contrast with the dipole coil design, the lattice quadrupole coils are not graded in current density. The winding of the two layers of each coil is made from the same stretch of cable in the double-pancake style: before starting the winding operation for the first layer, the amount of conductor needed for the second layer is stored on an intermediate storage bobbin. Once the inner layer is finished and cured, the winding of the second layer is performed on top of it, after placing the fish-bone and putting into place the joggle of the conductor for its passage between the two layers. This technique avoids the interlayer splices which, being numerous in the quadrupole, would be a significant load on the cryogenic system.

The turns of the inner block of conductors in the inner layer are spaced with respect to each other over the end region. This technique of diluting the cables avoids too high peak fields in this mechanically sensitive part of the coils. The end-spacers made of glass-resin composite or copper have warped surfaces, which are difficult to define theoretically but may be produced using numerically controlled machines or by injection moulding, after a certain number of prototype fittings. In fact, the critical point here is to find the shape of the end-spacers around which the rather stiff conductor bends naturally. The bending radius is considerably smaller than that at the corresponding location in the dipole coils.

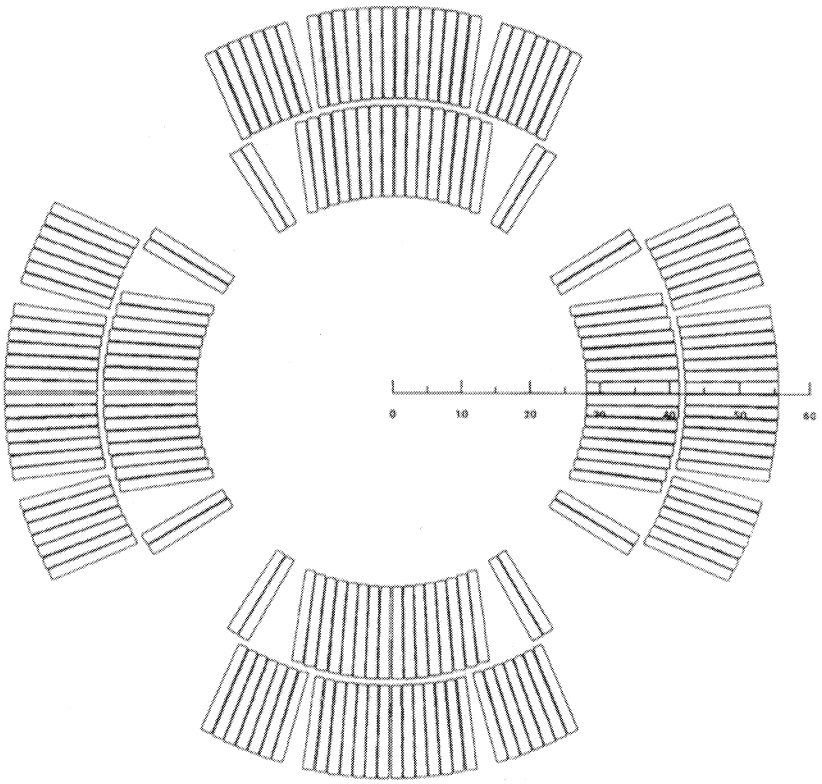

Figure 9: Conductor distribution in the main quadrupole cross-section

Mechanical structure

The quadrupole cross-section is shown in Fig. 10. The electromagnetic forces in the quadrupoles are considerably smaller than those in the dipoles. It is thus possible to contain the forces by the collar structure alone. The collars are made of austenitic steel laminations of 2.5 mm thickness. The pairs of half-collars are alternately turned by 90 degrees and are completed by two separate pole pieces.

The selection of the collar austenitic steel material is of the utmost importance. The permeability of this material, which can vary according to the basic quality of the steel and to details of its composition, must be low and homogeneous over the whole range of production.

The keying and pre-stressing of the assembly is done by eight lines of wedge-shaped stainless steel keys, which are progressively inserted in grooves on the outside of the collars. Between the coils and the collars a multilayer, polyimide-film ground insulation is placed and this also accommodates the 25 μm thick stainless steel quench heater strips.

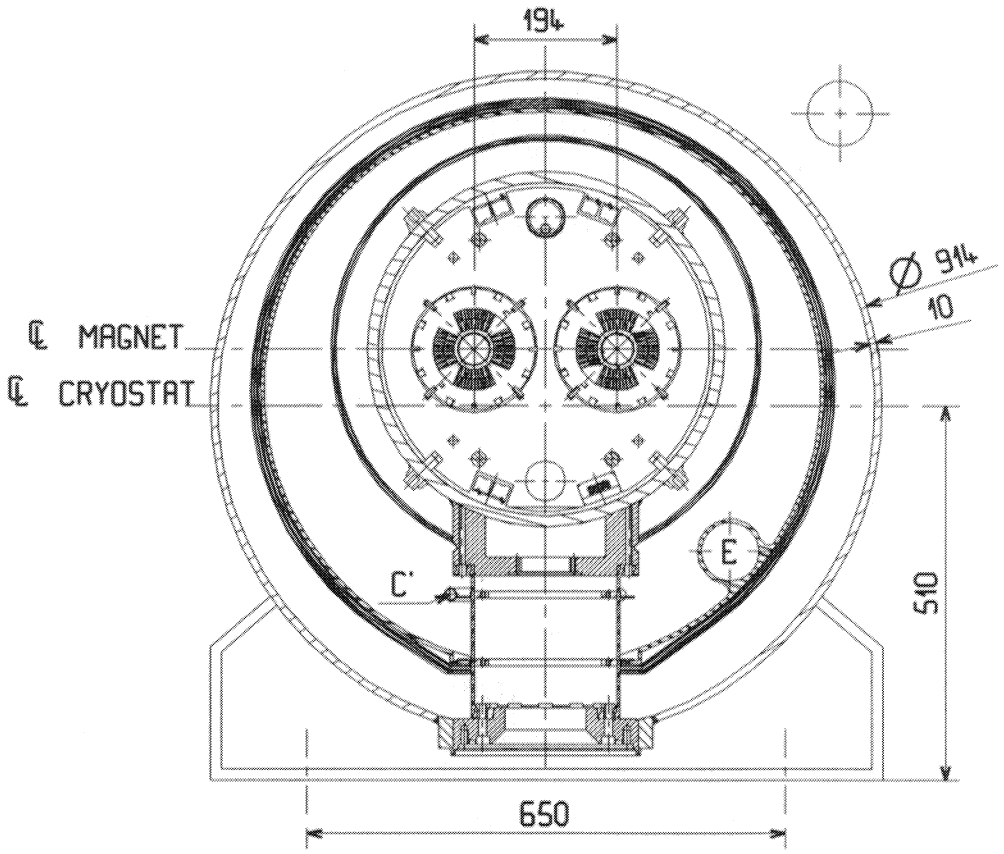

Figure 10: Schematic cross-section of the quadrupole

Once the coil-collar assemblies are completed and the coil interconnections done, the yoke is put around the two units. The yoke laminations are punched out of 6 mm thick low-carbon-steel plates. They are in one piece and are symmetric, with the exception that one side, top or bottom, is cut flat. They are placed around the pair of coil-collar assemblies and turned alternately by 180 degrees. The mechanical linkage between the collars and the yoke is made by four lines of keys placed in additional grooves on the outside of the collars and on the inner faces of the yoke laminations. Once the laminations are in place, they are compressed from the top and the bottom and locked with the keying rods. This centres and fixes the two coil-collar assemblies in place.

In order to stiffen the whole yoke assembly, a so-called inertia tube is placed around the yoke. This tube, made of stainless steel of 15 mm wall thickness, also serves as the helium vessel. The mechanical connection to the yoke laminations is done by keys fitting into grooves on the yoke outer surface. Lines of holes and flat surfaces, machined to a good precision along the inertia tube, serve as references. The keys are bolted to these surfaces and the yoke is centred inside the inertia tube, straight and without twist.

The inertia tube is about twice as long as the quadrupole magnet since it also houses octupole as well as dipole and sextupole correction magnets (see Section 1.3.3 below). The tightness is ensured by endplates and by specially formed caps welded over the mounting

holes. This technique of using an inertia tube has already been used for the HERA quadrupoles and, more recently, for the prototype magnets constructed by CEA-Saclay.

1.3.2 Corrector magnets in the arcs

In the regular machine lattice the corrector magnets can be subdivided into those installed in the short straight section cryostats and those installed in the dipole cryostats.

Combined arc sextupole and dipole corrector magnet MSCB

The longest corrector magnet in the short straight section combines a sextupole, operating between −1500 and +1500 T/m^2 to correct the lattice chromaticity, with a correction dipole operating between −1.5 and +1.5 T and used for orbit corrections. The coil of the sextupole magnet is mounted inside the coil of the dipole corrector magnet. Placing the sextupole close to the axis of the magnet minimizes the necessary excitation and the peak fields in the coils. Figure 11 shows a cross-section of a pair of these magnets — one will correct the horizontal orbit in one ring and the other the vertical orbit in the other ring. A gap between the magnets suppresses the cross talk. The dipole is designed for a very low current in order to reduce the cost of the room temperature power cables. It is therefore wound with many turns of a very thin wire. As it is difficult to make a regular winding with such small wire, the wires are preassembled in a 20-wire ribbon and the coil is wound from this ribbon. At the end of the ribbon the wires are connected in series [14]. The package of sextupole and dipole windings are surrounded by aluminium shrink rings which pre-stress the coils. The iron yokes have a rectangular shape which allows absorbtion of the return flux of the dipoles whilst still maintaining the intra-beam distance of 194 mm. The design parameters are given in Table 9. A prototype has been tested [15] and the results show that this magnet can cover the desired combinations of sextupole and dipole fields.

Table 9: Design parameters of the arc sextupole/dipole corrector MSCBH (V) and mid-arc dipole corrector MCBM

Name	Equipment description	Nominal Field at x, y (m) [T]	Coil aperture [mm]	Magnetic length [m]	Overall length [m]	Outer diameter [mm]	Current [A]
MSCB	Arc sextupole	1500 x^2	56	1.1	1.26	210	600
	Dipole corrector	1.5	80	1.03	1.26	210	32
MCBM	Mid-arc dipole corr.	3.0	56	0.30	0.53	185	50

The sextupoles will be connected in series through the machine cryostat to form four families — each ring has a family of focusing sextupoles placed in the cryostats of the focusing quadrupoles and a family of defocusing sextupoles which go together with the defocusing quadrupoles. In case of a quench, most of the energy of the whole family will be deposited in the quenching sextupole. It is expected that the quenching magnet can survive the resulting temperatures and voltages, but tests must be carried out to confirm

this. Otherwise, a pair of protection diodes (one for positive and one for negative currents) may prove necessary near each magnet or sub-group of magnets in order to by-pass the current along the quenching magnet. In the short straight section, at the centre of the arc, there is not sufficient length available for a pair of MSCB correctors. In this position the correctors are replaced by a pair of short mid-arc dipole correctors MCBM (Table 9).

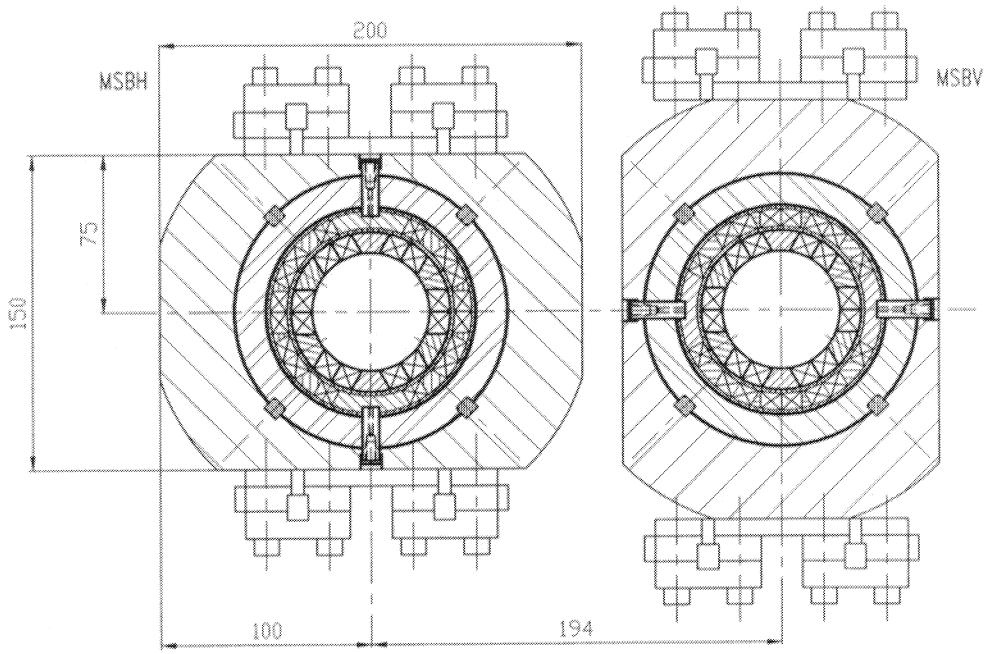

Figure 11: Cross-section of the MSCBH and MSCBV corrector

Each dipole will be powered individually. They need local current leads between ambient and 1.9 K. Thanks to the low current, the heat inleak into the helium amounts to only 70 mW. A study has been made [16] showing that one can reduce this heat leak even more if the cold part of these leads is made of high Tc superconductors. A prototype lead has been built to test the thermal behaviour and the reliability of such a lead. The cold part is made of high Tc material, whereas the conventional copper part is a simple braid cooled by thermalization using the 50–70 K helium tube. The first results are positive and it should be possible to reduce the power necessary for the cooling of the leads by a factor of three.

Arc octupole magnet MO

One short straight section in two will be equipped with an octupole magnet. These magnets will be powered in four families per sector subdividing them into focusing and defocusing magnets for Rings 1 and 2. Table 10 gives the main parameters for the two versions being considered: a superferric magnet and a cos θ coil magnet. The superferric design is more voluminous and yields a weaker field for the same magnet length but is expected to be cheaper. The coil needs fewer turns and less tight tolerances than the

cos θ type of coil. On the other hand the iron yoke must be very precise to obtain a good field quality. A superferric magnet is at present under construction to test the merits of such a design [17].

The present design is expected to be able to absorb the energy of the whole family in case of a quench without needing protection diodes. Tests will be necessary to confirm this.

Table 10: Design parameters of the arc octupole MO

Name	Equipment description	Nominal Field at x, y (m) [T]	Coil aperture [mm]	Magnetic length [m]	Overall length [m]	Outer diameter [mm]	Current [A]
MO	Arc octupole (superconducting)	$6.7\ 10^4\ x^3$	56	0.32	0.37	80	600
MO	Arc octupole (superferric)	$4.8\ 10^4\ x^3$	56	0.32	0.37	140	600

Sextupole and decapole correctors of the main dipoles

The main dipole magnets will be equipped with small sextupole and decapole corrector magnets [18] to compensate for the systematic sextupolar and decapolar field errors of the dipoles. Each bore will carry a sextupole corrector at one end and a decapole corrector at the opposite end. The sextupoles will be connected in series to form two families, one for each ring. The same will apply for the decapoles. The design parameters are given in Table 11. At the present stage of development it is not clear whether these correctors can absorb the energy of the family and survive a quench. The use of protection diodes may become necessary.

Table 11: Design parameters of the sextupole MCS and decapole MCD correctors

Name	Equipment description	Nominal Field at x, y (m) [T]	Coil aperture [mm]	Magnetic length [m]	Overall length [m]	Outer diameter [mm]	Current [A]
MCS	Sextupole corrector	$1970\ x^2$	56	0.100	0.15	120*	600
MCD	Decapole corrector	$1.3\ 10^6\ x^4$	56	0.063	0.10	110*	600

* Including shielding of nearby bus-bars

The sextupole and decapole correctors are mounted in the magnet end regions of the main dipoles. The bus-bars of the main magnets pass very close to these correctors and create important induction in the yoke of the correctors. A shield of some 5 mm thick iron will be necessary at about 5 mm distance from the yoke periphery to screen the yokes of the corrector magnets.

1.3.3 Short straight section cold mass and cryostat

The Short Straight Section (SSS) cryostats [19] of the standard arcs house the twin-aperture quadrupole MQD/F, two octupoles MOD/F, two combined sextupole-dipole correctors MSCBH/V, and the quench protection diodes for these magnets. The magnets and their diodes are mounted in a common inertia tube with end covers, forming the cold mass and thus the helium vessel, filled with pressurized helium II at 1.9 K. The present design of the SSS has the quadrupole centre located midway between the two adjacent dipoles. This implies that the corrector magnets are placed at each end of the quadrupole. The longitudinal cross-section of the whole assembly is shown in Fig. 12.

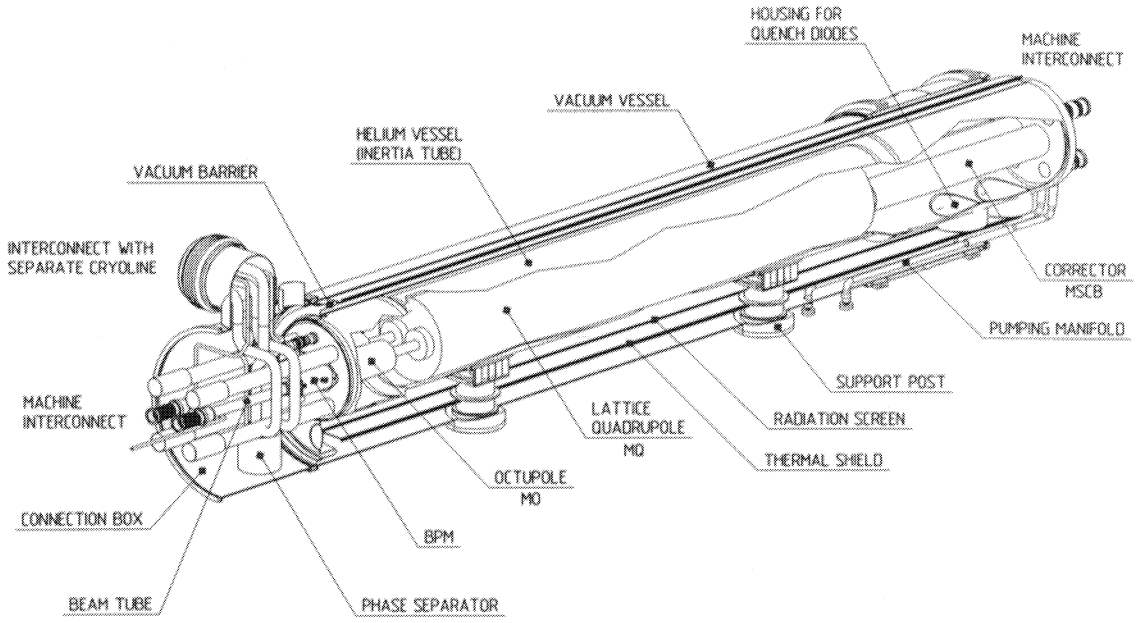

Figure 12: LHC short straight section, longitudinal view

The cryogenic Technical Service Module (QTSM), separated from the standard section of the cryomagnet by a vacuum barrier, is placed between the cold mass and the interconnection region of the next half-cell dipole. Vacuum manifolds, located on the rear side of the SSS cryostat, permit the pumping of the beam pipes every half-cell.

The inertia tube of the quadrupole provides mechanical support and reference for the corrector magnets. The alignment of these corrector magnets with reference to the quadrupole is obtained by supporting plates with a fitted key system, similar to that of the quadrupole, and this positions the corrector magnets in the inertia tube. Held in place by longitudinal spacer rods, the support plates also define the position of the bus-bars with their expansion loops.

The cold mass is assembled in the cryostat, which consists of a support system, the cryogenic piping, the radiative insulation, the thermal shield, and the vacuum vessel. Two support posts, essentially filament-wound, epoxy-glass columns glued between stainless-steel plates [20], transfer the magnet and helium vessel load onto cylindrical seats of the

vacuum vessel. As well as the cold mass load, the front support post will also restrain the 4000 daN axial force of the vacuum barrier during half-cell vacuum testing. To allow for the differential thermal contraction between the cold mass at 1.9 K and the vacuum vessel at ambient temperature, the rear support post slides longitudinally on a low-friction polyethylene plate, whilst the front one is fixed.

For measurement of the beam's position and the diagnostics of its dynamic behaviour, BPMs are mounted on the octupole side on the outside of the cold mass. A vertical and a horizontal 0.3 m long BPM, pre-aligned in a common fixture, are positioned by alignment jigs with reference to the inertia tube plugs and thus to the mechanical axis of the quadrupole. Welded onto the beam pipes, they form part of the LHC beam vacuum system. The BPMs are thermalized to 4.5 K.

A vacuum barrier permits separation of the insulating vacuum of each half-cell.

The basic SSS cryostat design was conceived in conjunction with the LHC dipole cryostat [10, 18].

Reference targets, adjusted on the vacuum vessel support points, and a level gauge enable alignment of the cryomagnet in the half-cell.

The QTSM consists of the half-cell cryogenic control valves, the helium phase separator, the instrumentation capillaries, the electrical feedthroughs for the correction dipole, the magnets, and a pair of Beam Position Monitors (BPMs). The functions of the cryogenic controls are described in more detail in Section 2, Cryogenics.

1.4 Magnets in the dispersion suppressors

The dispersion suppressor situated at the end of each arc consists of four pairs of regular arc dipoles, one arc quadrupole, and three 3.25 m long quadrupoles having the same cross-section as the main quadrupoles. As these quadrupoles are excited in series with those of the arcs, they are complemented by individually-powered trim quadrupoles MQLT. Other magnets in the dispersion suppressor are dipole orbit correctors, and skew quadrupoles (MQS), having the same (but rotated) cross-section as the trim quadrupoles, of 0.72 m in length.

Trim quadrupole MQLT

A number of trim quadrupoles are necessary for the tuning of the quadrupoles of the dispersion suppressor. The trim quadrupoles operate between 120 T/m and –120 T/m. The design is similar to that of a prototype single aperture tuning quadrupole already successfully built and tested [19]. The magnets are however assembled into a common two-in-one yoke using the same laminations as for the main quadrupoles but with a smaller inner aperture, adapted to the diameter of the tuning quadrupole coils. Since the field in the iron is low, the two trim quadrupoles are magnetically decoupled. A relatively small longitudinal spacing between the main and trim quadrupoles — about one coil aperture — is sufficient to avoid magnetic interference. The main parameters of the trim quadrupole are shown in Table 12.

Table 12: Design parameters of the magnets in the dispersion suppressor

Name	Equipment description	Nominal Field at x, y (m) [T]	Coil aperture [mm]	Magnetic length [m]	Overall length [m]	Outer diameter [mm]	Current [A]
MQLT	DS trim quadrupole	120 x	56	1.5	1.7	456*	600
MQS	Skew quadrupole	120 y	56	0.72	0.88	175	600
MCB	Dipole corrector	3.0	56	0.84	1.10	185	50

* Two-in-one yoke laminations of the MQ quadrupole

Skew quadrupole MQS

The skew quadrupoles MQS are identical to the prototype tuning quadrupoles [19], the only difference being that they have a different length and are mounted in pairs with a tilt of 45 degrees.

Dipole corrector MCB

The MCB is a short and strong dipole corrector magnet with a bore diameter of 56 mm. The current has been chosen very low, about 50 A, to reduce the cost of the warm power cables. As a result these magnets have a high inductance and produce high voltages in case of a quench. Tests will be made to see if this is acceptable.

1.5 Magnets for the insertions

1.5.1 Low-β insertions

The straight sections in low-β insertions (points 1, 2, 5, and 8) consist of an outer quadrupole triplet, a pair of separation/recombination dipoles, and an inner triplet.

The outer triplet (Q4–Q6) consists of two pairs plus one combination of three of the same 3.25 m twin-aperture quadrupoles MQL as found in the dispersion suppressor. These magnets are accompanied by MCB orbit correcting dipoles, and Q6 and Q4 have an MQS skew quadrupole adjacent to them. Pairs of 3.25 m long magnets rather than single longer units have been chosen in order to take advantage of the design and construction methods of the 3.1 m unit.

In the present layout the separation/recombination dipoles MBS (single aperture) and MBT (twin aperture) are 11.5 m long magnets of 88 mm inside diameter, where the single layer coil has the same dimensions as the outer coil of the main dipole. It has been verified that a twin-aperture version of such a magnet would provide the required 4.5 T at 4.6 K, with the field vector in the same direction in both channels.

Each inner triplet (Q1–Q3) uses four 5.5 m long, series connected, single-aperture (70 mm) quadrupoles, MQX. To permit the use of units of equal length, Q1 and Q3 are supplemented by 1.5 m long trim quadrupoles, MQXT. Local correctors include combined horizontal and vertical orbit correctors, and skew quadrupole and dodecapole correctors.

At the upstream side of points 2 and 8, Q4 must be equipped with a close-fitting cryostat to allow the passage of the injected beam.

The low-β quadrupole MQX

The low-β quadrupole is a single-bore, 5.5 m long magnet, whose main parameters are given in Table 13. Owing to the very large betatron amplitudes occurring in these magnets, the LHC performance depends critically on their field quality. In order to obtain the required field quality and to provide additional space for the cone of secondaries emanating from the interaction, a novel design, based on a graded coil with an aperture of 70 mm wound from NbTi keystoned cables cooled at 1.9 K, has been proposed. The design gradient of the magnet is 250 T/m for an excitation current of 5400 A.

The cross-section of the LHC low-β quadrupole is shown in Fig. 13. It features a four-layer coil [21] wound from two keystoned cables 8.20 mm wide with their current-carrying capacities graded by a factor of 1.5. The coils are assembled with the aid of thin quadrupole-type, stainless-steel collars locked with rods. A four-fold symmetric yoke is assembled around the collared coils and compressed with a tight-fitting outer shell. Because of their small width, the collars act as spacers, transferring the compressive forces from the tight-fitting ring to the coil. The yoke thus has both important magnetic and structural functions, as the magnetic forces are taken by the rigidity of the iron lamination pack. This design concept is currently being studied using a 1.3 m model magnet being developed in collaboration with an industrial firm [21].

Table 13: Parameters of the LHC low-β quadrupole

Operating quadrupole gradient	[T/m]	235
Peak field in conductor	[T]	8.6
Load line margin		85%
Operating current	[A]	5000
Magnetic length	[m]	5.5
Inner coil aperture	[mm]	70
Outer coil diameter	[mm]	138
Inner yoke aperture diameter	[mm]	158
Outer yoke diameter	[mm]	440
Collar material		Stainless steel
Yoke material		Low C iron
Cable width	[mm]	8.2
No. of turns per coil		77
Stored energy	[kJ]	1760
Inductance	[mH]	132

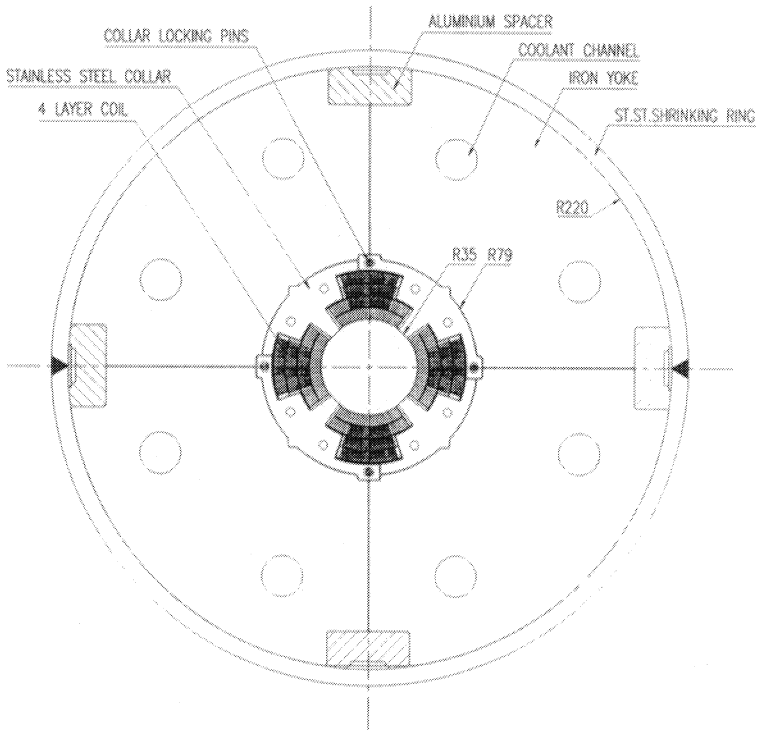

Figure 13: Low-β quadrupole

The low-β trim quadrupole MQXT

The inner triplet is tuned with two trim quadrupoles. These magnets are identical, quite powerful, and designed to work at a low current of 600 A, being individually powered. The quench temperature can become relatively high and this must be checked more closely. The parameters of the magnets are given in Table 14.

The low-β dipole corrector MCBX

In the inner triplets, a very short dipole corrector will be used, combining an inner coil yielding a vertical dipole field, and an outer coil yielding a horizontal dipole field. These coils are designed for 600 A. A lower current would create too high an inductance and therefore too high quench voltages. This magnet is used at a point where the two circulating beams pass through one single magnet aperture and where the magnet yoke diameter is not limited by the passage of the other beam, as is the case for all the other dipole correctors. The bore is large, 90 mm diameter, in order to make room for additional correction windings. The parameters of the MCBX dipole are given in Table 14.

Table 14: Design parameters of the other magnets in the low-β insertions

Name	Equipment description	Nominal Field at x, y (m) [T]	Coil aperture [mm]	Magnetic length [m]	Overall length [m]	Outer diameter [mm]	Current [A]
MQXT	Inner triplet trim quad	120 x	85	1.5	1.66	260	600
MCBX	Inner triplet dipole corr.						
	(horizontal)	3.2	90	0.31	0.6	540	600
	(vertical)	3.2	114	0.30	0.6	540	600
MCQS	Inner triplet (a2) corr.	28 y	90	0.36	0.6	140	25
MCDD	Inner triplet (b6) corr.	$3.2\ 10^6\ x^5$	76	0.50	0.6	140	25
MCDDS	Inner triplet (a6) corr.	$3.2\ 10^6\ y^5$	76	0.50	0.6	140	25

The low-β dodecapole and the skew quadrupole correctors MCDD, MCQS

Inside the bore of the MCBX corrector a dodecapole correction winding MCDD is to be placed. This corrector will also be used as a skew dodecapole (MCDDS) next to the Q3 magnet in combination with the skew quadrupole MCQS. The windings are mounted on tubes and placed concentrically around the vacuum tube. The parameters for the dodecapole and skew quadrupole are given in Table 14.

1.5.2 Cleaning insertions

The beam cleaning insertions, currently foreseen for points 3 and 7, use resistive dipoles and quadrupoles — except for Q6, which is a 3.25 m long superconducting quadrupole (MQL) as used in the dispersion suppressor. Two pairs of 3.6 m long dipoles, MBW (Table 15), between Q6 and Q5, take the beams from the 194 mm separation to 224 mm. Quadrupoles Q3, Q4, and Q5 are groups of three, four and five units of 3.5 m long warm twin-aperture magnets, MQW (Fig. 14). Each group of quadrupoles is accompanied by a pair of warm correctors, MCBW. Warm magnets are favoured, both because of the high risk of radiation in these regions and for reasons of economy.

Table 15: Parameters of the warm magnets in the cleaning insertion

Name	Equipment description	Nominal Field at x, y (m) [T]	Gap height [mm]	Magnetic length [m]	Overall length [m]	Outer dimensions [mm]	Current [A]
MBW	Warm separation dipole	1.5	50	3.4	3.6	1000×840	670
MQW	Warm quadrupole	37 x	44	2.9	3.1	800×680	685
MCBW	Warm dipole corrector	0.5	40	1.50	1.65	500	210

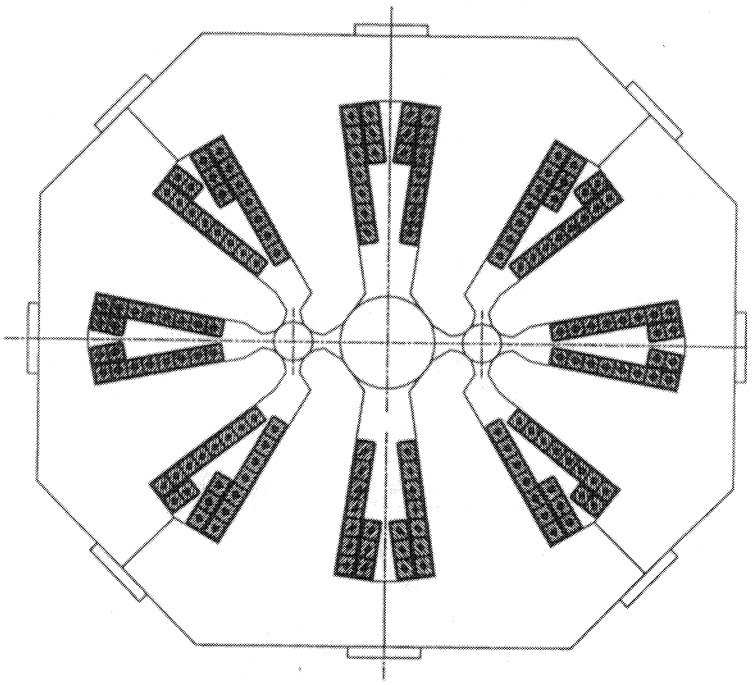

Figure 14: The warm quadrupole cross-section for the cleaning insertion

1.5.3 The RF insertion

In the present version of the LHC lattice the RF system is located in IR4. The insertion consists of a pair of dipoles that increase the beam separation from 194 mm to 420 mm, needed for placing two separate RF systems, and a matching section comprising five lattice-like quadrupoles.

It is presently envisaged that the separation dipoles will be built on the basis of the 80 mm aperture RHIC dipole, which has a magnetic length of 9.45 m. A total of 16 RHIC coils are necessary for both sides of the insertion, assembled in eight sections. Four of these coils are assembled in two two-in-one yoke configurations for the dipole (MBRT) which separates the beams at the entrance of the straight section on each side of the insertion. In order to accommodate the diverging beams, the two sections have beam separations of 194 mm and 222 mm. The other dipole of the separation pair (MBRS), which brings the beams onto collinear trajectories at the enlarged separation of 420 mm, is built of four complete RHIC cold masses assembled in two sections with beam separations of 392 mm and 420 mm.

Four matching quadrupoles per insertion side consist of one (Q2 and Q3) or two (Q4 and Q5) sections which have two separate cold masses assembled around the 3.1 m long lattice quadrupole coil with a separation of 420 mm. The last quadrupole of the section (Q6) consists of two lattice quadrupoles with a nominal separation of 194 mm.

This number of units is necessary for the tuning requirements of a low-β triplet that may eventually be introduced instead of the Q2 and Q3 quadrupoles. As with the other insertions, each quadrupole is equipped with an MCB dipole corrector, independently mounted at the ends of the two-in-one or separate cold masses.

1.5.4 The dump insertion

The matching section of the dump insertion comprises four quadrupoles, Q3–Q6, which are assembled as several 3.25 m long units. Q5 is composed of two 56 mm aperture (MQL) magnets while Q6 is made of three 3.1 m arc quadrupoles (MQ). Q3 and Q4, however, must be equipped with 70 mm aperture coils. These magnets are presently considered as being twin-aperture versions of the MQX magnets used in the low-beta insertions. Q3 is built from a single 3.25 m magnet of this kind (MQY) operated at 4.5 K, while Q4 features two of these special units operated at 1.9 K. In addition, Q3 must be provided with a close fitting cryostat to allow passage of the ejected beam. All quadrupoles are accompanied by corresponding dipole correctors — MCB for Q5 and Q6, and an enlarged aperture version MCBY for Q3 and Q4 quadrupoles (Table 16).

Table 16: Design parameters of the wide aperture magnets in the dump insertion

Name	Equipment description	Nominal Field at x, y (m) [T]	Coil aperture [mm]	Magnetic length [m]	Overall length [m]	Outer diameter [mm]	Current [A]
MQY	Wide aperture quadrupole	220 x	70	3.25	3.50	460	5000
MCBY	Wide aperture dipole corr.	3.0	70	0.82	1.10	230	50

1.6 Tests and measurements

The LHC will have a large number of dipoles, quadrupoles and correction elements (Annex 3). The time, effort and infrastructure required for testing these magnets may be extrapolated to a certain extent from the experience gained with HERA. The total amount of magnetic measurements for the LHC, assuming two per twin-aperture magnet, is about seven times that handled during the construction of HERA.

The procedure applied when testing the dipole and quadrupole main magnets consists of:

- Magnetic field measurement of all collared coils at room temperature at the factory, followed, if necessary, by shimming.
- Field measurements of the fully assembled magnet at room temperature with low current.
- Final overall acceptance tests of each magnet and its cryostat at CERN. These include dimensional and electrical tests, checks of instrumentation, vacuum, etc.

- Installation of the magnet on the measuring bench and connection to cryogenics and current supply.
- Cryogenic tests.
- Power test and quench behaviour.
- Magnetic measurements at injection and high fields.

After removal from the test stand, the magnet will be prepared for installation, i.e. fitted with protection diodes and beam screens and stored thereafter in batches according to field quality.

A series of test stands will be provided for the magnet tests at CERN. Each will be equipped with, amongst other things, a reference support and the necessary vacuum, cryogenic and electrical connections to energize the magnets. They will also include all the associated safety devices and controls. However, for reasons of economy, one power supply will serve several test benches. Since the actual time over which a magnet is energized is much less than the overall duration of a magnet test, including cool-down and warm-up, one power supply for three or four test stations may be acceptable. This would be consistent with HERA experience.

Assuming for LHC magnets a turn-round time per test bench and per twin magnet of about 200 h, about 16 test stands must be operated around the clock in order to accomplish the complete LHC test programme within four years. A decision on how many magnets will be tested and measured in cold condition will be taken after an initial production and a full test of about 10% of the total production. It is hoped that after this initial phase, confidence will be sufficient to allow testing of only one magnet in ten. If only a fraction of the magnets were to be tested, the number of stands will be correspondingly less. Possible test scenarios are described in Ref. [22].

In order to allow high field measurements of the cold magnet, an auxiliary stainless steel pipe is inserted into the cold magnet vacuum chamber. The annular vacuum gap filled with several layers of superinsulation provides adequate thermal insulation to keep the auxiliary inner pipe at room temperature. The magnetic measurements can readily be performed inside this room-temperature pipe. However, this reduces the diameter of the aperture accessible during the measurement to about 39 mm, which is still adequate for high-precision field measurements.

After initial checks and cool-down, the excitation curves will be measured, and the quench behaviour investigated. For the purpose of quench localization measurements it is proposed to use an array of pick-up coils placed inside both apertures. Thereafter, by rotating these coils from the outside through a high-precision rotating unit, the field quality, strength and field integrals of dipoles and quadrupoles will be measured. The orientation of the field with respect to the vertical orientation of the dipoles and the quadrupoles will also be measured by this unit employing high-precision encoders and inclinometers. In addition, the position of the axis of the quadrupoles will be measured by localizing the lateral position of the pick-up coil by a laser-beam system which will also serve to refer this axis to the outside fiducials. Calibration of the measuring coils will be made by NMR as well as in normal-conducting, high-precision reference dipoles and quadrupoles.

These techniques may be backed up or complemented for cross-checks by others such as the stretched wire technique, used extensively for HERA.

The measurement of the magnetic axis of quadrupoles and the field orientation of both dipoles and quadrupoles are of particular importance for these double-aperture magnets. Errors can no longer be taken care of by aligning the magnet accordingly, but only by combining 'faulty' magnets in order to compensate errors in a magnet-shuffling procedure.

Each measuring bench is connected to its own analog conditioning and acquisition electronics. This is in turn connected to a workstation used as an operator console to monitor the data acquisition and storage. All the other equipment (motorization, cryogenics, power supplies) is controlled by programmable logic controllers connected via an industrial network to the operator workstations. A particular effort is being made to use readily available equipment and keep to a minimum the in-house developments both for hardware and software.

1.7 Magnet quench protection

The quench protection of the LHC machine [23] is based on the so-called 'cold diode' concept.

In a group of series-connected magnets, if one magnet quenches, then, unless precautions are taken, the magnetic energy of all the magnets will be dissipated in the quenched magnet, thus destroying it. The solution to this problem is to by-pass the quenched magnet and then de-excite the remaining series-connected unquenched magnets. In this way, only the energy of the quenched magnet itself will be dissipated as heat internally in the magnet. For the LHC machine it is foreseen to use silicon diodes situated inside the cryostat — so-called 'cold diodes' as by-pass elements. These diodes will be located in the helium II vessel at a temperature of 1.9 K and will be exposed to a radiation of about 35 kGy and 1.5 10^{14} neutrons/cm^2 over a 10-year period [24]. Newly developed thin-base epitaxial diodes of 75 mm diameter, which can absorb the integral load of about 10^{10} A^{2}s, have been tested in an accelerator environment at liquid nitrogen temperature and seem to be sufficiently radiation hard for this application. Tests have also been carried out on 10 mm diameter samples at liquid helium and liquid nitrogen temperatures in a reactor. These tests confirm that the diodes should be able to protect the magnets for 10 years but that intermediate annealing (warming up to room temperature) of the most irradiated diodes may be necessary every one or two years. Manufacture of pre-production batches of 20 full-size diodes from two different manufacturers is under way. These will be used for further radiation and power-pulse tests in order to finalize the choice of materials and manufacturers.

The diodes will be situated in the cryostat of the magnet (Fig. 2).

The extremely high energy density of the LHC magnets, coupled with the relatively slow propagation speed of a 'natural' quench, can lead to excessive heating at the zone where a quench starts. It is therefore necessary to very quickly detect the incipient quench using sensitive radiation-hard isolation amplifiers, and then to fire strip heaters which provoke quenching along the outer layer of the magnet coil. This spreads the energy throughout a large volume of the winding, and so limits the maximum temperature rise and maximum internal voltages.

In order to avoid the quench spreading to other magnets and overheating of the cold diode, a fast de-excitation of the magnet chain must be initiated whenever a quench is detected. This fast de-excitation is achieved by switching high-power energy-dump resistors in series with the magnets, giving a de-excitation time constant of about 100 s (see Section 4.2).

The proposed power circuit of the LHC main ring magnet is shown in Section 4, Fig. 1. The machine is divided into eight sub-units (sectors of both rings together), powered separately and therefore electrically independent. This scheme has several important advantages compared to a series connection of all magnets:

- During fast de-excitation, because there are only two switched resistors per circuit, there is reduced risk of a build-up of voltage to earth due to switch timing and resonances.
- Earthing of the ring is more efficient since it is effectively at eight points around the ring.
- If quenches occur in only one limited region (one or more magnets in the same sector of the machine) then only this eighth of the machine has to be rapidly de-excited. This reduces the total eddy current losses during de-excitation, decreases the risk of false quench detection and quench provocation, and gives less wear on the switches.
- The eight autonomous sub-units give easier testing and setting-up possibilities.

The above advantages of a sub-divided system, compared with a series connection of all magnets, were considered sufficiently important to impose this choice. The main problem lies in the precision and tracking requirements of the eight separate power converters (Section 4.7).

A study is under way to see if it would be of interest to use superconducting links to connect through the odd access points of the machine, thereby connecting adjacent sectors and having a division of the machine into four instead of eight sub-units. This would save power converters and reference magnets but has penalties, including higher voltages to earth during de-excitation.

The protection system for the main-ring quadrupole magnets will be similar to that of the dipole magnets. Owing to the lower stored energy only one de-excitation energy-dump switched resistor is necessary per sector.

For the other series-connected multipole corrector magnets the decision as to whether they should be individually equipped with cold diodes as for the main-ring dipole magnets or whether they can be built with sufficient copper stabilization to absorb the total chain energy will be taken once cost and technical studies are complete.

References

[1] R. Perin, Magnet R&D for the CERN LHC, Proc. Workshop on Superconducting Magnets and Cryogenics, 1986, ed. Per F. Dahl (Brookhaven Nat. Lab., Upton, N.Y. Report BNL 52006) pp. 25–34.

[2] D. Leroy, R. Perin, G. de Rijk, W. Thomi, Design of a high-field twin aperture superconducting dipole model, IEEE Trans. Magn. **24** (1988) pp. 1373–1376.

[3] D. Leroy et al., Test results of 10 T LHC superconducting one-meter long dipole models, IEEE Trans. Appl. Supercond. **3** (1993) pp. 614–621.

[4] A. Yamamoto et al., Development of twin-aperture dipole magnets for the Large Hadron Collider, Proc. Appl. Superconductivity Conf., Boston, 1994 [IEEE Trans. Appl. Supercond. **5** (2)] pp. 61–3417.

[5] The LHC Magnet Team, reported by R. Perin, Status of the Large Hadron Collider magnet development, IEEE Trans. Magn. **30** No. 4 (1994) pp. 1579–1586, CERN LHC Note 244.

[6] R. Perin for the LHC Magnet Team, Status of LHC programme and magnet development, Proc. Appl. Superconductivity Conf., Boston, 1994, CERN LHC Note 296 [IEEE Trans. Appl. Supercond. **5** (2)] pp. 61–3417.

[7] Design features of the new LHC dipole long models (prototypes), Edited by R. Perin, CERN AT-MA Internal Note 94–103 (1994).

[8] D. Hagedorn and F. Rodrigez Mateos, Modelling of the quenching process in complex superconducting magnet system, IEEE Trans. Magn. **28** (1992) pp. 366–369.

[9] A.P. Verweij, R. Wolf, Field errors due to interstrand coupling currents in the LHC dipole and quadrupole, CERN AT-MA Internal Note 94–97 (1994).

[10] J.C. Brunet, J. Kerby, Ph. Lebrun, P. Rohmig, B. Szeless and L.R. Williams, Design of the LHC prototype dipole cryostats, Cryogenics **32** (1992) ICEC Supplement, CERN LHC Note 195 (1992).

[11] M. Blin, H. Danielson, B. Evans and M. Mathieu, Design, construction and performance of superconducting magnet support posts for the Large Hadron Collider, CERN LHC Note 235 (1993).

[12] E. Menant and J.P. Quesnel, Reference target positioning, CAS Magnetic Measurement and Alignment, Montreux, 16–20 March 1992, CERN Report 92–05.

[13] P. Genevey et al., Cryogenic tests of the first two LHC quadrupole prototypes, Proc. Appl. Superconductivity Conf., Boston, 1994 [IEEE Trans. Appl. Supercond. **5** (2)] pp. 61–3417.

[14] E. Baynham et al., Construction and tests of a model of the LHC superconducting corrector magnet MDSBV, LHC note 155, September 1991.

[15] A. Ijspeert et al., Test results of the prototype combined sextupole-dipole corrector magnet for LHC, LHC Note 201, November 1992.

[16] A. Ballarino, A. Ijspeert, Expected advantages and disadvantages of high Tc current leads for the Large Hadron Collider, paper submitted to the Cryogenic Engineering Conference, Albuquerque, USA, July 1993.

[17] G. Laurent, S. Russenschuck, N. Siegel, M. Traveria et al., Design, fabrication and cold tests of a superferric octupole corrector for the LHC, MT14, Tampere 11–16 June 1995.

[18] E. Baynham et al., Design of superconducting corrector magnets for LHC, IEEE Trans. Magn. **30**, No. 4 (1994) pp. 1823–26.

[19] H. Bidaurrazaga et al., Design and fabrication of the prototype superconducting tuning quadrupole and octupole correction winding for the LHC project, IEEE Trans. Magn. **28**, No. 1 (1992) pp. 342–345.

[20] A. Bézaguet, J. Casas-Cubillos, Ph. Lebrun, M. Marquet, L. Tavian, and R. van Weelderen, The Superfluid Helium model cryoloop for the CERN Large Hadron Collider, CERN AT/93–21, LHC Note 233.

[21] R. Ostojic, T.M. Taylor, G.A. Kirby, Design and construction of a one-metre model of the 70 mm aperture quadrupole for the LHC low-β insertions, IEEE Trans. Magn. **30**, No. 4 (1994) pp. 1750–1753.

[22] P. Sievers, Towards series measurements of LHC magnets, CERN LHC Note 267 (1994).

[23] L. Coull, D. Hagedorn, V. Remondino and F. Rodriguez-Mateos, LHC magnet quench protection system, 13th Int. Conf. on Magnet Technology, Victoria, Canada, 20–24 Sept. 1993 (IEEE Trans. Magnet. **30**, 1994) pp. 1525–2691.

[24] D. Hagedorn and L. Coull, Radiation resistant quench protection diodes for the LHC, Plenum Press, Advances in Cryogenic Engineering (Materials), Vol. 40B, pp. 1437–1444 (1994), CERN LHC Note 226 (1993).

2 Cryogenics

Most of the basic design criteria and constraints, as well as the main technical choices for the LHC cryogenic system remain those described in Chapter 6 of the 'Pink Book' [1], in Part III, Section of the 'White Book' [2], and more recently summarized in a review article [3]. In the following we shall only cover specific aspects of LHC cryogenics which have undergone important changes, or on which our knowledge has made significant progress, either through more detailed design or experimental verification on the basis of prototype work and model testing. This section concludes with a brief discussion of a few technical variants which could lead to simplifications, and hence economies on the cryogenic system.

2.1 General architecture

Reusing the civil engineering and technical infrastructure of the existing LEP collider, a basic approach to a cost-effective LHC can be made more efficiently and thoroughly after relaxing the requirement for co-existence of LEP and the LHC in the tunnel. The latter decision has opened the way to reconsidering the technical architecture of the machine, in particular the cryogenics, which was based until now on the eight-fold symmetry of the layout.

Acknowledging that the even-numbered areas of LEP are much more accessible, developed and already equipped with technical buildings and infrastructure [4], we decided to group together, as much as possible, all the active cryogenic equipment at these four points, and to transport the refrigeration power over the complete length of a sector, i.e. 3.3 km, instead of the previous 1.7 km half-octant. In view of prohibitive hydrostatic and frictional pressure drop limitations, this approach leads to an increase in the diameter of all the cryogenics pipes with respect to the previous eight-point feed scheme. As a consequence, the concept of integrating these pipes in the magnet cryostat loses much of its practicality — especially with regard to machine installation and interconnects — and in fact appears infeasible, given the limited transverse space available in the LHC tunnel. Therefore, the cryogenic headers distributing cooling power along a machine sector are now contained in a separate Cryogenic Distribution Line (CDL) running in the tunnel along the string of cryomagnets (Fig. 1), with jumper connections every 53.5 m for branching into half-cell cooling loops (Fig. 2).

These considerations result in the pseudo-four-point feed scheme sketched in Fig. 3: two split-coldbox helium refrigerators of the LEP type [5], serving the adjacent sectors, are installed at each even point. In this configuration, partial redundancy is easily obtained by means of a Cryoplant Interconnection Box (CIB), allowing distribution of the cryogenic loads of each sector to either or both cryoplants. Refrigeration at 1.8 K is provided by two Cold Compressor Boxes (CCB), installed underground at the level of the machine tunnel and fed from the 4.5 K refrigerators through the CIB. In this way, almost all of the cryogenic equipment is located in the technical service areas of the four even points, on the surface or underground. The cryogenic system for the LHC machine thus requires no infrastructure or utilities at the four odd-numbered points, apart from 1000 m^3 storage at 2 MPa for recovery of gaseous helium after a generalized resistive transition of the magnets in the octant concerned.

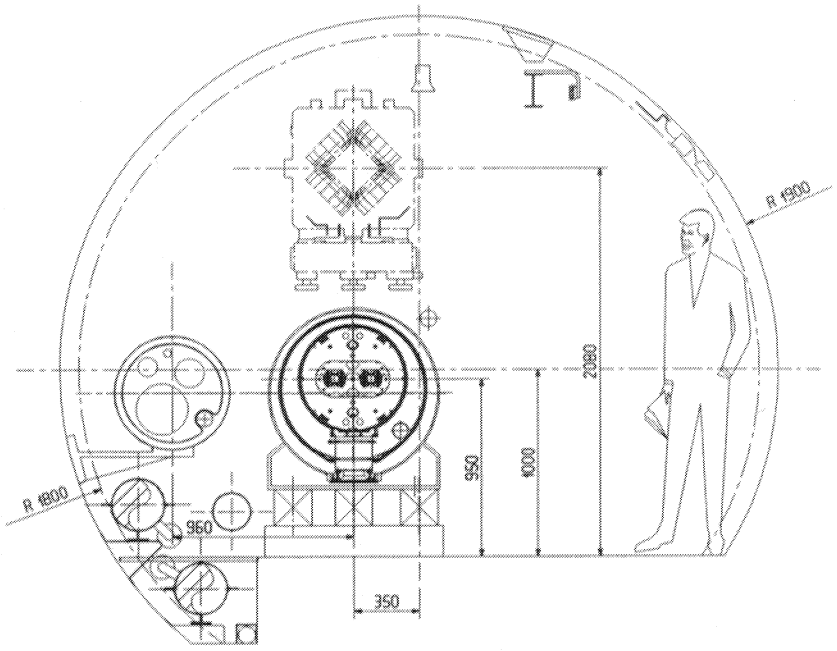

Figure 1: Transverse cross-section of the LHC tunnel at a dipole

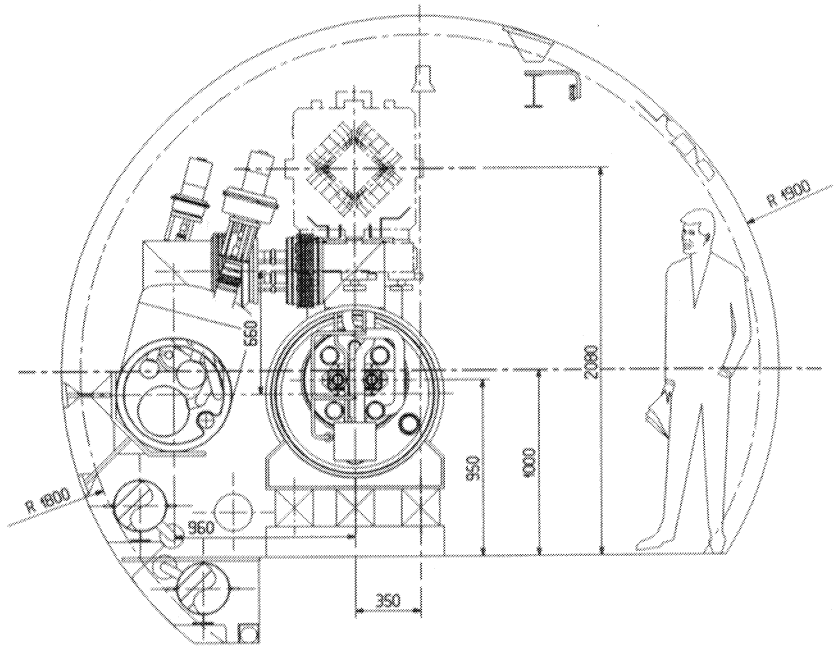

Figure 2: Transverse cross-section of the LHC tunnel at a short straight section

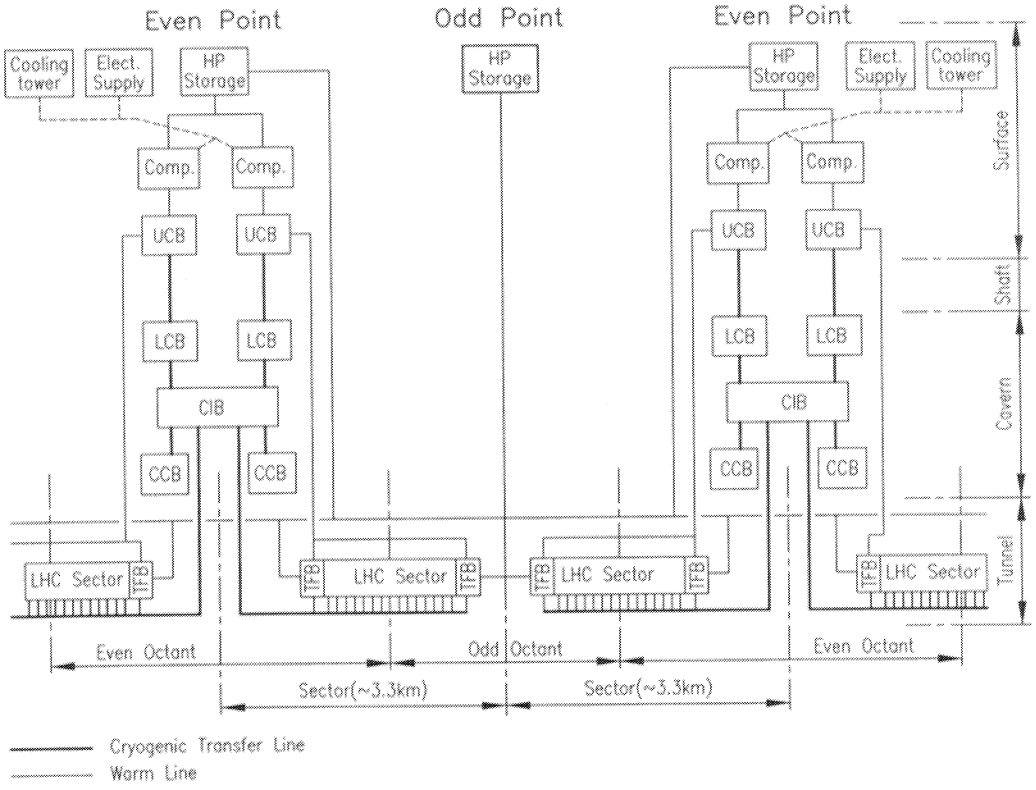

Figure 3: General architecture of the LHC cryogenic scheme

2.2 Temperature levels and heat loads

The staging of temperature levels envisaged for the LHC cryogenic system has been essentially maintained, with some minor adaptations in order to match the thermodynamic cycles of the LEP cryogenic plants [5]. These were supplied by two different manufacturers, and will be used for LHC refrigeration after suitable modification and upgrading. The temperature levels are:

- thermal shielding between 50 K and 75 K as a first major heat intercept, sheltering the cold mass from the bulk of heat inleaks from ambient;
- distribution of supercritical helium at 4.5 K for initial filling of the cryomagnets and lower temperature heat interception during operation; as previously, this circuit is used for non-isothermal cooling of the beam screens between 4.5 K and 20 K (instead of 10 K), a change which preserves the vacuum performance of the cold bore and beam screen cryopumping system and matches better the cryogenic plants, while reducing the entropic load resulting from induced losses (synchrotron radiation and image currents) falling on the beam screens;
- quasi-isothermal superfluid helium cooling the magnet cold mass at a maximum temperature of 1.9 K and transporting the applied heat loads across the length of a sector (3.3 km) to the CCBs operating at 1.8 K [6];

- normal helium cooling special superconducting magnets in insertion regions, superconducting acceleration cavities, and the lower sections of HTS current leads at a saturation temperature between 4.5 K and 4.7 K.

- gaseous helium cooling the resistive upper sections of HTS current leads, in forced flow between 50 K and ambiant.

The implementation of the first three temperature levels in the standard LHC dipole cryomagnet is shown in the cross-section of Fig. 1 of Part III, Section 1. Apart from the suppression of cryogenic headers, the basic design concepts of the cryostat have shown little evolution with respect to previous versions. Its expected thermal performance has however been assessed with better confidence and experimentally verified through several independent, yet converging approaches:

- thermal calculations, conducted on the basis of the detailed construction drawings established for industrial manufacturing of full-scale prototypes, have permitted heat inleak estimates to be refined and parametric sensitivity studies concerning the prototype dipole [7] and short straight section [8] cryostats, including auxiliaries and interconnection regions [9] to be performed;

- critical components of the cryostat thermal insulation system, for example radiative insulation [10, 11] and cold mass support posts [12, 13], as well as cold discharge valves [14] have been developed, investigated and thermally validated by precision heat inleak measurements;

- global measurements performed on the TAP cryomagnet [15]–[17], on long prototype cryomagnets [18, 19], the prototype test string [20], as well as on a dedicated full-scale thermal model [21], have confirmed the technical feasibility of efficient compound cryostats housing long superconducting magnets operating in superfluid helium.

Besides heat inleaks from the ambient temperature environment, the cryogenic components of the LHC will be subject to heat loads of two other kinds.

Resistive dissipation in the non-superconducting sections of the magnet excitation circuits (essentially current feedthroughs and splices in the superconducting cables) has now increased to an average of 0.11 W/m at full current. This is a result of the choice of separate excitation for dipoles and quadrupoles, and assuming a residual resistance per splice of 0.6 nΩ and 1.2 nΩ for the external and internal splices, respectively.

Heat loads deposited in the magnet cold mass through several processes and by the circulating and colliding proton beams have also been re-evaluated. As they depend strongly on the energy and intensity of the circulating beams, we use hereafter the values of these dynamic loads estimated for nominal (7 TeV, 2×0.536 A) and ultimate (7 TeV, 2×0.848 A) operating conditions [22] and for the whole machine:

- synchrotron radiation from the bending magnets, mostly absorbed by the beam screens, amounts to an average power of 0.41 W/m (nominal) and 0.65 W/m (ultimate);

- resistive heating due to image currents induced in the conducting walls and geometrical singularities of the beam channels yields a power of 0.33 W/m (nominal) and 0.83 W/m (ultimate);

- continuous loss of particles from the circulating beams, produced by nuclear inelastic beam–gas scattering, results in a distributed heat load in the helium II baths estimated to 0.06 W/m (nominal); this value is expected to decrease with running time due to improvement of the vacuum by beam cleaning;

- continuous loss of particles escaping the collimation sections may result in a locally deposited heat load estimated at 55 W (nominal) and 92 W (ultimate), over a length of a few tens of metres corresponding to the region of aperture restriction;

- absorption of secondaries in the cold mass of the superconducting magnets located close to the high-luminosity experimental areas will deposit large heat loads in the cryogenic environment:

  – at the 1.9 K level, from 500 W (nominal) to 1250 W (ultimate) in the inner triplets of low-β quadrupoles, as well as from 54 W (nominal) to 134 W (ultimate) in the dispersion suppressor magnets;

  – at the 4.7 K level, from 240 W (nominal) to 600 W (ultimate) in the beam separation and recombination dipoles.

The heat load estimates based on the above assumptions are given in Tables 1 and 2, Annex 4, for standard-cell dipoles and short straight sections, respectively; they have been established for nominal operating conditions and include auxiliary components and one interconnection region per cryostat. In a similar way, the budgeted heat loads for a 53.5 m long module of the CDL appear in Table 3, Annex 4. From these data, the heat loads corresponding to a standard half-cell (Table 4, Annex 4) and an arc (Table 5, Annex 4) have been assessed in four cases of interest for the cryogenic operation of the machine, namely:

- 'nominal operation' at 7 TeV beam energy, 2×0.536 A beam current and 1×10^{34} cm^{-2} s^{-1} luminosity;

- 'ultimate operation' at 7 TeV beam energy, 2×0.848 A beam current and 2.5×10^{34} cm^{-2} s^{-1} luminosity, assuming a two-fold reduction of residual pressure in the beam channels over long term operation;

- 'low beam intensity operation', still with full beam energy and thus full excitation current in the magnets;

- 'injection standby', characterized by negligible resistive dissipation and beam-induced heat loads in the magnets.

The temperature profiles in the pressurized helium II baths of the cryomagnets around the machine circumference, calculated in the four cases defined above, and with a very low pressure helium header (line B) diameter of 267 mm (DN250), are shown in Fig. 4.

For the purpose of comparison with former estimates, the average distributed heat loads in nominal operation in an arc of the LHC are presented in Table 6, Annex 4. The decrease in beam-induced heating at 1.9 K, essentially due to a lower beam–gas inelastic scattering, compensates the increase in resistive heating in cable joints, and the overall heat load at this temperature remains approximately constant. The additional heat load due to the CDL, although mostly seen on the thermal shield at 50–75 K, also contributes to raise the thermal budget at 1.9 K. Most of this increase, however, falls onto the large-diameter very low pressure helium line (line B), with limited effect on the cold compressor flow-rate. On the whole, the introduction of the CDL has a moderate thermodynamic impact on cryogenic power requirements.

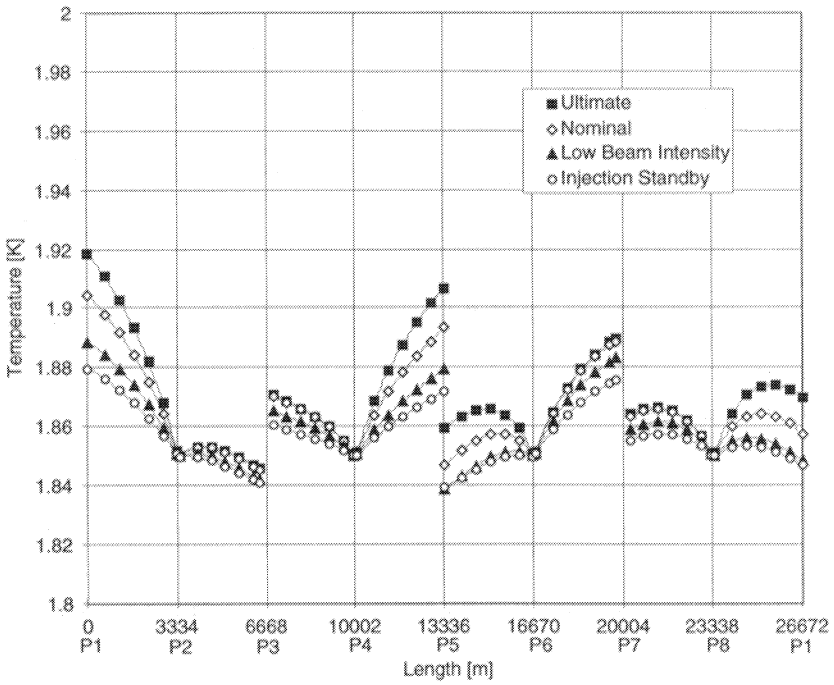

Figure 4: Temperature profiles in pressurized helium II baths

Since the detailed design of the superconducting magnets in the insertions has not yet been finalized, their expected heat loads have been assessed by approximate scaling from the better defined arc magnets. The results, displayed in Tables 7 and 8, Annex 4, reflect the variations in geometry, layout, functions and operating modes of the different LHC insertions. They also include specific components — for example, superconducting acceleration cavities, which require significant amounts of cryogenic refrigeration. Also appearing in these tables are the localized heat loads in the current leads of the different excitation circuits, and based on the generalized use of high-temperature superconductor (HTS) leads.

Compounding the above results yields the global estimates of heat loads in the sectors of the LHC, presented in Table 9, Annex 4 for the four previously defined modes of operation. Also accounted for in this table are the cooling requirements of the sections

of CDL bypassing the warm sections of the LHC, as well as those of the superconducting d.c. links electrically feeding the magnets in the tunnel from power converters located in the central technical caverns. Clearly, sectors 1–2, 8–1, 4–5 and 5–6, which house high-luminosity insertions, are subject to the largest 1.9 K heat loads, while sectors 3–4 and 4–5, which feature the strings of superconducting acceleration cavities, exhibit the largest 4.7 K heat loads. Also evident from Table 9, Annex 4 are the wide ranges of variation in the cooling power requirements at 1.9 K and 4.5–20 K, which the octant cryogenic plants will have to follow during LHC operation.

2.3 Ring cooling system

The essential principles of magnet string cooling have not changed. The magnets operate in static baths of pressurized superfluid helium, through which heat is transported by conduction to a linear cold source constituted by a heat exchanger tube threading its way through the string, and in which the heat is absorbed quasi-isothermally by gradual vaporization of flowing saturated superfluid helium (Fig. 5). This concept is implemented in independent cooling loops, each extending over 53.5 m — the length of a half-cell of the regular lattice (Fig. 6).

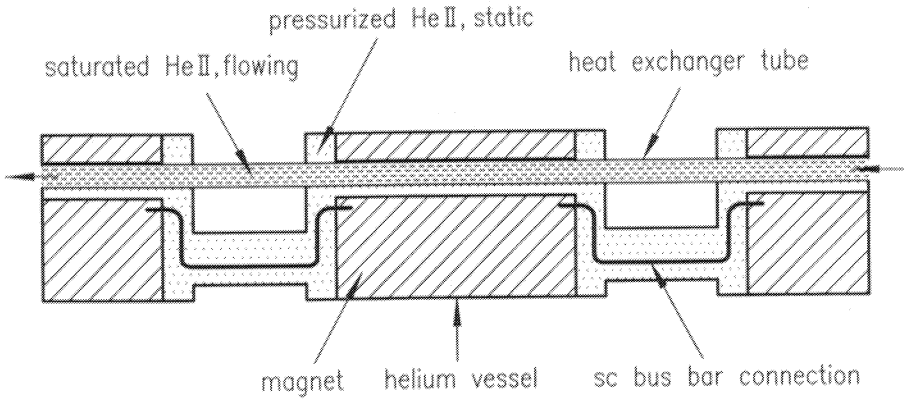

Figure 5: The LHC superfluid helium cooling scheme

Subcooled helium I from the sector refrigerator, distributed through line A, is expanded to saturation through valve TCV1 and fed to the far end of the heat exchanger tube, along which it gathers heat and gradually vaporizes as it flows back. The low saturation pressure is maintained on the flowing two-phase helium by pumping the vapour with minimum superheat through line B, over the length of a sector (3.3 km). Line C normally supplies supercritical helium to the beam screens equipping the magnet apertures, after intercepting residual conduction at 4.5 K on the magnet supports through line C. At the end of the sector, line C also supplies 4.5 K helium, when required, for cooling current leads in the electrical feedboxes. In normal operation, line D collects the bleed of line C and the beam screen circuits, controlled by valve TCV2, and returns it at 20 K to the sector refrigerator. To cope with uneven loading of the beam screens in the two channels,

the supercritical helium flows, in the neighbouring cooling pipes, are periodically merged and exchanged from one channel to the other, a solution which suppresses the need for a second control valve. Lines E and F circulate high-pressure helium, which intercepts primary heat loads on magnet supports and thermal shield between 50 and 75 K. The working characteristics of these lines in nominal conditions are listed in Table 10, Annex 4.

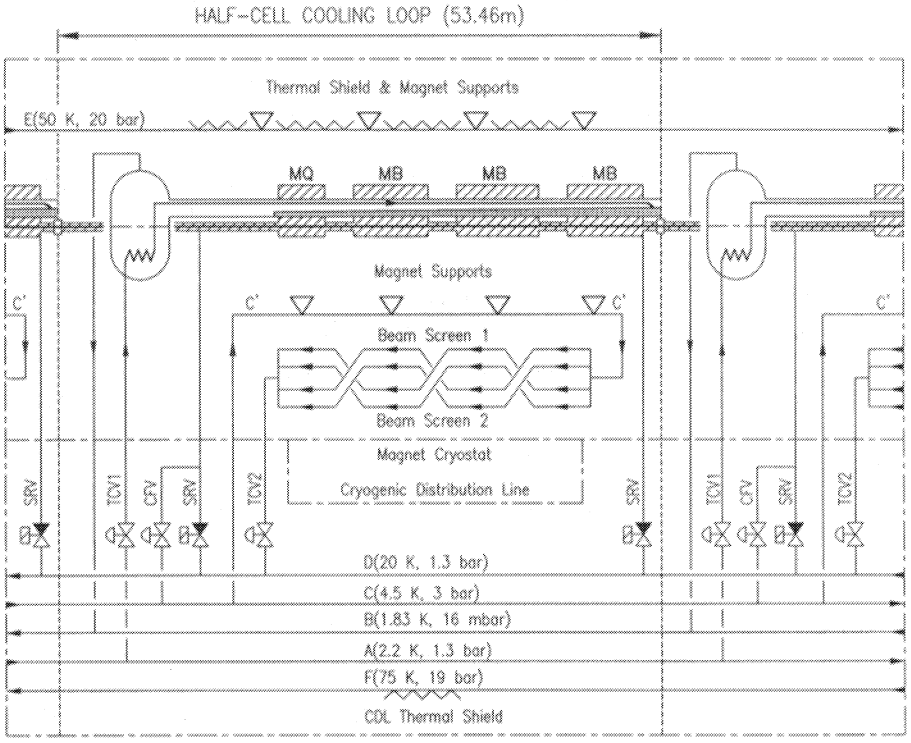

Figure 6: Cryogenic flow-scheme of an LHC half-cell

Cool-down and warm-up of each half-cell is achieved by forced circulation of high-pressure gaseous helium, supplied at variable temperature by line C, tapped through valve CFV, and returned to the refrigerator through valve SRV and line D. In case of magnet resistive transition, the resulting pressure rise [23, 24] is contained below the 2 MPa design pressure of the cryostat helium vessel by opening the SRV valves on the quench signal and discharging helium into line D. The low hydraulic impedance of this 150 mm diameter pipe, normally maintained at 20 K, proves very helpful in containing the helium discharge and buffering its subsequent release to gas storage vessels [25].

Following exploratory tests [26, 27] and model work [28] successfully conducted in a 20 m long thermohydraulic model loop, the validity of the superfluid helium cooling scheme was recently confirmed with full-scale prototype magnets on the test string [20]. Besides flow stability, heat transfer and cooling capacity, these tests addressed aspects of control strategy [29, 30], rendered delicate by the large dynamic range and rapid variations in heat loads, compounded with the strong non-linearities in physical properties of helium and solid materials below 2 K.

2.4 Cryogenic plants

On the basis of the revised heat load estimates for the LHC sectors, and allowing for some spare capacity, the refrigeration and liquefaction requirements to be simultaneously fulfilled by the cryogenic plants in each sector are listed in Table 11, Annex 4. With respect to previous values, the main changes concern the 50–75 K refrigeration and the liquefaction requirements. The 50–75 K non-isothermal refrigeration capacity has significantly increased: this is partly due to the increase in the cold surface area in the cryomagnet and CDL thermal shields, and partly to a more complete accounting of the numbers and types of cryogenic devices and ancillary equipment. The generalized use of HTS current leads has entirely replaced the liquefaction requirements with a non-isothermal refrigeration duty between 50 K and ambient, leading to a significant reduction in entropic load.

In spite of these changes, it appears that the highest entropic load applied to sectors not adjacent to high-luminosity experiments, could still be extracted by a cryogenic plant of an equivalent refrigeration capacity of about 18 kW at 4.5 K — i.e. within reach of the upgraded and suitably modified LEP installations [31]. Detailed studies involving the manufacturers of these cryogenic plants have assessed their effective capacity in LHC operation and defined the required adaptations and modifications. The new LHC cryogenic plants which will cool the high-loaded sectors adjacent to high-luminosity interaction regions will eventually require about 17% more capacity. In view of the expected gradual increase in operational luminosity of the machine, it cannot be excluded, at this stage, that this additional capacity is finally obtained — without any remaining safety margin — from the technical contingency applied to cryogenic plant design and construction.

Preliminary studies have been conducted on the cold compressor systems required for producing large-capacity refrigeration at 1.8 K. In order to cope with an overall pressure ratio approaching 80, and a dynamic range of 2:1, each CCB will require four to five stages of centrifugal compressors in series [32]. Design and development work is being carried out, in the framework of a collaboration agreement with the CEA in France, on procurement, construction and testing of prototype hydrodynamic and volumetric cold compressors and very-low-pressure heat exchangers, as well as on the definition and optimization of 1.8 K refrigeration cycles. Two monostage centrifugal compressors, supplied by European industry and featuring novel ideas in wheel design, as well as bearing and drive technology, are being commissioned and tested. The successful start-up and commissioning of the CEBAF cryogenic system [33], which features cold helium compressors of a type and size comparable to those required for the LHC, has also provided useful data and experience in this key technology.

2.5 Feeding and powering the LHC sectors

The progress in technical definition of the LHC has refined the equipment requirements for feeding and powering the strings of superconducting magnets in the LHC sectors from the cryogenic boxes and electrical power converters located in technical galleries or caverns. A proposed layout, meeting the requirements of the LHC sectors and compatible with a maximum reuse of the existing LEP infrastructure, is sketched in Figs. 7 to 14.

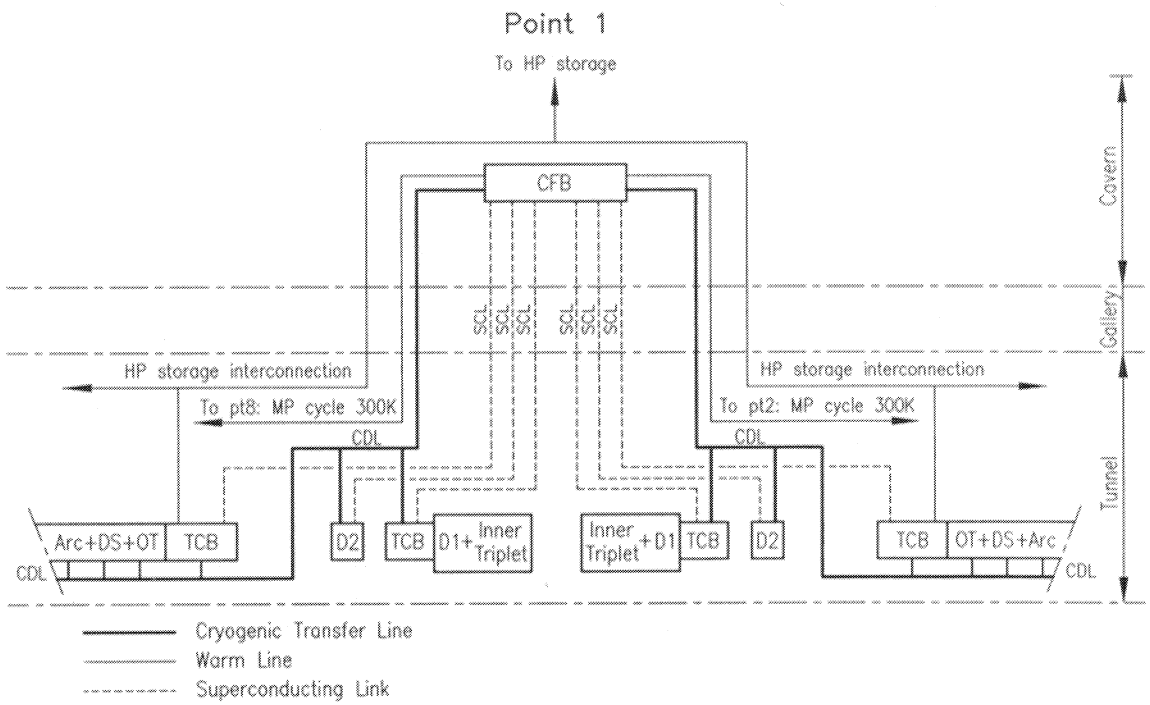

Figure 7: Layout of LHC sector feed at point 1

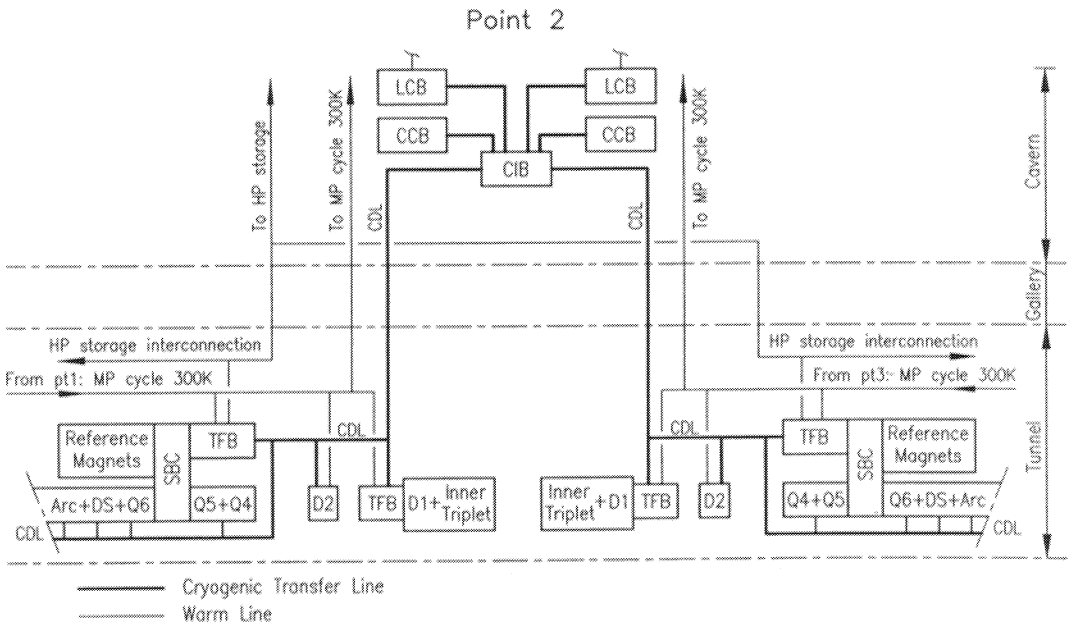

Figure 8: Layout of LHC sector feed at point 2

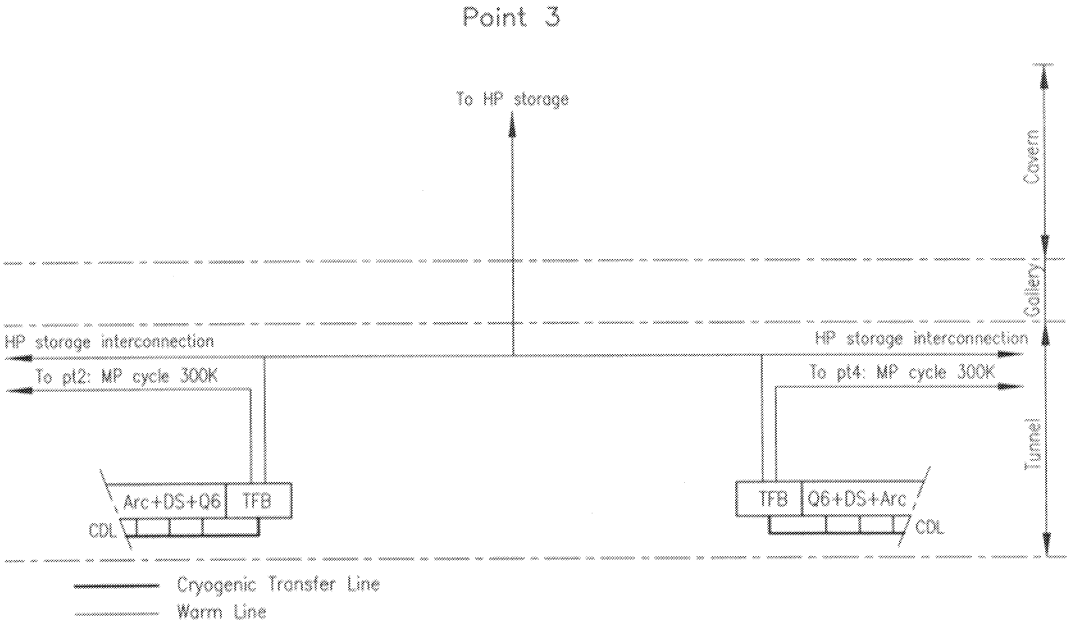

Figure 9: Layout of LHC sector feed at point 3

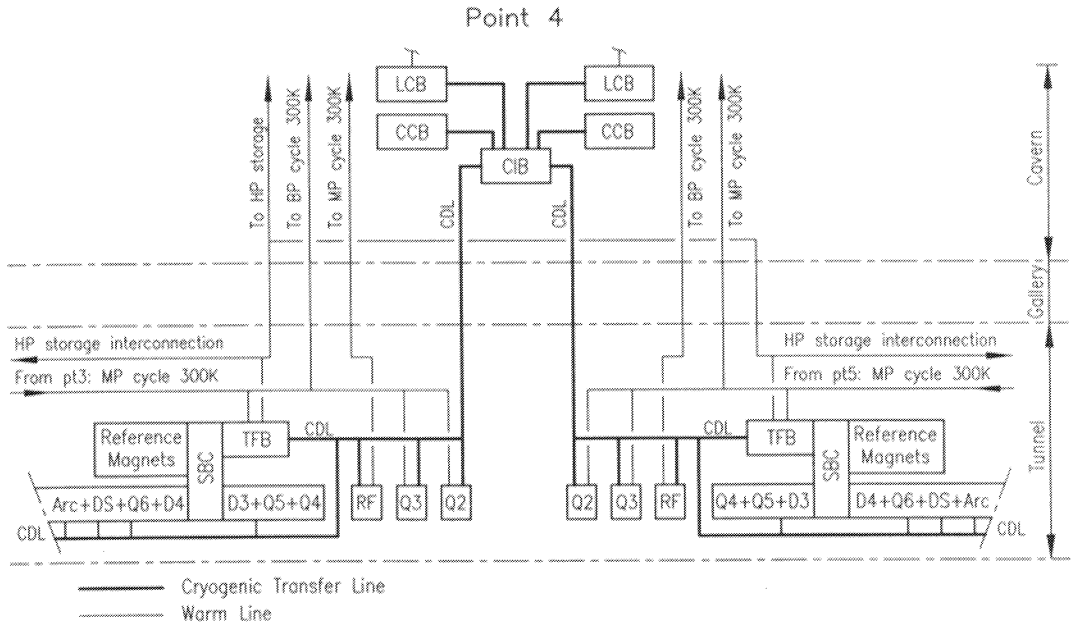

Figure 10: Layout of LHC sector feed at point 4

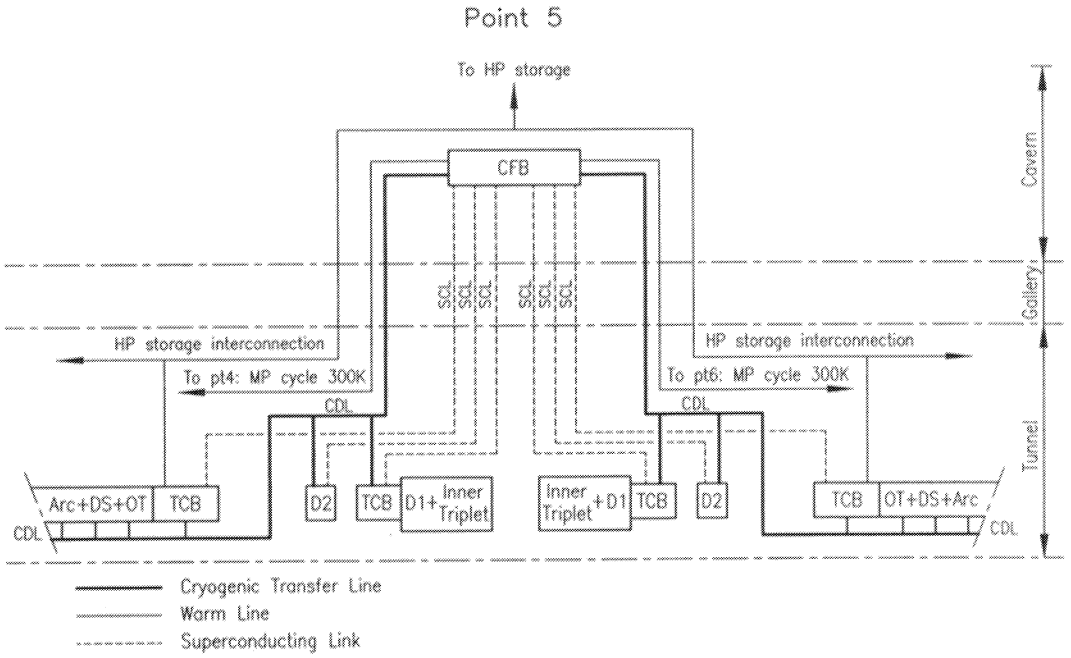

Figure 11: Layout of LHC sector feed at point 5

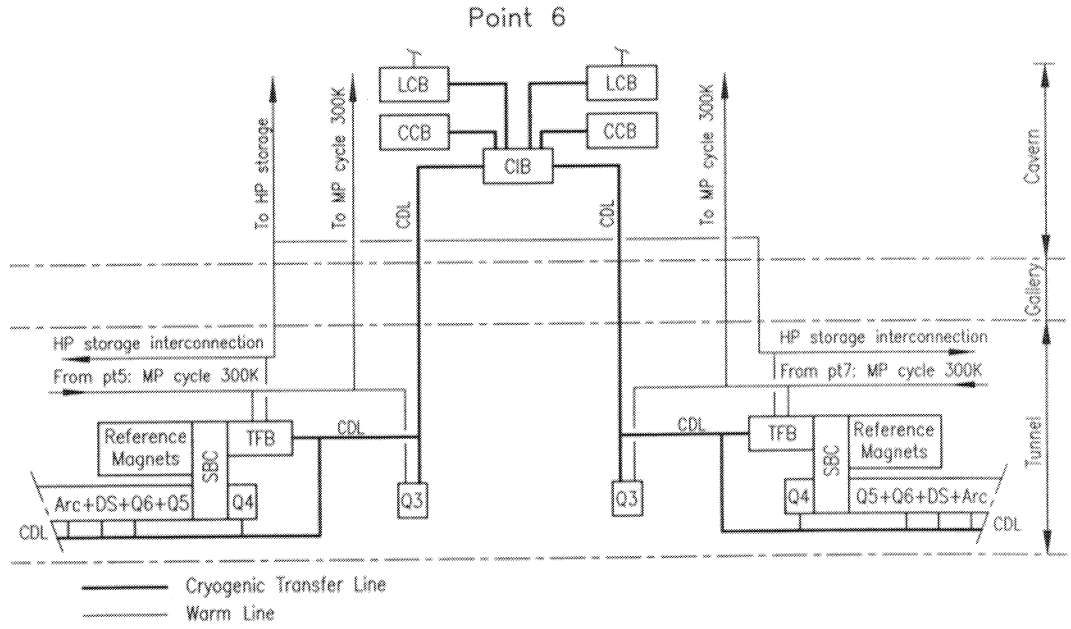

Figure 12: Layout of LHC sector feed at point 6

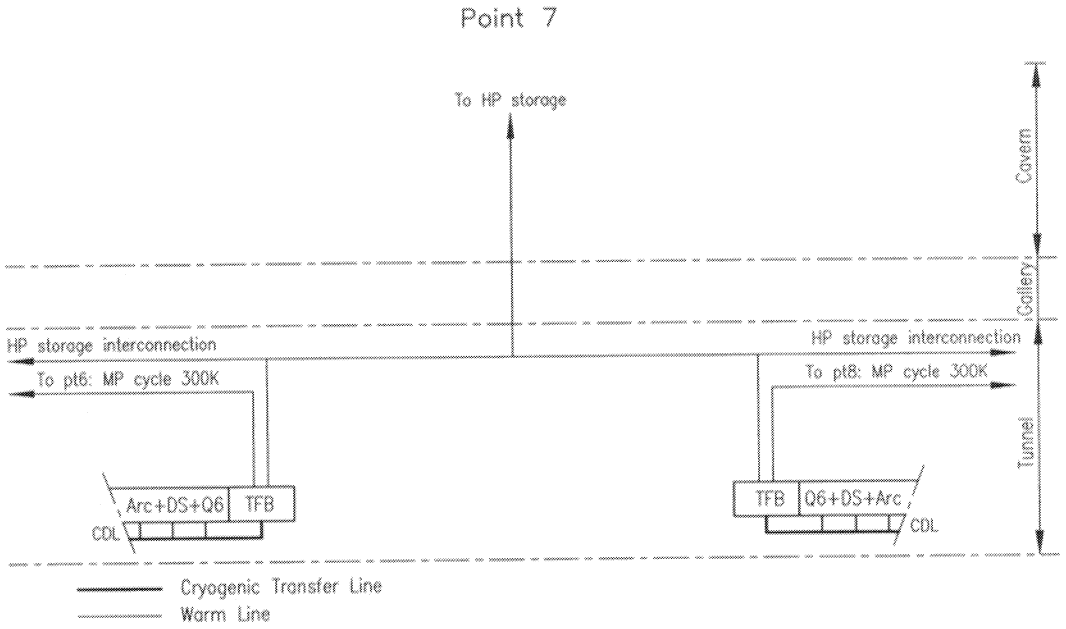

Figure 13: Layout of LHC sector feed at point 7

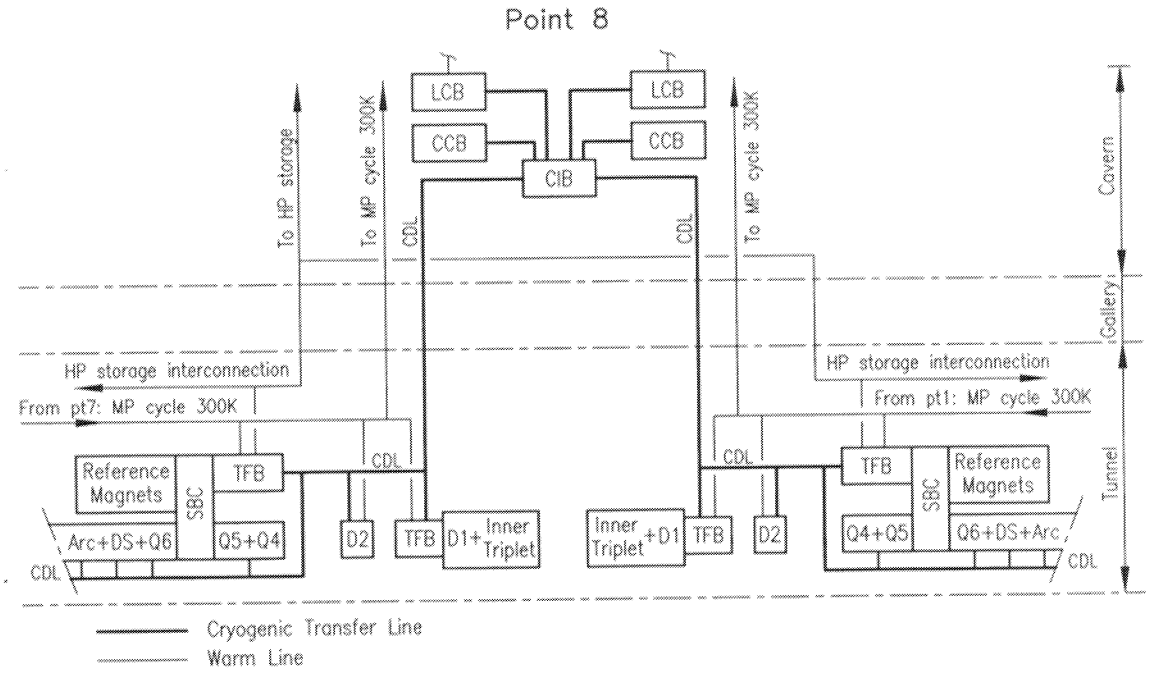

Figure 14: Layout of LHC sector feed at point 8

At every even-numbered point, CDLs connect the cryogenic sectors to the CIB, which constitutes the primary interface with the cryogenic refrigerator. In these insertions, which feature technical galleries paralleling the machine tunnel over the length of the long straight sections, the electrical power converters can be located close to the Tunnel Feed Boxes (TFB), which are used to terminate the magnet strings. Superconducting Bus Cryostats (SBC) are required to bridge the short strings of reference magnets to the main strings in the machine tunnel. At Points 1 and 5, the power converters can be located at the closest in the central cavern, thus requiring the use of d.c. superconducting links (SCL), terminating in Tunnel Connection Boxes (TCB) at one end, and a Cavern Current Feed Box (CFB) housing HTS current leads at the other end. Conceptual design studies of these components have permitted a first assessment of their complexity, space occupancy, and cooling requirements, but further work is required — in particular, the construction and testing of prototypes — to fully validate the system.

2.6 Helium inventory

A more precise assessment of the helium inventory in the LHC [34] has led to a total amount of 93500 kg, mostly in the cold mass of the magnet system (Fig. 15). Integrally storing this inventory in conventional form — i.e. gas at 2 MPa and 300 K — would result in large investment costs and siting difficulties due to the high visibility of the 250 m^3 reservoirs envisaged for the purpose [35]. Two complementary lines of action are being pursued in order to alleviate the burden of the LHC helium storage problem:

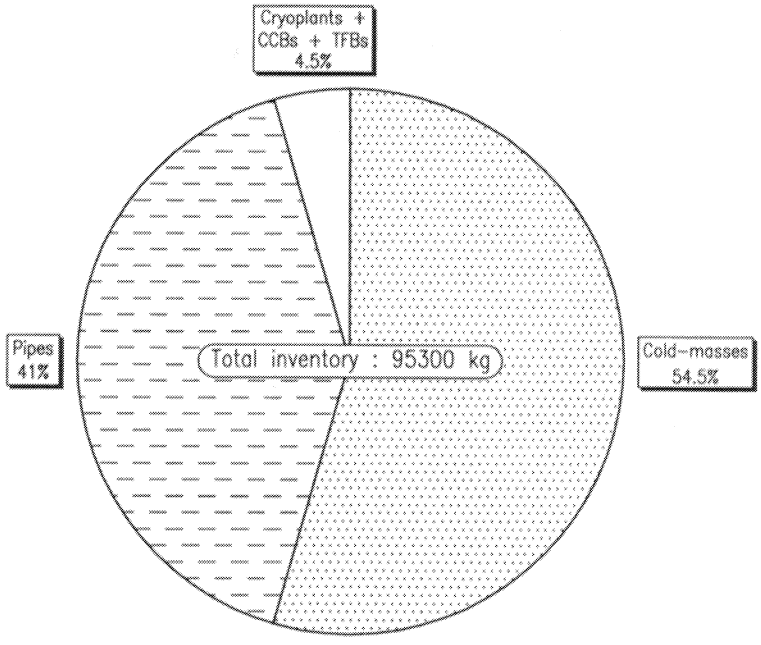

Figure 15: Repartition of the helium inventory in the LHC

- reduction of the helium stored inside the magnet cold mass to the minimum required for thermal buffering of rapid thermal transients and for conductive heat transport in pressurized superfluid helium towards the heat exchanger cold source;
- partial storage in liquid form, in a central storage or in standard 11000 gallon (about 40 m^3) industrial containers compatible with liquid helium handling by European distributors.

In any case, a minimum amount of medium-pressure gas storage will need to be installed locally for operational flexibility, enabling in particular the immediate recovery of the helium discharged after the quench of a half-octant. A possible helium storage and inventory management scheme for the LHC is sketched in Fig. 16.

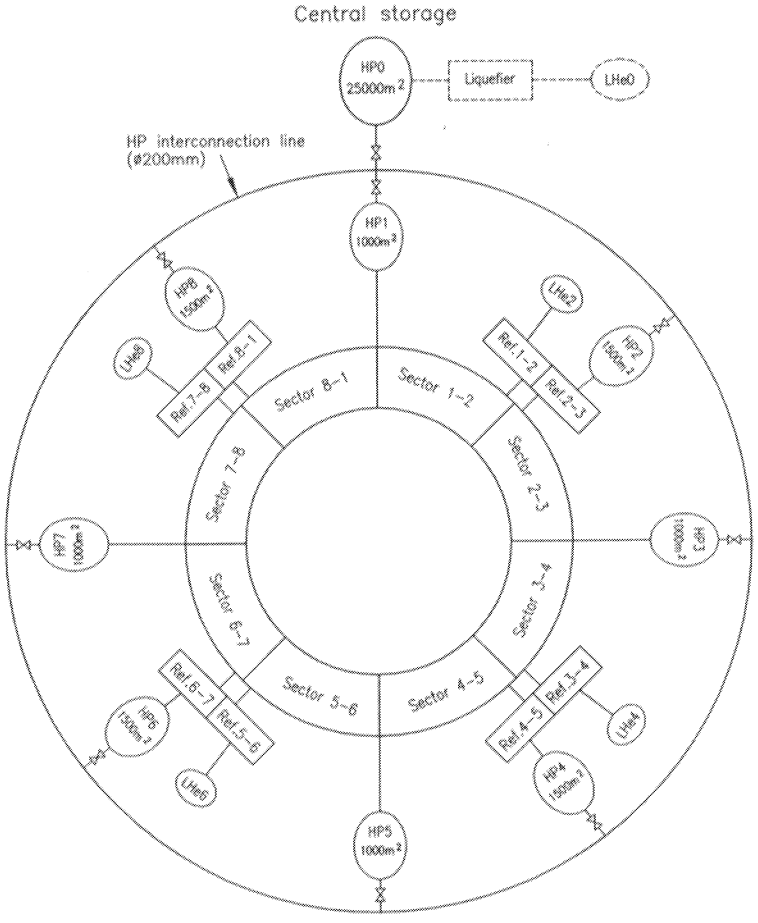

Figure 16: Storage and management of the LHC helium inventory

2.7 Instrumentation

The cryogenic operation of the LHC requires a large number of sensors, electronic conditioning units, and actuators, most of which will be located inside the machine tunnel and should therefore be radiation-resistant (Fig. 17). An inventory of the cryogenic instrumentation is shown in Table 12, Annex 4, and indicates the range and accuracy requirements for the whole data acquisition and processing chain. While a large number of sensors and actuators in this table are commercially available, specific development and qualification is required for others, in particular thermometers.

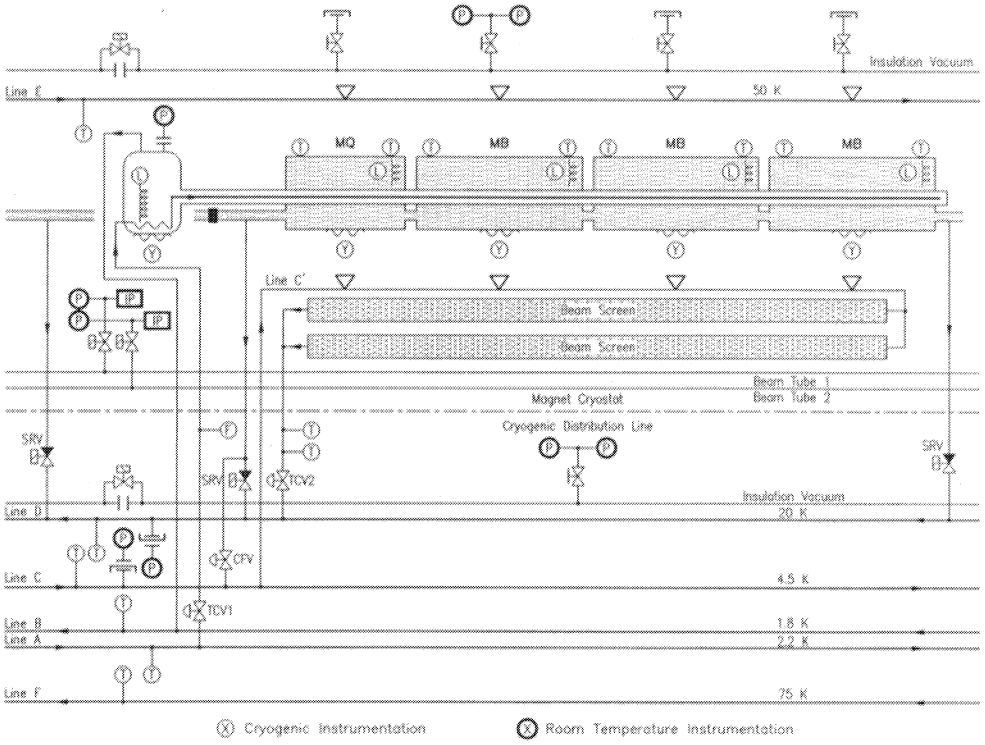

Figure 17: Layout of cryogenic instrumentation in an LHC half-cell

Cryogenic thermometry below 25 K employs sensors with a large scatter in their characteristics, thus requiring individual calibration. A strong effort is underway to improve temperature measurement in vacuum by developing a new type of thermometric block [36] to investigate the different types of commercially available temperature sensors suitable for the requirements and environment of the LHC. A similar effort is underway to design and maintain calibration facilities capable of handling a large number of sensors and providing the requested accuracy, to develop an adequate data base for managing thermometer reception and calibration data over the lifetime of the project, and to conduct long-term stability studies.

The low signal amplitude obtained when measuring cryogenic temperatures requires signal amplification in close proximity to the sensors. It is therefore very important to investigate low-noise, radiation-hardened amplifiers for this purpose. In order to try and

reduce cabling costs, signal multiplexing techniques can be used for routing signals to the radiation-shielded alcoves where delicate process-control equipment will be located.

During final cool-down and normal operation of the LHC it is very important to know when the cryomagnet cold mass is completely filled with pressurized superfluid helium. This information could be obtained alternatively from a cryogenic pressure transducer, or a superconducting level indicator, and investigations are underway to select an adequate and robust device.

2.8 Technical variants under study

The system described above fully meets the design constraints and technical requirements established for LHC cryogenics, and may therefore be implemented with confidence. However, several technical variants, compatible with the basic design principles and presently under study, exhibit a strong potential for simplifying the layout, improving efficiency and performance, as well as reducing costs. Examples of such variants are given below.

Operating the two-phase helium II heat exchanger tube in counter-current as well as in co-current flow of liquid and vapour would bring complete symmetry in the cryogenic layout of the half-cell cooling loop, independent of the tunnel slope. This mode of operation will be tested in the second phase of the LHC prototype string, and its limits investigated in the thermohydraulic test loop at CEA Grenoble (France).

Grouping all cryogenic headers in the CDL separately from the magnet cryostats, opens the way for finer sectorization of the LHC, an issue which could greatly shorten time spans for warm-up and cool-down of limited stretches of magnets to be replaced or repaired, and thus contribute to improving the availability of the LHC for physics.

Developing technology and establishing the performance and efficiency of several competing solutions for key cryogenic components, such as helium heat exchangers and compressors , over the useful ranges in the pressure and temperature domains, will allow the optimization of the thermodynamic cycles for large-capacity refrigeration at 1.8 K. This could lead to solutions based on cold, warm, or mixed compression schemes, which may prove more economical or easier to operate and interface with the 4.5 K refrigerators. This topic constitutes the subject of an ongoing R&D programme conducted in collaboration with CEA (France).

References

[1] The LHC Study Group, Design study of the Large Hadron Collider (LHC), CERN Report 91–03 (1991).

[2] The LHC Study Group, The Large Hadron Collider, Accelerator Project, eds. Y. Baconnier, G. Brianti, Ph. Lebrun, A. Mathewson and R. Perin, CERN/AC/93–03 (LHC) Report (1993).

[3] Ph. Lebrun, Superfluid Helium Cryogenics for the Large Hadron Collider Project at CERN, Cryogenics **34**, ICEC Supplement (1994) pp. 1–8, LHC Note 274.

[4] M. Barranco-Luque, J.P. Dauvergne, W. Erdt, P. Frandsen, D. Güsewell, F. Haug, A. Juillerat, G. Passardi, J. Schmid, G. Winkler, The refrigeration system for the LEP upgrade, Cryogenics **30**, September Supplement (1990) pp. 136–142.

[5] S. Claudet, W.K. Erdt, P.K. Frandsen, Ph. Gayet, N.O. Solheim and G. Winkler, Four 12kW/4.5 K Cryoplants at CERN, Cryogenics **34**, ICEC Supplement (1994) pp. 99–102.

[6] L. Tavian, Abaissement de la température de fonctionnement du LHC de 1.9 K à 1.8 K: faisabilité et implications, Note LHC 154 (1991).

[7] J.C. Brunet, J. Kerby, Ph. Lebrun, P. Rohmig, B. Szeless and L.R. Williams, Design of LHC prototype dipole cryostats, Cryogenics **32**, ICEC Supplement, 1992, pp. 191–194, LHC Note 195 (1992).

[8] B. Jenny, W. Cameron, G. Riddone, P. Rohmig and R. van Weelderen, Design and construction of a prototype superfluid helium cryostat for the short straight sections of the CERN Large Hadron Collider, Adv. Cryo. Eng. **39A** (1994) pp. 663–670, LHC Note 237 (1993).

[9] G. Riddone, Bilancio Termico della Semicella Prototipo dell'Acceleratore di Particelle LHC, Tesi di Laurea in Ingegnera Nucleare, Politecnico di Torino (1993).

[10] Ph. Lebrun, L. Mazzone, V. Sergo and B. Vullierme, Investigation and qualification of thermal insulation systems between 80 K and 4.2 K, Cryogenics **32**, ICMC Supplement, pp. 44–47, LHC Note 189 (1992).

[11] V. Benda, Ph. Lebrun, L. Mazzone, V. Sergo and B. Vullierme, Qualification of multilayer insulation systems between 80 K and 4.2 K, Proc. Kriogenika'94 Usti nad Labem (1994) pp. 107–110.

[12] H. Danielsson, Ph. Lebrun and J.M. Rieubland, Precision heat inleak measurements on cryogenic components at 80 K, 4.2 K and 1.8 K, Cryogenics **32**, ICEC Supplement, 1992, pp. 215–218, LHC Note 190 (1992).

[13] M. Blin, H. Danielsson, B. Evans, M. Mathieu, Design, construction and performance of magnet support posts for the Large Hadron Collider, Adv. Cryo. Eng. **39A** (1994) pp. 671–677, LHC Note 235 (1993).

[14] H. Danielsson, G. Ferlin, B. Jenninger, C. Luguet, S.E. Milner and J.M. Rieubland, Cryogenic performance of a superfluid helium relief valve for the LHC superconducting magnets, paper presented at CEC'95 Columbus (1995).

[15] M. Granier, Ph. Lebrun, M. Mischiatti, Design and construction of a superfluid helium cryostat for a ten-meter long high-field superconducting dipole magnet, Cryogenics **30**, September Supplement (1990) pp. 98–102.

[16] M. Granier, D. Hagedorn, K.N. Henrichsen, Ph. Lebrun, D. Leroy, R. Perin, J. Vlogaert, J. Deregel, P. Genevey, J.P. Jacquemin, F. Kircher, J. Le Bars, Performance of the twin-aperture dipole for the CERN LHC, Proc. EPAC'92 Berlin, eds H. Henke, H. Homeyer and C. Petit-Jean-Genaz (Ed. Frontières, Gif-sur-Yvette, 1992) pp. 1414–1416, LHC Note 179 (1992).

[17] J. Deregel, P. Genevey, J.P. Jacquemin, F. Kircher, J. Le Bars, A. Le Coroller, K.N. Henrichsen, Ph. Lebrun, J. Vlogaert, Cryogenic and magnetic tests of the twin-aperture prototype dipole in the Saclay Test facility, IEEE Trans. Appl. Supercond. **3** (1993) pp. 777–780.

[18] L. Rossi, V. Sergo, B. Szeless, L. Tavian, B. Vullierme, R. van Weelderen and L. Williams, Thermal behaviour and cryogenic performance of the first CERN/INFN prototype dipole cryomagnet for the CERN LHC project, Cryogenics **34**, ICEC Supplement, 1994, pp. 697–700, LHC Note 270 (1994).

[19] V. Benda, L. Dufay, G. Ferlin, Ph. Lebrun, J.M. Rieubland, G. Riddone, B. Szeless, L. Tavian and L.R. Williams, Measurement and analysis of thermal performance of LHC prototype dipole cryostats, paper presented at CEC'95 Columbus (1995).

[20] A. Bézaguet, J. Casas-Cubillos, B. Flemsaeter, B. Gaillard-Grenadier, Th. Goiffon, H. Guinaudeau, Ph. Lebrun, M. Marquet, L. Serio, A. Suraci, L. Tavian and R. van Weelderen, The superfluid helium cryogenic system for the LHC Test String: design, construction and first operation, paper presented at CEC'95 Columbus (1995).

[21] L. Dufay, G. Ferlin, Ph. Lebrun, G. Riddone, J.M. Rieubland, A. Rijllart, B. Szeless and L. Williams, A full-scale thermal model of a prototype dipole cryomagnet for the CERN LHC project, Cryogenics **34**, ICEC Supplement, 1994, pp. 693–696, LHC Note 271 (1994).

[22] P. Lefèvre and T. Pettersson, Review of energy deposition for cryogenics and vacuum estimations, summary of meeting held on 22 March 1995.

[23] Ph. Lebrun, Th. Wahlström, R. van Weelderen and L.R. Williams, Investigation of quench pressure transients in the LHC superconducting magnets, Cryogenics **34**, ICEC Supplement, 1994, pp. 705–708, LHC Note 272 (1994).

[24] G. Gerin, B. Vullierme and R. van Weelderen, Measurement of the thermo-hydraulic behaviour of LHC dipole prototypes after quench, paper presented at CEC'95 Columbus (1995).

[25] L. Brue, Modélisation thermohydraulique des écoulements transitoires d'hélium cryogénique induits dans la ligne de récupération du demi-octant par les transitions résistives des aimants du LHC, Note LHC 262 (1994).

[26] A. Cyvoct, Ph. Lebrun, M. Marquet, L. Tavian, R. van Weelderen, Heated two-phase flow of saturated helium II over a length of 24 m, LHC Note 169 (1991).

[27] J. Casas-Cubillos, A. Cyvoct, Ph. Lebrun, M. Marquet, L. Tavian and R. van Weelderen, Design concept and first experimental validation of the superfluid helium system for the Large Hadron Collider (LHC) project at CERN, Cryogenics **32**, ICEC Supplement, 1992, pp. 118–121, LHC Note 191 (1992).

[28] A. Bézaguet, J. Casas-Cubillos, Ph. Lebrun, M. Marquet, L. Tavian, R. van Weelderen, The superfluid helium model cryoloop for the CERN Large Hadron Collider (LHC), Adv. Cryo. Eng. **39A** (1994) pp. 649–656, LHC Note 233. (1993)

[29] J. Casas-Cubillos and R. van Weelderen, Modèle de simulation de la dynamique du transfert de chaleur dans une boucle cryogénique d'hélium superfluide, Note LHC 223 (1993).

[30] B. Flemsaeter, Contribution to the dynamic analysis and optimal control of the superfluid helium cooling loop for the LHC magnet string, Diploma Thesis, Norwegian Institute of Technology, Trondheim (1995).

[31] L. Tavian, Utilisation des réfrigérateurs LEP200 pour LHC: conditions de fonctionnement et interfaces, Note LHC 164 (1991).

[32] J.Ph. Guignard, Contribution à l'étude de la stabilité de fonctionnement et de l'adaptation de charge des compresseurs centrifuges cryogéniques multiétages, Travail d'option 'Machines-Energétique', Ecole des Mines de Paris (1993).

[33] C.H. Rode, CEBAF cryogenic system, paper presented at PAC'95, Dallas (1995).

[34] L. Tavian, Stockage hélium et interconnexion des différents points du système cryogénique du LHC, Note LHC 198 (1992).

[35] B. Bianchi, A. Dagan, G. Mazzone, R. Principe, A. Scaramelli, L. Tavian, Compte rendu du groupe de travail pour le stockage de l'hélium du LHC, Communication privée (1992).

[36] C. Balle and J. Casas-Cubillos, Industrial-type cryogenic thermometer with built-in heat interception, paper presented at CEC'95 Columbus (1995).

3 LHC Vacuum

3.1 Introduction

With the present design energy of 7.0 TeV, combined with a bending radius of 2784.32 m, the critical energy of the synchrotron radiation emitted by the protons is 44.1 eV. At the maximum current of 536 mA, each beam will emit a power of 0.206 Wm^{-1} and a photon flux of 9.44 10^{16} photons s^{-1} m^{-1}.

The total synchrotron radiation power emitted by the two beams is 0.41 Wm^{-1}. This, combined with the resistive wall power loss of similar value for the two beam tubes, would be an excessive heat load for a 1.9 K system. Thus a so-called beam screen, maintained at a temperature between 5 K and 20 K by gaseous helium flow, is inserted inside the magnet cold bore to intercept this power.

The synchrotron radiation photons incident on the beam screen will desorb gas molecules from the near surface layer (primary desorption) which will then be cryopumped again onto the same surface. These physisorbed molecules are rather loosely bound to the surface and easily re-desorbed by the photons (secondary desorption). In addition, more and more gas may build up on the surface of the screen until, when a monolayer or so is exceeded, the thermal vapour pressure of the H_2 component will increase rapidly to a level incompatible with the required beam–gas lifetime of 100 h. The ion-induced desorption yields from this condensed gas layer also increase with increasing quantity — yet again deteriorating the vacuum. Cryopumping on the beam screen alone will be insufficient to meet the beam vacuum requirements for long periods of operation.

In order to limit the pressure increase due to the above effects, the beam screen will be perforated over a few per cent of its surface, to allow pumping by the 1.9 K cold bore surface where the vapour pressure of all gases (except He) is negligible and the condensed gas is shielded from synchrotron radiation and ion bombardment.

3.2 Beam screen design

A more realistic estimation of the mechanical tolerances in the magnet assemblies and a review of the beam optics requirements, in particular for the beam cleaning system, have revealed that the available aperture in the previous square section beam screen [1] was not optimized [2].

The present design of the LHC beam screen is now based on a 1 mm thick stainless steel tube with a round cross-section, flattened top and bottom. This gives an enlarged aperture for beam halo particles at 45°. The new shape is also less sensitive to alignment errors and gives the same horizontal aperture of 44 mm, but a reduced vertical aperture of 36 mm. The space between it and the surrounding 1.9 K cold bore is just sufficient for the supports and the cooling pipes (fixed to the outside) which maintain the screen temperature between 5 K and 20 K. This is shown schematically in Fig. 1 and the cross-section with dimensions are given in Fig 2.

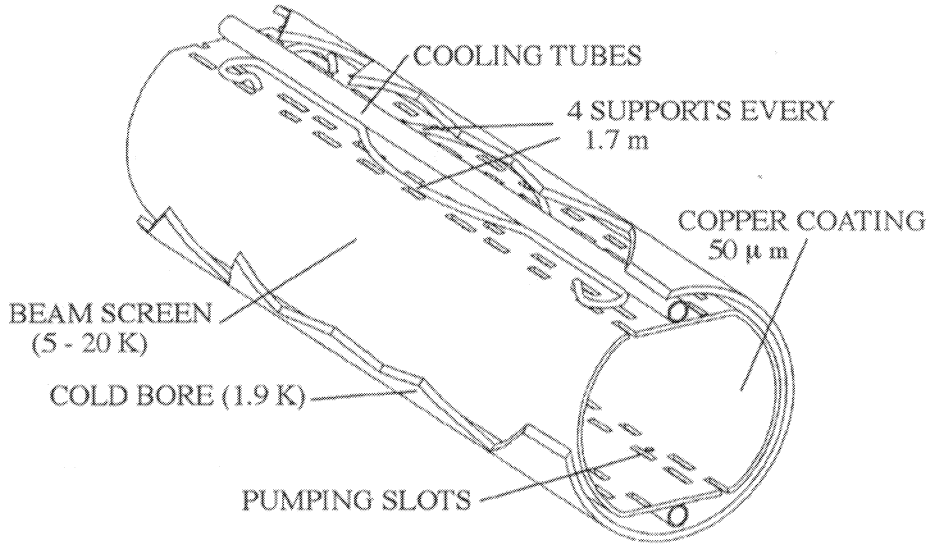

Figure 1: A schematic view of the beam screen showing the supports, the cooling pipes and the slots

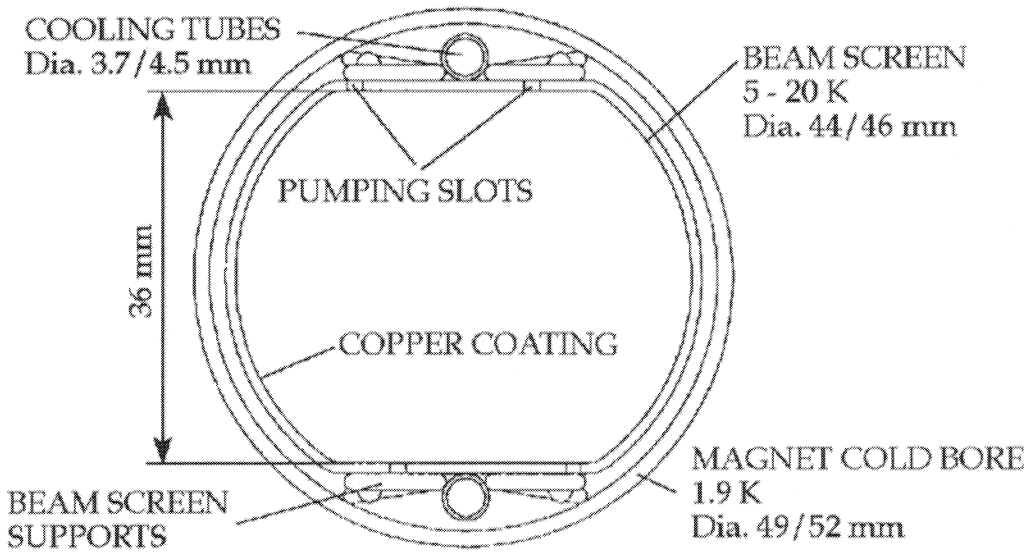

Figure 2: A cross-section of the beam screen showing the principal dimensions

To minimize the beam coupling impedance of the screen the interior surface must have a high electrical conductivity. A suitable material is copper, which can be deposited either by electroplating [3] or in bulk form by an overlay process [4].

Detailed studies of the manufacturing steps reveal that the overlay method will necessitate making the beam screen from two plates forming half shells, and then welding them together. If the screen were to be electroplated, starting from either half shells or a complete square section tube which could be deformed to give the flat top and bottom, would be possible. The final choice will be based on the manufacturing process that meets the required specifications at the lowest cost.

3.3 Pumping holes

The pumping holes in the beam screen represent discontinuities for the image currents of the beam and result in an increased beam-coupling impedance. An additional effect in the high frequency range comes from the real part of the impedance. Power is coupled through the holes into the coaxial space between the beam screen and the vacuum chamber and propagates in synchronism with the beam. This gradually builds up in strength and leaks back into the beam screen, further adding to the real part of the coupling impedance.

A suitable pumping hole shape which minimizes the impedance for a given pumping area is that of a slot with rounded ends. In order to avoid any contribution to the impedance from trapped modes, the length and position of the slots will be randomized [5]. This randomization of the slot length leads to a frequency spread and thus to an effective detuning of possible trapped modes, which have been theoretically predicted to appear just below the screen cut-off frequency and are potentially dangerous for beam stability. An equivalent mechanism to reduce the effective impedance of these modes would be to introduce a random variation (at the per mil level) in the transverse dimensions of the beam screen.

A randomization of the slot spacing helps to suppress higher frequency modes associated with the slot periodicity. In particular, it reduces the forward- and backward-scattered power both within the beam screen and in the outer coaxial region between the screen and the cold bore.

Theoretical and experimental investigations are continuing in order to clarify the role of trapped modes and the penetration of beam-induced microwave power through the slots.

The current design has 4.4% of the total beam screen surface perforated by eight rows of lengthwise slots of width 1.5 mm, and length (8 + x) mm, with x randomly distributed in the interval (–2, 2) and longitudinally spaced by (16 + y) mm between the axes of the slots, and with y randomly distributed in the interval (–2, 2). This pattern will be repeated every 500 mm, with a distance of (20 + z) mm between sets of slots where z is randomly distributed in the interval (–10, 10).

3.4 Beam screen vacuum behaviour

The vacuum behaviour of the perforated beam screen is now better understood [6] and to illustrate this we consider one metre of screen: assume that only H_2 is desorbed by the photons, and that the beam screen temperature is less than 20 K and hence some H_2 is cryopumped.

Let the total cryopumping speed of the inner beam screen wall and holes together be S (l s^{-1} m^{-1}) and the conductance of the holes alone be s (l s^{-1} m^{-1}), with s typically 4.4% S. The gas load pumped by the holes is Ps (molecules s^{-1} m^{-1}), where P (molecules ℓ^{-1}) is the gas density in the beam screen, i.e. the amount of gas passing through the holes is proportional to P.

It is the gas density which interests the storage ring vacuum system builder since it is the molecular density encountered by the circulating beam which scatters the particles and, with time, gradually reduces the beam intensity.

Although most ultra-high vacuum gauges actually measure the molecular density, conventionally they are calibrated in pressure, which is a force per unit area. If the temperature T (K) of the molecules is known, the pressure can always be converted to density and vice versa using the relationship

$$1 \text{ Torr is equivalent to } 9.65\ 10^{21}/\mathrm{T} \text{ molecules } \mathrm{l}^{-1} \ .$$

The synchrotron radiation photon flux Γ (photons s^{-1} m^{-1}) incident on the wall gives rise to a desorbed molecular flux $\eta\Gamma$ (molecules s^{-1} m^{-1}), where η (molecules photon^{-1}) is the photon-induced gas desorption yield. Therefore when the synchrotron radiation is first switched on the initial gas density, P_i in the beam screen is given by

$$P_i = \eta\Gamma/S \text{ (molecules } \ell^{-1}) \ .$$

As the photon-induced desorption continues, and H_2 molecules are pumped (cryosorbed) on the wall, the gas density increases as a result of both the thermal vapour pressure and the redesorption by photons from this physisorbed surface layer. With increasing density (P), the amount of gas removed by the holes also increases, since it is directly proportional to P, and an equilibrium P_e is reached when the incoming gas is all removed by the holes — i.e. when

$$P_e s = \eta\Gamma$$

and the gas density therefore increases to

$$P_e = \eta\Gamma/s \text{ (molecules } \ell^{-1}) \ .$$

The final gas density therefore stabilizes at $P_e = P_i S/s$ which, if s = 0.044 S, is a factor of 22.7 above that of the initial density. However, S depends on the sticking coefficient for the gas on the cold surface, which can be < 1. Thus the factor S/s may be much less and the initial gas density, P_i, higher, but the limiting density will be unchanged.

The holes in the beam screen are therefore a way of limiting the pressure (density) increases, and if the conductance of holes is sufficient and the primary desorption yields are low enough the resulting beam–gas lifetimes may be acceptable.

Without the beam screen the H_2 pressure (density) would increase almost without limit due to the interplay of the various desorption mechanisms (in particular secondary photon and ion-induced desorption) with the progressive build-up of the primary desorbed gas on the now exposed cold bore surface.

3.5 Photon-induced desorption yields

Until now, almost all measurements of photon-induced desorption yields have been made at room temperature, but in the LHC the desorbing surfaces are at a temperature between 5 K and 20 K. Moreover, in warm systems the secondary desorption effects from the accumulation of a condensed layer are completely absent.

In order to quantify the desorption yields at temperatures below ambient and verify the predicted vacuum behaviour, a collaboration was arranged with the Budker Institute for Nuclear Physics, in Novosibirsk, Russia to make the necessary measurements at cryogenic temperatures and at a critical energy as close as possible to that of the 44.1 eV in the LHC. A specially designed cryostat was installed on a dedicated beam line on the VEPP 2M Electron Storage Ring [7], which was run at an energy of 300 MeV corresponding to a critical energy of 50 eV.

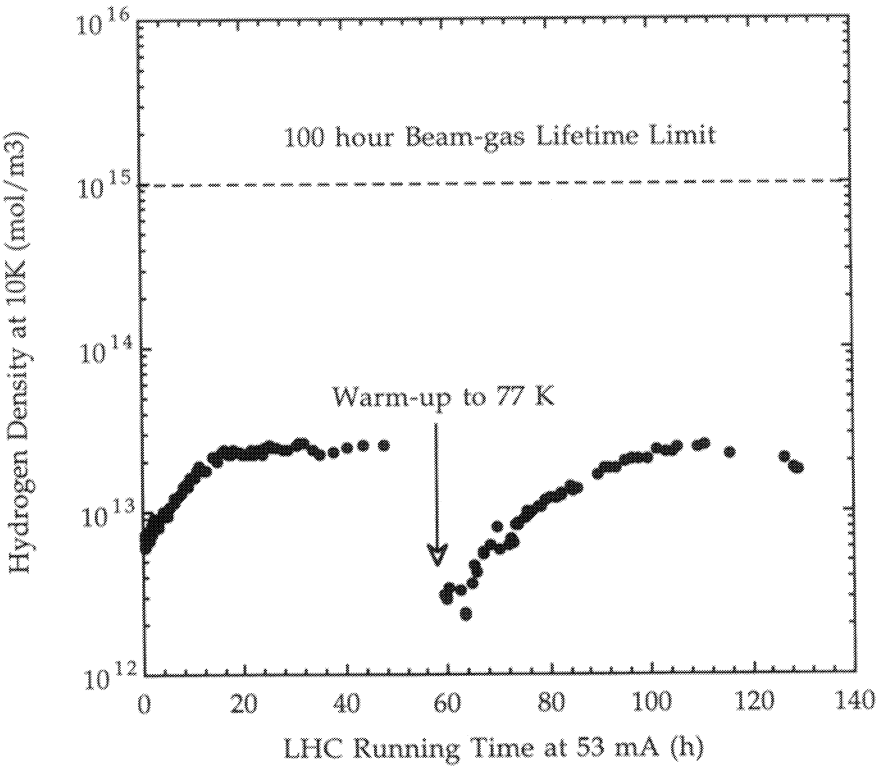

Figure 3: The H_2 density in the LHC as a function of the running time with 53 mA beam current and a 10 K beam screen with 2% pumping holes surrounded by a 3 K 'cold bore'

The results of the desorption yield measurements at 10 K from a prototype beam screen which consisted of a perforated 1 m long square section 304L stainless steel tube (38 mm × 38 mm diagonally), with strips of Cu 0.2 mm thick and 18 mm wide bonded to each of the flat sides are shown in Fig. 3. The perforations were in the form of slots 10 mm × 1 mm and covered 2% of the surface. The bonding was carried out by a skive inlay process [4]. The data were scaled to the LHC at 7.0 TeV and an initial beam current of

1/10 nominal, i.e. 53 mA. It can be seen that the limiting gas density for H_2 observed at 53 mA is well below the 100 h lifetime level. After removing the H_2 by warming to 77 K, the gas density returned, on irradiation, to the same limiting value. It must be remarked that this first Novosibirsk experiment was unable to detect CO and CO_2, and thus the desorption yields at cryogenic temperatures are still unknown. However, since these gases could dominate the beam–gas lifetime due to their high nuclear scattering cross-section, further measurements will be undertaken.

3.6 Adsorption isotherms

The adsorption isotherms of H_2 and mixtures of H_2 with CH_4, CO and CO_2, the gases desorbed by the synchrotron radiation, have been measured at 4.2 K [8]. The results are shown in Fig. 4 for pure H_2 and various concentrations of CO_2. Similar results have been obtained for mixtures containing CH_4 and CO. In general, the addition of a contaminating gas to pure H_2 at 4.2 K substantially reduces the saturated vapour pressure of the H_2.

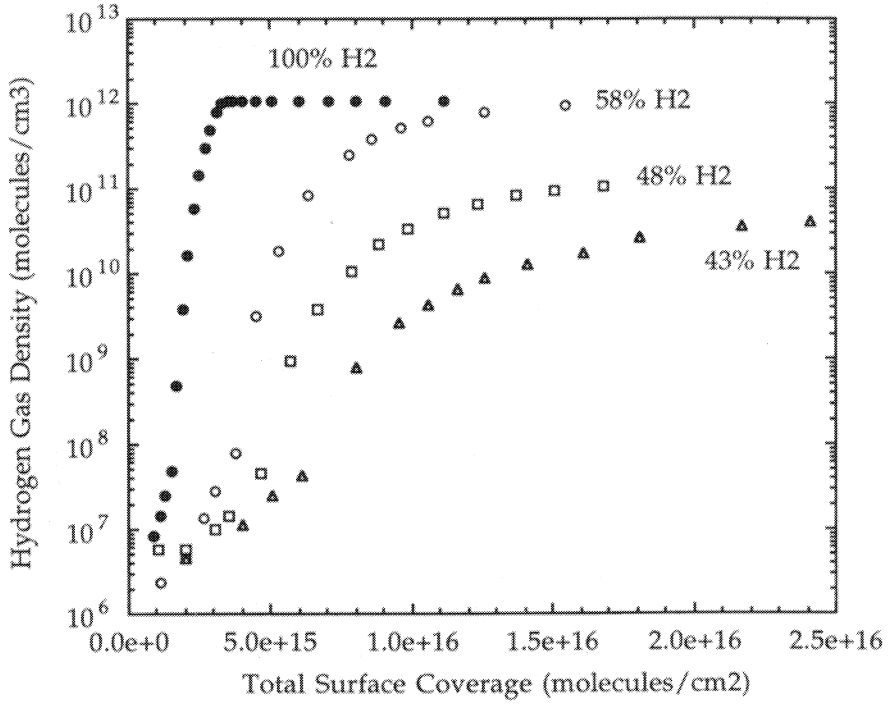

Figure 4: The adsorption isotherms at 4.2 K of pure H_2, and H_2 with various concentrations of CO_2

3.7 Stainless steel permeability

With the beam screen and its cooling pipes, top and bottom, it has been shown that a magnetic permeability of less than 1.005 (in the temperature range 5 K to 20 K) is necessary to avoid significant magnetic field distortion [9]. Since the conventional 300

series stainless steels have permeabilities well in excess of 1.005 at low temperature, several other grades of stainless steel containing high concentrations of Mn and giving acceptably low permeabilities are being evaluated for the construction of the beam screen. Taking into account the possible manufacturing steps, the weldability and magnetic properties of the welds in these steels are also being investigated.

3.8 Quench forces

A 1 m long square section beam screen with a complete internal Cu coating of 100 μm has been successfully tested in a short model dipole magnet. No damage occurred to the Cu layer or the screen after a total of 25 quenches from 8.5 T [10].

Revised estimates which mimimize the thickness of the Cu layer, and hence the quench-induced forces, have shown that 50 μm will be acceptable. Coating of the complete surface is necessary, except for two thin strips where half shells would be welded together. These resistive strips will also help to reduce eddy currents and magnetic field distortion during ramping [11].

3.9 String test experience

During the first few weeks of running the LHC string test with one quadrupole and two dipole magnets it was observed that the pressure in the beam vacuum, measured at room temperature, was in the low 10^{-9} Torr range. There was no beam screen installed in the 1.9 K cold bore tube. The actual pressure in the cold bore is certainly much lower than that indicated by the room temperature gauge [12].

The first pumpdown of the insulation vacuum from atmospheric pressure to 1 10^{-2} Torr, where the turbomolecular pumps can be turned on and an He leak detection started, was about 30 h. After a return to atmospheric pressure using dry N_2, the second pumpdown to the same level took only about 14 h.

In the insulation vacuum the total pressure before cool-down was in the low 10^{-4} Torr range and consisted mainly of H_2O. After cool-down, the total pressure, measured with gauges at room temperature, was in the low 10^{-6} Torr range and again consisted of H_2O [13, 14].

In order to define better the pressure in the insulation vacuum near to the 1.9 K magnet a Penning gauge has been mounted inside the 55–75 K thermal shield.

3.10 Measurement of pressure in cold beam tubes

The measurement of pressure or, to be more precise, gas density, in the cold parts of the beam vacuum system has always been considered to be problematic since all conventional measuring instruments have been designed to operate at room temperature and may dissipate a few watts.

The obvious solution of simply taking one of the conventional vacuum gauges mounted on a test vacuum chamber and immersing it all in liquid He at 4.2 K was tried and proved to be successful [12] in that the gauge head worked and gave meaningful readings. How-

ever, this particular gauge head dissipated almost 2 W, which of course was consequently absorbed by the liquid He.

A second, more elegant method of measuring the gas density in the beam vacuum consists of collecting the electron current produced by ionization of the residual gas using a system of biased electrodes placed at intervals around the ring [15]. The collected current is proportional to the gas density. For vacuum diagnostic purposes, a test proton beam could be debunched, the electron current (gas density) measured around the machine, and then this beam would be dumped. In addition to measuring the average residual gas density around the ring, this method could be used to detect He leaks long before they were able to be detected by the room temperature measuring devices placed at widely spaced intervals around the machine [16, 17]. Similar diagnostics have previously been used in the CERN Intersecting Storage Rings and Antiproton Accumulator.

3.11 Sector valves

To increase the reliability of the sector valves, a design with two sealing surfaces has been produced in collaboration with industry, for use at room temperature. A prototype was delivered and subjected to a series of opening and closing cycles without baking [18]. After 4300 cycles, leaks were observed on both valve seats. The valve was repaired and testing continued for a further 700 cycles to a total of 5000 cycles. It was then baked at 320°C for 24 h after which it was He leak tested every 300 cycles up to a total of 10000 cycles and no leaks $> 2\ 10^{-10}$ mbar l s^{-1} were detected.

3.12 Ongoing experimental and design programme

The measurement of the adsorption isotherms for H_2 and various gas mixtures is continuing at 4.2 K and will be extended to higher temperatures. In order to quantify the speed at which He from a leak will propagate along the 1.9 K cold bore tube [16, 17] measurements of this will be made in the LHC string.

To measure the desorption yields at the working temperature of the beam screen for all the desorbed gases and to verify the long-term vacuum behaviour of a beam screen under realistic working conditions — i.e. at a temperature of about 10 K with synchrotron radiation and a cold bore at 1.9 K, a full scale experiment is presently being designed. This will eventually be installed on a dedicated synchrotron radiation beam line on the CERN Electron Positron Accumulator (EPA) [19].

Work is also continuing on the effect of quench-induced forces on Cu-plated beam screen prototypes, complete with slots, in a 1 m model superconducting dipole.

Model beam screens have also been built to measure beam-coupling impedance parameters.

Design of the intermagnet connection with its bellows and RF bridge is also continuing. When completed, prototypes will be manufactured and mounted in a full-scale warm model complete with beam screen, cooling pipes and supports in the cold bore tube.

A set of square section screen tubes, cooling tubes and cold bore tubes in lengths up to 11 m have been delivered from industry. The resulting geometric tolerances have been checked and found to be within the required specification. These will be used to make

prototypes for testing the Cu plating process, perforating the pumping slots, fixing the cooling tubes, mounting the supports, and for the insertion of a complete beam screen in the cold bore with an intermagnet connection.

Fixing the He cooling pipes to the beam screen by laser welding has proved to be promising in that, compared to brazing or welding, little heat is transferred to the inner surface and this operation can therefore be carried out in air after the Cu plating process. Two 11 m long sample square section beam screens with laser-welded cooling tubes have been ordered from industry to check the reliability of the method and any adverse influence on the mechanical tolerances of the beam screen.

These tests on the square section tubes which are available now, and the techniques which are being investigated will give results which can be easily adapted to the beam screen in its revised form.

In parallel, strips of high Mn content stainless steel with the required magnetic properties have been ordered from industry with a view to testing the Cu plating properties of this steel and the Cu cladding process before fabricating prototype beam screens by forming and welding.

A summary of the vacuum equipment for the vacuum system in the cold arcs is given in Tables 1 and 2, Annex 5. Table 3, Annex 5, lists the vacuum equipment for the warm straight sections.

References

[1] B. Angerth, F. Bertinelli, J.-C. Brunet, R. Calder, F. Caspers, P. Cruikshank, J.-M. Dalin, O. Gröbner, N. Kos, A. Mathewson, A. Poncet, C. Reymermier, F. Ruggiero, T. Scholz, S. Sgobba and E. Wallén, The Large Hadron Collider Vacuum System, Particle Accelerator Conference, Dallas, May (1995).

[2] Y. Baconnier, J.-B. Jeanneret and A. Poncet, LHC Beam Aperture and Beam Screen Geometry, MT Division Internal Note, MT/95–11 (ESH), LHC Note 326, June (1995).

[3] J.Cl. Puippe and W. Saxer, Electrodeposition of Copper on the Internal Walls of Colliders in Beam tubes, Werner Flühmann AG, Ringstrasse 9, Dübendorf 1, CH-8600, Switzerland, XVth Int. Conf. on High Energy Accelerators, Hamburg, Germany, July 20–24, 1992, Supercollider 4, Edited by J. Nonte, Plenum Press, New York (1992).

[4] Technical Materials, Inc., 5 Wellington Road, Lincoln, Rhode Island, USA.

[5] S. Kurennoy, Trapped Modes in Waveguides with Many Small Discontinuities, Phys. Rev. **E51**, No. 5 (1995) 2498–2509.

[6] V.V. Anashin, G. Derevyankin, V.G. Dudnikov, O.B. Malyshev, V.N. Osipov, C.L. Foester, F.M. Jacobsen, M.W. Ruckman, M. Strongin, R. Kersevan, I.L. Maslennikov, W.C. Turner and W.A. Lanford, J. Vac. Sci. Technol. A (12) 4, 1663, July/August (1994).

[7] V.V. Anashin, O.B. Malyshev, V.N. Osipov, I.L. Maslennikov and W.C. Turner, J. Vac. Sci. Technol. A (12) 5, 2917, Sep/Oct (1994).

[8] E. Wallén (Note to be published).

[9] B. Angerth, F. Bertinelli, J.-C. Brunet, R. Calder, F. Caspers, O. Gröbner, A.G. Mathewson, A. Poncet, C. Reymermier, F. Ruggiero and R. Valbueno, Fourth European Particle Conference (EPAC 94), London, UK, July 1994 (World Scientific, Singapore, 1994).

[10] A. Jacquemod, M. Karppinen, A. Poncet, I. Vanenkov and R. Veness, MT Division Internal Note, MT–ESH/94–14, (1994).

[11] R. Wolf, Estimation of the Magnet Field due to Eddy Currents during Ramp in the LHC Dipole Spacers in the LHC Beam Screen, Magnet Group Internal Note 94–112, March 1995.

[12] V. Baglin, A. Grillot and A. Mathewson, Fonctionnement d'une jauge à ionisation à la température de l'hélium liquide, Vacuum Group Technical Note 95–01, January, 1995.

[13] G. Engelmann (private communication).

[14] P. Cruikshank (private communication).

[15] A. Poncet, Pressure MT Division Internal Note, MT/95–01, (ESH), LHC Note 316, March, (1995).

[16] D. Edwards Jr. and P. Limon, J. Vac. Sci. Technol., 15 (3), 1186 (1978).

[17] J.P. Hobson and K.M. Welch, J. Vac. Sci. Technol. **A11** (4), July/August 1993.

[18] M. Brouet, Acceptance Tests of the VAT Prototype Sector Valve for the LHC, Vacuum Group Technical Note 95–12, September, 1994.

[19] O. Gröbner, A.G. Mathewson and A. Poncet, A Synchrotron Radiation Beam Line Facility at EPA Dedicated to Photon Induced Neutral Gas Desorption Studies, Vacuum Group Technical Note 91–02, February, 1991.

4 Powering

4.1 Introduction

Recent studies have been directed towards the optimum use of the existing infrastructure of LEP, which is concentrated at the even points. This has become known as the 'four feed point' version. While LEP requires high voltage and low current for its loads, the LHC will require very large currents and rather small voltages, being a superconducting machine. Although it was relatively easy and inexpensive to install the power converters for LEP on the surface and cable them to their underground loads, such an approach would be prohibitive for the LHC because of the high d.c. currents. Fortunately, the LHC will not need the large RF complex used for LEP2, and neither will any future electron machine installed with the LHC. Thus the large RF galleries, parallel to the tunnel at the even points, can be vacated to allow the underground installation of high-current power converters very close to the current feedthroughs.

In the new powering scheme all the lattice elements are fed from the even points (Main Dipoles, Quadrupoles, Sextupoles, Octupoles and Spool Pieces), left and right, thus segmenting the machine into eight sections rather than the sixteen of the previous version. This eliminates the need for any lattice power converters at the odd points (Figs. 1, 2, 3 and 4). Furthermore, the main quadrupoles, MQD and MQF, have been separated from the dipole circuit so as to give more tune flexibility to the machine.

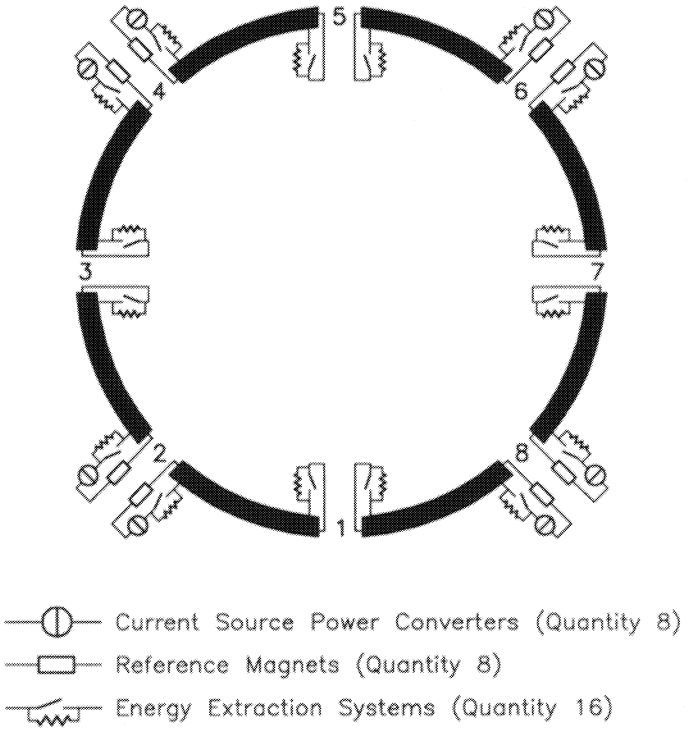

Figure 1: Main dipole circuits/segmentation by 8

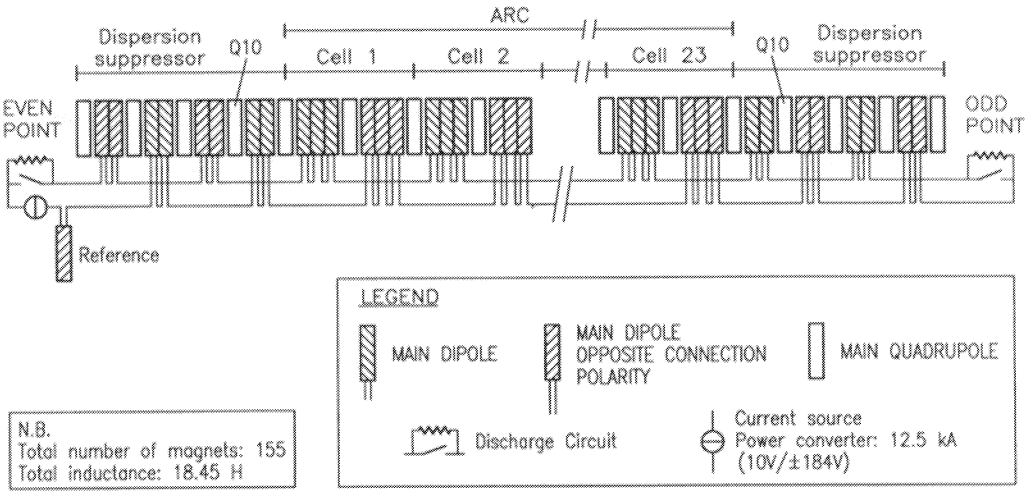

Figure 2: Main dipole powering scheme (for one sector)

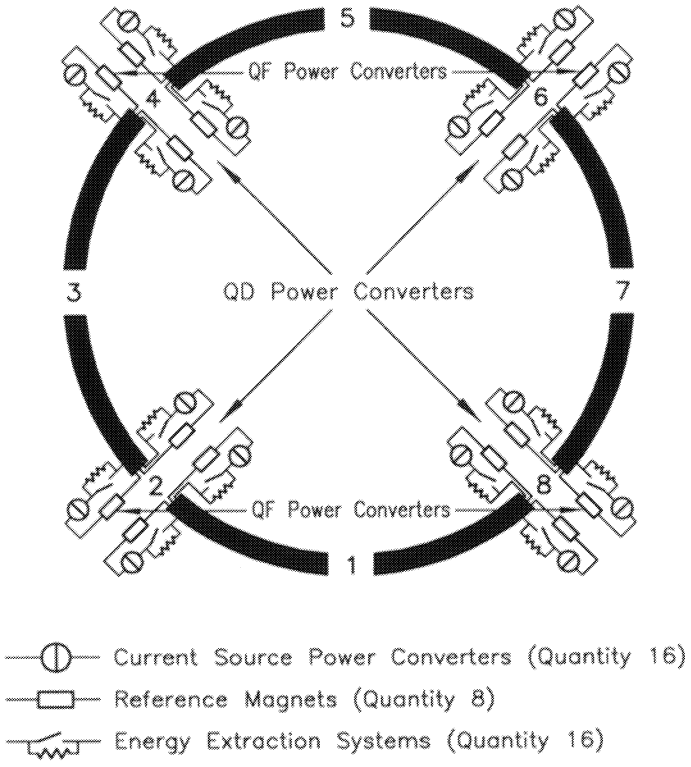

Figure 3: Main quadrupole circuits/segmentation by 8

This also minimizes installation at the odd points, since the bus-bars of the main quadrupoles (MQD and MQF) continue into the insertion regions and are used to power the quadrupoles of the dispersion suppressor and, where appropriate, other quadrupoles of the insertion (Fig. 4). Low-current trim quadrupoles, placed next to these quadrupoles, adjust the necessary overall field gradient. The associated small power converters can more easily be located underground at the odd points. In the cleaning insertions of points IR3 and IR7, the FODO cell and separators use warm magnets which will be powered from the surface using existing surface buildings and cabling of LEP.

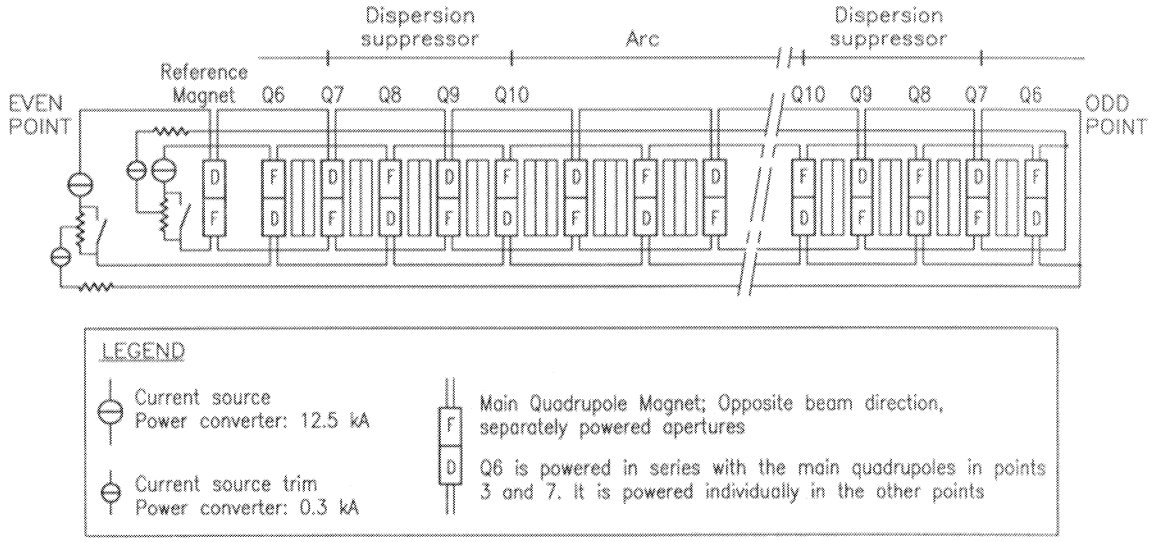

Figure 4: Main quadrupole powering scheme (for one sector)

During recent studies, the use of d.c. superconducting links has been considered wherever it was felt that they would be economically and technically feasible. However, the extent of their application will depend on more detailed studies, and precautions will be taken so that a fall-back solution is available should they prove too risky or too costly.

The main and perhaps only justification for their use comes from points 1 and 5, where the high-luminosity insertions of the experiments require individual powering of the outer triplets, situated 250 m from the intersection. To power these with warm connections, alcoves would need to be created at about 250 m on either side of the intersection point in order to house the high-current power converters. By using d.c. superconducting links, the current feedthroughs can be brought to the central area of the experiments, thus facilitating the installation of the power converters with other equipment in a common central cavern. This also allows some magnets to be connected in series, left and right, thus halving the number of power converters for these magnets. These superconducting links could be combined with the cryoline feeding the low-β magnets and the current feedbox thus giving an economical solution.

Points 3 and 7 have been specifically designed to need only low-current supplies so that conventional warm cabling can be used. The only justification for the use of a superconducting link at these points would be to reduce the segmentation of the lattice

circuits to four which at the moment is not considered feasible from a quench protection point of view.

For the even points the use of d.c. superconducting links is not justified, as the klystron galleries allow the power converters to be placed very close to the start of the machine cryostat, thus requiring very short warm connections to the current feedthroughs.

4.2 Powering of lattice circuits

All lattice circuits are powered, left and right, from the even points. Table 9, Annex 6 gives the circuits, ratings and locations of all the lattice circuits.

4.2.1 The main dipoles

One sector (1/8 of the machine) of the main dipole circuit is shown in Fig. 2. The eight current source power converters are placed at points 2, 4, 6 and 8 (Fig. 1). The total inductance of a sector is about 18 H and is divided equally between the go and the return lines. This is done by using two types of dipole magnet, with connections to either the go or the return bus, as shown in Figs. 2 and 5. Two sets of extraction resistors and shorting switches are distributed along the circuit in order to minimize the voltage to earth during energy extraction. The centre point of one of these resistors is connected to earth. The cold diodes of the quench protection system are housed in the interconnect region of each magnet and their polarities are changed between sectors with a beam crossing (Fig. 5). To achieve a ramp of ±10 A/s, a voltage of ±185 V will be needed. On the flat top the current source converter will need about 10 V to feed the resistive part of the connections. The electrical time constant of the circuit is about 20 000 seconds.

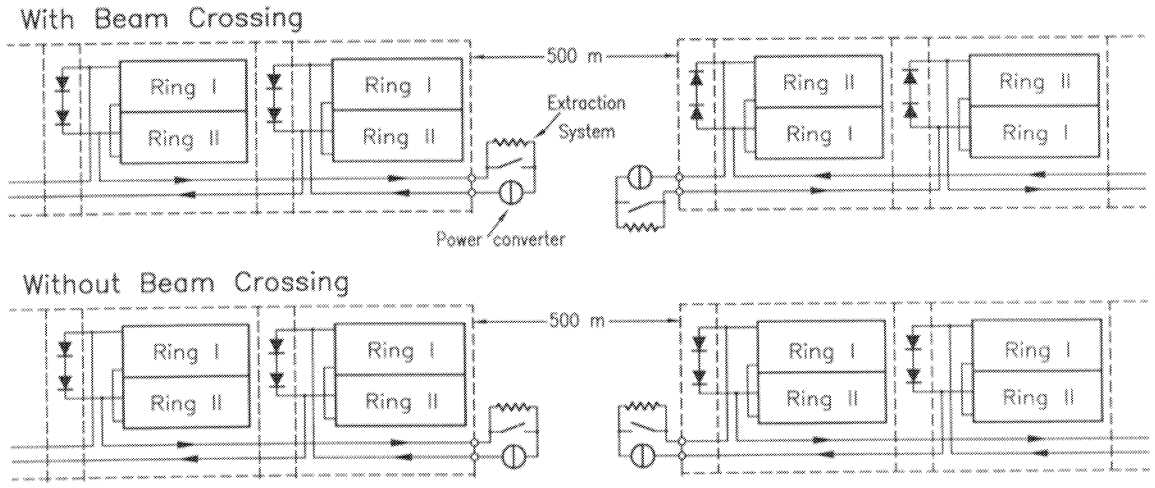

Figure 5: Main dipole connection

4.2.2 The main quadrupoles

One sector of the main quadrupole circuits is shown in Fig. 4, and the overall layout in Fig. 3. The current is fed from the power converters through Ring 1 and returns through Ring 2 with a trim line connected to the mid-point. The MQD and MQF circuits are separately powered to allow different vertical and horizontal phase advances. This gives a total of 16 circuits. The trim line is powered by a small bipolar trim supply and protected by a current limiting resistor. The trim supply is needed to correct the difference of sign in the b_2 of the main dipole. It is hoped that a different way of correcting this will be found and thus eliminate the trim line. The relatively low inductance of the main quadrupole circuit means that only one energy extraction system is needed per circuit and one current source power converter of 15V is sufficient. The electrical time constant of the circuit is about 350 s.

4.2.3 Lattice sextupoles and octupoles

Each sector has four families of sextupole circuits (F1, D1, F2, D2) powered from the even points, using in total 32 low-current unipolar power converters. Exactly the same configuration is used for the octupole circuits except that the low-current power converters are bipolar (reversible in current and voltage).

4.2.4 Spool piece circuits

There are two families of sextupole and two families of decapole spool piece circuits per sector. They are powered by low-current bipolar power converters. The sub-division into two families is made to avoid the need for bypass diodes by limiting the stored energy in each circuit. For convenience this division is made into Ring 1 and Ring 2 although it is not necessary from an optics point of view. This will be studied further.

4.3 Reference magnets

Past experience with accelerators, and in particular those using superconducting magnets, has demonstrated the importance of reference magnets. Each of the main magnet circuits (dipoles and quadrupoles) will have a reference magnet associated with it. In principle it should be sufficient to provide one reference magnet per type or manufacturer. However, the solution to attach a reference magnet to each independent circuit is justified by the fact that the field-to-current relationship in a superconducting magnet is a complex function of past powering. There are therefore eight dipole reference magnets for the eight dipole power converters and eight quadrupole reference magnets, providing sixteen reference values (one per aperture and per sector) for the sixteen quadrupole power converters. The question of reference magnets and the necessary control of the machine will be the subject of more detailed investigations in the future.

4.4 Powering of the insertions

Tables 1 and 8 of Annex 6 give the circuits for each of the points. These tables include the lattice circuits. Since the exact physical layouts and dynamic requirements of the power converters have not yet been finalized, the stated voltages should be considered as provisional.

The powering of the insertions can be placed in four categories:

1. **Points 1 and 5 (see Fig. 6)**
   Points 1 and 5 have low-β insertions and beam crossings but no lattice supplies. However, these points do not have klystron galleries and, as mentioned earlier, use superconducting links to bring the current feedthroughs into the central caverns. Because of this it is relatively simple to power magnets left and right of the insertion in series, where the optics permit. Thus the skew quadrupoles and separator dipoles on the left are powered in series with those on the right. However, because of small differences in the emittance of the two beams, and in order to preserve flexibility in the insertions, both apertures of the quadrupoles of the outer triplets (Q4, 5 and 6) are individually powered left and right of the insertion. The low-β quadrupoles are individually powered on either side of the intersection, with each set of four magnets (Q1, 2 $\times$ Q2, Q3) being connected in series. Trim quadrupoles Q01 and Q03 provide adjustments. The low-β magnets also require dipole, skew quadrupole, dodecapole and skew dodecapole correctors. The quadrupoles of the dispersion suppressors are powered from the adjacent even points by the main quadrupole buses and use trim quadrupoles (MQLT) locally powered with 600 A to make adjustments. Skew quadrupoles (MQS) next to each aperture of Q4, Q6, Q8 and Q10 are powered by 600 A bipolar power converters, and connected as detailed above. The 12.5 kA circuits of the main dipole are brought out to the extraction system located at the end of the arc and connected nearby in the tunnel. The complete lists for points 1 and 5 are given in Tables 1 and 5 in Annex 6. They are electrically identical and need 191 power converters. The total current handled per insertion is 215 kA.

2. **Points 2 and 8 (see Fig. 7)**
   Points 2 and 8 have low-β insertions as well as beam crossings. From a powering point of view they are identical. The low-β quadrupoles are powered in an identical way to those of points 1 and 5. The single-aperture dipoles D1 are powered individually left and right because of the distance separating them, as is D2, which also has each of its separate apertures powered individually because of differences in the trajectories of rings 1 and 2.

   The need to squeeze the β's, combined with the requirement to detune the machine, imposes the independent powering of the outer triplet quadrupoles. Because of the distance between them (500 m), they are individually powered left and right.

   The dispersion suppressor quadrupoles are placed in series with the relevant main quadrupole circuit. Small, individually powered trim quadrupoles allow adjustment. Skew quadrupoles are placed next to each aperture of Q4, Q6, Q8 and Q10, and, because of the distance separating them, are powered independently left and right.

All these power converters as well as those of the main lattice and orbit correction are located in the klystron galleries, which run parallel to the main tunnel for ±250 m on each side of the intersection point. The complete lists for points 2 and 8 are given in Tables 2 and 8 in Annex 6. There are 236 power converters supplying a total of 338 kA at each point.

3. **Points 4 and 6 (see Figs. 8 and 9)**
Points 4 and 6 have simpler insertions and no beam crossing, nor low-β.

Point 4 contains the RF insertion where the beams are separated from 194 mm to 420 mm. Existing high-voltage power converters from LEP will be used to supply the klystrons. They are located on the surface. All quadrupoles (Q2 to Q6) will be independently powered in both apertures. Quadrupoles Q2 and Q3 will be cooled to 4.5 K and will therefore need only 9 kA. The others (Q4 to Q6) will be equipped with power converters capable of powering them to their full gradient. The separators D3 and D4 are connected in series but powered individually on each side of the intersection.

Point 6 houses the beam dump. A warm septum magnet ($\sim$ 1 MW) will be powered from the surface. The quadrupoles Q5 and Q6 need to produce the full gradient and will be cooled to 1.9 K and powered with 12.5 kA. The quadrupoles Q3 and Q4 are special, requiring 6 kA.

The lattice and dispersion suppressors are powered in an identical way to those of points 2 and 8. Skew quadrupoles next to each aperture of Q10 and Q8 are powered in series, making a total of four families for the two rings, left and right of the insertion. Again all power converters, with the exception of the septum supply for point 6 and the klystron supplies for point 4, are located in the klystron galleries. The complete lists for points 4 and 6 are given in Tables 4 and 6, Annex 6. Point 4 uses 202 power converters supplying 340 kA, while point 6 uses 193 power converters supplying 256 kA.

4. **Points 3 and 7 (see Fig. 10)**
Points 3 and 7 are used for betatron and momentum cleaning, respectively, and do not have beam crossings. The beam separation is increased from 194 mm to 224 mm by D3 and D4. The powering is deliberately simple at these points as it is desirable that the civil engineering be kept to a complete minimum, or if possible avoided. The FODO quadrupoles and dipoles D3 and D4 have been designed as warm magnets, with the minimum possible current. In this way they can be powered from existing surface buildings and use LEP cabling. The quadrupoles of the dispersion suppressors are powered from the adjacent even points by the main quadrupole buses. The 12.5 kA circuits of the main dipole are brought out at the end of the arcs, where the extraction switch and resistor are located. Power converters of 600 A are used for the trim and skew quadrupoles as at points 4 and 6. It is assumed that these can be located in the existing underground infrastructure. The complete lists for points 3 and 7 are given in Tables 3 and 7 in Annex 6. There are 150 power converters and the total current handled per insertion is 24 kA. The

two points have the same circuits, the only difference being in the voltages needed for the warm magnet because of different cable distances.

4.5 Closed orbit correctors

Independently powered superconducting dipole correctors are provided next to each arc quadrupole around the machine. These are fed via local current feedthroughs and therefore need long warm connections to the power converters located at the intersection points. To facilitate this, the magnets have been designed with a low current of 32 A. They will need bipolar power converters. The cold dipole correctors in the insertions and at the mid-arcs use 50 A. The warm correctors need 210 A. The latter is less of a problem because of the relatively short connection distances. Where space exists underground, the power converters will be placed there — otherwise they will be located on the surface.

4.6 Distribution of a.c. power

The LHC will make extensive use of the existing power distribution of LEP. Some modifications will be required in order to match the new requirements. The distribution is shown in Fig. 11. The following modifications need to be made:

- To accommodate the new experimental area at point 5, an 18 kV link will be made from point 6. It will be supplied from the existing 66/18 kV 38 MVA transformer at point 6. New high-voltage sub-stations and low-voltage distribution will be needed for the machine services and experiments. Much of this will be underground.

- The new experimental area at point 1 will be supplied from the 18 kV network already located at point 1. However, as part of a general upgrade, it will be reinforced by a new 66 kV link from the substation at the CERN Prévessin (F) site. Again, new high-voltage substations and low-voltage distribution will be needed for the machine services and experiments.

- The cryogenic installations on the surface at the even points will require new high-voltage distribution. The power will be taken from the existing 66/18 kV transformers.

- The power converters, installed underground at points 1, 2, 4, 5, 6 and 8, will require an extension of the 18 kV surface networks in order to feed them. New low-voltage sub-stations will be needed underground.

- Modifications and additions will need to be made to the low-voltage distribution in the underground areas of points 3 and 7.

A first estimate of the power requirements of each of the points is given in Table 10, Annex 6. This will need further refinement.

4.7 Power converters

A provisional list of power converters is given in Table 11, Annex 6. Further optimization of the voltages and types will be carried out once the physical layouts and dynamic requirements of the power converters have been finalized. In all, there will be about 1550 power converters requiring a total steady state input power of about 19 MW and a peak power of 41 MW. They will supply a total current of about 1750 kA and are generally characterized by high current and low voltage. To meet these requirements, as well as the need for compact, reliable high-performance power converters, switch-mode techniques will be used. Of particular interest is the use of modular concepts where several high-current sources can be placed in parallel to make up the required power converter and even provide redundancy if needed.

Switch-mode power converters will also be used for the large quantity of auxiliary circuits, such as the dipole correction elements, where above all, considering the quantities, an economic and reliable design will be needed. In fact, it is hoped that switch-mode power converters will supply most, if not all, of the LHC loads.

However, novel topologies will be needed for the main dipole power converters, which need to have a very large dynamic range to supply ±185 V during acceleration and normal de-excitation of the machine, but only about 1 V while at injection energy.

Some of the advantages of segmentation of the machine are outlined in Part III, Section 1.7. This also means that sector corrections can be made around the machine for performance differences — both static and dynamic — between magnets from different manufacturers. Nevertheless, this segmentation of the machine imposes an order of magnitude improvement on the static and dynamic performance of the main power converters which, coupled to parameters such as the tune tolerance, will result in an overall precision approaching 10^{-6}. Over the last year much progress has been made in this area, with the development of new ADC techniques and a greater understanding of high-current DCCTs. These developments, along with the progress in DSP techniques, mean that adaptive digital control technologies can be used to solve some of these problems. This, coupled to the high dynamic performance of switch-mode power converters, will be used to achieve the performance goals.

Collaboration with industry and research institutes in developing and defining the best overall solution for the LHC powering system will continue. It is hoped that it will be possible to broaden such outside involvement in the future, calling on institutes to help with particularly difficult technical problems and on industry for design studies.

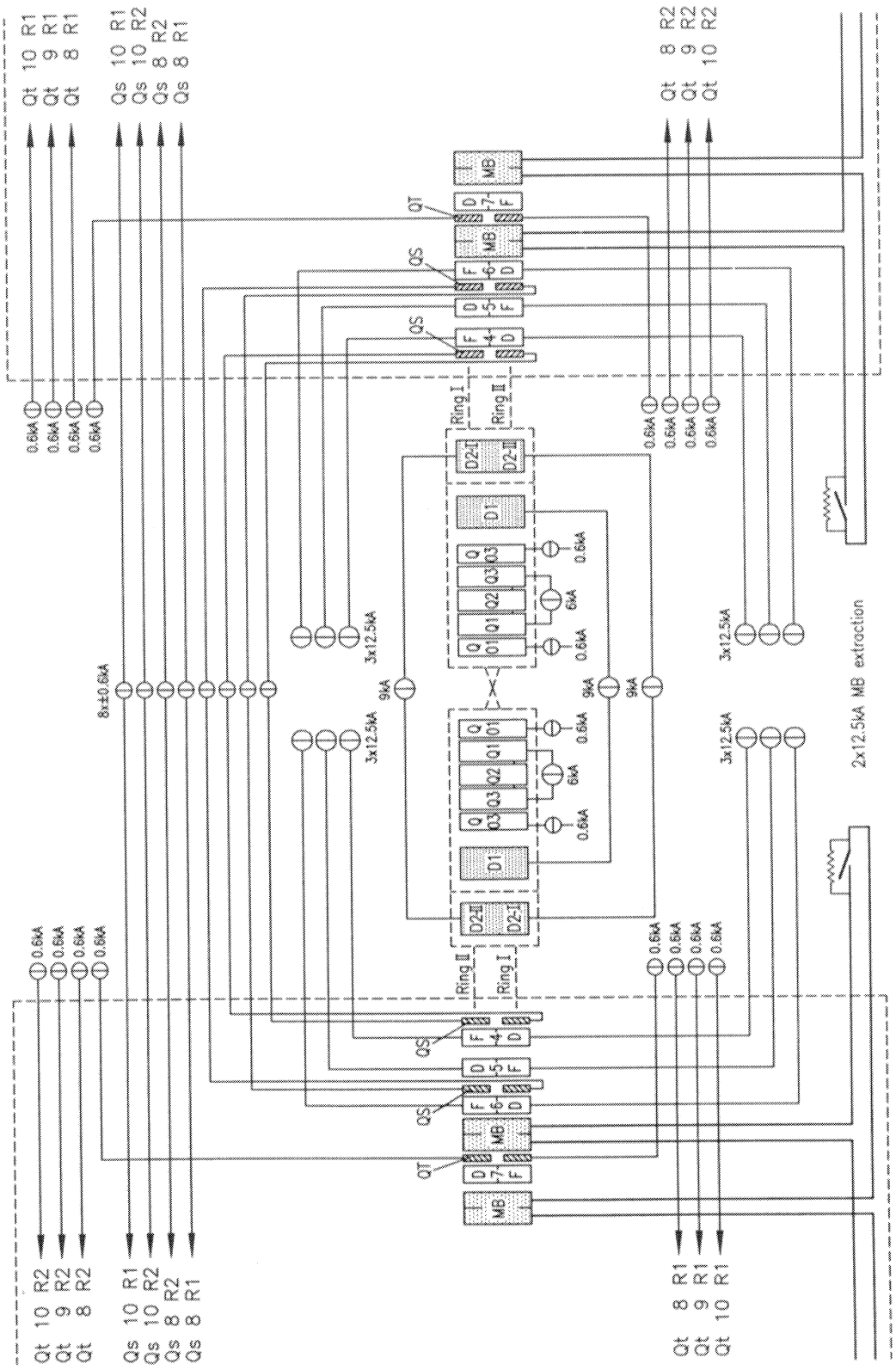

Figure 6: Odd point with low-beta insertion (i.e. P1 or P5)

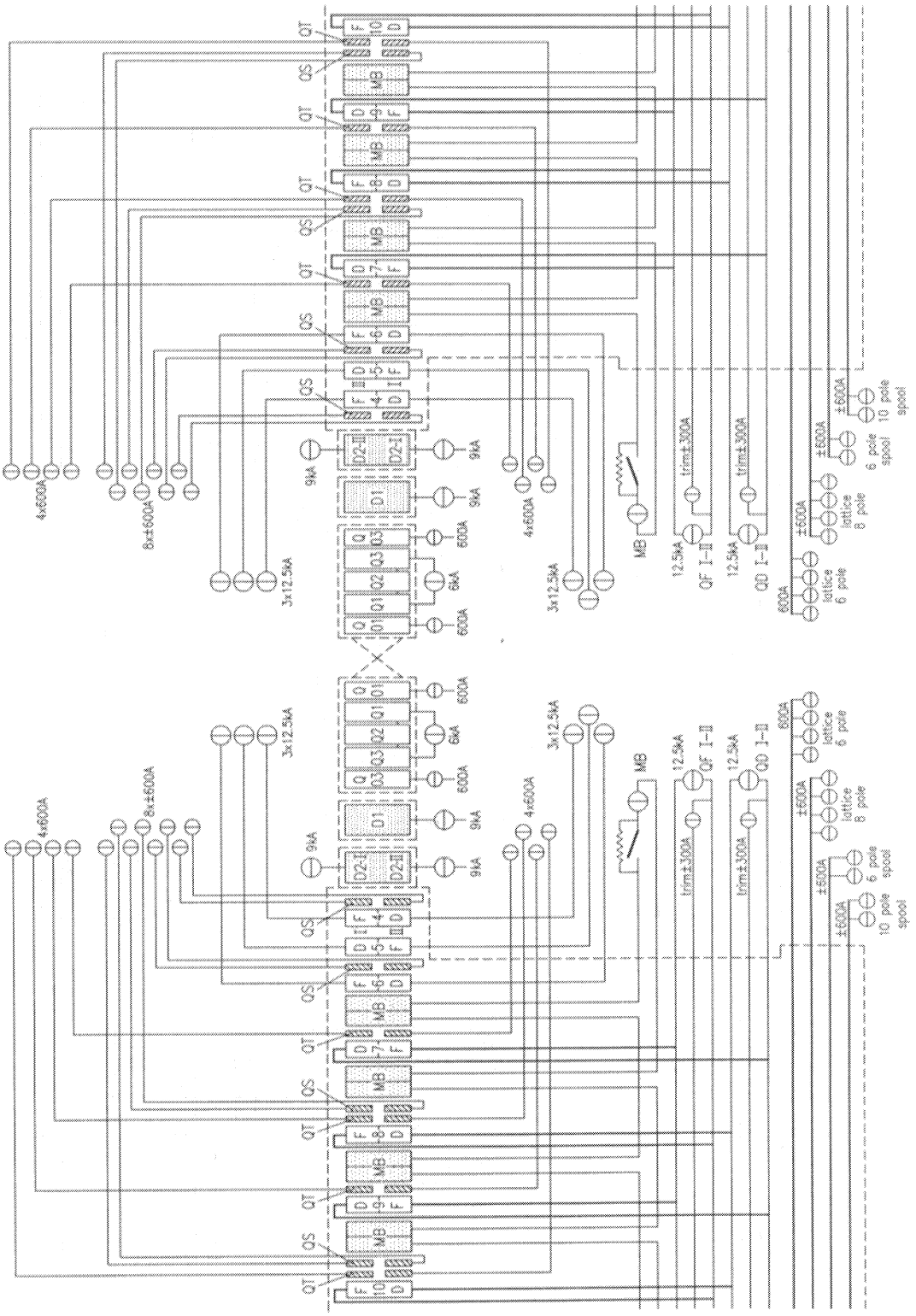

Figure 7: Even point with low-beta insertion (i.e. P2 or P8)

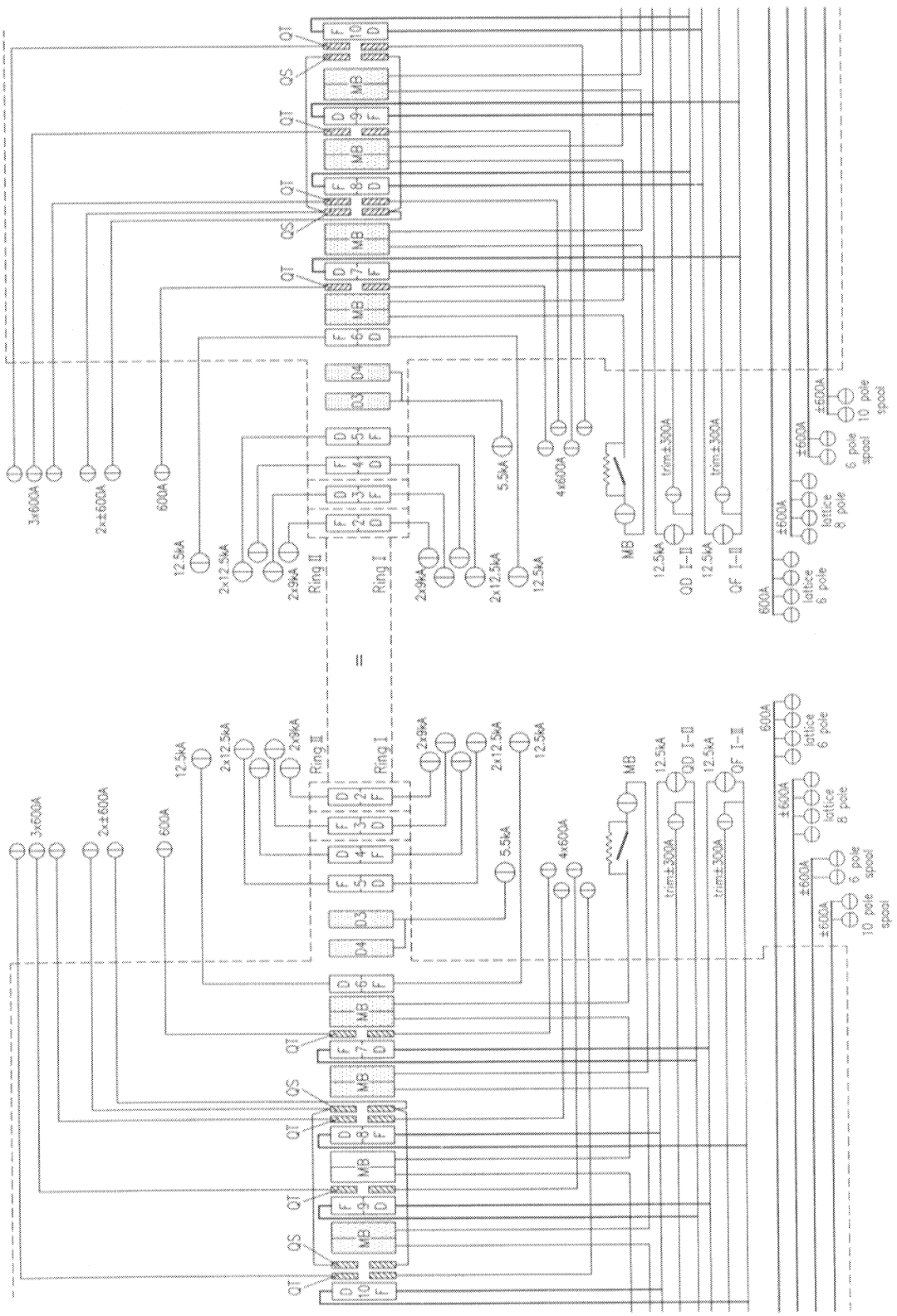

Figure 8: Point 4, insertion with RF

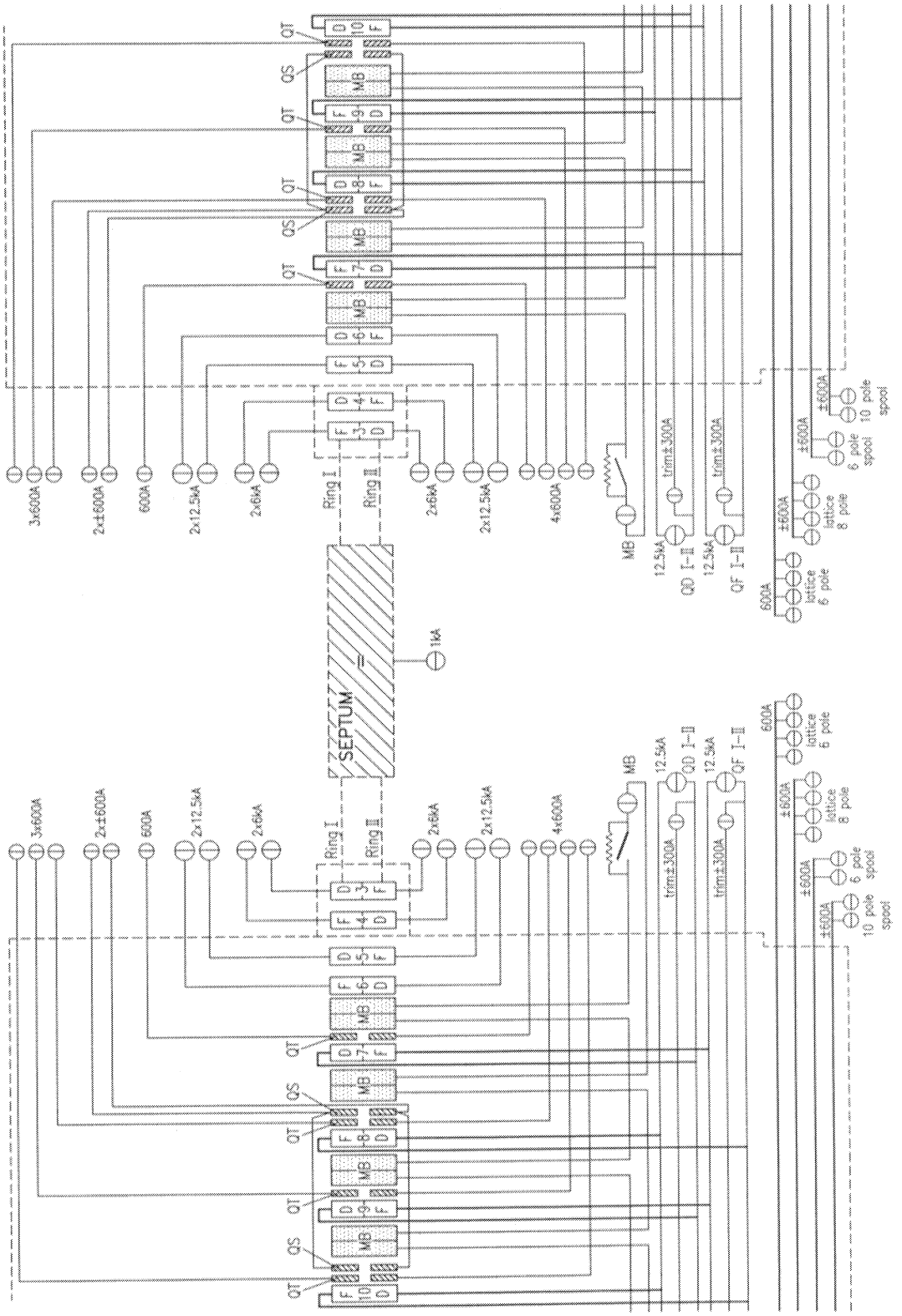

Figure 9: Point 6, beam dump insertion

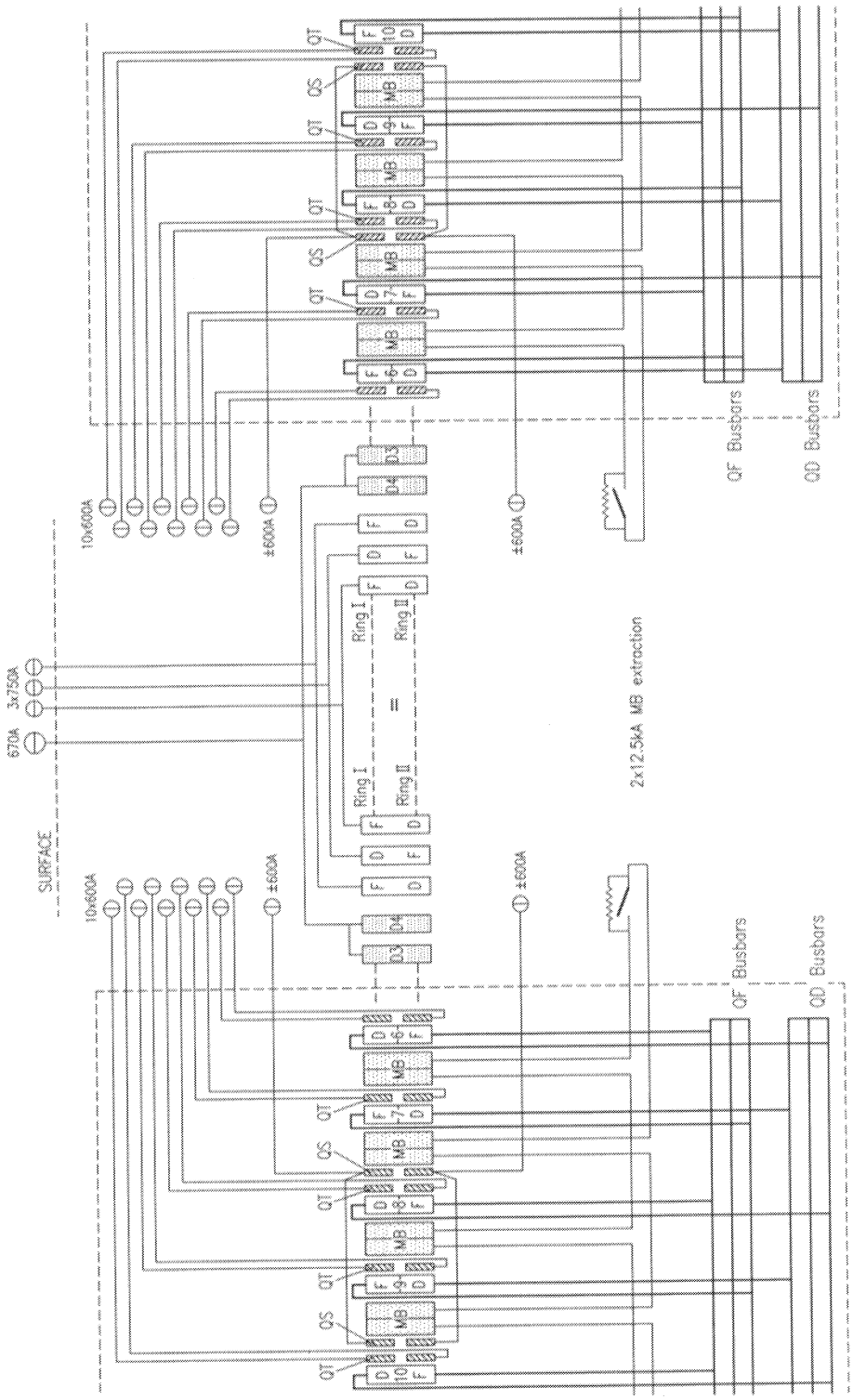

Figure 10: Point 7, warm insertion (Note: P3 is identical, except for polarity; e.g. beam I and II swapped as well as QF and QD)

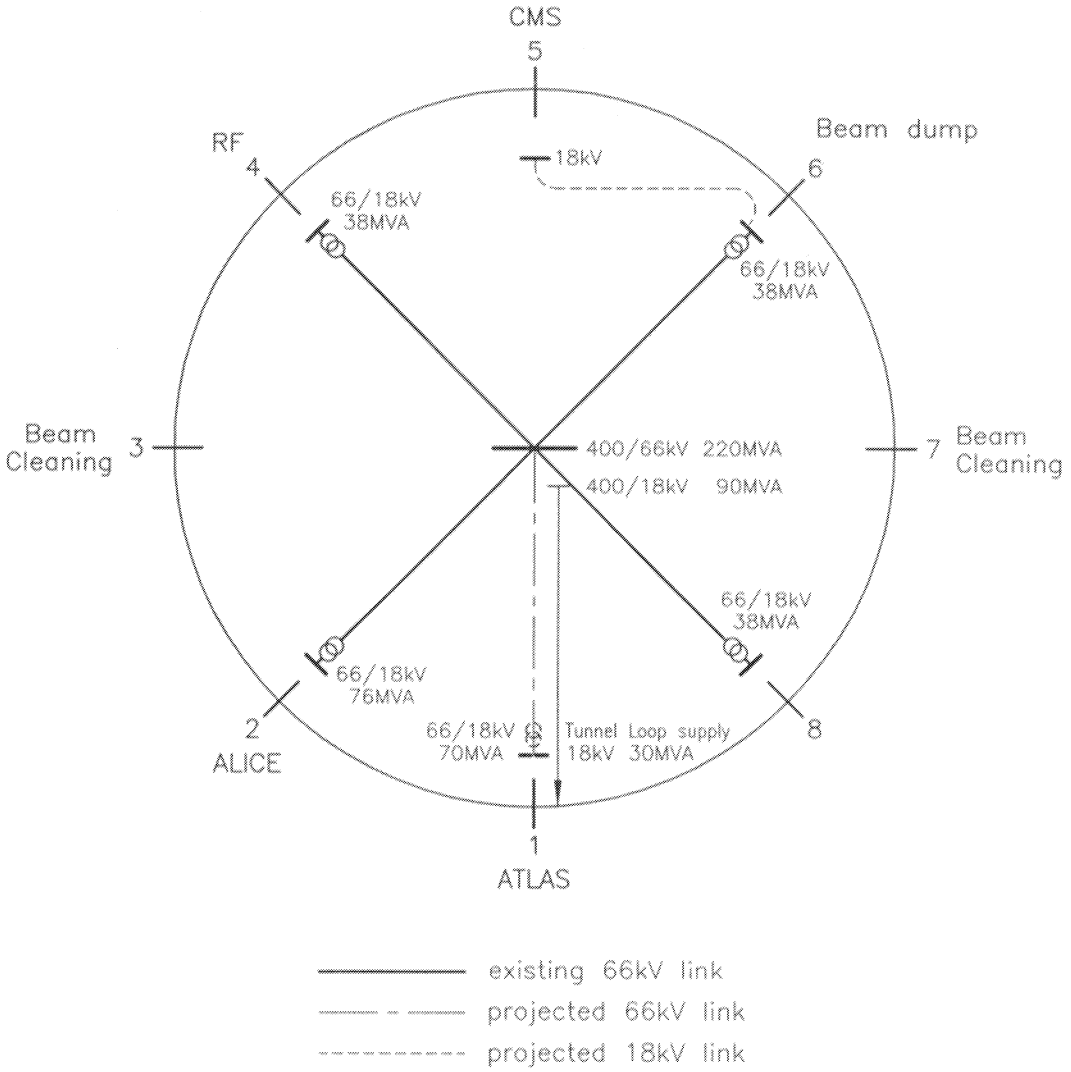

Figure 11: LHC main power distribution

Annex 1

Lists of machine parameters

Table 1: The LHC Parameters

		Injection	Collision
Geometry			
Ring circumference	[m]	26658.883	
Ring separation in arcs	[mm]	194	
Vacuum screen height	[mm]	44	
Vacuum screen width	[mm]	36	
Main Magnet			
Number of main bends		1232	
Length of main bends	[m]	14.200	
Field of main bends	[T]	0.539	8.386
Magnetic rigidity	[T.m]	1501.04	23349.50
Bending radius	[m]	2784.32	
Lattice			
Max dispersion in the arc	[m]	2.145	
Min dispersion in the arc	[m]	1.018	
Max β in the arc	[m]	182.700	
Min β in the arc	[m]	30.200	
Horizontal tune		63.28	
Vertical tune		63.31	
Momentum compaction	10^{-4}	3.47	
Eta η	10^{-4}	3.430	3.473
Gamma transition γ_{tr}		53.7	
RF System			
Revolution frequency	[kHz]	11.2455	
Harmonic Number		35640	
Number of bunches		2835	
Number of bunch places		3564	
RF Frequency	[MHz]	400.789	400.790
Total RF voltage	[MV]	8	16
Synchrotron tune		0.006	0.00212
Synchrotron frequency	[Hz]	62	21
Bucket area	[eV.s]	1.460	8.7
Bucket half height (dE/E)	[10^{-3}]	1	0.36

Table 2: The LHC Parameters (cont.)

		Injection	Collision
Beam Data			
Proton energy	[GeV]	450	7000
Relativistic factor		479.6	7461
Number of particles per bunch		$1.05\ 10^{11}$	
Circulating beam current	[A]	0.536	
Stored Energy per beam	[MJ]	21.5	334
Transverse normalised emittance	[μm.rad]	3.75	
Transverse physical emittance	[nm.rad]	7.82	0.503
H r.m.s beam size in arc	[mm]	1.20	0.303
V r.m.s beam size in arc	[mm]	1.20	0.303
Longitudinal emittance(4σ)	[eV.s]	1.00	2.50
r.m.s energy spread	[10^{-3}]	0.468	0.111
r.m.s bunch length	[ns]	0.434	0.257
r.m.s bunch length	[cm]	13	7.7
Interaction Data			
Number of collision points		2	
Crossing angle at IP	[μrad]	200	
Inelastic cross section	[mb]	60.0	
Total Cross section	[mb]	100.0	
β at IP	[m]	0.50	
r.m.s x,y beam size at IP	[μm]	15.9	
r.m.s x,y beam divergence at IP	[μrad]	31.7	
Beam-beam parameter		0.00342	
Bunch spacing	[m]	7.48	
Bunch separation	[ns]	24.95	
Luminosity reduction factor		1.112	
Expected luminosity	[$\mathrm{cm}^{-2}\ \mathrm{s}^{-1}$]	$1.00\ 10^{34}$	
Luminosity per collision	[cm^{-2}]	$3.14\ 10^{26}$	
Number of event per crossing		18.84	
Beam current lifetime	[h]	22	
Luminosity lifetime	[h]	10	
Nb of inelast events /sec /Xing	[s^{-1}]	$6.01\ 10^{8}$	
Power inelast events /sec /Xing	[W]	673.70	
Synchrotron radiation			
Instantaneous power loss per p	[W]	$3.15\ 10^{-16}$	$1.84\ 10^{-11}$
Power loss per m in main bends	[Wm^{-1}]	0.00	0.206
Synch rad power per ring	[W]	$6.15\ 10^{-2}$	$3.60\ 10^{3}$
Energy loss per turn	[eV]	$1.15\ 10^{-1}$	$6.71\ 10^{3}$
Critical photon energy	[eV]	0.01	44.14
Photon nb per s per p	[s^{-1}] [$10^{6}\ \mathrm{s}^{-1}$]	0.544	8.46
Longitudinal damping time	[h]	48489.1	12.9
Intrabeam scattering			
Long. Emittance growth time	[h]	37.34	60.65
Hor. Emittance growth time	[h]	61.89	115.16

Table 3: The main parameters of the LHC injectors

	Unit	RFQ	Linac2	PSB	PS	SPS
Design parameters						
Energy (kinetic)	[GeV]	0.00075	0.05	1.4	25	450
Repetition time	[s]	1.2	1.2	1.2	3.6	16.8
Number of pulses[1]		1	1	2	3	2×12
Intensity	[mA]	200	≤180			
Pulse length	[μs]	25	25			
Particles/pulse	10^{12}			4.3	8.4	24.3
Particles/bunch	10^{11}				1.0	1.0
Number of bunches/pulse					84	243
Bunch spacing	[ns]				25	25
Transverse emittance[2]	[μm]	0.5	1.2	2.5	3.0	3.5[3]
Longitudinal emittance 2σ	[eV.s]				0.7	1.0
RF systems parameters						
Main system frequency	[MHz]	200	200	0.6–1.7	3.5–7.6[4]	200
Harmonic number				1	8/16	∼ 4620
Second harmonic	[MHz]			1.2–3.4		
LHC bunch generation	[MHz]				40	
Harmonic number					84	
PS/SPS transfer matching	[MHz]				40, 80	200
SPS/LHC transfer matching	[MHz]					400

[1] To fill the downstream machine.
[2] Normalized emittance: $\epsilon^* = (\beta\gamma)\sigma^2/\beta$.
[3] Emittance in the LHC reduced during commissioning to 1 μm for 1.7 10^{10} protons per bunch.
[4] Including a bunch-splitting operation on a 3.5 GeV/c flat top.

Table 4: The LHC parameters: Lead-ion collider (125 ns bunch spacing at SPS injection, one low-β experiment).

Lead-ion collider				
Energy per charge[a]	E/Q	[TeV/charge]	7	
Energy per nucleon[b]	E/A	[TeV/u]	2.76	
Centre-of-mass total	E_{CM}	[TeV]	1148	
Dipole field	B_{MAX}	[T]	8.386	
Transverse normalized emittance	ϵ^*	[μm]	1.5	
β at IP. *(coll.)*	β^*	[m]	0.5	
r.m.s beam radius at IP.	σ^*	[μm]	15	
Crossing angle (per beam)		[μrad]	≤ 100	
Longitudinal emittance *(inj.)*	ϵ_{l}	[eV.s/charge]	1	
Longitudinal emittance *(coll.)*	ϵ_{l}	[eV.s/charge]	2.5	
r.m.s bunch length *(coll.)*	σ_{s}	[cm]	7.5	
r.m.s energy spread *(coll.)*	$\sigma_{\mathrm{E/E}}$	10^{-3}	0.114	
Bunch spacing	l_{b}	[ns]	124.75	
Bunch harmonic number	h_{b}	Not integer	(712.8)	
Number of bunches per ring	n_{b}		608	
Filling time per LHC ring		[min]	9.8	
Number of ions per bunch	N_{b}	10^7	6.3	9.4
Number of ions per beam	N	10^{10}	3.5	5.2
Ion intensity per beam		[mA]	5.2	7.8
Initial luminosity per bunch	$\mathcal{L}_0^{\mathrm{b}}$	[10^{24} cm^{-2} s^{-1}]	1.4	3.2
Initial total luminosity	$\mathcal{L}_0$	[10^{27} cm^{-2} s^{-1}]	0.85	1.95
IBS emittance growth *(inj.)*		[h]	7.6	5.1
IBS emittance growth *(coll.)*		[h]	14.6	9.8
Luminosity lifetime		[h]	10	6.7

[a] $^{208}Pb^{82+}$ Mass number A = 208, Atomic number Z = 82, fully stripped i.e. charge state Q = 82.

[b] 1 atomic mass unit (amu) = 931.502 MeV/c^2 the rest mass of the fully stripped lead ion as expressed in amu is $M_i = 207.93 \approx$ A. By analogy with other publications the energy will be quoted as E/A instead of E/M_i.

Annex 2

Equipment names and lists

Table 1: LHC System prefixes

LHC Systems Prefix Definitions [a]	
Letter	System description
A	Acceleration, RF and dampers
B	Beam instrumentation
C	Communication and controls
D	Electrical distribution
E	Electricity
F	Fluids (Demineralized water excluded)
G	Geodesy and geometry
H	Mechanics, supports and handling
I	Injection and transfer lines
J	Infrastructure
K	Civil engineering
L	Layouts
M	Magnetic elements
N	Particle sources
O	
P	Personnel safety
Q	Cryogenics
R	Power converters
S	General safety
T	Targets, dump and collimators
U	Ventilation and air conditioning
V	Vacuum
W	Demineralized water
X	Experiments
Y	Access systems
Z	Electrostatic systems

[a] No change has been introduced in system type identification. The first letter identifies a system as defined in the document 'Naming conventions for the LHC components', edited by P. Faugeras, AC.DI/FA Note 92–04.

Table 2: Magnet system equipment

Magnet equipment names	
Name	Equipment description
MB(A)	Arc dipole
MB(D)	Dispersion suppressor dipole
MBS	Separation dipole (Single aperture)
MBT	Separation dipole (Twin aperture)
MBRS	Separation dipole (Single aperture, RF)
MBRT	Separation dipole (Twin aperture, RF)
MBW	Warm separation dipole (Single aperture, Cleaning)
MBI	Injection line dipole
MQ	Arc quadrupole
MQL	Dispersion suppressor quadrupole
MQLT	Dispersion suppressor trim quadrupole
MQX	Inner triplet quadrupole (Single aperture)
MQXT	Inner triplet trim quadrupole
MQY	Wide aperture quadrupole (Twin aperture)
MQW	Cleaning warm quadrupole (Twin aperture)
MQS	Skew quadrupole
MQI	Injection line quadrupole
MSCBH	Arc sextupole/dipole corrector (Horizontal)
MSCBV	Arc sextupole/dipole corrector (Vertical)
MO	Arc octupole
MCBH(V)	Dipole corrector Horizontal (Vertical)
MCBI	Injection line dipole corrector
MCBM	Mid-arc dipole corrector
MCBX	Inner triplet (H/V) dipole corrector
MCBY	Wide aperture dipole corrector
MCBW	Warm dipole corrector
MCQS	Inner triplet (a2) corrector
MCS	Sextupole corrector
MCD	Decapole corrector
MCDD	Inner triplet (b6) corrector
MCDDS	Inner triplet (a6) corrector
MKI	Injection kicker
MKE	Ejection (dump) kicker
MSI	Injection septum
MSE	Ejection (dump) septum

Table 3: Target, Beam monitoring and Acceleration system equipment

Target equipment names	
Name	Equipment description
TAN	Beam absorber (neutrals)
TAS	Beam absorber (secondaries)
TDE	Dump for ejected beam (external)
TDI	Beam stopper for injection (internal)
TCA	30° secondary collimator (cleaning)
TCB	90° secondary collimator (cleaning)
TCC	150° secondary collimator (cleaning)
TCI	Collimator (injection lines)
TCPH(V,S)	Primary collimator in cleaning Horizontal (Vertical, Skew)

Beam monitoring equipment names	
Name	Equipment description
BPM	Beam position monitor Horizontal and Vertical
BPMH(V)	Beam position monitor Horizontal (resp Vertical)
BPME	Beam position monitor enlarged, Horizontal and Vertical
BPMD	Beam position monitor, directional, Horizontal and Vertical
BCT	Beam current transfomer
BEUV	Synchrotron radiation telescope
BEGH(V)	SEM grid Horizontal (resp Vertical)
BEWH(V)	Wire scanner Horizontal (resp Vertical)
BGWC	Wall current monitor
BLM	Beam loss monitor
BSH	Horizontal Schottky monitor
BSV	Vertical Schottky monitor
BSL	Longitudinal Schottky monitor
BTV	Screen and TV camera

Acceleration equipment names	
Name	Equipment description
ACS	Superconducting cavities
ADT	Transverse damper
ADL	Longitudinal damper
ABW	Wideband pick-up for RF control
ABD	Beam pick-up for dampers and RF control

Table 4: Cryogenic and Vacuum system equipment

Cryogenic equipment names	
Name	Equipment description
QWCS	Warm compressor station
QUCB	Upper cold box
QLCB	Lower cold box
QCIB	Cryoplant interconnection box
QCCB	Cold compressor box
QCFB	Cavern current feed box
QTCB	Tunnel connection box
QTFB	Tunnel current feed box
QTSM	Technical service module
QCDL	Cryogenic distribution line
QSCL	d.c. superconducting links
QSBC	Superconducting bus cryostat
Vacuum equipment names	
Name	Equipment description
VVP	Vacuum valve and pumping station
VVPE	Vacuum valve and pumping station enlarged

Annex 3

List of magnet parameters

Table 1: Total number of magnets

Name	Equipment description	Total Number
MB	Arc dipole	1232
MBS	Separation dipole	8
MBT	Separation dipole	8
MBRS	Separation dipole	8
MBRT	Separation dipole	4
MBW	Warm separation dipole	16
MQ	Arc quadrupole	386
MQR	RF quadrupole	24
MQL	DS quadrupole	112
MQLT	DS trim quadrupole	68
MQX	Inner triplet quadrupole	32
MQXT	Inner triplet trim quadrupole	16
MQY	Wide aperture quadrupole	6
MQW	Cleaning warm quadrupole	48
MQS	Skew quadrupole	96
MSCBH	Arc sextupole/dipole corrector (horizontal)	360
MSCBV	Arc sextupole/dipole corrector (vertical)	360
MO	Arc octupole	360
MCB	Dipole corrector	228
MCBM	Mid-arc dipole corrector	16
MCBX	Inner triplet (h/v) dipole corrector	16
MCBY	Wide aperture dipole corrector	8
MCBW	Warm dipole corrector	24
MCQS	Inner triplet (a2) corrector	8
MCS	Sextupole corrector	2464
MCD	Decapole corrector	2464
MCDD	Inner triplet (b6) corrector	16
MCDDS	Inner triplet (a6) corrector	8

Table 2: Main parameters of the magnets for the arcs

Name	Equipment description	Nominal field at x, y [m] [T]	No. of apertures	Coil aperture [mm]	Magnetic length [m]	Temp. [K]	Number
MB	Arc dipole	8.4	2	56	14.2	1.9	1104
MQ	Arc quadrupole	223 x	2	56	3.1	1.9	360
MSCBH	Arc sextupole/dipole corr. (horizontal)	$1.5/1500^2$	1	56	1.1/1.03	1.9	352
MSCBV	Arc sextupole/dipole corr. (vertical)	1.5/1500 x^2	1	56	1.1/1.03	1.9	352
MO	Arc octupole	6.7 10^4 x^3	1	56	0.32	1.9	360
MCBM	Mid-arc dipole corrector	3.0	1	56	0.30	1.9	16
MCS	Sextupole corrector	1970 x^2	1	56	0.10	1.9	2208
MCD	Decapole corrector	1.3 10^6 x^4	1	56	0.063	1.9	2208

Table 3: Main parameters of the magnets for the dispersion suppressors

Name	Equipment description	Nominal field at x, y [m] [T]	No. of apertures	Coil aperture [mm]	Magnetic length [m]	Temp. [K]	Number
MB	Arc dipole	8.4	2	56	14.2	1.9	128
MQ	Arc quadrupole	223 x	2	56	3.1	1.9	16
MQL	DS quadrupole	223 x	2	56	3.25	1.9	48
MQLT	DS trim quadrupole	120 x	2	56	1.5	1.9	64
MQS	Skew quadrupole	120 y	1	56	0.72	1.9	64
MSCBH	Arc sextupole/dipole corr. (horizontal)	1.5/1500 x^2	1	56	1.1/1.03	1.9	8
MSCBV	Arc sextupole/dipole corr. (vertical)	1.5/1500 x^2	1	56	1.1/1.03	1.9	8
MCB	Dipole corrector	3.0	1	56	0.84	1.9	96
MCS	Sextupole corrector	1970 x^2	1	56	0.10	1.9	256
MCD	Decapole corrector	1.310^6 x^4	1	56	0.063	1.9	256

Table 4: Main parameters of the magnets for the insertions

Name	Equipment description	Nominal field at x, y [m] [T]	No. of apertures	Coil aperture [mm]	Magnetic length [m]	Temp. [K]	Number
Low-β	(4 Insertions)						
MBS	Separation dipole (D1)	4.5	1	88	11.5	4.5	8
MBT	Separation dipole (D2)	4.5	2	88	11.5	4.5	8
MQL	DS quadrupole	223 x	2	56	3.25	1.9	56
MQX	Inner triplet quadrupole	235 x	1	70	5.5	1.9	32
MQXT	Inner triplet trim quad	120 x	1	85	1.5	1.9	16
MQS	Skew quadrupole	120 y	1	56	0.72	1.9	32
MCB	Dipole corrector	3.0	1	56	0.84	1.9	96
MCBX	Inner triplet (h/v) dip. corr.	3.2	1	90	0.31	1.9	16
MCQS	Inner triplet (a2) corrector	28 y	1	90	0.36	1.9	8
MCDD	Inner triplet (b6) corrector	$3.2\ 10^6$ x^5	1	76	0.50	1.9	16
MCDDS	Inner triplet (a6) corrector	$3.2\ 10^6$ y^5	1	76	0.50	1.9	8
Cleaning	(2 Insertions)						
MBW	Warm separation dipole	1.5	2	50	3.4	–	16
MQL	DS quadrupole	223 x	2	56	3.25	1.9	4
MQLT	DS trim quadrupole	120 x	2	56	1.5	1.9	4
MQW	Warm quadrupole	37 x	2	44	2.9	–	48
MCB	Dipole corrector	3.0	1	56	0.84	1.9	8
MCBW	Warm dipole corrector	0.5	1	44	1.5	–	24
Dump	(1 Insertion)						
MQ	Arc quadrupole	223 x	2	56	3.1	1.9	6
MQL	DS quadrupole	223 x	2	56	3.25	1.9	4
MQY	Wide aperture quadrupole	220 x	2	70	3.25	1.9	4
MQY	Wide aperture quadrupole	170 x	2	70	3.25	4.5	2
MCB	Dipole corrector	3.0	1	56	0.84	1.9	8
MCBY	Wide aperture dipole corr.	3.0	1	70	0.82	1.9	4
MCBY	Wide aperture dipole corr.	2.0	1	70	0.82	4.5	4
RF	(1 Insertion)						
MBRS	Separation dipole (D3)	4.5	1	76	9.45	4.5	8
MBRT	Separation dipole (D4)	4.5	2	76	9.45	4.5	4
MQ	Arc quadrupole	223 x	2	56	3.1	1.9	4
MQR	RF quadrupole	223 x	1	56	3.1	1.9	16
MQR	RF quadrupole	170 x	1	56	3.1	4.5	8
MCB	Dipole corrector	3.0	1	56	0.84	1.9	12
MCB	Dipole corrector	2.0	1	56	0.84	4.5	8

Annex 4

List of heat loads and cryogenic parameters

Table 1: Heat loads in dipole cryostats in nominal conditions (no contingency)

Source of heat load	Temperature levels		
	50–75 K [W]	4.5–20 K [W]	1.9 K [W]
Heat inleaks			
Support posts	14.4	1.12	0.13
Thermal shield	43.8		
Radiative insulation		0.04	1.68
Instrument feedthroughs	0.430		0.26
Conduction-beam screen supports			0.23
Total	58.6	1.17	2.31
Resistive heating			
Cold mass (9 splices)			1.03
Interconnection (6 splices)			0.48
Total			1.51
Beam-induced heating			
Synchrotron radiation		5.85	
Image currents		2.34	
Longitudinal impedance		2.84	
Beam-gas scattering			0.90
Total		11.0	0.90
Total heat load	58.6	12.2	4.71

Table 2: Heat loads in short straight section in nominal conditions (no contingency)

Source of heat load	Temperature levels		
	50–75 K [W]	4.5–20 K [W]	1.9 K [W]
Heat inleaks			
Support posts	9.57	0.75	0.09
Thermal shield	18.1		
Radiative insulation		0.02	0.70
Conduction-beam screen supports			0.10
Vacuum barrier	9.16	0.03	0.41
Technical service module	0.41		0.03
Beam-position monitor	3.58		0.82
Feedthroughs	1.34		0.27
Dipole-corrector feedthroughs	2.80		0.06
Total	45	0.80	2.47
Resistive heating			
Cold mass (9 splices)			0.71
Interconnections (6 splices)			0.48
Dipole corrector feedthroughs	1.90		
Total	1.90		1.19
Beam-induced heating			
Synchrotron radiation			
Image currents		0.97	
Longitudinal impedance		1.17	
Beam gas scattering			0.37
Total		2.14	0.37
Total heat load	46.9	2.94	4.03

Table 3: Heat loads in a Cryogenic Distribution Line module (53.5 m; no contingency)

Source of heat load	Temperature levels		
	50–75 K [W]	4.5–20 K [W]	1.9 K [W]
Heat inleaks			
Supports	8.59	0.34	0.52
Thermal shield	108.8		
Radiative insulation		1.74	2.59
Quench valve	0.72		0.80
Valves	2.25	0.11	0.42
Vacuum barrier		0.20	0.65
Total	120.4	2.39	4.98

Table 4: Heat loads for a half-cell (3 dipoles + 1 short straight section and Cryogenic Distribution Line module; no contingency)

Mode	Temperature levels		
	50–75 K [W]	4.5–20 K [W]	1.9 K [W]
Nominal operation	343	41.9	23.2
Ultimate operation	343	78.9	22.5
Low-beam-intensity operation	343	6.69	20.1
Injection standby	341	6.69	14.4

Table 5: Heat loads for an arc (46 half-cells; no contingency)

Mode	Temperature levels		
	50–75 K [W]	4.5–20 K [W]	1.9 K [W]
Nominal operation	15778	1928	1065
Ultimate operation	15778	3630	1036
Low-beam-intensity operation	15778	308	924
Injection standby	15691	308	662

Table 6: Distributed heat loads in an arc (no contingency)

Source of heat load	Temperature levels		
	50–75 K [W/m]	4.5–20 K [W/m]	1.9 K [W/m]
Heat inleaks	6.38	0.125	0.269
Resistive heating	0.036		0.107
Beam-induced heating nominal		0.659	0.057
Beam-induced heating ultimate		1.35	0.045
Total nominal	6.42	0.784	0.433
Total ultimate	6.42	1.48	0.421

Table 7: Heat loads in half insertions 1 to 4 in nominal conditions (no contingency)

Heat load source	Temperature levels				Gas helium consumption 50–300 K
	50–75 K	4.5–20 K	4.7 K	1.9 K	
	[W]	[W]	[W]	[W]	[g/s]
Insertion 1					
Heat inleaks	2544	19.2	24.4	58.6	4.62
Resistive heating	797		3.02	37.1	3.03
Synchrotron radiation		46.8	8.41		
Image currents		26.4	8.48	15.1	
Longitudinal impedance		31.9	10.3	18.3	
Beam-gas scattering			3.25	15.9	
Secondary particle losses			60.0	152.0	
Total	3341	124.3	117.8	296.9	7.65
Insertion 2					
Heat inleaks	3195	21.0	29.3	67.3	7.32
Resistive heating	1262		3.02	39.8	4.79
Synchrotron radiation		46.8	8.41		
Image currents		26.2	3.44	13.0	
Longitudinal impedance		31.8	4.17	15.8	
Beam-gas scattering			1.32	15.1	
Secondary particle losses					
Total	4457	125.8	49.7	150.9	12.1
Insertion 3					
Heat inleaks	1107	13.5	3.80	38.7	1.10
Resistive heating	190			24.0	0.72
Synchrotron radiation		46.8			
Image currents		26.4		1.79	
Longitudinal impedance		31.9		2.17	
Beam-gas scattering				10.8	
Secondary particle losses					
Total	1297	118.6	3.80	77.4	1.82
Insertion 4					
Heat inleaks	2608	17.8	189.4	54.1	5.96
Resistive heating	1028		1.19	29.0	3.91
Synchrotron radiation		46.8			
Image currents		26.2	3.66	1.35	
Longitudinal impedance		31.8	4.44	1.63	
Beam-gas scattering			1.40	10.6	
Secondary particle losses					
RF cavities			160.0		
Total	3636	122.7	360.1	96.7	9.87

Table 8: Heat loads in half-insertions 5 to 8 in nominal conditions (no contingency)

Source of heat load	Temperature levels				Gas helium consumption 50–300 K
	50–75 K	4.5–20 K	4.7 K	1.9 K	
	[W]	[W]	[W]	[W]	[g/s]
Insertion 5					
Heat inleaks	2544	19.2	24.4	58.6	4.62
Resistive heating	797		3.02	37.1	3.03
Synchrotron radiation		46.8	8.41		
Image currents		26.4	8.48	15.1	
Longitudinal impedance		31.9	10.3	18.3	
Beam-gas scattering			3.25	15.9	
Secondary particle losses			60.0	152.0	
Total	3341	124.3	117.8	296.9	7.65
Insertion 6					
Heat inleaks	2885	17.8	24.9	60.2	6.82
Resistive heating	1176		1.19	32.6	4.47
Synchrotron radiation		46.8			
Image currents		26.2	0.93	9.12	
Longitudinal impedance		31.8	1.12	11.0	
Beam-gas scattering			0.36	13.6	
Secondary particle losses					
Total	4061	122.7	28.5	126.5	11.3
Insertion 7					
Heat inleaks	1107	13.5	3.80	38.7	1.10
Resistive heating	190			24.0	0.72
Synchrotron radiation		46.8			
Image currents		26.4		1.79	
Longitudinal impedance		31.9		2.17	
Beam-gas scattering				10.8	
Secondary particle losses					
Total	1297	118.6	3.80	77.4	1.82
Insertion 8					
Heat links	3197	21.0	29.3	67.4	7.32
Resistive heating	1262		3.02	39.8	4.79
Synchrotron radiation		46.8	8.41		
Image currents		26.2	3.44	13.0	
Longitudinal impedance		31.8	4.17	15.8	
Beam-gas scattering			1.32	15.1	
Secondary particle losses					
RF cavities					
Total	4459	125.8	49.7	151.0	12.1

Table 9: Heat loads in sectors (including interconnecting cryogenic transfer lines and superconducting power links; no contingency)

Source of heat load		Temperature levels				Gas helium consumption 50–300 K
		50–75 K	4.5–20 K	4.7 K	1.9 K	
		[W]	[W]	[W]	[W]	[g/s]
Sector 1–2	Nominal op.	26883	2243	235	1653	19.8
	Ultimate op.	26883	4172	374	1976	19.8
	Low-beam-intensity op.	26883	415	127	1213	19.8
	Injection standby	24739	415	121	874	11.9
Sector 2–3	Nominal op.	23424	2219	53	1418	13.9
	Ultimate op.	23424	4148	70	1470	13.9
	Low-beam-intensity op.	23424	391	36	1163	13.9
	Injection standby	21887	391	33	838	8.4
Sector 3–4	Nominal op.	23633	2253	364	1369	11.7
	Ultimate op.	23633	4181	376	1409	11.7
	Low-beam-intensity op.	23633	424	354	1172	11.7
	Injection standby	22329	424	193	857	7.1
Sector 4–5	Nominal op.	26062	2240	545	1599	17.5
	Ultimate op.	26062	4169	680	1884	17.5
	Low-beam-intensity op.	26062	411	445	1189	17.5
	Injection standby	24151	411	281	861	10.6
Sector 5–6	Nominal op.	26487	2240	214	1629	18.9
	Ultimate op.	26487	4169	339	1939	18.9
	Low-beam-intensity op.	26487	411	121	1198	18.9
	Injection standby	24428	411	117	867	11.4
Sector 6–7	Nominal op.	23318	2230	32	1400	13.1
	Ultimate op.	23318	4159	35	1439	13.1
	Low-beam-intensity op.	23318	401	30	1156	13.1
	Injection standby	21866	401	29	838	7.9
Sector 7–8	Nominal op.	23941	2238	53	1434	13.9
	Ultimate op.	23941	4166	70	1486	13.9
	Low-beam-intensity op.	23941	409	36	1180	13.9
	Injection standby	22404	409	33	854	8.4
Sector 8–1	Nominal op.	26885	2243	235	1653	19.8
	Ultimate op.	26885	4172	374	1976	19.8
	Low-beam-intensity op.	26885	415	127	1213	19.8
	Injection standby	24741	415	121	874	11.9

Table 10: Working characteristics of cryogenic lines in nominal conditions (close to cryoplants)

Pipe	Name	Diameter [mm]	T [K]	P [bar]
A	Subcooled LHe Supply	40	2.2	1.3
B	Pumping Return	267	1.8	0.016
C	Supercritical He Supply	100	4.6	3
C′	Beam screen supply	15	4.6	3
D	GHe Return	150	20	1.3
E	Thermal Shield Supply	80	50	20
F	Thermal Shield Return	80	75	19

Table 11: Installed cryogenic power requirements

Source of heat load	Temperature levels				Gas helium consumption 50–300 K [g/s]
	50–75 K [kW]	4.5–20 K [kW]	4.7 K [kW]	1.9 K [kW]	
Sector 1–2	40.4	4.30	0.45	2.80	30.0
Sector 2–3	35.2	4.25	0.10	2.45	21.0
Sector 3–4	35.5	4.30	0.65	2.45	18.0
Sector 4–5	39.1	4.30	0.95	2.75	27.0
Sector 5–6	39.8	4.30	0.40	2.80	29.0
Sector 6–7	35.0	4.30	0.10	2.45	20.0
Sector 7–8	36.0	4.30	0.10	2.50	21.0
Sector 8–1	40.4	4.30	0.45	2.80	30.0

Table 12: Cryogenic Instrumentation in the LHC

Type of Sensor or Actuator	Range	Total	Accuracy	Availability
Temperature	1.6–40 (300) K	3024	1%	Allen Bradley, Carbon thin-film, TVO, Cernox
Temperature	1.6–300 K	3616	0.5%	Carbon thin-film, TVO, Cernox or pair of Allen Bradley + Pt100
Total T > 1.6 K		6640		
Temperature > 50 K	50–300 K	2512	1%	Platinum thermometer
Liquid He meter at 1.8 K	100 mm	536	3%	Commercial
Cold mass filling test at 2.2 K	LHe full?	1808		Helium level dipstick or cryogenic pressure transducer (TO DEFINE)
Pressure at 300 K	0–70 mbar	520	0.1% FS	Commercial
Pressure at 300 K	0–10 bar	159	1% FS	Commercial
Pressure at 300 K	0–4 bar	159	1% FS	Commercial
Pressure at 300 K	$10^{3} - 10^{-3}$ mbar	1040	10%	Commercial
Pressure at 300 K	$10^{-3} - 10^{-8}$ mbar	1040	50%	Commercial
Pressure at 300 K	$10^{-3} - 10^{-10}$ mbar	1040	50%	Commercial
Flow meter at 2.2 K	0–10 g/s	520	3% FS	Usefull if available
Flow meter at 300 K	various ranges	576	3%	Commercial
Cryoheater at 2 K	0–10 W	2264	2%	Commercial
Current leads heater	36	576		CERN
Cryogenic Control Valves		1368		Commercial
Control valves		896		Commercial
Quench relief valves		960		CERN
Digital valves		5200		Commercial
Electrovalves		6160		Commercial

Annex 5

Lists of vacuum equipment

Table 1: Cold Arcs Beam Vacuum

Item	Number
Dipole Beam Screen ($\sim$ 16 m long)	$\sim$ 2500
Quadrupole Beam Screen ($\sim$ 6.5 m long)	$\sim$ 850
Intermagnet Connection (RF Screened Bellows)	3104
30 l/s Ion Pumps	976
Ion Pump Power Supplies (1 per 8 or 2 pumps)	152
Ionization Gauges	104
Ionisation Gauge Power Supplies (1 per 8 or 2 gauges)	68
Pirani Gauges (2 per vacuum sector)	72
Pirani Gauge Power Supplies	72
All-Metal Right-Angle Roughing Valves	904
All-Metal Double-Seal Sector Valves (aperture $\sim$ 50 mm)	112
Sector Valve Controls	64
All-Metal Right-Angle Roughing Valves for Double-Seal Sector Valve	64
Overpressure Membrane-Type Safety Valve	48
Lateral Transitions	864
Active Charcoal Trap for He on Lateral Transitions	864
Longitudinal Warm-cold Transitions	112

Table 2: Cold Arcs Insulation Vacuum

Item	Number
Combined Gauges (1000 Torr–1 10^{-9} Torr)	476
Combined Gauges Power Supplies	476
Viton-Sealed Manual Roughing Valves	500
He Sorption Panels	1280
Vacuum Barrier Bypass Manifold	218
Pneumatic Valve on Bypass	218
Bypass Control	218

Table 3: Warm Straights

Item	**Total**
Cu Vacuum Chambers 10 m long, Ø100 mm	382
LEP Type RF Screened Bellows	916
Pumping Manifold	384
All-Metal Right-Angle Roughing Valves	80
Ion Pumps 60 l/s	384
Ion Pump Power Supplies (1 per 8 pumps)	64
Ti Sublimation Pumps	384
Ti Sublimation Pump Power Supplies	384

Annex 6

Lists of powering elements

Table 1: Point 1 – List of circuits

PC/Equip. Location	Circuit	Current (kA)	U Peak (V)	Qty of Circuits	Qty of Feedthru.	Pow. Con. Type	Remark
	(Q7,Q8,Q9,Q10)						Powered by Main Quad Buses
Tunnel	MB Energy extraction	12.5		2	4	–	Extraction switch and resistor (Left and Right)
UR15	Outer triplet, Q4,5,6	12.5	8	12	14	3	Individual powering (R1, R2, left and right)
UR15	Dispersion Trim Q7,8,9,10	0.6	12	16	32	7	Individual powering (R1, R2, left and right)
UR15	Skew Quads next to Q4,6,8,10	±0.6	±12	8	16	8	Left and right in series, R1 and R2
Central	Arc CODs	±0.032	±115	88	Local	12	23 half cells × R1,R2 × Left, Right (–Q10)
Central	Mid-arc CODs	±0.05	±115	2	Local	15	
Central	Q4 CODs	±0.05	±50	8	Local	11	R1,R2 × Left, Right × 2 (Horiz + Vert.)
Central	Q5 to Q10 CODs	±0.05	±50	24	Local	11	R1,R2 × Left, Right
Central	D2 CODs	±0.05	±50	8	Local	11	R1,R2 × Lefts, Right × 2 (Horiz. + Vert.)
UR15	Separators D1	9	10	1	2	4	Left and right in series
UR15	Separators D2	9	10	2	4	4	R1 left in series with R2 right, etc.
UR15	Low-β Q1,2,3.	6	10	2	4	5	Series connected, Individual powering left and right
UR15	Low-β trim Q01,03	0.6	12	4	8	7	Individual powering
UR15	Low-β Dipole Corr.	±0.6	±12	8	16	8	Left and Right, Horiz. and Vert. × 2
Central	Low-β Skew Quad. Corr.	±0.025	±8	2	4	14	Left and Right
Central	Low-β Dodecap. Corr.	±0.025	±8	4	8	14	Left and Right × 2
Central	Low-β Skew Dodecap.	±0.025	±8	2	4	14	Left and Right

Total Power Converters (PC) Current 216 kA Qty PC's 191

Total Current in Feedthroughs 347 kA

PC/Equip. Location	Circuit	Current (kA)	U Peak (V)	Qty of Circuits	Qty of Feed-thru.	Pow. Con. Type	Remark
	(Q7,Q8,Q9,Q10)						Powered by Main Quad Buses
Left UA	MB Energy extraction	12.5		1			Extraction switch and resistor
Left UA	MB	12.5	±195	1	2	1	Left Main Dipole, Ring 1 in series with Ring 2
Left UA	QD	12.5	15	1	2	2	Left QD Ring 1 in series with Ring 2
Left UA	QF	12.5	15	1	2	2	Left QF Ring 1 in series with Ring 2
Left UA	QD Trim	±0.3	±20	1	1	9	Ring 1/2 Trim
Left UA	QF Trim	±0.3	±20	1	1	9	Ring 1/2 Trim
Left UA	Lattice Sextupole F1,2,D1,2	0.6	12	4	8	7	Left Lattice Sextupoles
Left UA	Lattice Octupole F1,2,D1,2	±0.6	±12	4	8	8	Left Lattice Octupoles
Left UA	Sextupole Spool Piece	±0.6	±12	2	4	8	Left Sextupole Spool Pieces Ring 1,2
Left UA	Decapole Spool Piece	±0.6	±12	2	4	8	Left Decapole Spool Pieces Ring 1,2
Left UA	Outer triplet, Q4,5,6	12.5	8	6	7	3	Individual powering, Separate R1, R2
Left UA	Dispersion Trim Q7,8,9,10	0.6	12	8	16	7	Individual powering, Separate R1, R2
Left UA	Skew Quads next to Q4,6,8,10	±0.6	±12	8	16	8	Individual powering, Separate R1, R2
Left UA	Separators D1	9	10	1	2	4	Individual powering
Left UA	Separators D2	9	10	2	3	4	Individual powering, Separate R1, R2
Left UA	Low-β Q1,2,3	6	10	1	2	5	Series connected
Left UA	Low-β trim Q01,03	0.6	12	2	4	7	Individual powering
Left UA	Low-β Dipole Corr.	0.6	12	4	8	7	Horiz. and Vert. × 2
Left UA	Low-β Skew Quad. Corr.	±0.025	±8	1	2	14	
Left UA	Low-β Dodecap. Corr.	±0.025	±8	2	4	14	× 2
Left UA	Low-β Skew Dodecap.	±0.025	±8	1	2	14	
Central	Arc CODs	±0.032	±115	88	Local	12	23 half cells × R1,R2 × Left, Right (–Q10)
Central	Mid-arc CODs	±0.05	±115	2	Local	15	
Central	Q4 CODs	±0.050	±50	8	Local	11	R1,R2 × Left, Right × 2 (Horiz. + Vert.)
Central	Q5 to Q10 CODs	±0.050	±50	24	Local	11	R1,R2 × Left, Right
Central	D2 CODs	±0.050	±50	8	Local	11	R1,R2 × Left, Right × 2 (Horiz. + Vert.)

Table 2: Point 2 – List of circuits (cont.)

PC/Equip. Location	Circuit	Current (kA)	U Peak (V)	Qty of Circuits	Qty of Feed-thru.	Pow. Con. Type	Remark
Right UA	Separators D1	9	10	1	2	4	Individual powering
Right UA	Separators D2	9	10	2	3	4	Individual powering, Separate R1, R2
Right UA	Low-β Q1,2,3	6	10	1	2	5	Series connected
Right UA	Low-β trim Q01,03	0.6	12	2	4	7	Individual powering
Right UA	Low-β Dipole Corr.	0.6	12	4	8	7	Horiz. and Vert. $\times$ 2
Right UA	Low-β Skew Quad. Corr.	$\pm$0.025	$\pm$8	1	2	14	
Right UA	Low-β Dodecap. Corr.	$\pm$0.025	$\pm$8	2	4	14	$\times$ 2
Right UA	Low-β Skew Dodecap.	$\pm$0.025	$\pm$8	1	2	14	
Right UA	MB	12.5	$\pm$195	1	2	1	Right Main Dipole, Ring 1 in series with Ring 2
Right UA	QD	12.5	15	1	2	2	Right QD Ring 1 in series with Ring 2
Right UA	QF	12.5	15	1	2	2	Right QF Ring 1 in series with Ring 2
Right UA	QD Trim	$\pm$0.3	$\pm$20	1	1	9	Ring 1/2 Trim
Right UA	QF Trim	$\pm$0.3	$\pm$20	1	1	9	Ring 1/2 Trim
Right UA	Lattice Sextupole F1,2,D1,2	0.6	12	4	8	7	Right Lattice Sextupoles
Right UA	Lattice Octupole F1,2,D1,2	$\pm$0.6	$\pm$12	4	8	8	Right Lattice Octupoles
Right UA	Sextupole Spool Piece	$\pm$0.6	$\pm$12	2	4	8	Right Sextupole Spool Pieces Ring 1,2
Right UA	Decapole Spool Piece	$\pm$0.6	$\pm$12	2	4	8	Right Decapole Spool Pieces Ring 1,2
Right UA	Outer triplet, Q4,5,6	12.5	8	6	7	3	Individual powering, Separate R1,R2
Right UA	Dispersion Trim Q7,8,9,10	0.6	12	8	16	7	Individual powering, Separate R1,R2
Right UA	Skew Quads next to Q4,6,8,10	$\pm$0.6	$\pm$12	8	16	8	Individual powering, Separate R1,R2
Right UA	MB Energy extraction (Q7,Q8,Q9,Q10)	12.5		1			Extraction switch and resistor Powered by Main Quad Buses

Total Power Converters (PC) Current 338 kA Qty PC's 236
Total Current in Feedthroughs 522 kA

Table 3: Point 3 – List of circuits

PC/Equip. Location	Circuit	Current (kA)	U Peak (U)	Qty of Circuits	Qty of Feedthru.	Pow. Con. Type	Remark
Tunnel	(Q6,Q7,Q8,Q9,Q10) MB Energy extraction	12.5		2	4		Powered by Main Quad Buses Extraction switch and resistor (Left and Right)
UJ33	Trim on Q6	0.6	12	2	8	7	Individual powering, Separate R1,R2, Left
UJ33	Dispersion Trim Q7,8,9,10	0.6	12	8	32	7	Individual powering, Separate R1,R2, Left
UJ33	Skew Quads next to Q8,Q10	±0.6	±12	2	8	8	Individual powering, Separate R1,R2, Left
UJ33	Trim on Q6	0.6	50	2	8	20	Individual powering, Separate R1,R2, Right
UJ33	Dispersion Trim Q7,8,9,10	0.6	50	8	32	20	Individual powering, Separate R1,R2, Right
UJ33	Skew Quads next to Q8,Q10	±0.6	±50	2	8	21	Individual powering, Separate R1,R2, Right
SR3	Separators D3, D4	0.67	650	1	Warm	16	All in series, left/right, R1/R2
SR3	Q3,Q4,Q5	0.75	450	3	Warm	18	Series connected left/right, R1/R2
UJ33	Arc CODs	±0.032	±115	44	Local	12	23 half cells × R1,R2 × Left
UJ33	Mid-arc CODs	±0.05	±115	2	Local	15	
UJ33	Insertion CODs	±0.05	±15	10	Local	13	R1,R2, Left
UJ33	Insertion CODs warm	±0.21	±60	6	Warm	10	R1,R2, Left
UJ33	Arc CODs	±0.032	±115	44	Local	12	22 half cells × R1,R2 × Right
UJ33	Insertion CODs	±0.05	±15	10	Local	13	R1,R2 × Right
UJ33	Insertion CODs warm	±0.21	±60	6	Warm	10	R1,R2, Right

Total Power Converters (PC) Current 24 kA Qty PCs 150

Total Current in Feedthroughs 79 kA

PC/Equip. Location	Circuit	Current (kA)	U Peak (U)	Qty of Circuits	Qty of Feedthru.	Pow. Con. Type	Remark
	(Q6,Q7,Q8,Q9,Q10)						Powered by Main Quad Buses
Left UA	MB Energy extraction	12.5		1			Extraction switch and resistor
Left UA	MB	12.5	±195	1	2	1	Left Main Dipole, Ring 1 in series with Ring 2
Left UA	QD	12.5	15	1	2	2	Left QD Ring 1 in series with Ring 2
Left UA	QF	12.5	15	1	2	2	Left QF Ring 1 in series with Ring 2
Left UA	QD Trim	±0.3	±20	1	1	9	Ring 1/2 Trim
Left UA	QF Trim	±0.3	±20	1	1	9	Ring 1/2 Trim
Left UA	Lattice Sextupole F1,2,D1,2	0.6	12	4	8	7	Left Lattice Sextupoles
Left UA	Lattice Octupole F1,2,D1,2	±0.6	±12	4	8	8	Left Lattice Octupoles
Left UA	Sextupole Spool Piece	±0.6	±12	2	4	8	Left Sextupole Spool Pieces Ring 1,2
Left UA	Decapole Spool Piece	±0.6	±12	2	4	8	Left Decapole Spool Pieces Ring 1,2
Left UA	Dispersion Trim Q7,8,9,10	0.6	12	8	16	7	Individual powering, Separate R1, R2
Left UA	Skew Quads next to Q8,Q10	±0.6	±12	2	4	8	Qs8/Qs10 in series, Separate R1, R2
Left UA	Insertion Quads, Q4,Q5,6	12.5	8	6	9	3	Individual powering, Separate R1,R2
Left UA	Insertion Quads, Q2,3	9	10	4	8	4	Individual powering, Separate R1,R2
Left UA	Separators D3,D4	5.5	5	1	4	5	All in series, two cryostats
Central	Arc CODs	±0.032	±115	88	Local	12	23 half cells × R1,R2 × Left, Right
Central	Mid-arc CODs	±0.05	±115	2	Local	15	
Central	Q2 to Q10 CODs	±0.05	±50	36	Local	11	R1,R2 × Left, Right

Table 4: Point 4 – List of circuits (cont.)

PC/Equip. Location	Circuit	Current (kA)	U Peak (V)	Qty of Circuits	Qty of Feed-thru.	Pow. Con. Type	Remark
Right UA	Insertion Quads Q4,5,6	12.5	8	6	9	3	Individual powering, Separate R1, R2
Right UA	Insertion Quads, Q2,3	9	10	4	8	4	Individual powering, Separate R1, R2
Right UA	Separators D3,D4	5.5	5	1	4	5	All in series, two cryostats
Right UA	MB	12.5	±195	1	2	1	Right Main Dipole, Ring 1 in series with Ring 2
Right UA	QD	12.5	15	1	2	2	Right QD Ring 1 in series with Ring 2
Right UA	QF	12.5	15	1	2	2	Right QF Ring 1 in series with Ring 2
Right UA	QD Trim	±0.3	±20	1	1	9	Ring 1/2 Trim
Right UA	QF Trim	±0.3	±20	1	1	9	Ring 1/2 Trim
Right UA	Lattice Sextupole F1,2,D1,2	0.6	12	4	8	7	Right Lattice Sextupoles
Right UA	Lattice Octupole F1,2,D1,2	±0.6	±12	4	8	8	Right Lattice Octupoles
Right UA	Sextupole Spool Piece	±0.6	±12	2	4	8	Right Sextupole Spool Pieces Ring 1,2
Right UA	Decapole Spool Piece	±0.6	±12	2	4	8	Right Decapole Spool Pieces Ring 1,2
Right UA	Dispersion Trim Q7,8,9,10	0.6	12	8	16	7	Individual powering, Separate R1, R2
Right UA	Skew Quads next to Q8,Q10	±0.6	±12	2	4	8	Qs8/Qs10 in series, Separate R1, R2
Right UA	MB Energy extraction (Q6,Q7,Q8,Q9,Q10)	12.5		1			Extraction switch and resistor Powered by Main Quad Buses

Total Power Converters (PC) Current 340 kA Qty PC's 202
Total Current in Feedthroughs 411 kA

PC/Equip. Location	Circuit	Current (kA)	U Peak (U)	Qty of Circuits	Qty of Feedthru.	Pow. Con. Type	Remark
	(Q7,Q8,Q9,Q10)						Powered by Main Quad Buses
Tunnel	MB Energy extraction	12.5		2	4		Extraction switch and resistor (Left and Right)
US55	Outer triplet, Q4,5,6	12.5	8	12	14	3	Individual powering (R1, R2, left and right)
US55	Dispersion Trim Q7,8,9,10	0.6	12	16	32	7	Individual powering (R1, R2, left and right)
US55	Skew Quads next to Q4,6,8,10	±0.6	±12	8	16	8	Left and right in series, R1 and R2
Central	Arc CODs	±0.032	±115	88	Local	12	23 half cells × R1, R2 × Left, Right
Central	Mid-arc CODs	±0.05	±115	2	Local	15	
Central	Q4 CODs	±0.05	±50	8	Local	11	R1, R2 × Left, Right × 2 (Horiz. + Vert.)
Central	Q5 to Q10 CODs	±0.05	±50	24	Local	11	R1, R2 × Left, Right
Central	D2 CODs	±0.05	±50	8	Local	11	R1, R2 × Left, Right × 2 (Horiz. + Vert.)
US55	Separators D1	9	10	1	2	4	Left and right in series
US55	Separators D2	9	10	2	4	4	R1 left in series with R2 right, etc.
US55	Low-β Q1,2,3.	6	10	2	4	5	Series connected, Individual powering left and right
US55	Low-β trim Q01,03	0.6	12	4	8	7	Individual powering
US55	Low-β Dipole Corr.	±0.6	±12	8	16	8	Left and Right, Horiz. and Vert. × 2
Central	Low-β Skew Quad. Corr.	±0.025	±8	2	4	14	Left and Right
Central	Low-β Dodecap. Corr.	±0.025	±8	4	8	14	Left and Right × 2
Central	Low-β Skew Dodecap.	±0.025	±8	2	4	14	Left and Right

Total Power Converters (PC) Current 216 kA Qty PC's 191
Total Current in Feedthroughs 347 kA

PC/Equip. Location	Circuit	Current (kA)	U Peak (V)	Qty of Circuits	Qty of Feedthru.	Pow. Con. Type	Remark
	(Q7,Q8,Q9,Q10)						Powered by Main Quad Buses
Left UA	MB Energy extraction	12.5		1			Extraction switch and resistor
Left UA	MB	12.5	±195	1	2	1	Left Main Dipole, Ring 1 in series with Ring 2
Left UA	QD	12.5	15	1	2	2	Left QD Ring 1 in series with Ring 2
Left UA	QF	12.5	15	1	2	2	Left QF Ring 1 in series with Ring 2
Left UA	QD Trim	±0.3	±20	1	1	9	Ring 1/2 Trim
Left UA	QF Trim	±0.3	±20	1	1	9	Ring 1/2 Trim
Left UA	Lattice Sextupole F1,2,D1,2	0.6	12	4	8	7	Left Lattice Sextupoles
Left UA	Lattice Octupole F1,2,D1,2	±0.6	±12	4	8	8	Left Lattice Octupoles
Left UA	Sextupole Spool Piece	±0.6	±12	2	4	8	Left Sextupole Spool Pieces Ring 1,2
Left UA	Decapole Spool Piece	±0.6	±12	2	4	8	Left Decapole Spool Pieces Ring 1,2
Left UA	Dispersion Trim Q7,8,9,10	0.6	12	8	16	7	Individual powering, Separate R1, R2
Left UA	Skew Quads next to Q8,Q10	±0.6	±12	2	4	8	Qs8/Qs10 in series, Separate R1, R2
Left UA	Outer triplet, Q5,6	12.5	8	4	8	3	Individual powering, Separate R1, R2
Left UA	Q3,4	6	8	4	8	6	Individual powering, Separate R1, R2
SR6	Septum	1	1000	1	Warm	19	Left and right in series
Central	Arc CODs	±0.032	±115	88	Local	12	23 half cells × R1, R2 × Left, Right
Central	Mid-arc CODs	±0.05	±115	2	Local	15	
Central	Q3 to Q10 CODs	±0.05	±50	32	Local	11	R1, R2 × Left, Right

Table 6: Point 6 – List of circuits (cont.)

PC/Equip. Location	Circuit	Current (kA)	U Peak (V)	Qty of Circuits	Qty of Feedthru.	Pow. Con. Type	Remark
Right UA	Outer triplet, Q5,6	12.5	8	4	8	3	Individual powering, Separate R1, R2
Right UA	Q3,4	6	8	4	8	6	Individual powering, Separate R1, R2
Right UA	MB	12.5	±195	1	2	1	Right Main Dipole, Ring 1 in series with Ring 2
Right UA	QD	12.5	15	1	2	2	Right QD Ring 1 in series with Ring 2
Right UA	QF	12.5	15	1	2	2	Right QF Ring 1 in series with Ring 2
Right UA	QD Trim	±0.3	±20	1	1	9	Ring 1/2 Trim
Right UA	QF Trim	±0.3	±20	1	1	9	Ring 1/2 Trim
Right UA	Lattice Sextupole F1,2,D1,2	0.6	12	4	8	7	Right Lattice Sextupoles
Right UA	Lattice Octupole F1,2,D1,2	±0.6	±12	4	8	8	Right Lattice Octupoles
Right UA	Sextupole Spool Piece	±0.6	±12	2	4	8	Right Sextupole Spool Pieces Ring 1,2
Right UA	Decapole Spool Piece	±0.6	±12	2	4	8	Right Decapole Spool Pieces Ring 1,2
Right UA	Dispersion Trim Q7,8,9,10	0.6	12	8	16	7	Individual powering, Separate R1, R2
Right UA	Skew Quads next to Q8,Q10	±0.6	±12	2	4	8	Qs8/Qs10 in series, Separate R1, R2
Right UA	MB Energy extraction (Q7,Q8,Q9,Q10)	12.5		1			Extraction switch and resistor Powered by Main Quad Buses

Total Power Converters (PC) Current 256 kA Qty PC's 193

Total Current in Feedthroughs 452 kA

Table 7: Point 7 – List of circuits

PC/Equip. Location	Circuit	Current (kA)	U Peak (V)	Qty of Circuits	Qty of Feedthru.	Pow. Con. Type	Remark
Tunnel	(Q6,Q7,Q8,Q9,Q10) MB Energy extraction	12.5		2	4		Powered by Main Quad Buses Extraction switch and resistor (Left and Right)
UJ76	Trim on Q6	0.6	50	4	8	20	Individual powering, Separate R1, R2, Left, Right
UJ76	Trim on Q7,8,9,10	0.6	50	16	32	20	Individual powering, Separate R1, R2, Left, Right
UJ76	Skew Quads next to Q8,Q10	±0.6	±50	4	8	21	Qs8/Qs10 in series, Separate R1, R2, Left, Right
SR7	Separators D3,D4	0.67	650	1	Warm	16	All in series, left/right, R1/R2
SR7	Q3,Q4,Q5	0.75	450	3	Warm	18	Series connected left/right, R1/R2
UJ76	Arc CODs	±0.032	±115	88	Local	12	23 half cells × R1,R2 × Left, Right
UJ76	Mid-arc CODs	±0.05	±115	2	Local		
UJ76	Insertion CODs	±0.05	±50	20	Local	11	R1,R2, Left, Right
UJ76	Insertion CODs warm	±0.21	±60	12	Local	10	R1,R2, Left, Right

Total Power Converters (PC) Current 24 kA Qty PC's 150
Total Current in Feedthroughs 79 kA

Table 8: Point 8 – List of circuits

PC/Equip. Location	Circuit	Current (kA)	U Peak (V)	Qty of Circuits	Qty of Feedthru.	Pow. Con. Type	Remark
	(Q7,Q8,Q9,Q10)			1			Powered by Main Quad Buses
Left UA	MB Energy extraction	12.5					Extraction switch and resistor
Left UA	MB	12.5	±195	1	2	1	Left Main Dipole, Ring 1 in series with Ring 2
Left UA	QD	12.5	15	1	2	2	Left QD Ring 1 in series with Ring 2
Left UA	QF	12.5	15	1	2	2	Left QF Ring 1 in series with Ring 2
Left UA	QD Trim	±0.3	±20	1	1	9	Ring 1/2 Trim
Left UA	QF Trim	±0.3	±20	1	1	9	Ring 1/2 Trim
Left UA	Lattice Sextupole F1,2,D1,2	0.6	12	4	8	7	Left Lattice Sextupoles
Left UA	Lattice Octupole F1,2,D1,2	±0.6	±12	4	8	8	Left Lattice Octupoles
Left UA	Sextupole Spool Piece	±0.6	±12	2	4	8	Left Sextupole Spool Pieces Ring 1,2
Left UA	Decapole Spool Piece	±0.6	±12	2	4	8	Left Decapole Spool Pieces Ring 1,2
Left UA	Outer triplet, Q4,5,6	12.5	8	6	7	3	Individual powering, Separate R1, R2
Left UA	Dispersion Trim Q7,8,9,10	0.6	12	8	16	7	Individual powering, Separate R1, R2
Left UA	Skew Quads next to Q4,6,8,10	±0.6	±12	8	16	8	Individual powering, Separate R1, R2
Left UA	Separators D1	9	10	1	2	4	Individual powering
Left UA	Separators D2	9	10	2	3	4	Individual powering, Separate R1, R2
Left UA	Low-β Q1,2,3.	6	10	1	2	5	Series connected
Left UA	Low-β trim Q01,03	0.6	12	2	4	7	Individual powering
Left UA	Low-β Dipole Corr.	0.6	12	4	8	7	Horiz. and Vert. $\times$ 2
Left UA	Low-β Skew Quad. Corr.	±0.025	±8	1	2	14	
Left UA	Low-β Dodecap. Corr.	±0.025	±8	2	4	14	$\times$ 2
Left UA	Low-β Skew Dodecap. Corr.	±0.025	±8	1	2	14	
Central	Arc CODs	±0.032	±115	88	Local	12	23 half cells $\times$ R1, R2 $\times$ Left, Right
Central	Mid-arc CODs	±0.05	±115	2	Local	15	
Central	Q4 CODs	±0.050	±50	8	Local	11	R1, R2 $\times$ Left, Right $\times$ 2 (Horiz. + Vert.)
Central	Q5 to Q10 CODs	±0.050	±50	24	Local	11	R1, R2 $\times$ Left, Right

Table 8: Point 8 – List of circuits (cont.)

PC/Equip. Location	Circuit	Current (kA)	U Peak (V)	Qty of Circuits	Qty of Feedthru.	Pow. Con. Type	Remark
Central	D2 CODs	±0.050	±50	8	Local	11	R1, R2 × Left, Right × 2 (Horiz. + Vert.)
Right UA	Separators D1	9	10	1	2	4	Individual powering
Right UA	Separators D2	9	10	2	3	4	Individual powering, Separate R1, R2
Right UA	Low-β Q1,2,3	6	10	1	2	5	Series connected
Right UA	Low-β trim Q01,03	0.6	12	2	4	7	Individual powering
Right UA	Low-β Dipole Corr.	0.6	12	4	8	7	Horiz. and Vert. × 2
Right UA	Low-β Skew Quad. Corr.	±0.025	±8	1	2	14	
Right UA	Low-β Dodecap. Corr.	±0.025	±8	2	4	14	× 2
Right UA	Low-β Skew Dodecap. Corr.	±0.025	±8	1	2	14	
Rigth UA	MB	12.5	±195	1	2	1	Right Main Dipole, Ring 1 in series with Ring 2
Right UA	QD	12.5	15	1	2	2	Right QD Ring 1 in series with Ring 2
Right UA	QF	12.5	15	1	2	2	Right QF Ring in series with Ring 2
Right UA	QD Trim	±0.3	±20	1	1	9	Ring 1/2 Trim
Right UA	QF Trim	±0.3	±20	1	1	9	Ring 1/2 Trim
Right UA	Lattice Sextupole F1,2D1,2	0.6	12	4	8	7	Right Lattice Sextupoles
Right UA	Lattice Octupole F1,2D1,2	±0.6	±12	4	8	8	Right Lattie Octupoles
Right UA	Sextupole Spool Piece	±0.6	±12	2	4	8	Right Sextupole Spool Pieces Ring 1,2
Right UA	Decapole Spool Piece	±0.6	±12	2	4	8	Right Decapole Spool Pieces Ring 1,2
Right UA	Outer triplet Q4,5,6	12.5	8	6	7	3	Individual powering, Separate R1, R2
Right UA	Dispersion Trim Q7,8,9,10	0.6	12	8	16	7	Individual powering, Separate R1, R2
Right UA	Skew Quads next to Q4,6,8,10	±0.6	±12	8	16	8	Individual powering, Separate R1, R2
Right UA	MB Energy extraction (Q7,Q8,Q9,Q10)	12.5		1			Extraction switch and resistor Powered by Main Quad Buses

Total Power Converters (PC) Current 338 kA Qty PC's 236
Total Current in Feedthroughs 522 kA

Table 9: Lattice circuits

Power Converter Circuits	Function	Current (kA)	Steady-state Voltage (v)	Charging Voltage (v)	Points	Total Quantity	Remarks
Main Dipoles	R1R2	12.5	10	±185	2,4,6,8	8	Sector feed (1/8), left and right
Main Quadrupoles	F1F2, D1D2	12.5	10	±5	2,4,6,8	16	Sector feed (1/8), left and right
R1/R2 Quad. Trim		±0.3	±20		2,4,6,8	16	Sector feed (1/8), left and right
Lattice Sextupole	F1,D1,F2,D2	0.6	8	4	2,4,6,8	32	Sector feed (1/8), left and right
Octupole Correction	F1,D1,F2,D2	±0.6	±8	±4	2,4,6,8	32	Sector feed (1/8), left and right
Sextupole, Spoolpiece	R1,R2	±0.6	±8	±4	2,4,6,8	16	Sector feed (1/8), left and right
Decapole, Spoolpiece	R1,R2	±0.6	±8	±4	2,4,6,8	16	Sector feed (1/8), left and right

Table 10: Provisional LHC Power Consumption (Beam Transfer Lines not included)

Point	Cryogenics *** (MW)	Power Converters (MW)	Power Converters Peak (MW)	Cooling/ Ventilation Absorbed (MW)	Cooling/ Ventilation Installed (MVA)	Experiments (MW)	Others Dump/ RF,etc. (MW)	Total Steady State (MW)	Feeder
1		1.5	1.8	4.0	9.6	5.0	1.0	11.5	SE1
2	11.8	2.7	8.0	3.5	9.8	6.0	1.0	25.0	66 kV
3		2.5	2.6	0.5	1.0		0.5	3.5	18 kV Loop
4	11.8	2.8	8.0	2.9	9.8		5.0	22.5	66 kV
5		1.5	1.8	4.0	9.6	4.0	1.0	10.5	New 18 kV from pt 6
6	11.8	3.2	8.3	2.9	9.8		1.5	19.4	66 kV
7		2.2	2.3	0.5	1.0		0.5	3.2	18 kV Loop
8	11.8	2.7	8.0	3.4	9.8		1.0	18.9	66 kV
TOTAL	47	19	41	22		15	12	114	
General Services on the 18 kV loop = 10 MW Total including General Services 125.75 MW									

*** Ultimate power consumption

Table 11: LHC Power Converter List

(OUTPUT PARAMETERS)							
Type	Current (kA)	Steady State Voltage (V)	Peak Voltage (V)	Steady State Power (kW)	Peak Power (kW)	Qty	Application
1	12.5	10	±195	125.0	2437.5	8	Main Dipole
2	12.5	10	15	125.0	187.5	16	Main Quadrupole
3	12.5	6	8	75.0	100.0	68	Outer Triplet
4	9	6	10	54.0	90.0	26	Separators
5	6	6	10	36.0	60.0	10	Low-β, D3–4 pt 4
6	6	5	5	30.0	30.0	8	Q3, Q4 (pt 6)
7	0.6	8	12	4.8	7.2	154	Qtrims, Sextupoles
8	±0.6	±5	±12	3.0	7.2	154	Qs, Spool Piece, Octupoles
9	±0.3	±20	±20	6.0	6.0	16	Main Quadrupole Trim
10	±0.21	±60	±60	12.6	12.6	24	Warm insertion CODs
11	±0.05	±50	±50	2.5	2.5	258	Insertion CODs
12	±0.032	±115	±115	3.7	3.7	704	Arc CODs
13	±0.05	±15	±15	0.8	0.8	10	Insertion CODs pt 3
14	±0.025	±8	±8	0.2	0.2	32	Low-β correctors
15	±0.05	±115	±115	5.8	5.8	16	Mid-arc CODs
16	0.75	650	650	487.5	487.5	2	Separators D3 D4 (pt 3)
18	0.75	450	450	337.5	337.5	6	Warm Quads (pt 3 and 7)
19	1	1000	1000	1000.0	1000.0	1	Beam Dump Septum
20	0.6	46	50	27.6	30.0	30	Qtrim pt 3 and 7
21	±0.6	±43	±50	25.8	30.0	6	Qskew pt 3 and 7

Total Current 1,752 kA
Total Quantity of PCs 1,549